INSTITUTE FOR OIL SANDS INNOVATION AT THE UNIVERSITY OF ALBERTA
Breakthrough Energy Research | Advanced Environmental Technologies

Imperial ALBERTA INNOVATES FACULTY OF ENGINEERING

IOSI PROJECT FINAL REPORT

Project Number	IOSI 2015-03
Project Title	**Multifunctional non-precious upgrading catalysts**
Project Budget and Tenure	$138,750 (NSERC CRD), $138,750 (IOSI) Three years: April 1, 2016 to July 31, 2019
Principal Investigator	Natalia Semagina, University of Alberta semagina@ualberta.ca
HQP	Ali Mansouri (PhD student) Jing Shen (PDF) Amir Rouhi (PhD student)
Stewards	Mustafa Al-Sabawi Murray R. Gray
Report Prepared by	Natalia Semagina
Date	October 31, 2019

DISCLAIMERS

Alberta Innovates (AI) and Her Majesty the Queen in right of Alberta make no warranty, express or implied, nor assume any legal liability or responsibility for the accuracy, completeness, or usefulness of any information contained in this publication, nor that use thereof infringe on privately owned rights. The views and opinions of the author expressed herein do not necessarily reflect those of AI or Her Majesty the Queen in right of Alberta. The directors, officers, employees, agents and consultants of AI and the Government of Alberta are exempted, excluded and absolved from all liability for damage or injury, howsoever caused, to any person in connection with or arising out of the use by that person for any purpose of this publication or its contents.

The University of Alberta makes no warranty, express or implied, nor assumes any legal liability or responsibility for the accuracy, completeness, or usefulness of any information contained in this publication, nor that use thereof infringes on privately owned rights. The views and opinions of the author expressed herein do not necessarily reflect those of the University of Alberta. The directors, officers, employees, agents, students and consultants of the University of Alberta are exempted, excluded and absolved from all liability for damage or injury, howsoever caused, to any person in connection with or arising out of the use by that person for any purpose of this publication or its contents.

EXECUTIVE SUMMARY

Energy-saving technologies are in increasingly high demand in all sectors of processing and manufacturing. The use of catalysts is a key to sustainable development as they significantly reduce the temperature and pressure requirements and allow for process miniaturization and environmental care. The more active the catalyst is in any process, the lower the greenhouse gas emissions and the higher the economic benefits are. Their use in fossil fuel industries is indispensable and will further augment as we search for more environmentally friendly and economically viable technologies, addressing at the same time the problem of the worsening quality of the feedstocks.

This NSERC-CRD project resulted in the development of multifunctional Earth-abundant catalysts with the potential to a paradigm shift in partial upgrading of bitumen. The catalysts combine the functions that are currently performed by two different types of catalysts (metallic and acidic); one of the functions requires significantly lower temperatures than the current catalysts and does not lead to the product loss to light fractions. We also gained mechanistic insight into the currently practiced upgrading operation that potentially can further reduce the energy requirements.

The studies were performed using a model feed with sulfur, nitrogen and olefin compounds. Several catalysts were identified for further exploration in a real feed. The catalysts rely on the use of hydrogen gas, although potentially may be extended to other hydrogen donors.

Three young researchers have been trained in this project in the area of chemical and materials engineering and are currently employed in industry and academia. Two manuscripts were published (ACS Catalysis and ACS Applied Nano Materials) and one more is to be submitted to the Chemical Engineering Science.

TABLE OF CONTENTS

1 INTRODUCTION

1.1 Project objectives

The project addresses the development of a multifunctional catalyst for the upgrading of a complex model feed via hydrodesulfurization (HDS), hydrodenitrogenation (HDN), hydrogenation (HYD) and hydrocracking (HCK). The suggested catalyst, based on scarce literature data, is based on niobium (Nb) because its sulfide and oxide are acidic and were shown to be highly active in the above-mentioned hydrotreating model reactions. However, bulk Nb oxide is a highly thermodynamically stable compound, and harsh sulfidation conditions were needed to synthesize the active sulfided form. This was believed to prevent Nb use in hydrotreating operations.

In the proposal, based on thermodynamic considerations, we suggested using a copper (Cu) promoter to synthesize the required Nb active sites. Fig. 1(a) demonstrates how Cu addition removes the thermodynamic limitations for the Nb sulfide formation.

The overarching project objective was not to find the replacement for commercial Co-Mo or Ni-Mo catalysts but to exploit their alternatives possessing different functional abilities and evaluate if such catalysts could provide some benefit for alternative hydrotreating applications. The fundamental objective, which can be applied to the general catalysis field, was to demonstrate that a properly selected promoter can catalyze synthesis of required active sites. The set objectives were achieved, mostly, as expected, based on theoretical predictions from our proposal, with some findings that may affect the low-temperature hydrotreating process development in partial upgrading.

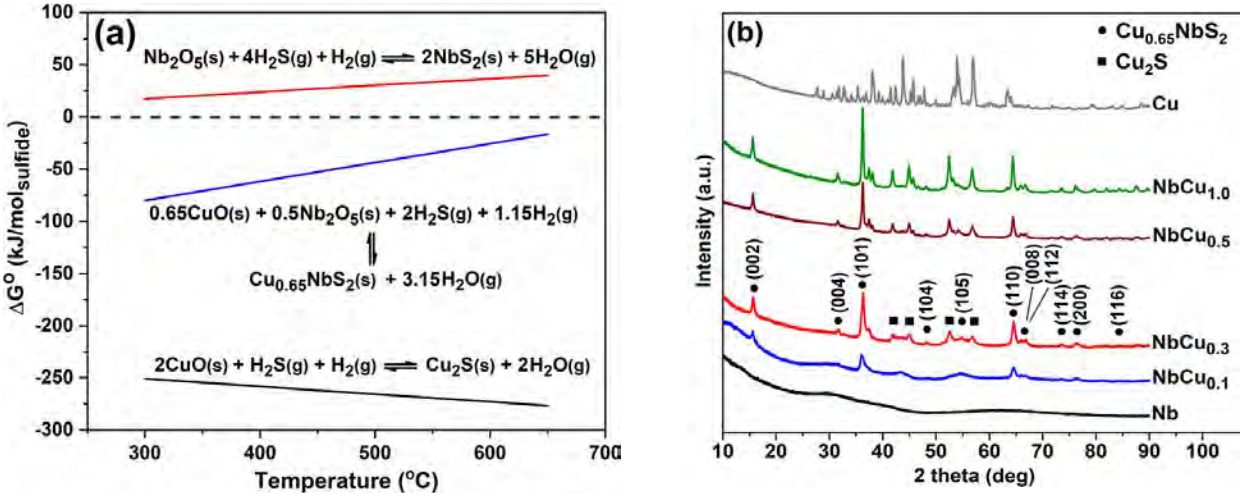

Fig. 1. (a). Theoretical prediction of how Cu addition to Nb_2O_5 removes thermodynamic limitations of its sulfidation; (b) experimental proof of the hypothesis: X-ray diffraction pattern of the sulfided catalysts: note that no NbS_2 peaks are present for the Nb-only sample. Reprinted with permission from A. Mansouri, N. Semagina, ACS Catalysis 2018, 8, 7621. © 2018 ACS

1.2 Progress made towards these objectives as a result of the grant

Promotion of active site synthesis. The foremost objective was to demonstrate a rather new concept in catalysis that a promoter is not necessarily needed to affect the catalytic function but rather to serve as a catalyst for active site synthesis. This was achieved in the project. In addition, what we did not expect, but it was a fascinating discovery, is that at a certain ratio, this promoter was only a spectator during the catalytic performance. At its lack, the active sites formation was not achieved, while its excess led to the active site blockage and activity loss.

We demonstrated that Cu addition during Nb_2O_5 sulfidation results in the formation of sulfided Nb that is active in all four reactions of interest (HDS, HDN, HYD, and HCK). The thorough catalyst characterization before and after sulfidation was performed for different Nb/Cu ratios. We used a variety of state-of-the art methods to prove the required phase formation. Fig. 1(b) shows X-ray diffraction patterns demonstrating the copper effect. It is important that the sulfidation occurred at industrially relevant conditions of 400 ^oC, instead of 700 ^oC as other authors demonstrated earlier as a required temperature for Nb_2O_5 to NbS_2 sulfidation. The detailed report can be found in Section 2.

HDS, HYD and HCK performance of bulk catalysts. The HDS performance of different synthesized catalysts were shown for a model feed containing dibenzothiophene (DBT) at 325 ^oC and 3 MPa H_2. We indeed observed an enhanced desulfurization product yield for some NbCu catalysts. Fig. 2 shows the yield of S-free and hydrocracking products for various catalysts. The hydrocracking occurred to monocyclic hydrocarbons, and no lights formation (at least on the bench-scale) was observed. The NbCu catalyst surpassed the HDS activity of unpromoted MoS_2, which is often reported as a catalyst for slurry hydrotreaters, thus, the former material can be recommended to replace MoS_2. It could not, however, surpass the HDS activity of promoted CoMo conventional catalysts, but was different from CoMo as it enhanced the DBT hydrocracking to benzene and toluene (with no lights formation).
Potentially, the Nb and/or NbCu catalysts could be beneficial for hydrotreatment of high molecular-weight feeds due to their enhanced cracking and hydrogenating ability, as opposed to CoMo and Mo. The detailed report can be found in Section 2.

Carbon-supported catalysts for HDS, HYD and HCK. To increase the catalyst activity per Nb atom, carbon-supported catalysts were synthesized. The use of an oxalate precursor lessened the thermodynamic complications connected to the bulk Nb_2O_5 oxidation, and NbS_2 phase formation was achieved without the use of Cu. In this case, Cu blocked the active sites, as seen in Fig. 3.
The carbon-supported catalysts were rather unusual in their behavior. Most likely due to the lower active particle size and the higher fraction of Nb oxides, they possessed a significantly enhanced cracking activity at 325 ^oC (again, no lights formation was observed, but only monocyclic semi-hydrogenated hydrocarbons), in addition to the sulfur removal ability. In comparison, the carbon-supported Mo only and MoNi catalysts showed cracking selectivity below 5%. The detailed report can be found in Section 4.

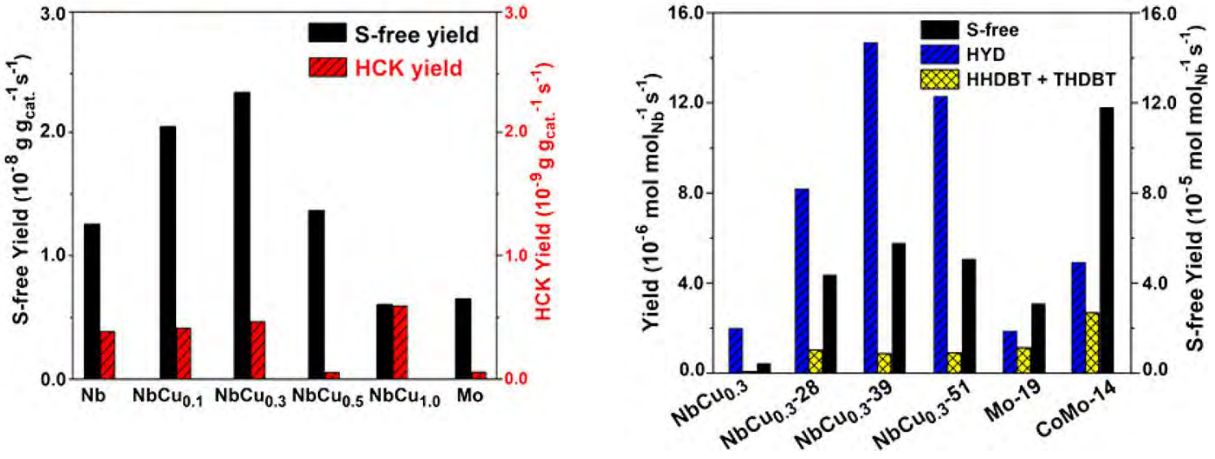

Fig. 2. Weight-time product yields in HDS of DBT at 325 °C and 3 MPa H_2 after 24 hours on stream. The subscript in the catalyst notation refers to the Cu/Nb atomic ratio. The number after the dash shows the surface area of the materials after sulfidation (where omitted, the areas were < 10 m^2/g). HHDBT and THDBT are S-containing hydrogenation products. Reprinted with permission from A. Mansouri, N. Semagina, ACS Catalysis 2018, 8, 7621. © 2018 ACS

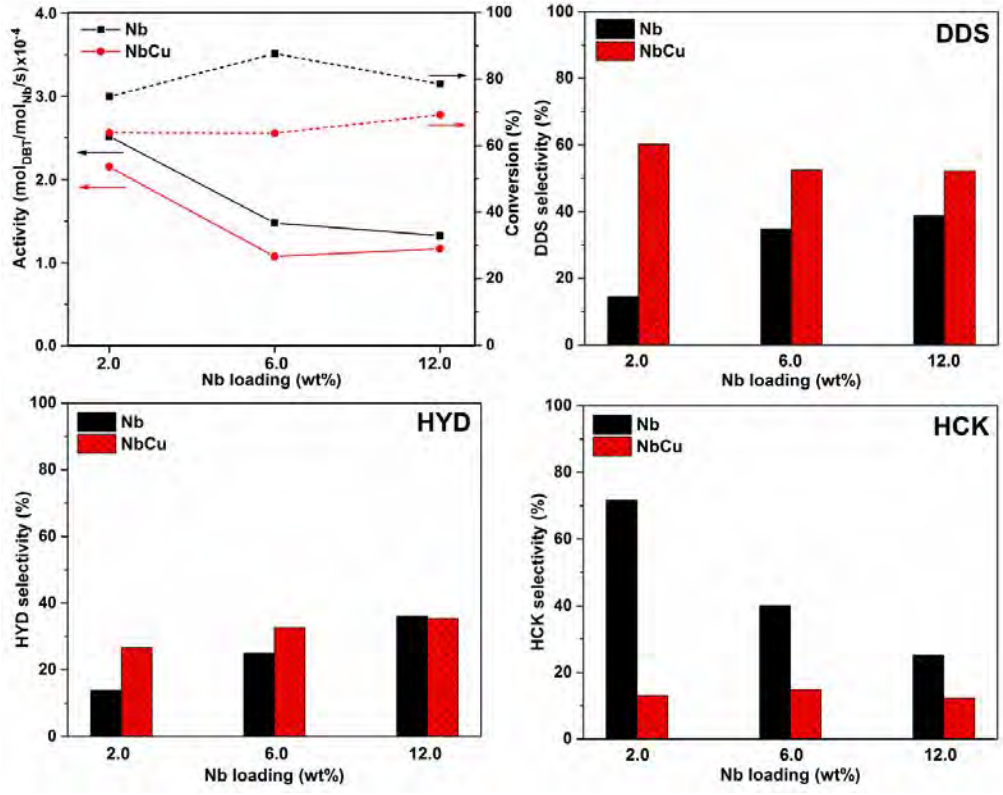

Fig. 3. Direct desulfurization (DDS), hydrogenation (HYD) and cracking to monocyclic hydrocarbons (HCK) using carbon-supported Nb and Nb-Cu catalysts with different Nb loading during HDS of DBT at 325 °C and 3 MPa H_2 after 24 hours on stream. Reprinted from A. Mansouri, Ph.D. Thesis, University of Alberta, 2017.

Colloidal catalysts for HDS, HYD and HCK. Another way to lessen the thermodynamic constraints of bulk Nb_2O_5 oxidation is to use the approach of colloidal nanoparticle synthesis. The colloidal NbS_2 catalysts could also be beneficial if slurry hydrotreatment is targeted. We developed a versatile procedure to synthesize a variety of colloidal NbS_2 nanoparticles (Fig. 4), and tested them in the HDS of DBT. The electron microscopy images of the spent catalysts after 24 h of HDS revealed the structural stability of the nanostructures with no signs of aggregation and deformation. As shown in Table 1, the highest HDS activity was obtained by NbS_2 nanohexagons, followed by nanorods, nanospheres, and single-layer nanosheets. Although the nanospheres possessed a smaller size (25 nm), the nanohexagons delivered higher activity, which can be attributed to the enhanced fraction of corner and edge active sites. The HDS reaction rate and the sulfur-free yield delivered by the nanohexagon catalyst were about an order of magnitude higher than that of Nb-based bulk catalyst discussed above. The detailes report can be found in Section 3.

Table 1. HDS of DBT over supported NbS_2 catalysts at 325 °C and 3.0 MPa after 24 h.

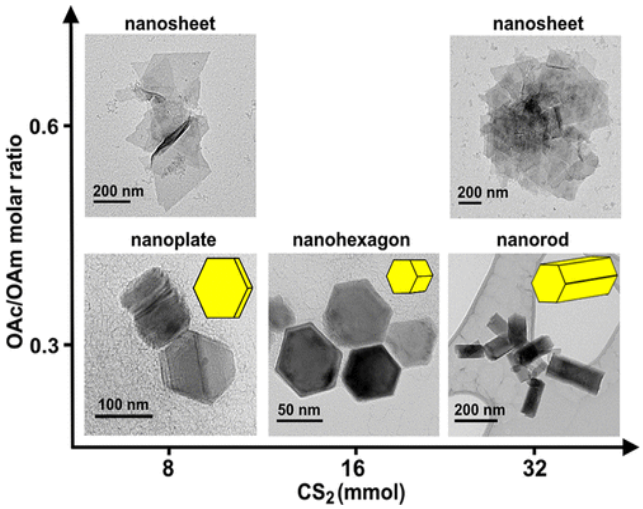

Catalyst	Activity (10^{-5} mol_{DBT} mol_{Nb}^{-1} s^{-1})	Yield of sulfur-free products (10^{-5} mol mol_{Nb}^{-1} s^{-1})
Single-layer nanosheets	7	6
Multilayers nanosheets	4	2
Nanohexagon	98	49
Nanorod	61	40
Nanosphere	33	26

Fig.4. NbS_2 structure dependence on the molar ratio of OAc to OAm (oleic acid and oleyamine used for synthesis) and the amount of CS_2. Reprinted from A. Mansouri, N. Semagina, ACS Applied Nano Materials 2018, 1, 4408. © 2018 ACS

Nitrogen effect on the HDS. The bulk catalysts were also demonstrated to perform the hydrodenitrogenation of quinoline at 325 °C. The nitrogen compound, as expected, inhibited the sulfur removal and cracking performance.

Without quinoline, DBT was converted by hydrogenation and direct desulfurization path rather equally. Quinoline completely suppressed the hydrogenation path of DBT conversion, but not the direct desulfurization path. Quinoline was mostly hydrogenated with some N removal. A rather similar N effect on active sites was observed at lower temperatures, as shown below.

Table 2. HDS of DBT (1,000 ppm S) and HDN of quinoline (Q, 300 ppm N) over bulk $NbCu_{0.3}$ catalyst at 325 °C and 3 MPa.

HDS of DBT		HDN of Q		
DBT conversion	BP selectivity	Q conversion	Denitrogenation selectivity	Hydrogenated Q intermediates selectivity
14%	94%	33%	26%	74%

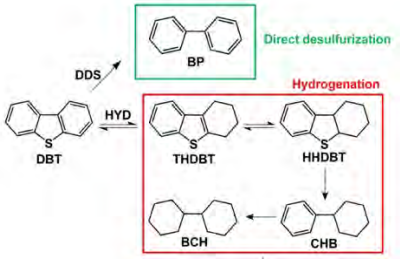

Low-temperature low-pressure hydrotreating (Fig. 5, 6). We assessed a variety of catalysts for hydrogenation of internal conjugated diolefin 2,5-dimethyl-2,4-hexadiene in the presence of dibenzothiophene (up to 1,000 ppm S) and quinoline (up to 250 ppm N) at mild conditions (150 – 180 °C and 10 – 20 bar H_2). The approach is not new, and it is practiced to hydrogenate olefins over a conventional Ni-Mo catalyst after thermal cracking prior feeding to the naphtha hydrotreater. The purpose is to remove diolefins to avoid addition and condensation reactions and prevent fouling. The process is also of interest for partial upgrading, to meet the pipeline specifications for olefin content.

In the past few years, the reaction kinetics, catalyst deactivation, and reactor fouling during (di)olefin hydrogenations were mostly assessed from the viewpoint of (di)olefin conversion only, with and without added sulfur in the feed. The assessed catalyst had been a conventional hydrotreating sulfided Ni-Mo catalyst. In this project, we assessed how the presence of a basic nitrogen compound (quinoline) affects the hydrogenation of refractory internal conjugated diolefins for a variety of catalysts. The main potentially valuable finding was not only that N significantly inhibits diolefin hydrogenation with no paraffin formation, but also that the use of a sulfided nickel-only catalyst may provide increased hydrogenation ability as compared to the typically used Ni-Mo catalyst. Note that the used Ni-Mo catalyst was prepared in-house and may not show the same behavior as the commercial Ni-Mo catalyst.

Fig. 5 demonstrates the N poisoning effect on a variety of non-precious metal catalysts. As it is seen on the reaction schematic for this model feed, no DBT conversion occurs, quinoline is hydrogenated and diolefin is hydrogenated to internal olefins. No alkane formation was observed (the products were identified by gas chromatography-mass spectrometry). Thus, although the diene number can be decreased, the process is limited to decrease the olefin number for monoolefins with an internal double bond.

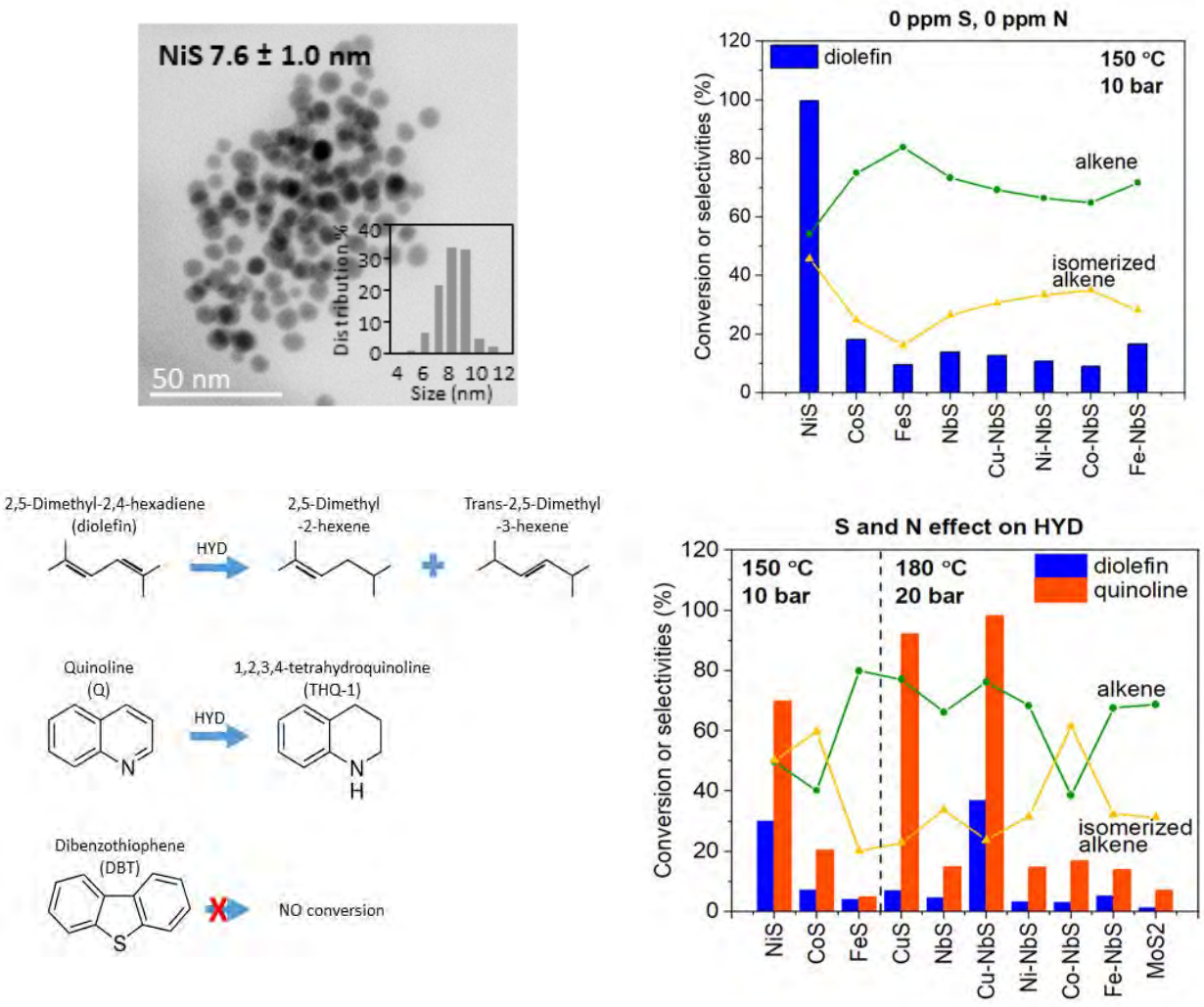

Fig. 5. An example of a synthesized catalyst (Ni sulfide) and the activity of sulfided catalysts in the hydrogenation of diolefin in the presence of quinoline and DBT. Feed: 0.5 wt% diolefin, 300 ppm S (0.17 wt% DBT) and 100 ppm N (0.09 wt% Q), balanced in decalin with n-C_{12} internal standard.

The reaction kinetics was evaluated for the most active NiS catalyst (Fig. 6). Without nitrogen presence, diolefin hydrogenation follows an expected 1st order (not shown here). In the presence of quinoline, diolefin hydrogenation demonstrates 0th order with respect to diolefin and -1st order to the total nitrogen concentration. The quinoline and its hydrogenation product apparently poison one of the two types of active sites available for diolefin hydrogenation, which can explain the shifting reaction order assuming the Langmuir-Hinshelwood reaction mechanism. This hypothesis is in line with the 0th order to quinoline hydrogenation (Fig. 6c). In-house "near-conventional" Ni-Mo sulfide catalyst shows much lower activity than the Mo-free catalyst. The detailed report can be found in Chapter 5.

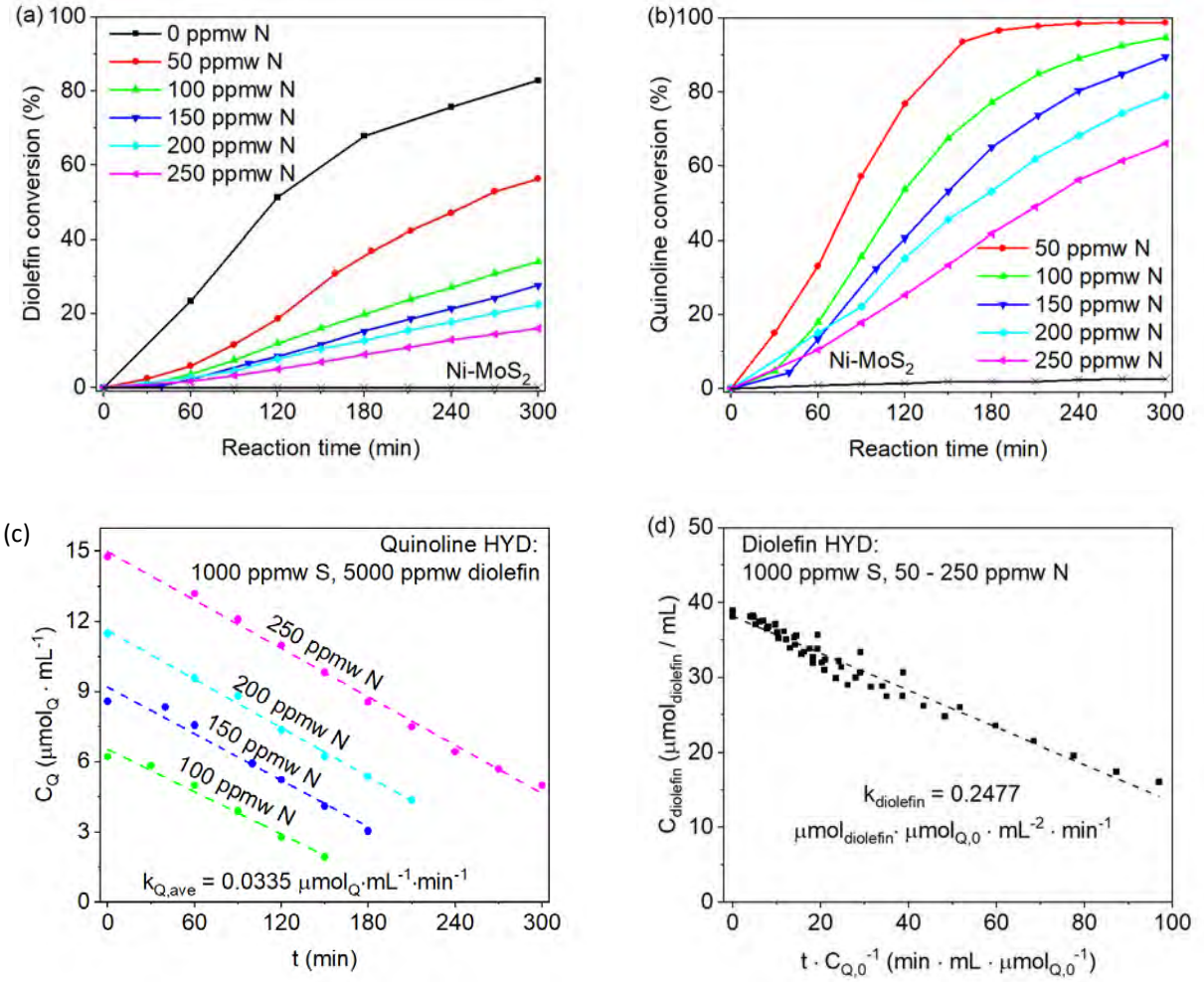

Fig. 6. Kinetic study of 2,5-dimethyl-2,4-hexadiene hydrogenation over 3 g of NiS/γ-Al_2O_3 catalyst at 150 °C, 10 bar H_2, with the presence of 1000 ppm S (5.8 wt% DBT) and 0 – 250 ppm N (0.23 wt% Q). (a,b) diolefin and quinoline conversions vs time; (c,d) rate constants and a graphical evaluation of reaction orders to quinoline and diolefin.

Deviations from the original objectives.

There were no significant deviations, except that we used different nitrogen and olefin model compounds that were more representative of the real feed. The quinoline choice and model compound concentrations were recommended by the project stewards.

Highly qualified personnel trained (HQP).

Three young researchers have been trained in this project in the area of chemical and materials engineering and are currently employed in industry and academia (Canada and Germany).

Scientific and/or engineering significance of the results achieved.

The primary scientific significance is that we suggested and demonstrated a concept that a promoter may catalyze synthesis of active sites. During the catalytic action, the promoter behaves only as a spectator, unless it is used at high surface concentrations. We proved the concept for the sulfided catalysts, but it can be applied for other catalysts that could not be synthesized otherwise because of thermodynamic limitations.

In terms of applied knowledge, we identified Nb-based catalysts as materials with similar HDS and HDN functions as conventional CoMo or NiMo catalysts, but in addition, they possess high hydrocracking activity towards monocyclic hydrocarbons, with no lights formation. Potentially, the Nb catalysts could be beneficial for hydrotreatment of high molecular-weight feeds due to their enhanced cracking and hydrogenating ability, as opposed to CoMo and Mo.

The Nb catalysts could also be used for low-severity hydrotreatment, but they were surpassed by more active and less expensive NiS. The latter demonstrated the higher activity to diolefin hydrogenation than the conventional NiMo catalyst (prepared in-house). None of the open studies, to our knowledge, had addressed the effect of basic nitrogen compounds on olefin/diolefin hydrogenation and catalyst deactivation during low-severity hydrogenations. The nitrogen presence not only suppresses the hydrogenation rate but also changes the reaction order. These findings must be beneficial to practitioners working on olefin hydrogenation of the thermally cracked feed. We recommend comparing the industrial NiMo catalyst with NiS only, as the in-house catalysts showed the superior ability of the Ni-only catalyst for conjugated diolefin and quinoline hydrogenation.

2 PROMOTION OF NIOBIUM OXIDE SULFIDATION BY COPPER AND ITS EFFECTS ON HYDRODESULFURIZATION CATALYSIS

This Section was published as
*Mansouri A., Semagina N. Promotion of niobium oxide sulfidation by copper and its effects on hydrodesulfurization catalysis, **ACS Catalysis**, 8, 7621-7632 (2018).*
It is reprinted here with the permission from American Chemical Society, the permission is attached to the report.

2.1 Abstract

Niobium sulfide (NbS_2) has shown a promising performance in versatile applications, but its formation from Nb oxide is thermodynamically limited, which hinders its usage. We predicted, based on thermodynamic calculations, and experimentally verified that the addition of copper (Cu) to niobium promotes Nb oxide sulfidation at practical temperatures. A series of bimetallic bulk NbCu structures at varying Cu/Nb molar ratios were synthesized via a coprecipitation technique. X-ray photoelectron spectroscopy (XPS) and temperature-programmed reduction (TPR) results revealed that copper facilitated sulfidation and reduction of niobium oxide. The synthesized NbCu catalysts were evaluated in hydrodesulfurization (HDS) of dibenzothiophene (DBT) at 325 °C and 3 MPa. Copper promotes sulfidation but does not change the turnover frequency of surface NbS_2 and behaves as a spectator. The optimal Cu/Nb molar ratio was found to be 0.3, below which there is not enough Cu to ensure maximum sulfidation and above which copper segregates to the catalyst surface and blocks NbS_2 active sites. The weight-based sulfur-removal activity of the optimal catalyst was doubled in the presence of copper. This study demonstrates that the bimetallic earth-abundant NbCu catalyst could be a promising candidate for hydrotreating catalysis. Since Cu-promoted NbS_2 was found more active than molybdenum sulfide per mass and surface area, the copper addition may be recommended for thermodynamically limited niobium oxide sulfidation to promote NbS_2 formation as a potential alternative to MoS_2 for a variety of emerging applications with transition metal sulfides. The study also demonstrates that the concept of promotion in catalysis can be extended to the assisted increase of the number of active sites, with no effect on their performance during catalysis.

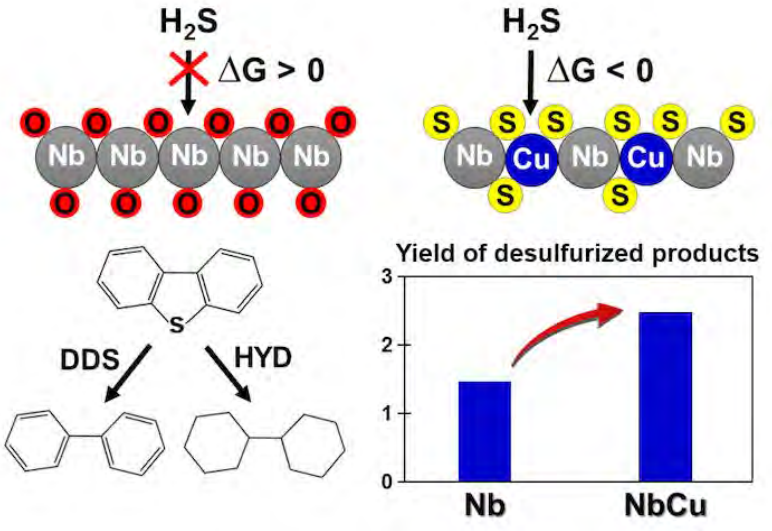

2.2 Introduction

Transition metal sulfides (TMS) are known as efficient catalysts in the production of fuels from petroleum-based feedstocks, renewable bio-oils, and syngas.[1–9] The tunable structural and electronic properties of TMS also make them attractive and versatile for optoelectronics,[10] energy storage materials,[11–13] and solar cells,[14,15] and as photo- and electro-catalysts for hydrogen evolution[16–19] and CO_2 reduction[20,21]. For instance, ultrathin layered niobium disulfide (NbS_2) behaves as a semiconductor,[22] while bulk NbS_2 is known for its superconductivity at low temperatures.[23] The interest in TMS has been ignited for the purpose of fuel upgrading and coal liquefaction.[24] For decades, molybdenum sulfide-based catalysts have been used in petroleum hydrotreating units for removing heteroatoms such as nitrogen, oxygen, and sulfur;[1,25–33] however, other TMS across the periodic table from Group IVB to Group VIIIB also have shown HDS activities better than MoS_2.[34] Lacroix et al.[35] investigated HDS of DBT and hydrogenation of biphenyl (BP) for the first- and second-row unsupported TMS. Following noble metal sulfides, NbS_2 was the highest intrinsically active TMS, more active than MoS_2 and WS_2 catalysts. Among the TMS examined, NbS_2 hydrocracked BP to single-ring products that revealed the particular cracking and isomerization properties of an Nb species.[35,36] Nb-based catalysts are acidic in sulfide and oxide states.[35,37,38] The higher HDS activities of niobium sulfides were further verified in several studies.[39,40] Niobium as dopant improved the DBT HDS and tetralin hydrogenation activities of an industrial $NiMo/Al_2O_3$ catalyst.[41] Opposed to the strong effects of H_2S on the performance of conventional HDS catalysts, the activity and durability of NbS_2 was found insensitive to H_2S partial pressure.[36,42,43] Moreover, Nb made the MoS_2/Al_2O_3 catalyst insensitive to the H_2S partial pressure as compared to $NiMo/Al_2O_3$.[44] Nb is 16 times more abundant than Mo in the Earth's crust[45] and, thus, represents a competitive alternative to MoS_2 in affected applications.

NbS_2 and niobium trisulfide (NbS_3) are the most common structures of niobium sulfides. NbS_2 exhibits the same structural features as MoS_2, a lamellar arrangement of trigonal prisms $[NbS_6]$[46,47] in which metal layers are sandwiched between two sulfur layers within a hexagonal cell.[48] Mean sulfur bond energy in NbS_2 is 66 kcal/mol, which is similar to that of MoS_2 at 60 kcal/mol. Both elements have high energy of sulfur extraction;[49] however, the *d*-band filling of NbS_2 is different than that of MoS_2.[49] NbS_3 consists of the same prismatic units, but the infinite-fiber Nb-S slabs are formed by sharing the triangular face of $[NbS_6]$ prisms.[39] NbS_3 is more active in HDS than NbS_2, which is likely due to the presence of anionic vacancies functioning as active sites;[35,36,39,50] however, in general, the thermal stabilities of trisulfide structures (NbS_3, MoS_3, WS_3) are low, and they transform to disulfides (NbS_2, MoS_2, WS_2) under hydrotreatment conditions, depending on reaction temperature, H_2S partial pressure, and the textural properties of the material.[35,36]

Despite the above-mentioned benefits of Nb-based catalysts, sulfidation of niobium oxides is not as facile as sulfidation of MoO_3 and WO_3.[37,39,51] The high affinity of niobium to oxygen results in extremely stable niobium pentoxide (Nb_2O_5) and niobium dioxide (NbO_2) compounds with heats of formation at -380 and -395 kJ/mol, respectively, which are greater than MoO_3 (-248 kJ/mol) and WO_3 (-279 kJ/mol).[22] Reportedly, the hydrogen reduction of bulk Nb_2O_5

initiates at 800 °C, which reduces to bulk Nb_2O_4 at 1300 °C.[52] The Gibbs free energies for the sulfidation of NbO_2 and Nb_2O_5 with H_2S at 600 K are positive, $\Delta G°$= +82 and +108 kJ/mol, respectively, as compared to MoO_3 ($\Delta G°$= -119 kJ/mol);[51] however, bulk NbS_x can be obtained from the elemental mixture of niobium and sulfur at elevated temperatures (i.e., 700 °C for NbS_3 and above 800 °C for NbS_2), which leads to sintering and low surface area (less than 3 m^2/g).[22,36,46,50] Such a high reduction/sulfidation temperature in a reductive atmosphere is not industrially operable that hinders the usage of NbS_x-based catalysts in many applications. It is important to note that a strong metal-support interaction between Nb and oxide supports further impedes its sulfidation.[39,50,51,53] Allali et al.[39] reported that a higher sulfidation of Nb and, thus, HDS activity was obtained on carbon support as compared to alumina.

The objective of the present work was to demonstrate that the concept of promotion in catalysis can be extended to the assisted increase of the number of active sites, with no effect on their performance during catalysis. Herein, the sulfidation extent of Nb_2O_5 at a practically relevant temperature was increased with the addition of a promoter, copper being selected based on thermodynamic calculations. The synthesized bulk catalysts were evaluated in HDS of DBT (Scheme 1) at 325 °C and 3 MPa. The addition of copper led to higher Nb sulfidation, DBT conversion, and improved sulfur extraction from hydrogenated sulfurous intermediates, and it doubled the weight-time yield of sulfur-free products. Up to a certain Cu/Nb ratio, copper promotes sulfidation but does not change the turnover frequency of surface NbS_2 and behaves as a spectator. Above the optimal ratio, copper segregates to the catalyst surface and blocks NbS_2 active sites. This is the first report on bimetallic NbCu as an HDS catalyst and as a promotion of Nb_2O_5 reduction and sulfidation by copper addition.

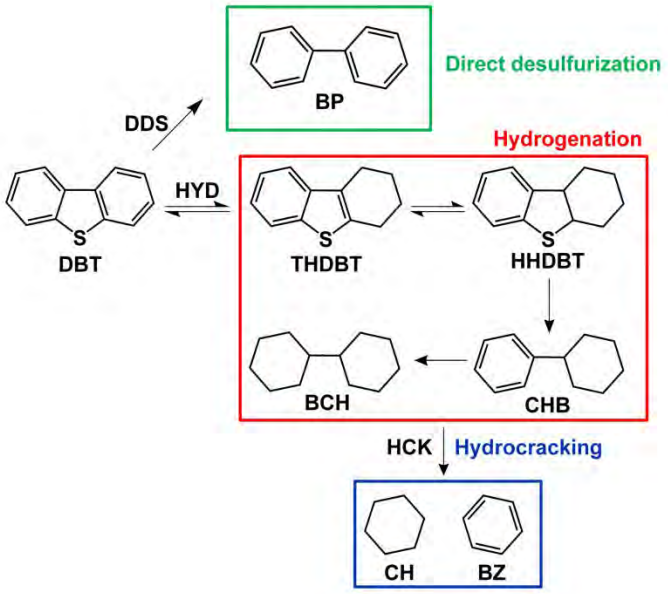

Scheme 1. DBT hydrodesulfurization pathways. A similar product distribution was reported earlier.[54]

2.3 Experimental

2.3.1 Materials

Copper (II) nitrate trihydrate, $Cu(NO_3)_2 \cdot 3H_2O$, ammonium niobate (V) oxalate hydrate ($C_4H_4NNbO_9 \cdot xH_2O$), niobium (V) chloride ($NbCl_5$), ammonium heptamolybdate tetrahydrate ($H_{24}Mo_7N_6O_{24}.4H_2O$), and cobalt (II) nitrate hexahydrate ($Co(NO_3)_2.6H_2O$) from Sigma–Aldrich were used for catalyst preparation. Pluronic P123 triblock co-polymer ($(EO)_{20}(PO)_{70}(EO)_{20}$, ethylene oxide (EO), propylene oxide (PO), MW= 5800, from Sigma Aldrich) was employed to synthesize high surface area catalysts. Gamma-alumina (γ-Al_2O_3, 150 mesh, 100 µm diameter, average pore diameter of 58 Å, BET=155 m^2/g) from Sigma-Aldrich was used as the catalyst support. Ammonium hydroxide (50 vol. %) from Ricca Chemical Company was used as a precipitating agent. 1000 ppmw sulfur as dibenzothiophene (DBT, $C_{12}H_8S$, Sigma-Aldrich) was dissolved in *n*-decane (Fisher Scientific) as a solvent with 3.5 wt% *n*-dodecane (Sigma-Aldrich) as the internal standard, and it was used as a model fuel for HDS reaction. Carbon disulfide (CS_2, Sigma-Aldrich) was dissolved in *n*-decane at 10 wt% and was used for sulfidation. Ultra-high purity (99.999%) argon and hydrogen gases were purchased from Praxair Canada.

2.3.2 Catalyst preparation

A series of bulk bimetallic $NbCu_x$ catalysts (x represents the molar ratio of copper to niobium) catalysts were prepared via a coprecipitation method using oxalate species and ammonium hydroxide as the precipitating agents. Ammonium niobate (V) oxalate hydrate and niobium chloride were used as the niobium precursors. The former precipitates copper species without using external precipitant.[55] Ammonium hydroxide was used as the precipitant in the case of niobium chloride precursor. High surface area catalysts were prepared via a soft-templating approach.

Preparation of low surface area catalysts (BET below 10 m^2/g): The low BET surface area catalysts were prepared using niobium oxalate species. Typically, to synthesize $NbCu_{0.3}$, about 18.8 mmol of niobium precursor would be dissolved in 20 ml of distilled water to reach a clear solution; however, the copper-containing solution was prepared by dissolving 4.6 mmol of $Cu(NO_3)_2 \cdot 3H_2O$ in 5 ml of distilled water. Next, the copper solution was quickly injected into the niobium solution while mixing vigorously, which led to the formation of a blue precipitate. The slurry was mixed for 30 min to achieve a homogeneous mixture, and then it was dried at 110 °C for 24 h without filtration. The synthesized catalysts were calcined in static air at 400 °C for 4 h before characterization and reaction (based on the TGA profile, Figure S1 in Supporting Information). Monometallic Nb, Cu, and Mo catalysts were prepared by calcination of a corresponding dried precursor (110 °C, overnight) at 400 °C for 4 h.

Preparation of high surface area catalysts (BET above 10 m^2/g): Pluronic P123 triblock co-polymer was used to increase the BET surface areas of the bulk catalysts. The high BET surface area catalysts are labelled as $NbCu_x$-M where M represents the value of BET surface area

measured after sulfidation at 400 °C for 20 h. The amount of P123 in the synthesis solution was optimized to achieve the highest BET surface area for $NbCu_{0.3}$ sample, as the best Nb-based bimetallic catalyst in HDS catalysis. To synthesize $NbCu_{0.3}$-51 catalyst (BET=51 m^2/g), 28.2 mmol of $NbCl_5$ was dissolved in 20 ml of ethanol in which 6.9 mmol of $Cu(NO_3)_2{\cdot}3H_2O$ was then added resulting in the formation of a green solution with no precipitation. The obtained solution was added dropwise into 50 ml ethanol containing 3.5 g P123. After 1 h of mixing at room temperature, ammonium hydroxide was added dropwise to form a blue precipitate at the pH of 11.0. The slurry was mixed for 1 h at room temperature and then at 50 °C for 24 h. Similarly, in the case of oxalate precipitation, 28.2 mmol of niobium oxalate in 20 ml distilled water was added into 50 ml ethanol containing P123. After 1 h mixing, the copper solution was added to form a blue precipitate; however, the humidity of the slurry was kept consistent by adding ~40 ml of distilled water. Monometallic Mo-19 catalyst was prepared by dropwise addition of an aqueous solution of molybdenum 2 M in 50 ml ethanol containing P123. Bulk CoMo-14 was prepared by incipient wetness impregnation (IWI) of calcined Mo-19 with an aqueous cobalt solution to reach Co/Mo molar ratio of 0.3. All the synthesized catalysts were dried at 65 °C and then 110 °C for two successive days followed by 4 h calcination in static air at 400 °C.

Conventional Al_2O_3-supported CoMo catalyst (CoMo/γ-Al_2O_3, 12.0 wt% Mo and 2.0 wt% Co) was synthesized via a successive IWI method (first Mo and then Co) with interval drying at 100 °C and 4 h calcination at 500 °C. Before each HDS test, the catalysts were grounded and sieved to 125 µm particle size.

2.3.3 Catalyst characterization

High-resolution transmission electron microscopy (HRTEM) and scanning transmission electron microscopy (STEM) coupled with energy dispersive X-ray spectroscopy (EDS) analyses were conducted using a JEOL JEM-ARM200cF S/TEM, which is equipped with a cold Field-Emission Gun (cFEG) and a probe Cs corrector. EDX maps were acquired on the gold TEM grids using a Silicon Drift (SDD) EDS detector at an acceleration voltage of 200 kV. Field Emission Scanning Electron Microscopy (FESEM) images coupled with energy dispersive X-ray spectroscopy (EDS) were recorded using a scanning electron microscope (Zeiss Sigma FESEM/ EDS & EBSD). Silicon wafer was used for EDS analysis. XPS analyses were performed with a Kratos Axis 165 X-ray photoelectron spectrometer using a Mono Al Kα source that operates at 14 kV and 15 mA. Angle-resolved XPS analyses at 0 and 60 degrees were acquired on thin pelettized forms of samples. Peak analyses were performed using a CasaXPS software package, and the XPS spectra were corrected with C 1s at 284.8 eV. X-ray diffraction (XRD) patterns were recorded using a Rigaku Ultima IV diffractometer equipped with a D/Tex detector, iron filter, and Co Kα radiation (λ = 1.78899 Å). The diffraction patterns were collected from 5 to 90 degrees on a continuous scan at 2 degrees 2-theta per minute with a step size of 0.02 degrees. Data interpretation was performed using JADE 9.6 with the 2016 ICDD and 2016 ICSD databases. Specific surface area (BET) analyses were conducted using an Autosorb-iQ Quantachrome. About 0.3 g of sample was degassed under vaccuum at 130 °C for 2 h before each analysis. Hydrogen temperature-programed reduction (H_2-TPR) was performed using a Micromeritics Autochem II 2920 apparatus equipped with a thermal conductivity detector (TCD). About 100 mg of the calcined

catalysts were degassed by helium (He) at 150 °C for 1 h. TPR analysis was performed using a 10 ml/min of 10 mol% H_2 in argon (Ar) at the heating rate of 10 °C/min from room temperature up to 900 °C. Ammonia (NH_3) chemisorption analyses were performed using the same device. The sulfided sample was treated with He at 120 °C for 1 h and then cooled down to 100 °C. Next, a 5 mol% NH_3/He was micropulsed to determine the amount of adsorbed NH_3. Diffuse-reflectance infrared Fourier-transform (DRIFT) spectra of the calcined samplese were collected using NEXUS 670 FT-IR fitted with a smart diffuse reflectance accessory. About 50 mg of the sample was mixed with 500 mg of dried KBr for each measurement. DRIFT spectra were recorded three times against a KBr standard with 256 scans and a resolution of 4 cm^{-1}. The resolution enhancement and data processing were performed with OMNIC software. Thermogravimetric analysis (TGA) was performed using a Mettler Toledo TGA/DSC1 STARe System. About 20 mg of the dried sample was loaded in an alumina crucible, and the temperature was increased to 700 °C at a rate of 10 °C/min under 50 ml/min nitrogen gas.

2.3.4 Catalytic experiments

HDS of DBT was conducted at 325 °C and 3.0 MPa hydrogen pressure using a fixed-bed plug-flow reactor (stainless steel, L=22”, i.d.=0.5”). The catalysts were diluted with silicon carbide (mesh 120, 14:1 weight ratio) to achieve isothermal plug-flow conditions in the reactor. The effects of the reactor wall and axial dispersion were calculated as negligible.[56] The absence of external and internal mass transfer limitations was verified by Mears and Weisz-Prater criteria, respectively. The heat transfer limitations were found to be negligible by Mears criterion.[57] The calculation procedure was explained elsewhere.[58] The catalysts were sulfided *in situ* before each HDS reaction. The sulfidation method was optimized to achieve the highest HDS activity at practical operating conditions. Typically, the pressurized reactor (with pure hydrogen gas at 3.0 MPa) was heated at a rate of 8 °C/min up to 175 °C where the sulfidation feed (10 wt% CS_2 in *n*-decane) was introduced into the reactor downward at 0.05 ml/min using a Series II high-pressure pump. The amount of CS_2 in *n*-decane during sulfidation corresponded to pH_2S/pH_2 of 0.01. The liquid feed was pre-mixed with 100 ml/min hydrogen gas before it was fed into the reactor. Then, the temperature ramped at 5 °C/min up to 400 °C, where it was maintained for an additional 20 h. After cooling down the system to 325 °C under sulfidation conditions, a model liquid fuel containing 1000 ppmw sulfur as DBT in *n*-decane (as solvent) with 3.5 wt% *n*-dodecane as the internal standard was then introduced into the reactor at 0.05 ml/min. The liquid feed was mixed with 100 ml/min hydrogen gas to reach the hydrogen-to-liquid molar ratio of 16. The used WHSV are listed in the Supporting Information (Table S1). All the HDS experiments were performed for 24 h on-stream with overnight stabilization to reach the steady-state conditions. The difference in conversion between 6 and 24 h on-stream was below 5%. During the HDS reaction, the pH_2S/pH_2 was adjusted at 2.55×10^{-4} using the concentration of DBT in the feed stream to stabilize the structure in its sulfide state. This ratio is 7 orders of magnitude higher than the required thermodynamic value as shown below.[51]

Indentification of the reaction products was carried out off-line by a gas chromatography coupled with mass spectrometry (GC-MS) using a Hewlett Packard G1800A GCD GC-MS

equipped with a DB5-MS column (25 m, 0.25 mm, 0.25 µm film thickness) and an enhanced ChemStation G17001AA, version A.03.00. The quantitative analyses of DBT and the reaction products were performed using the internal standard in the feed with a calibrated Agilent 7890A gas chromatograph equipped with a H-PONA Agilent capillary column (50 m, 0.25 mm, 0.25 µm film thickness) with a flame ionization detector. No cracking of the solvent and internal standard alkanes was observed by GC-MS. The carbon mass balance was above 96%. Selectivities were reported on molar basis as a fraction of mole of product per mole of all reaction products. As indicated in Scheme 1, the reaction products were categorized into direct desulfurization (DDS), hydrogenation (HYD), and hydrocracking (HCK). The selectivity to the direct desulfurization (DDS) path was the selectivity to biphenyl. The selectivity to the HYD path was the summation of selectivities to cyclohexylbenzene (CHB), bicyclohexyl (BCH), tetrahydrodibenzothiophene (THDBT), and hexahydrodibenzothiophene (HHDBT). HCK selectivity includes benzene and cyclohexane. For the reaction rate calculation, rate constants were calculated from exit conversions based on a first-order rate law, followed by the constant multiplication by the initial concentration of DBT in the feed. The reported conversions are subject to 10% experimental error. For selectivities, two standard deviations were 3%.

2.4 Results and discussion

2.4.1 Thermodynamics of niobium oxide sulfidation

The target was to overcome the thermodynamic limitations of the NbS_x phase formation by alloying with another metal sulfide in such a way that the resulting structure would maintain similarities with a catalytically active NbS_x edge. To achieve this, the second metal should have a significantly low negative Gibbs free energy (ΔG°) of sulfidation to offset the high positive ΔG° of Nb_2O_5 sulfidation. Furthermore, the promoter should possess lower surface free energy than niobium and should form sulfide that is less stable than NbS_x. This way, the promoter would concentrate on the surface of Nb and provide active sites for S activation through H_2S dissociation. Once the sulfur is adsorbed on the promoter, its migration to Nb should be favored, which is possible if Nb sulfide free energy is lower than the promoter sulfide free energy. As an example,[59] when sulfur adsorbs on Pt, it stays on its surface instead of migrating into the bulk because of the much lower surface free energy of sulfur than Pt. On the other hand, Cu and Zn have lower surface free energies than Pt when they concentrate on the surface, but Zn does not promote Pt sulfidation. This is due to the much stronger Zn-S bond that prohibits the migration of sulfur from the surface into the bulk of Pt; whereas, the Cu-S bond is less strong than the Pt-S bond at facilitating sulfur migration into Pt bulk.[59]

According to the above-mentioned criteria, we investigated several metal sulfides as an alloying component for Nb, such as Cu, Fe, Co, Mo, V, Cd, Cr, Zn, W, and Mn. We excluded Pt-group metals in this study because of their high cost and limited availability in nature. Based on the thermodynamic data,[51] Fe, Co, Ni, Cr, Zn, and Mn have a positive or not low enough negative ΔG° of sulfidation to promote Nb_2O_5 sulfidation. Vanadium sulfide was found to be more stable than niobium sulfide. The stability of MoS_2 and WS_2 are slightly lower than that of NbS_2,[51] which

may not provide a sufficient driving force for sulfur migration from Mo or W to niobium. Overall, only Cu and Cd satisfied the selection criteria; however, Cd is one of six hazardous materials listed in the Restriction of Hazardous Substances Directive adopted in 2003 by the European Union. This leaves Cu as the potential candidate to promote niobium oxide sulfidation.

Literature indicates that $Cu_{0.65}NbS_2$ is the most abundant Cu-Nb-S species.[60,61] Its preparation from individual oxides is described below:

$$0.65\ CuO(s) + 0.5\ Nb_2O_5(s) + 2\ H_2S(g) + 1.15\ H_2(g) \Leftrightarrow Cu_{0.65}NbS_2(s) + 3.15\ H_2O(g) \quad (1)$$

The Gibbs energy of formation of $Cu_{0.65}NbS_2$ from elements can be calculated based on the approach proposed for mixed sulfides from individual sulfides (i) based on the assumption of ideal mixing. N_i is the mole fraction of a component sulfide in the formation reaction, which is 0.65/2 for Cu_2S and 1 for NbS_2.[62]

$$\Delta G_f^o = \sum[N_i\, \Delta G_{f,i}^o] + 5.02\ R\ T\ \sum[N_i \ln N_i] \quad (2)$$

Figure 1a shows the Gibbs free energies of formation of mono- and bimetallic sulfides from corresponding oxide structures using H_2S and H_2 as a function of temperature in the range of 300–650 °C. The thermochemical analysis reveals that the addition of Cu to Nb_2O_5 removes the thermodynamic limitation for sulfidation of Nb_2O_5. The large difference between the stability of NbS_2 ($\Delta G^o_{(f),\ 600\ K}$ = -330 kJ/mol) and Cu_2S ($\Delta G^o_{(f),\ 600\ K}$ = -56 kJ/mol) should promote sulfur migration from copper sulfide to NbO_x species. Figure 1b displays the required H_2S to H_2 partial pressure ratios for the stability of the alloyed sulfide NbCu structure as a function of temperature. The low ratio in the order of 10^{-9} indicates that the sulfide will be stable under typical hydrotreating conditions.

The structure of $Cu_{0.65}NbS_2$ was described previously.[60,61] Niobium ions are present in the centers of the trigonal prisms of sulfur ions that are similar to NbS_2, which may provide a similar performance in catalytic reactions. However, the stacking of copper-intercalated NbS_2 differs from the pure NbS_2 crystal, which may provide synergistic or antagonistic effects as compared to the pure NbS_x. Besides, the lower surface energy of copper may prevent its migration to the bulk of the Nb material and can even block niobium active sites. Thus, in the following experimental work, we synthesized, characterized, and evaluated the HDS activity of NbCu materials with different Nb/Cu ratios.

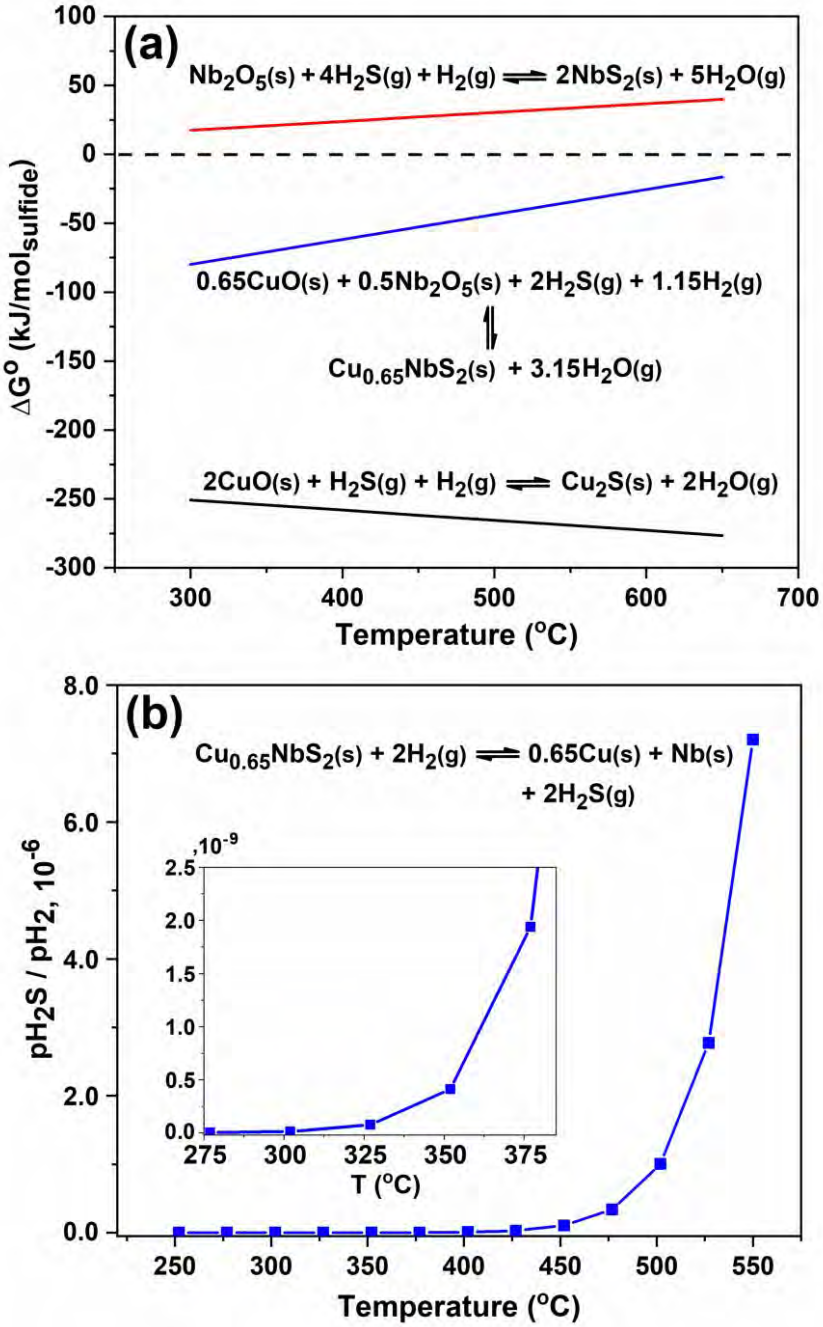

Figure 1. (a) Gibbs free energy of formation of metal sulfides from oxide structures using H_2S and H_2; (b) required H_2S/H_2 partial pressure for stability of bimetallic NbCu sulfide as a function of temperature.

2.4.2 Catalyst characterization

Table 1 illustrates the physicochemical properties of the synthesized mono- and bimetallic catalysts. The surface areas were measured after sulfidation under pH_2S/pH_2 of 0.01 and 400 °C for 20 h. The adsorption-desorption isotherms are shown in the Supporting Information. Precipitation using oxalate species resulted in the low surface area materials (below 10 m^2/g), which is in agreement with previous studies for the Nb materials.[22,36,46,50] The surface areas were improved up to 53 m^2/g using a Pluronic P123 template. The highest BET surface area obtained for Mo-based sample was 19 m^2/g which reduced to 14 m^2/g after the addition of cobalt. Table 1 also lists the amounts of chemisorbed ammonia, as an indication of the acidic properties of the sulfided catalysts. Niobium-based catalysts exhibited the higher ammonia uptakes per surface area as compared to the Mo and CoMo catalysts, which agrees with the acidic nature of the oxidized niobium.[35,37,38] The addition of copper reduced the amount of ammonia uptakes concomitant with the sulfidation degree and surface blockage by copper, as demonstrated below in the XPS section.

Table 1. Physicochemical properties of the synthesized catalysts.

Catalyst	Metal loading[d] (wt%)		P123/Nb (mol)	S_{BET}[e] (m^2/g)	Chemisorbed NH_3	
	Nb	Cu			$\mu mol_{NH3}/g_{cat}$	$\mu mol_{NH3}/m^2$
Nb	70	0	0.0	3	10	3.3
$NbCu_{0.1}$	65	6	0.0	3	9	2.8
$NbCu_{0.3}$	61	10	0.0	6	14	2.3
$NbCu_{0.5}$	54	18	0.0	4	10	2.6
$NbCu_{1.0}$	44	30	0.0	6	13	2.2
Nb-53	70	0	0.75	53	192	3.6
$NbCu_{0.3}$-28	61	10	1.50	28	7	2.7
$NbCu_{0.3}$-39[a]	61	10	0.05	39	97	2.6
$NbCu_{0.3}$-51[a]	61	10	0.75	51	130	2.6
Mo[b]	0	0	0.0	10	9	0.9
Mo-19[b]	0	0	1.50	19	18	1.1
CoMo-14[b]	0	0	1.50	14	14	1.0
$CoMo/Al_2O_3$[c]	0	0	–	94	198	2.1

[a] prepared by Nb chloride precursor; [b] Mo loading 67%; [c] Mo loading 12 wt% and Co loading 2 wt%; [d] metal loadings balanced with oxygen in the calcined samples; [e] BET surface areas of sulfided catalysts.

Figure 2 exhibits the TPR profiles of selected calcined catalysts. The amount of monometallic Nb and Cu catalysts corresponds to the niobium oxide (Nb_2O_5) and copper oxide (CuO) content of

the $NbCu_{0.5}$ sample. The reduction of monometallic bulk niobium oxide (Nb_2O_5) and copper oxide (CuO) occur at around 730 °C and 350 °C, respectively, which is in agreement with previous studies.[52,63] For bimetallic catalysts, the reduction peak of Nb_2O_5 shifted to lower temperatures in the presence of copper and partially merged with the CuO reduction peak. The small peak at 585 °C disappeared when Cu/Nb was increased. This finding indicates the facilitative effect of copper on the reduction of Nb_2O_5 and suggests the formation of a bimetallic $Cu_xNb_yO_z$ structure. A decrease in the reduction temperature of CuO in the bimetallic catalysts that is lower than bulk Cu catalyst also could be due to the formation of dispersed CuO species in the presence of niobium.[64]

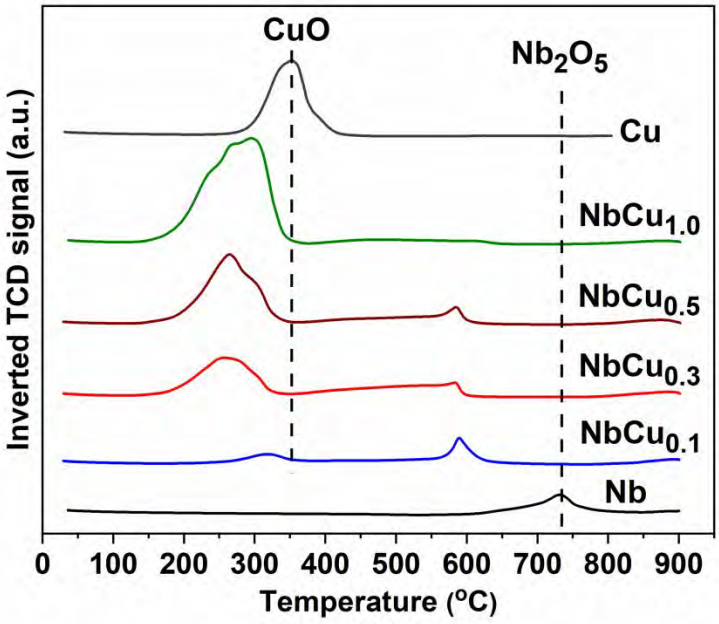

Figure 2. TPR profiles of calcined catalysts. The inverted TCD signal reflects hydrogen consumption. The amounts of monometallic Nb and Cu catalysts corresponds to the Nb_2O_5 and CuO content of $NbCu_{0.5}$ sample.

XPS analyses of calcined and sulfided catalysts are shown in Figure 3 and Table 2. The high-resolution XPS spectrum of bulk calcined Nb shows two peaks at the BEs of 207.3 and 210.1 eV, respectively, which corresponds to Nb $3d_{5/2}$ and Nb $3d_{3/2}$ core levels of Nb^{5+} in Nb_2O_5.[65,66] These peaks shifted to the lower BEs in the calcined bimetallic samples, which correlated to the Cu/Nb molar ratio (Figure 3a). For instance, the Nb $3d_{5/2}$ peak moved from 207.3 eV in Nb to 207.0 and 206.7 eV in the case of the $NbCu_{0.5}$ and $NbCu_{1.0}$ samples, respectively. On the other hand, the Cu 2p core levels in bimetallic materials shifted to the higher BEs as compared to bulk Cu (Figure 3c). This reveals the charge transfer between niobium and copper species and the formation of bimetallic $Cu_xNb_yO_z$ structure, in agreement with the TPR results (Figure 2). Compared to the calcined samples, the Nb 3d peaks of sulfided catalysts shifted to the lower BEs at 203.7 eV and 206.5 eV where the BEs of niobium disulfide (NbS_2) occur[22,67] (Figure 3b

and Table 2). This also correlates with the Cu/Nb ratio in the sample and implies the facilitative effects of copper on niobium oxide sulfidation. The Cu 2p doublets in the XPS spectra of sulfided samples negatively shifted toward the BEs of copper sulfide (Figure 3d). The S $2p_{3/2}$ and S $2p_{1/2}$ peaks at BEs of 162.0 and 163.1 eV further confirms the formation of NbS_2 (Figure 3e).[67] Note that the NIST XPS database does not contain information on the $Cu_xNb_yS_z$ materials. The Nb $3d_{5/2}$ peak of niobium carbide and metallic niobium at BEs of 202.5 eV and 202.2 eV, respectively, were not observed in the XPS spectra of the sulfided materials.[65,68]

Table 2. Binding energy values of Nb 3d and Cu 2p in selected sulfided catalysts.

Sample	Binding Energy (eV)							
	NbS_2		NbO_x		Nb_2O_5		Cu $2p_{3/2}$	Cu $2p_{1/2}$
	Nb $3d_{5/2}$	Nb $3d_{3/2}$	Nb $3d_{5/2}$	Nb $3d_{3/2}$	Nb $3d_{5/2}$	Nb $3d_{3/2}$		
Nb	203.9	206.7	205.2	207.9	208.0	210.7	–	–
$NbCu_{0.1}$	203.8	206.6	205.1	207.8	207.3	210	932.5	952.3
$NbCu_{0.3}$	203.8	206.5	204.7	207.6	207.0	209.6	932.7	952.6
$NbCu_{0.5}$	203.7	206.4	204.6	207.4	206.8	209.5	932.6	952.5
$NbCu_{1.0}$	203.7	206.4	204.5	207.3	206.6	209.3	932.5	952.4

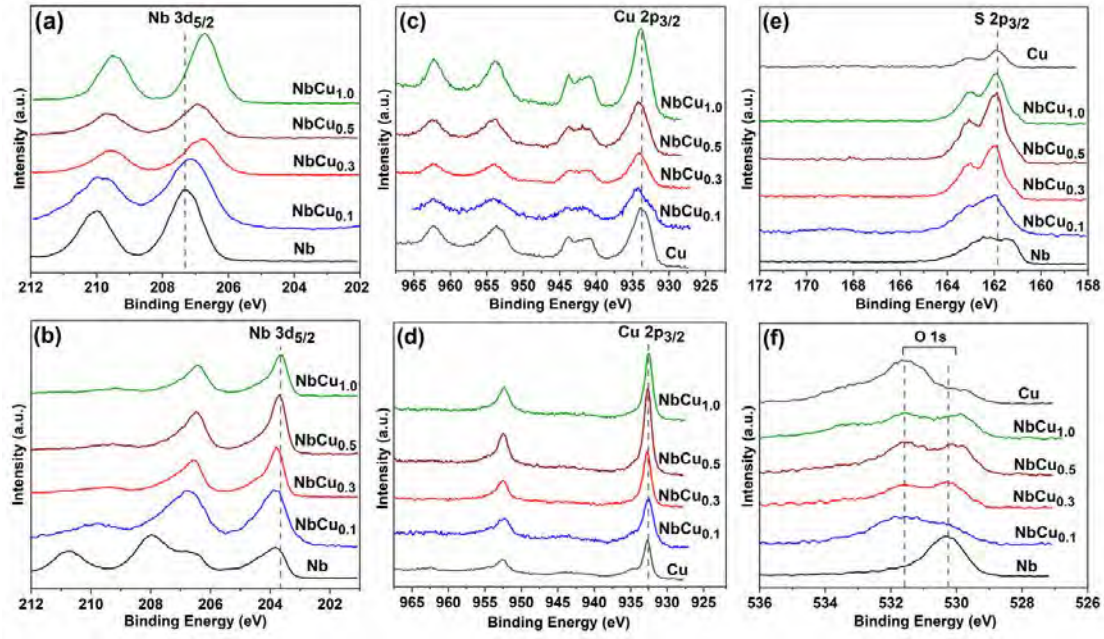

Figure 3. XPS spectra: Nb 3d core levels of (a) calcined and (b) sulfided samples; Cu 2p core levels of (c) calcined and (d) sulfided materials; (e) S 2p core levels of sulfided samples, and (f) O 1s core levels of sulfided catalysts; sulfidation at 400 °C for 20 h.

Deconvolution of the XPS spectra revealed that oxide and sulfide phases are simultaneously present in the sulfided samples (Figure 4a and Table 3). The Nb sulfidation ratio (fraction of NbS_2 in the sample) was calculated based on the area of deconvoluted peaks that correspond to NbS_2, unreduced Nb_2O_5, and partially reduced Nb_2O_5 shown by NbO_x. Most likely, Nb_2O_5 undergoes a reduction process to form niobium oxides with lower oxidation states (a mixture of NbO_2 and NbO shown by NbO_x) and then transforms to the NbS_2 structure.

Niobium sulfidation increased with the sulfidation temperature and duration (Figure 4b) as well as operating pressure; however, it was more sensitive to temperature, while sulfidation time was only pronounced at low temperatures below 400 °C. For example, a 50-degree increase in the sulfidation temperature from 350 to 400 °C led to a 33% enhancement in the niobium sulfidation ratio. Unlike sulfidation at 350 °C, no significant difference was observed in Nb sulfidation at 400 °C between 4 h and 20 h. On the other hand, pressurizing the system from 0.1 to 3.0 MPa at 400 °C promoted niobium sulfidation by around 20%. The highest Nb sulfidation was obtained above 400 °C, in agreement with a previous study[39] in which the highest HDS activity of carbon-supported niobium catalyst was obtained by sulfidation at 400 °C. No appreciable sulfidation enhancement was observed by increasing the sulfidation temperature from 400 °C to 450 °C (Figure 4b), and given that higher temperatures approach the autoignition temperature of hydrogen, temperatures above 450 °C were not assessed. The BET surface area had a minor effect on the sulfidation ratio of niobium. Increasing the surface area of $NbCu_{0.3}$ sample from 6 to 28 m^2/g only enhanced the fraction of NbS_2 from 60 to 68 %. Chlorine species were not identified in the XPS spectra, confirming a complete decomposition of $NbCl_5$ precursor during calcination and sulfidation. The sulfidation ratio of bulk Mo under identical conditions was 74% (Figure S3, Supporting Information), which is close to Mo-19 and CoMo-14 samples with 80 % MoS_2 fraction. Allali et al.[39] reported that the highest niobium sulfidation ratio at 400 °C using H_2S was obtained over the Nb-based catalyst that dried at room temperature. Here we found that the dried $NbCu_{0.5}$ sample exhibited a negligible sulfidation ratio. The formation of NbS_2 also grew when increasing copper content of the materials. It maximized at around 64% for the Cu/Nb molar ratio of 0.5 and then leveled off for higher copper content in the catalysts (Figure 4c and Table 3).

Elemental surface composition obtained by angle-resolved XPS (Table 3) shows that the surface composition of sulfided $NbCu_{0.3}$ and $NbCu_{1.0}$ materials is similar to the bulk composition and does not change with a depth between 0 and 60 degrees acquisition angles that approximately correspond to top 8 and 4 nm.[69] On the other hand, copper was more concentrated on the surface of the $NbCu_{0.5}$ catalyst, even though this catalyst was supposed to reflect the desired $Cu_{0.65}NbS_2$ material described in section 3.1. This could be due to the higher surface free energy of copper versus niobium.

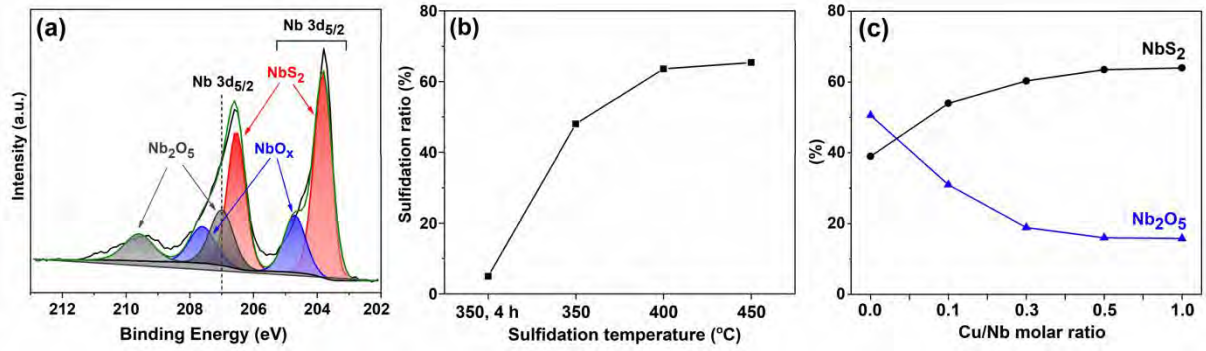

Figure 4. (a) Deconvoluted XPS spectra of sulfided $NbCu_{0.3}$ (sulfidation at 400 °C, 20 h); (b) effects of temperature and duration on Nb sulfidation ratio (sulfidation was performed for 20 h unless otherwise specified); (c) fraction of NbS_2 and Nb_2O_5 as a function of Cu/Nb molar ratio in the catalyst sulfided at 400 °C for 20 h.

Table 3. Surface amounts of sulfided, partially reduced, and unreacted Nb_2O_5 in the sulfided catalysts calculated by the areas of corresponding deconvoluted peaks; and elemental surface composition in sulfided samples determined by angle-resolved XPS at 0 and 60˚.

Sulfided samples	Amount in the sample (%)			Surface atomic composition (%) at 0˚			Surface ratios at 0 and 60˚			
	NbS_2	NbO_x	Nb_2O_5	Nb	Cu	S	Cu/Nb, 0˚	Cu/Nb, 60˚	S/Nb, 0˚	S/Nb, 60˚
Nb	39	10	51	51	–	49	–	–	0.96	–
$NbCu_{0.1}$	54	15	31	32	11	57	0.34	–	1.8	–
$NbCu_{0.3}$	60	21	19	37	9	54	0.24	0.26	1.5	1.3
$NbCu_{0.5}$	64	20	16	24	21	56	0.87	0.98	2.3	2.0
$NbCu_{1.0}$	64	20	16	22	19	59	0.86	–	2.7	–
Nb-53	44	10	46	52	–	48	–	–	0.92	–
$NbCu_{0.3}$-28	68	11	21	32	9	59	0.28	–	1.8	–
$NbCu_{0.3}$-39	52	10	38	39	4	57	0.10	–	1.5	–
$NbCu_{0.3}$-51	51	10	37	40	5	55	0.12	–	1.4	–

The XRD patterns of sulfided bimetallic samples in Figure 5 show the formation of copper niobium sulfide ($Cu_{0.65}NbS_2$) crystallite along with the presence of copper sulfide (Cu_2S) in bimetallic samples. The XRD peaks of bimetallic samples can be indexed with the hexagonal $Cu_{0.65}NbS_2$ structure (PDF 00-015-0409, space group: p63/mmc). The structure also was identified in the XRD patterns of high surface area $NbCu_{0.3}$ sulfide materials (Figure S3 in the Supporting Information). Monometallic sulfided Nb catalysts were found amorphous irrespective of the utilized synthesis techniques, niobium precursors, and the BET surface area.

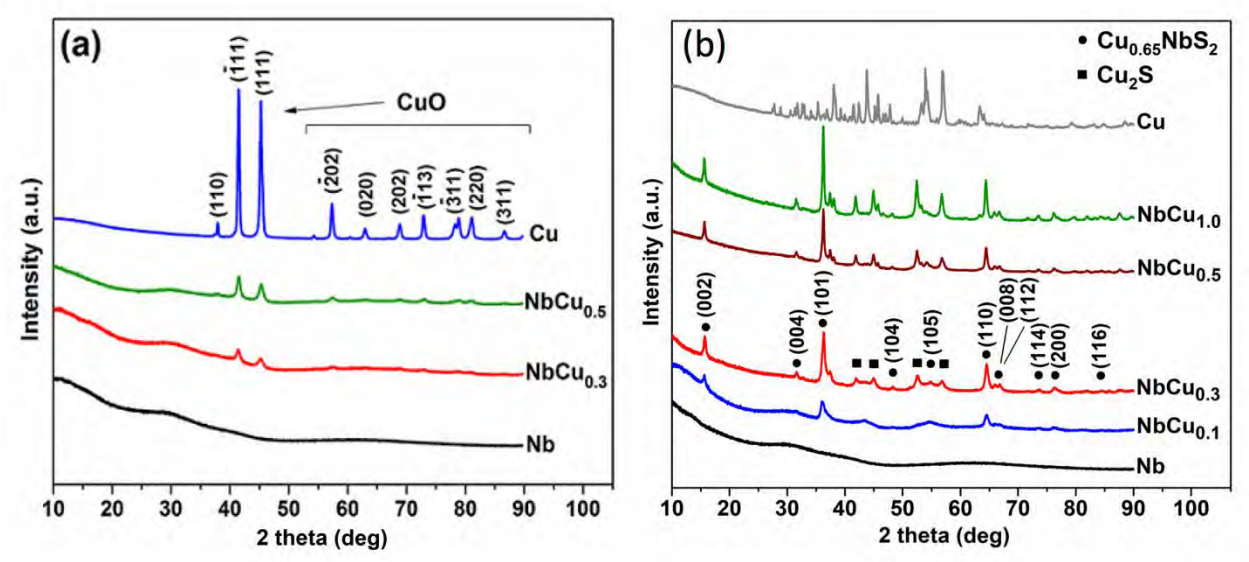

Figure 5. XRD patterns of calcined (a) and sulfided (b) samples; peaks assignment according to the PDF 00-015-0409 for $Cu_{0.65}NbS_2$ and 97-010-0333 for Cu_2S.

The XRD patterns of calcined samples (Figure 5a) show the significant suppression of monometallic CuO peaks when Cu is added to the amorphous NbO_x. The possible formation of $Cu_xNb_yO_z$ structures, which was also seen from the XPS and TPR results (Figures 2 and 3), was further verified by DRIFTS of the calcined samples. The bimetallic calcined $NbCu_x$ materials do not show characteristic bands of the calcined Cu, while the peaks of calcined Nb were significantly affected (Figure 6). Such intimate degree of interaction between Nb and Cu in the calcined samples may be beneficial for the further copper-assisted sulfidation, but at the same time may affect the properties of required Nb sulfide phase, which will be assessed in the catalytic section 3.3.

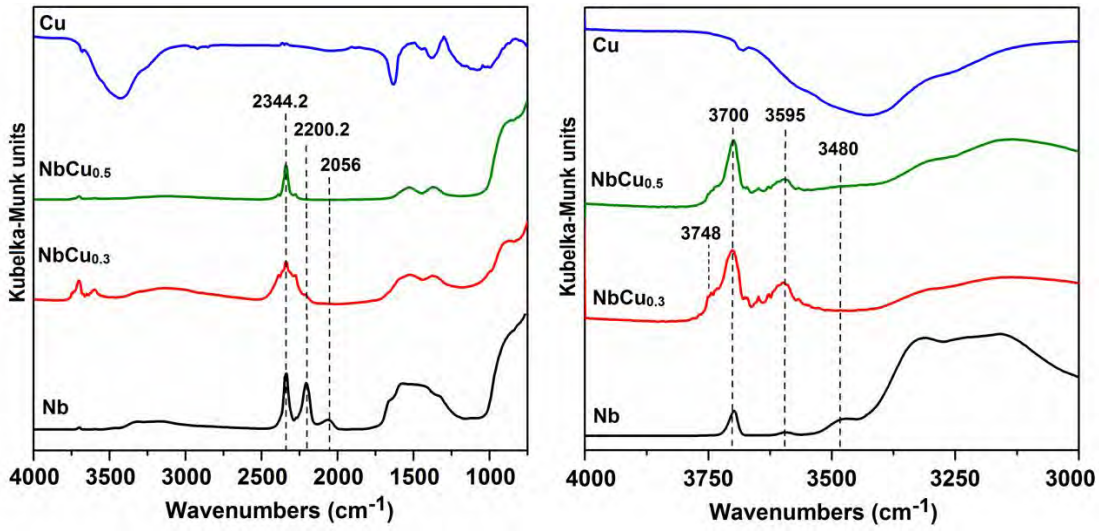

Figure 6. DRIFT spectra of calcined catalysts with the enlarged hydroxyl region ca. 3500 cm^{-1}.

Figure 7 shows the typical surface views of the mono- and bimetallic catalysts after calcination and sulfidation at 400 °C. The addition of copper promoted the formation of small flake-like structures in the sulfided state. According to the FESEM-EDS mapping analysis (Figure 8) these structures are rich with copper that could be copper sulfide (Cu_2S) structure as identified in the XRD patterns. This is also in line with the XPS tilting experiment, revealing that copper species are concentrated on the surface of $NbCu_{0.5}$ sample (Table 3). These isolated small flakes may behave as spacer between the sulfided layers, leading to the BET surface area enhancement as observed in the case of $NbCu_{0.3}$ catalyst.

HRTEM image of sulfided Nb and bimetallic $NbCu_{0.3}$ catalysts (high- and low-surface areas) along with their STEM-EDS analyses are shown in Figure 8 and Figure S4 (Supporting Information). Monometallic Nb and Nb-53 catalysts were found amorphous (Figure 8a and Figure S4), which agrees with the XRD data; however, the layered NbS_2 phase partially formed after sulfidation with an interplanar spacing of 7.0 Å corresponding to the (002) plane of NbS_2. On the contrary, bimetallic $NbCu_{0.3}$ samples were crystalline with hexagonal fast Fourier transform (FFT) patterns and fringe spacings of 2.9 Å, 3.2 Å, and 6.6 Å that can be attributed to the (100), (004), and (002) planes of $Cu_{0.65}NbS_2$ structure, respectively (Figure 8b and Figure S4b-c), which also agrees with the XRD data (Figure 5b and Figure S3). The EDS elemental mappings of bimetallic NbCu samples exhibit a homogeneous association between niobium, copper, and sulfur, suggesting the formation of bimetallic structures (Figure 8c and Figure S4b-c), with some copper segregation to the surface (Figure 8c).

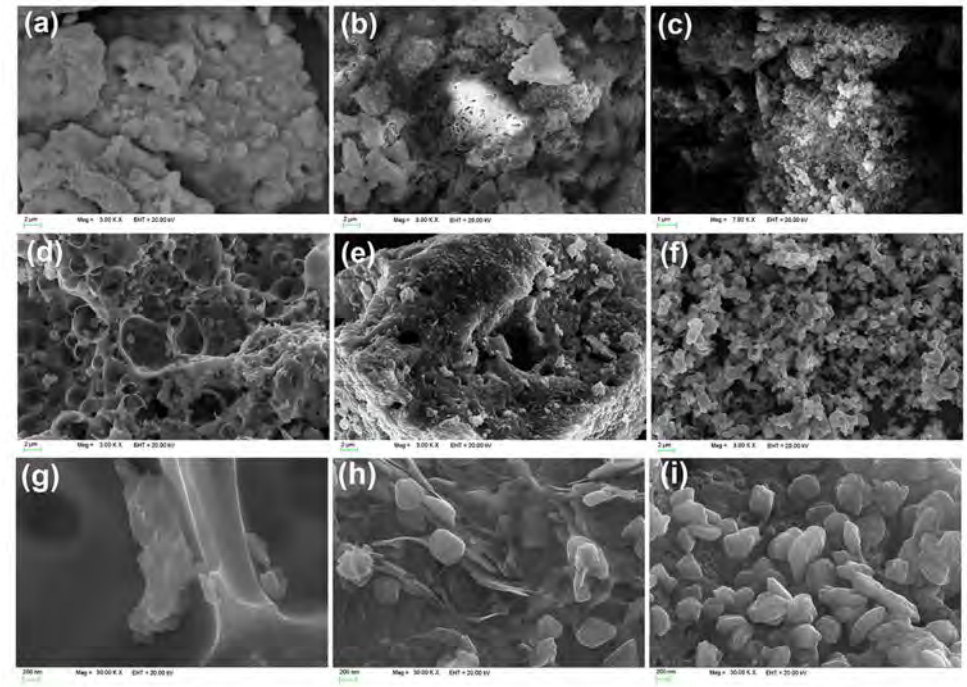

Figure 7. FESEM images of selected materials: calcined Nb (a), $NbCu_{0.3}$ (b), and $NbCu_{0.5}$ (c) catalysts; sulfided Nb (d,g), $NbCu_{0.3}$ (e,h), and $NbCu_{0.5}$ (f,i) samples. High-magnification FESEM images of sulfided Nb (g), $NbCu_{0.3}$ (h), and $NbCu_{0.5}$ (i).

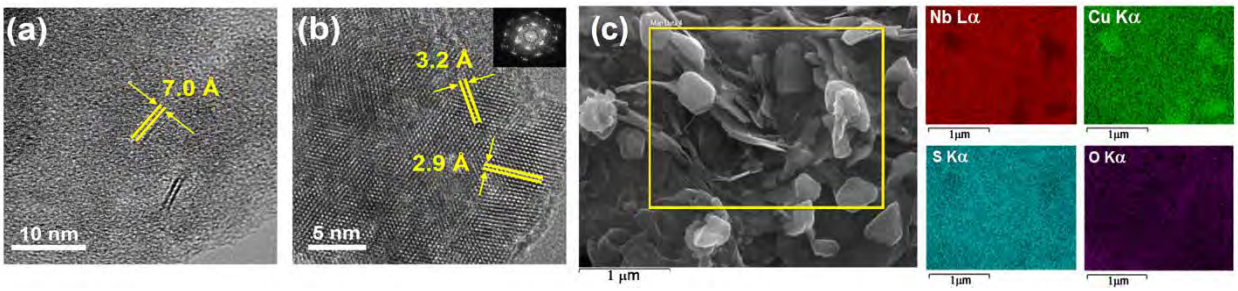

Figure 8. HRTEM images of Nb (a) and $NbCu_{0.3}$ (b) catalysts; (c) FESEM-EDS mapping of $NbCu_{0.3}$ catalyst; all after sulfidation at 400 °C; inset in (b): fast Fourier transform (FFT) pattern.

Thus, the characterization results revealed that the copper addition to Nb promoted its sulfidation and led to the formation of $Cu_{0.65}NbS_2$ material, with some Cu_2S crystallites concentrated on the surface, depending on the synthesis method, and residual unsulfided NbO_x.

2.4.3 Catalytic performance in HDS of DBT

The catalytic properties of the synthesized catalysts were assessed in the continuous HDS of DBT at 325 °C and 3.0 MPa for 24 h on-stream (Figure 9, Table S1). The catalysts were presulfided *in situ* at 400 °C for 20 h before each HDS test. The amount of sulfur in the feed during sulfidation and reaction was 9 and 7 orders of magnitude higher than the required ratio of partial pressure of pH_2S/pH_2 to stabilize NbS_2, respectively (Figure 1b). Figure 8a compares the DBT consumption rates of sulfided Nb, NbCu and Mo catalysts at the same amount of niobium (or molybdenum) in the reactor. A negligible conversion obtained over a reduced unsulfided Nb catalyst (around 1% DBT conversion after 24 h) confirmed the necessity of Nb sulfide for the HDS catalysis and relative inactivity of NbO_x for hydrocracking. Sulfided Nb exhibited a higher activity than the Mo catalyst consistent with previous studies,[35,40] even though Mo sulfidation extent was found to be similar to the NbCu materials (74%, Figure S5). Figure 8a exhibits the reaction rates as a function of Cu/Nb molar ratio, calculated based on the first-order reaction at the initial concentration of DBT in the feed. The activities are normalized per molar amount of Nb and fraction of NbS_2 (or MoS_2) in the catalysts determined from XPS spectra (Table 3). Compared to the monometallic Nb, the addition of copper enhanced the HDS activity per total Nb loading in the reactor (Figure 9a), while monometallic Cu catalyst was found inactive. The reaction rate depends on the Cu/Nb molar ratio following a volcano trend; it increased with the copper loading in the sample and maximized at Cu/Nb molar ratio of 0.3 and then decreased for the higher Cu/Nb ratios (Figure 9a,b).

The characterization results showed that copper addition resulted in the increased amount of sulfided Nb. To assess whether the sulfidation promoter has any effect on the intrinsic catalytic activity of sulfided Nb, turnover frequencies (TOF) were calculated based on the reaction rates of DBT consumption. The amounts of the active sites (sulfided Nb) were calculated from the total Nb content in the sample normalized per catalyst surface area (Table 1) and per molar

fraction of the sulfided Nb in the uppermost surface layer as determined from XPS with 60° tilting (Table 3). For the three samples of Nb, $NbCu_{03}$ and $NbCu_{0.5}$, such normalization resulted in the same TOF of $(3.6\pm0.4)\cdot10^{-8}$ $mol_{DBT}/(m^2_{NbS2}\cdot s)$. Selectivities to DDS and HYD paths remained unchanged at similar DBT conversions (Table S1). The increased sulfur extraction from sulfurous intermediates in the presence of copper (Figure 9c) may also be ascribed to the increased sulfidation degree. This indicates that copper presence does not affect the electronic properties of sulfided Nb for HDS of DBT and copper behaves as a spectator.

The volcano trends observed in Figures 9a-d can be explained by the increased amount of sulfided Nb active sites in the presence of copper, that above a certain point (Cu/Nb ratio of 0.3) segregates to the catalyst surface (as seen from XPS, Table 3, and EDS mapping, Figure 8c) and blocks active sites. This site blockage also manifests itself in the drop of catalyst acidity as measured by NH_3 chemisorption (Table 1) and suppressed contribution of the DBT hydrogenation path versus direct desulfurization (Scheme 1). Thus, at high concentrations, copper becomes detrimental to the catalyst performance and serves as a textural negative promoter.

To increase the mass-based catalyst activity, relatively high surface area materials were also prepared. Their catalytic behavior is summarized in Figures 9e,f and Table S1 (Supporting Information). As expected, an order-of-magnitude higher surface area resulted in the similar increase of mass-based rates and weight-time yields. The catalyst activities surpassed those of sulfided Mo and approached the activity of a promoted CoMo bulk catalyst.

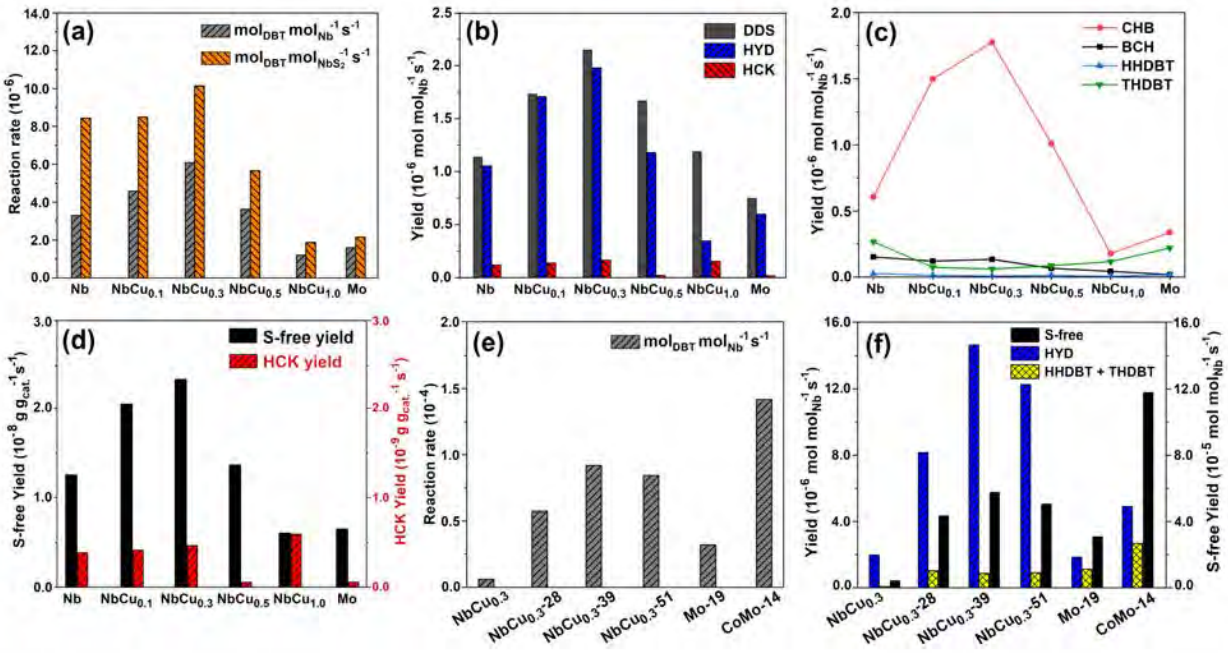

Figure 9. Reaction rates and products yields in HDS of DBT at 325 °C and 3.0 MPa after 24 h on-stream for (a-d) low-surface-area and (e-f) high-surface-area materials. The samples were presulfided *in situ* at 400 °C, 20 h.

For a reference, the total catalyst mass-based activity of a supported $CoMo/Al_2O_3$ catalyst (12 wt.% Mo, 2 wt% Co) was 7-fold higher than the activity of bulk $NbCu_{0.3}$-39 sample (Table S1). In the present report, we did not aim to complete the development of a supported catalyst to surpass the activity of industrial $CoMo/Al_2O_3$ catalyst. Our objective was to demonstrate the concept of a promoter selection for the otherwise thermodynamically-unfavorable preparation of transition metal sulfides. In terms of a practical application of the developed bulk materials, the $NbCu_{0.3}$ sulfide surpasses the HDS activity of unsupported MoS_2 (Figure 9a, e) and may be recommended to replace the latter in relevant applications, such as in slurry hydrotreaters and bitumen partial upgrading.[70,71]

2.5 Conclusions

Sulfidation extent of Nb oxide to HDS-active NbS_2 was improved by the addition of copper that removes the thermodynamic limitations of the sulfide phase formation. A series of bulk bimetallic sulfided NbCu catalysts at Cu/Nb molar ratios of 0, 0.1, 0.3, 0.5, and 1.0 were prepared. The formation of a $Cu_{0.65}NbS_2$ structure and an increased degree of Nb sulfidation in the presence of copper was confirmed by XRD, TEM, and XPS. The Cu/Nb molar ratio of 0.3 showed the highest activity of DBT HDS, which could correlate with the fraction of sulfided niobium. Copper surface segregation at the Cu/Nb ratio of 0.5 was observed by angle-resolved XPS, which resulted in the activity loss. The copper presence did not affect the intrinsic activity of available surface sulfide Nb and copper behaves as a spectator. However, the copper excess above Cu/Nb ratio of 0.3 results in activity loss due to active site blockage, where copper can be regarded as a textural negative promoter. The weight-time yield of the sulfur-free products for the optimal $NbCu_{0.3}$ catalyst exceeded the value for the Mo catalyst, at the same catalyst mass loading in the reactor. The study demonstrates that an earth-abundant NbCu structure could be a promising candidate for hydrotreating technologies. Copper addition may be recommended for thermodynamically-limited niobium oxide sulfidation to promote NbS_2 formation as a potential alternative to MoS_2 for a variety of emerging applications.

2.6 References

(1) Bara, C.; Plais, L.; Larmier, K.; Devers, E.; Digne, M.; Lamic-Humblot, A. F.; Pirngruber, G. D.; Carrier, X. Aqueous-phase preparation of model HDS catalysts on planar alumina substrates: support effect on Mo adsorption and sulfidation. J. Am. Chem. Soc. 2015, 137, 15915–15928.
(2) Liu, G.; Robertson, A. W.; Li, M. M. J.; Kuo, W. C. H.; Darby, M. T.; Muhieddine, M. H.; Lin, Y. C.; Suenaga, K.; Stamatakis, M.; Warner, J. H.; Tsang, S. C. E. MoS_2 monolayer catalyst doped with isolated Co atoms for the hydrodeoxygenation reaction. Nat. Chem. 2017, 9, 810–816.
(3) Chianelli, R. R.; Berhault, G.; Torres, B. Unsupported transition metal sulfide catalysts: 100 years of science and application. Catal. Today 2009, 147, 275–286.
(4) Wang, H.; Male, J.; Wang, Y. Recent advances in hydrotreating of pyrolysis bio-oil and its oxygen-containing model compounds. ACS Catal. 2013, 3, 1047–1070.

(5) Ge, H.; Wen, X. D.; Ramos, M. A.; Chianelli, R. R.; Wang, S.; Wang, J.; Qin, Z.; Lyu, Z.; Li, X. Carbonization of Ethylenediamine Coimpregnated CoMo/Al_2O_3 Catalysts Sulfided by Organic Sulfiding Agent. ACS Catal. 2014, 4, 2556–2565.
(6) Infantes-Molina, A.; Romero-Pérez, A.; Sánchez-González, V.; Pawelec, B.; Fierro, J. L. G.; Jiménez-López, A.; Rodríguez-Castellón, E. Role of Cs on Hydrodesulfurization Activity of RuS_2 Catalysts Supported on a Mesoporous SBA-15 Type Material. ACS Catal. 2011, 1, 175–186.
(7) Larabi, C.; Nielsen, P. K.; Helveg, S.; Thieuleux, C.; Johansson, F. B.; Brorson, M.; Quadrelli, E. A. Bulk Hydrodesulfurization Catalyst Obtained by $Mo(CO)_6$ Grafting on the Metal–Organic Framework Ni_2(2,5-dihydroxoterephthalate). ACS Catal. 2012, 2, 695–700.
(8) Li, H.; Liu, J.; Li, J.; Hu, Y.; Wang, W.; Yuan, D.; Wang, Y.; Yang, T.; Li, L.; Sun, H.; Ren, S.; Zhu, X.; Guo, Q.; Wen, X.; Li, Y.; Shen, B. Promotion of the inactive iron sulfide to an efficient hydrodesulfurization catalyst. ACS Catal. 2017, 7, 4805–4816.
(9) Morrill, M. R.; Thao, N. T.; Shou, H.; Davis, R. J.; Barton, D. G.; Ferrari, D.; Agrawal, P. K.; Jones, C. W. Origins of Unusual Alcohol Selectivities over Mixed MgAl Oxide-Supported K/MoS_2 Catalysts for Higher Alcohol Synthesis from Syngas. ACS Catal. 2013, 3, 1665–1675.
(10) Wang, Q. H.; Kalantar-Zadeh, K.; Kis, A.; Coleman, J. N.; Strano, M. S. Electronics and optoelectronics of two-dimensional transition metal dichalcogenides. Nat. Nanotechnol. 2012, 7, 699–712.
(11) Pang, Q.; Liang, X.; Kwok, C. Y.; Nazar, L. F. Advances in lithium–sulfur batteries based on multifunctional cathodes and electrolytes. Nat. Energy 2016, 1, 16132-16143.
(12) Lai, C. H.; Lu, M. Y.; Chen, L. J. Metal sulfide nanostructures: synthesis, properties and applications in energy conversion and storage. Mater. Chem. 2012, 22, 19–30.
(13) Ou, X.; Xiong, X.; Zheng, F.; Yang, C.; Lin, Z.; Hu, R.; Jin, C.; Chen, Y.; Liu, M. In situ X-ray diffraction characterization of NbS_2 nanosheets as the anode material for sodium ion batteries. J. Power Sources 2016, 325, 410–416.
(14) Montoya, J. H.; Seitz, L. C.; Chakthranont, P.; Vojvodic, A.; Jaramillo, T. F.; Nørskov, J. K. Materials for solar fuels and chemicals. Nat. Mater. 2016, 16, 70–81.
(15) Tsai, M. L.; Su, S. H.; Chang, J. K.; Tsai, D. S.; Chen, C. H.; Wu, C. I.; Li, L. J.; Chen, L. J.; He, J. H. Monolayer MoS_2 Heterojunction Solar Cells. ACS Nano 2014, 8, 8317–8322.
(16) Kibsgaard, J.; Chen, Z.; Reinecke, B. N.; Jaramillo, T. F. Engineering the surface structure of MoS_2 to preferentially expose active edge sites for electrocatalysis. Nat. Mater. 2012, 11, 963–969.
(17) Staszak-Jirkovský, J.; Malliakas, C. D.; Lopes, P. P.; Danilovic, N.; Kota, S. S.; Chang, K. C.; Genorio, B.; Strmcnik, D.; Stamenkovic, V. R.; Kanatzidis, M. G.; Markovic, N. M. Design of active and stable Co–Mo–S_x chalcogels as pH-universal catalysts for the hydrogen evolution reaction. Nat. Mater. 2015, 15, 197–203.
(18) Benck, J. D.; Hellstern, T. R.; Kibsgaard, J.; Chakthranont, P.; Jaramillo, T. F. Catalyzing the hydrogen evolution reaction (HER) with molybdenum sulfide nanomaterials. ACS Catal. 2014, 4, 3957–3971.
(19) Benck, J. D.; Chen, Z.; Kuritzky, L. Y.; Forman, A. J.; Jaramillo, T. F. Amorphous molybdenum sulfide catalysts for electrochemical hydrogen production: insights into the origin of their catalytic activity. ACS Catal. 2012, 2, 1916–1923.

(20) Asadi, M.; Kumar, B.; Behranginia, A.; Rosen, B. A.; Baskin, A.; Repnin, N.; Pisasale, D.; Phillips, P.; Zhu, W.; Haasch, R.; Klie, R. F.; Král, P.; Abiade, J.; Salehi-Khojin, A. Robust carbon dioxide reduction on molybdenum disulphide edges. Nat. Com. 2014, 5, 4470-4478.
(21) Asadi, M.; Kim, K.; Liu, C.; Addepalli, A. V.; Abbasi, P.; Yasaei, P.; Phillips, P.; Behranginia, A.; Cerrato, J. M.; Haasch, R.; Zapol, P.; Kumar, B.; Klie, R. F.; Abiade, J.; Curtiss, L. A.; Salehi-Khojin, A. Nanostructured transition metal dichalcogenide electrocatalysts for CO_2 reduction in ionic liquid. Science 2016, 353, 467–470.
(22) Dash, J. K.; Chen, L.; Dinolfo, P. H.; Lu, T. M.; Wang, G. C. A Method Toward Fabricating Semiconducting 3R-NbS_2 Ultrathin Films. J. Phys. Chem. C 2015, 119, 19763–19771.
(23) Chhowalla, M.; Shin, H. S.; Eda, G.; Li, L. J.; Loh, K. P.; Zhang, H. The chemistry of two-dimensional layered transition metal dichalcogenide nanosheets. Nat. Chem. 2013, 5, 263–275.
(24) Chianelli, R. R. Periodic trends transition metal sulfide catalysis: intuition and theory. Oil & Gas Science and Technology-Revue de l'IFP 2006, 61, 503–513.
(25) Aray, Y.; Zambrano, D.; Cornejo, M.; Ludeña, E. V.; Iza, P.; Vidal, A. B.; Coll, D. S.; Jímenez, D. M.; Henriquez, F.; Paredes, C. First-Principles Study of the Nature of Niobium Sulfide Catalyst for Hydrodesulfurization in Hydrotreating Conditions. J. Phys. Chem. C 2014, 118, 27823–27832.
(26) Gutiérrez, O. Y.; Singh, S.; Schachtl, E.; Kim, J.; Kondratieva, E.; Hein, J.; Lercher, J. A. Effects of the Support on the Performance and Promotion of (Ni)MoS_2 Catalysts for Simultaneous Hydrodenitrogenation and Hydrodesulfurization. ACS Catal. 2014, 4, 1487–1499.
(27) Eijsbouts, S.; Anderson, G. H.; Bergwerff, J. A.; Jacobi, S. Economic and technical impacts of replacing Co and Ni promotion in hydrotreating catalysts. Appl. Catal. A Gen. 2013, 458, 169–182.
(28) Zhou, W.; Liu, M.; Zhang, Q.; Wei, Q.; Ding, S.; Zhou, Y. Synthesis of NiMo Catalysts Supported on Gallium-Containing Mesoporous Y Zeolites with Different Gallium Contents and Their High Activities in the Hydrodesulfurization of 4,6-Dimethyldibenzothiophene. ACS Catal. 2017, 7, 7665–7679.
(29) Rangarajan, S.; Mavrikakis, M. On the Preferred Active Sites of Promoted MoS_2 for Hydrodesulfurization with Minimal Organonitrogen Inhibition. ACS Catal. 2017, 7, 501–509.
(30) van Haandel, L.; Bremmer, M.; Kooyman, P. J.; van Veen, J. A. R.; Weber, T.; Hensen, E. J. M. Structure–Activity Correlations in Hydrodesulfurization Reactions over Ni-Promoted $Mo_xW_{(1-x)}S_2/Al_2O_3$ Catalysts. ACS Catal. 2015, 5, 7276–7287.
(31) Rangarajan, S.; Mavrikakis, M. DFT insights into the competitive adsorption of sulfur-and nitrogen-containing compounds and hydrocarbons on Co-promoted molybdenum sulfide catalysts. ACS Catal. 2016, 6, 2904–2917.
(32) Baubet, B.; Girleanu, M.; Gay, A. S.; Taleb, A. L.; Moreaud, M.; Wahl, F.; Delattre, V.; Devers, E.; Hugon, A.; Ersen, O.; Afanasiev, P.; Raybaud, P. Quantitative Two-Dimensional (2D) Morphology–Selectivity Relationship of CoMoS Nanolayers: A Combined High-Resolution High-Angle Annular Dark Field Scanning Transmission Electron Microscopy (HR HAADF-STEM) and Density Functional Theory (DFT) StudyACS Catal. 2016, 6, 1081–1092.
(33) Suresh, C.; Santhanaraj, D.; Gurulakshmi, M.; Deepa, G.; Selvaraj, M.; Rekha, N. R. S.; Shanthi, K. Mo–Ni/Al-SBA-15 (sulfide) catalysts for hydrodenitrogenation: effect of Si/Al ratio on catalytic activity. ACS Catal. 2012, 2, 127–134.

(34) Pecoraro, T. A.; Chianelli, R. R. Hydrodesulfurization catalysis by transition metal sulfides. J. Catal. 1981, 67, 430–445.
(35) Lacroix, M.; Boutarfa, N.; Guillard, C.; Vrinat, M.; Breysse, M. Hydrogenating properties of unsupported transition metal sulfides. J. Catal. **1989**, 120, 473–477.
(36) Danot, M.; Afonso, J.; Des, C. T.; Portefaix, J. L.; Breysse, M. Catalytic properties of niobium sulphides in the conversion of nitrogen containing molecules. Catal. Today 1991, 10, 629–643.
(37) Ziolek, M. Niobium-containing catalysts-the state of the art. Catal. Today 2003, 78, 47–64.
(38) Jehng, J. M.; Wachs, I. E. The molecular structures and reactivity of supported niobium oxide catalysts. Catal. Today 1990, 8, 37–55.
(39) Allali, N.; Marie, A. M.; Danot, M.; Geantet, C.; Breysse, M. Carbon-supported and alumina-supported niobium sulfide catalysts. J. Catal. 1995, 156, 279–289.
(40) Hermann, N.; Brorson, M.; Topsøe, H. Activities of unsupported second transition series metal sulfides for hydrodesulfurization of sterically hindered 4,6-dimethyldibenzothiophene and of unsubstituted dibenzothiophene. Catal. Letters 2000, 65, 169–174.
(41) Gaborit, V.; Allali, N.; Geantet, C.; Breysse, M.; Vrinat, M.; Danot, M. Niobium sulfide as a dopant for hydrotreating NiMo catalysts. Catal. Today 2000, 57, 267–273.
(42) Stanislaus, A.; Marafi, A.; Rana, M. S. Recent advances in the science and technology of ultra low sulfur diesel (ULSD) production. Catal. Today 2010, 153, 1–68.
(43) Egorova, M.; Prins, R. Hydrodesulfurization of dibenzothiophene and 4,6-dimethyldibenzothiophene over sulfided NiMo/γ-Al_2O_3, CoMo/γ-Al_2O_3, and Mo/γ-Al_2O_3 catalysts. J. Catal. 2004, 225, 417–427.
(44) Gaborit, V.; Allali, N.; Danot, M.; Geantet, C.; Cattenot, M.; Breysse, M.; Diehl, F. Hydrotreating properties of mixed $Nb_xMo_{1-x}S_2$ alumina supported catalysts. Catal. Today 2003, 78, 499–505.
(45) *CRC Handbook of Chemistry and Physics*, 93rd ed.; Haynes, W. M., Ed.; CRC Press: Boca Rantion, 2012, p. 14-18.
(46) Kadijk, F.; Jellinek, F. J. The system niobium-sulfur. J. Less Common Met. 1969, 19, 421–430.
(47) Liu, Z. L.; Cai, L. C.; Zhang, X. L. Novel high pressure structures and superconductivity of niobium disulfide. J. Alloys Compd. 2014, 610, 472–477.
(48) Jellinek, F.; Brauer, G.; Müller, H. Molybdenum and niobium sulphides. Nature 1960, 185, 376–377.
(49) Afanasiev, P.; Bezverkhyy, I. Ternary transition metals sulfides in hydrotreating catalysis. Appl. Catal. A Gen. 2007, 322, 129–141.
(50) Geantet, C.; Afonso, J.; Breysse, M.; Allali, N.; Danot, M. Niobium sulfides as catalysts for hydrotreating reactions. Catal. Today 1996, 28, 23–30.
(51) Zdražil, M. Recent advances in catalysis over sulphides. Catal. Today 1988, 3, 269–365.
(52) Wachs, I. E.; Briand, L. E.; Jehng, J. M.; Burcham, L.; Gao, X. Molecular structure and reactivity of the group V metal oxides. Catal. Today 2000, 57, 323–330.
(53) Wachs, I. E.; Jehng, J. M.; Deo, G.; Hu, H.; Arora, H. Redox properties of niobium oxide catalysts. Catal. Today 1996, 28, 199–205.

(54) Infantes-Molina, A.; Romero-Pérez, A.; Finocchio, E.; Busca, G.; Jiménez-López, A.; Rodríguez-Castellón, E. HDS and HDN on SBA-supported RuS_2 catalysts promoted by Pt and Ir. J. Catal. 2013, 305, 101–117.
(55) Jongen, N.; Bowen, P.; Lemaître, J.; Valmalette, J. C.; Hofmann, H. Precipitation of self-organized copper oxalate polycrystalline particles in the presence of hydroxypropylmethylcellulose (HPMC): control of morphology. J. Colloid Interface Sci. 2000, 226, 189–198.
(56) Pérez-Ramírez, J.; Berger, R. J.; Mul, G.; Kapteijn, F.; Moulijn, J. A. The six-flow reactor technology: a review on fast catalyst screening and kinetic studies. J. A. Catal. Today 2000, 60, 93–109.
(57) Fogler, H. S. *Elements of chemical reaction engineering*, 4th ed.; Prentice Education: Boston, 2005; p. 841.
(58) Mansouri, A.; Semagina, N. Palladium islands on iron oxide nanoparticles for hydrodesulfurization catalysis. Catal. Sci. Technol. 2018, 8, 2323–2332.
(59) Kuhn, M.; Rodriguez, J. A. The interaction of sulfur with Cu/Pt (111) and Zn/Pt (111) surfaces: copper-promoted sulfidation of platinum. Catal. Letters 1995, 32, 345–355.
(60) Van Arkel, A. E.; Crevecoeur C. Quelques sulfures et séléniures complexes. J. Less Common. Met. 1963, 5, 177–180.
(61) Koerts, K. The crystal structure of $Cu_{0.65}NbS_2$ and some related compounds. Acta Cryst. 1963, 16, 432–433.
(62) Craig, J. R.; Barton, P. B. Thermochemical approximations for sulfosalts. Econ. Geol. 1973, 68, 493–506.
(63) Mansouri, A.; Khodadadi, A. A.; Mortazavi, Y. Ultra-deep adsorptive desulfurization of a model diesel fuel on regenerable Ni–Cu/γ-Al_2O_3 at low temperatures in absence of hydrogen. J. Hazard. Mater. 2014, 271, 120–130.
(64) Xiang, Y.; Barbosa, R.; Li, X.; Kruse, N. Ternary Cobalt–Copper–Niobium Catalysts for the Selective CO Hydrogenation to Higher Alcohols. ACS Catal. 2015, 5, 2929–2934.
(65) Da Silva, V. L. S. T.; Schmal, M.; Oyama, S. T. Niobium carbide synthesis from niobium oxide: study of the synthesis conditions, kinetics, and solid-state transformation mechanism. J. Solid State Chem. 1996, 123, 168–182.
(66) Izawa, K.; Ida, S.; Unal, U.; Yamaguchi, T.; Kang, J. H.; Choy, J. H.; Matsumoto, Y. A new approach for the synthesis of layered niobium sulfide and restacking route of NbS_2 nanosheet. J. Solid State Chem. 2008, 181, 319–324.
(67) Wu, X.; Tao, Y.; Ke, X.; Zhu, J.; Hong, J. Catalytic synthesis of long NbS_2 nanowire strands. J. Mater. Res. Bull. 2004, 39, 901–908.
(68) Badrinarayanan, S.; Sinha S. X-ray photoelectron spectroscopy studies of the reaction of N^{+2} -ion beams with niobium and tantalum metals. Appl. Phys. 1991, 69, 1141.
(69) *Surface Analysis: The Principal Techniques*, 2nd ed.; Vickerman, J. C., Gilmore I. S., Ed.; Wiley-VCH, 2009. p. 89.
(70) Almao, P. P. In situ upgrading of bitumen and heavy oils via nanocatalysis. Can. J. Chem. Eng. 2012, 90, 320-329.
(71) Zhang, S.; Liu, D.; Deng, W.; Que, G. A review of slurry-phase hydrocracking heavy oil technology. Energy Fuels 2007, 21, 3057-3062.

2.7 Supporting Information

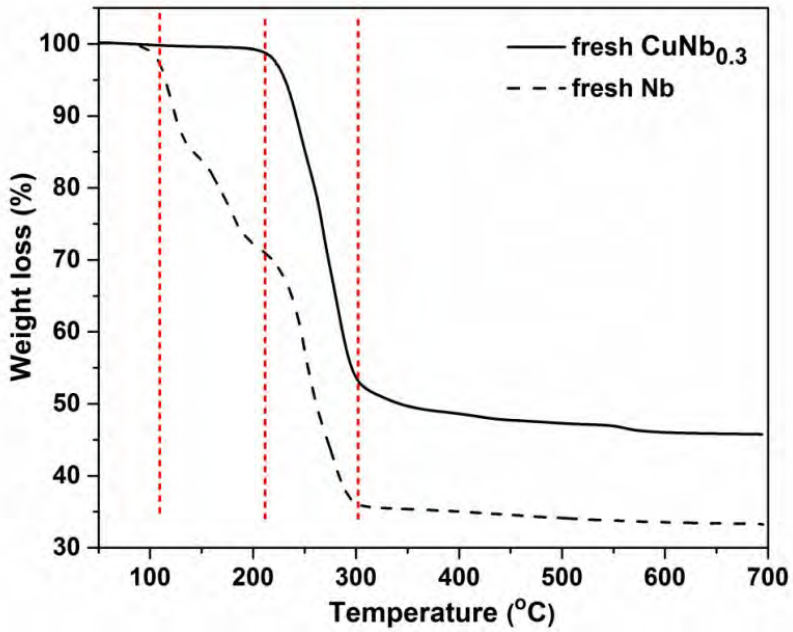

Figure S1. TGA profiles of Nb oxalate hydrate (fresh Nb) and dried $CuNb_{0.3}$ material performed under 50 ml/min N_2 from 30 °C to 700 °C on 10 °C/min.

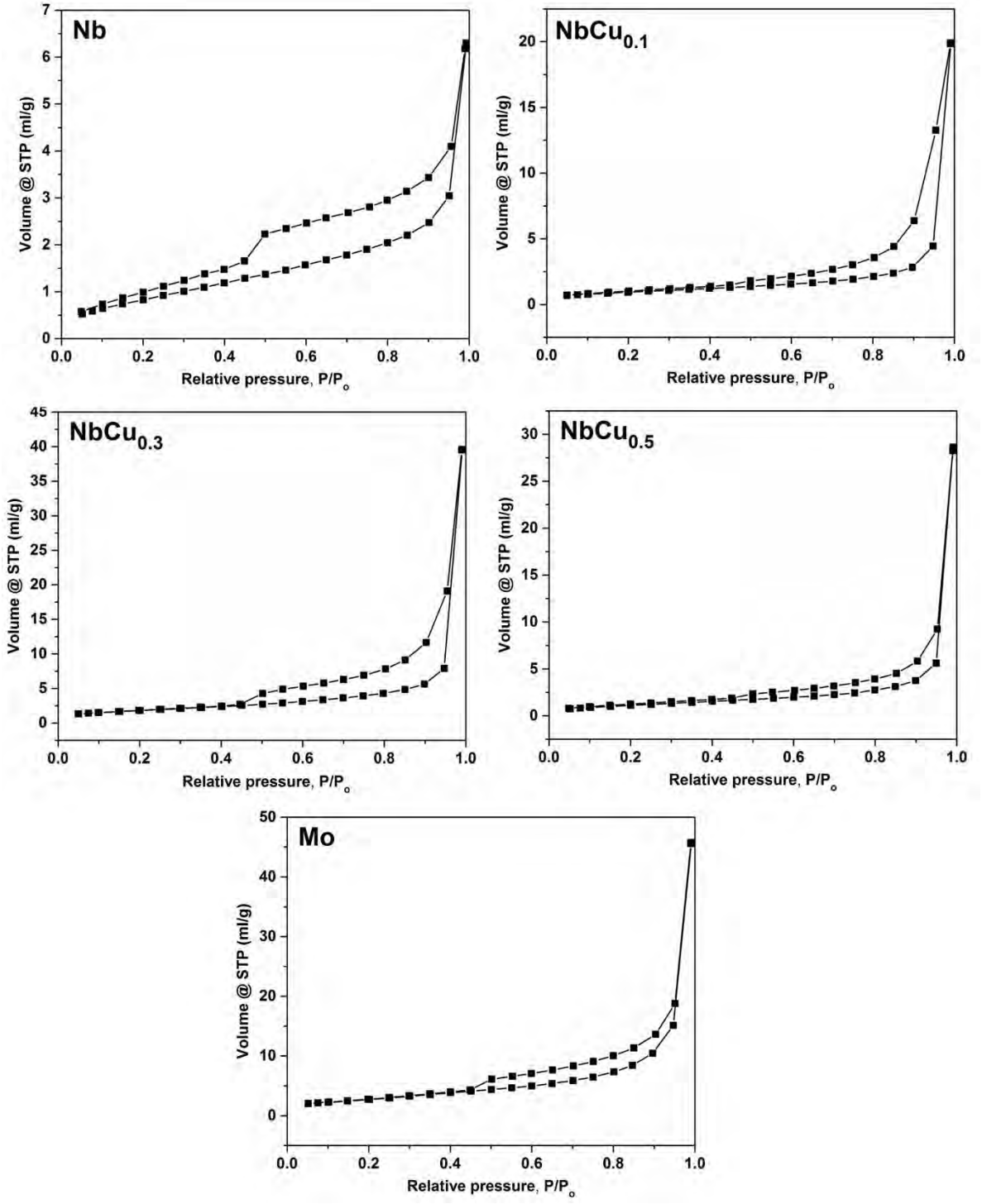

Figure S2. Nitrogen adsorption-desorption isotherms of the sulfided catalysts; sulfidation at 400 °C for 20 h.

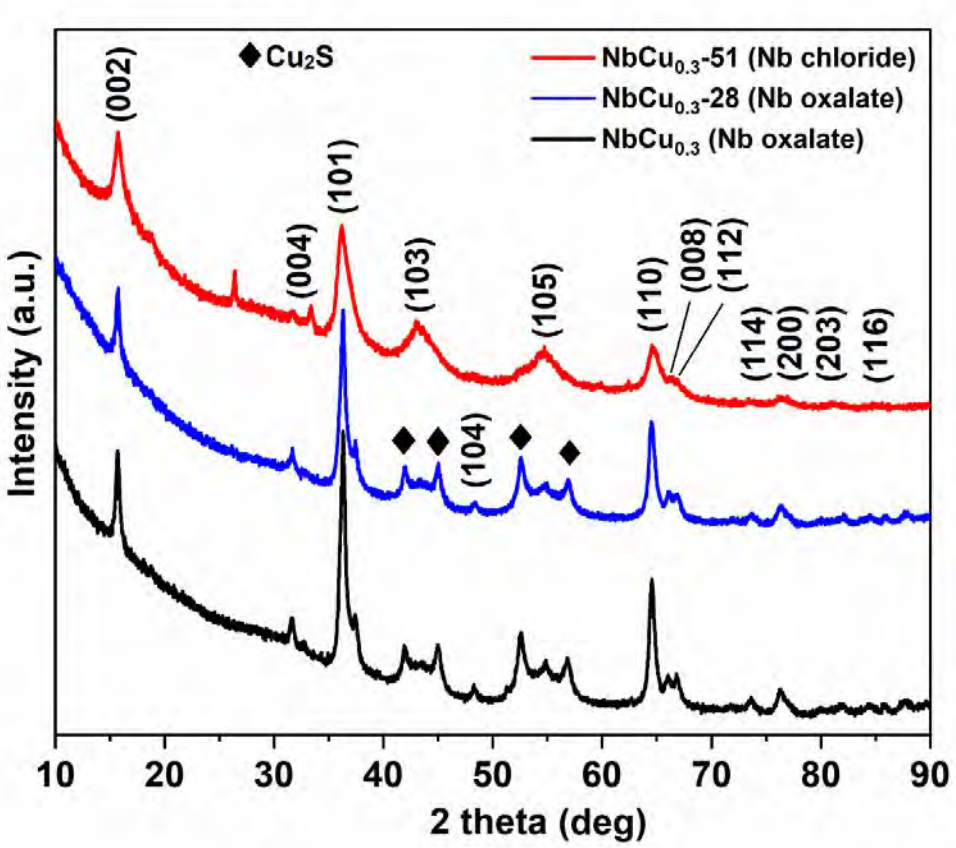

Figure S3. XRD patterns of sulfided $NbCu_{0.3}$ and $NbCu_{0.3}$-28 (both prepared from Nb oxalate), and $NbCu_{0.3}$-51 (prepared from Nb chloride); peaks assignment according to the PDF 00-015-0409 for $Cu_{0.65}NbS_2$ and 97-010-0333 for Cu_2S.

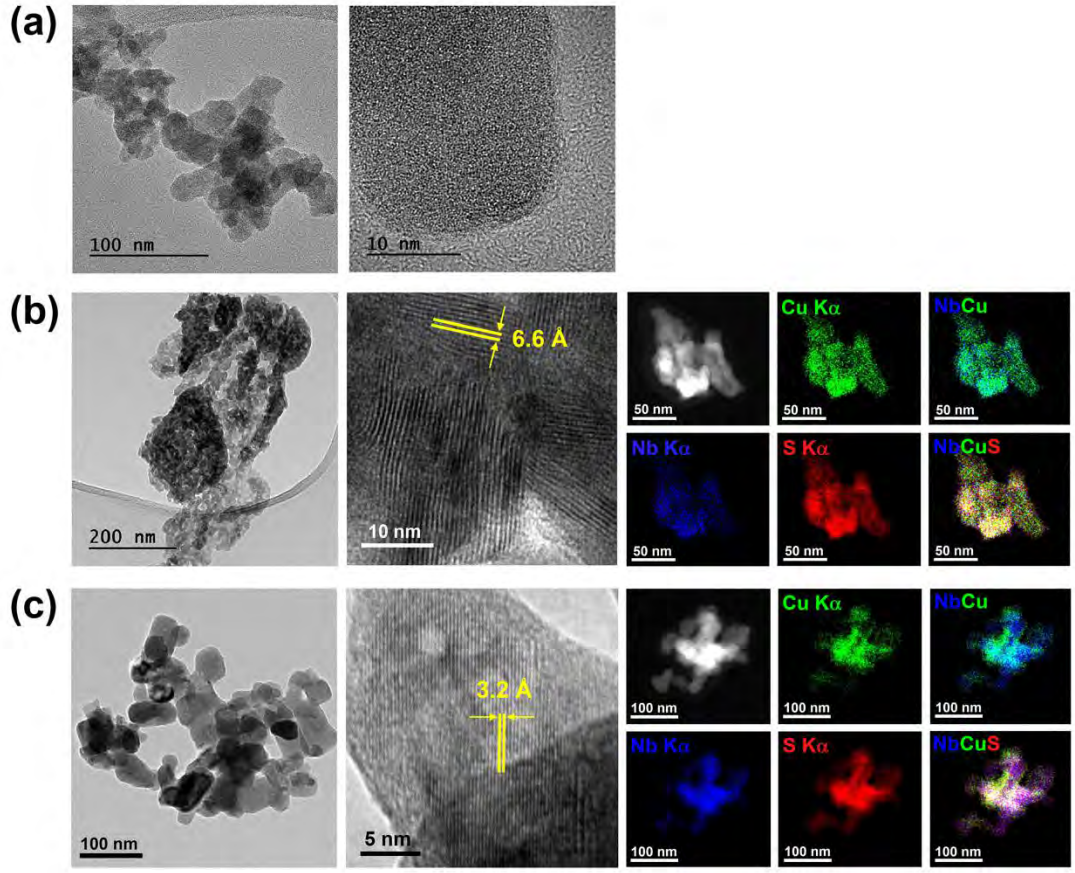

Figure S4. TEM, HRTEM, and STEM-EDS images of sulfided catalysts: (a) Nb-53, (b) $NbCu_{0.3}$-28, and (c) $NbCu_{0.3}$-51.

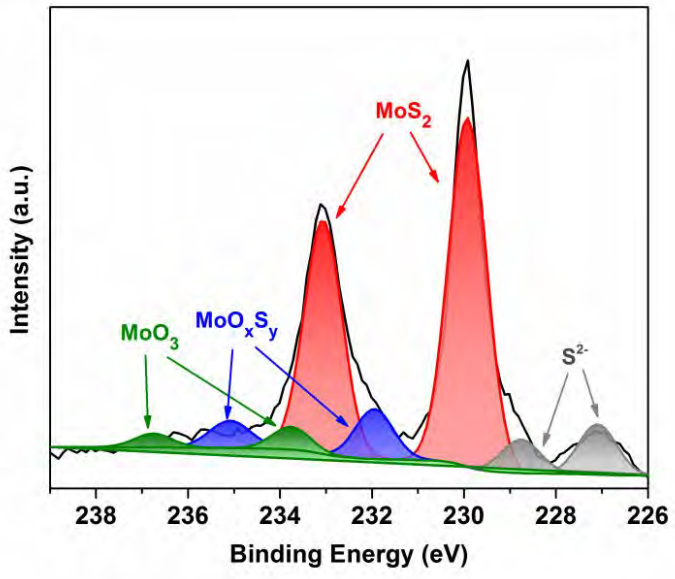

Figure S5. Deconvoluted XPS spectrum of Mo after sulfidation at 400 °C for 20 h.

Table S1. Products distribution in HDS of DBT at 325 ºC and 3.0 MPa after 24 h on-stream

Catalyst	WHSV (h^{-1})	Mass of cat. (g)	DBT conversion (%)	Rate* (10^{-5} mol_{DBT} kg_{cat}^{-1} s^{-1})	Selectivity (mol %)						
					DDS	HYD				HCK	
					BP	BCH	CHB	HHDBT	THDBT	BZ	CH
Nb	7.5	0.3	32	2.5	49	7	26	1	12	5	<1
$NbCu_{0.1}$	7.0	0.322	41	3.2	48	3	42	<1	2	4	<1
$NbCu_{0.3}$	6.5	0.343	50	4.0	50	3	41	<1	1	4	<1
$NbCu_{0.5}$	5.8	0.388	34	2.1	58	2	35	<1	3	1	<1
$NbCu_{1.0}$	4.8	0.47	12	0.6	70	3	11	<1	7	6	3
Mo	7.5	0.3	16	1.1	54	2	25	1	16	1	<1
$NbCu_{0.3}$-28	90	0.05	37	37.8	81	1	15	<1	2	<1	<1
$NbCu_{0.3}$-39	90	0.05	52	60.5	71	3	21	<1	2	3	<1
$NbCu_{0.3}$-51	90	0.05	49	55.4	75	2	20	<1	2	1	<1
Mo-19	90	0.05	24	22.7	90	<1	2	1	2	5	<1
CoMo-14	360	0.025	24	90.0	96	<1	2	<1	2	<1	<1
$CoMo/Al_2O_3$	360	0.025	73	431.0	95	<1	4	<1	<1	<1	<1

* Based on rate constant calculated from a first-order rate law and initial concentration of DBT in the feed.

3 COLLOIDAL SYNTHESIS PROTOCOL OF SHAPE- AND DIMENSIONALLY-CONTROLLED TRANSITION-METAL CHALCOGENIDES AND THEIR HYDRODESULFURIZATION ACTIVITIES

This Section was published as

Mansouri A., Semagina N. Colloidal synthesis protocol of shape- and dimensionally-controlled transition-metal chalcogenides and their hydrodesulfurization activities, ***ACS Applied Nano Materials***, 1, 4408-4412 (2018).

It is reprinted here with the permission from American Chemical Society, the permission is attached to the report.

3.1 Abstract

We present a single-step ligand-directed colloidal synthesis protocol for a selective growth of dimensionally- and shape-controlled niobium disulfide (NbS_2) nanostructures. A systematic modulation of the reaction conditions resulted in the development of monolayer nanosheets, which alternatively grew as laterally confined (< 100 nm) 2D nanostructures using an appropriate mixture of coordinating ligands with different functional groups. The lateral size reduced to ~50 nm by increasing the amount of chalcogen source (CS_2), which promoted the planar growth to form 0D nanohexagons and 1D hexagonal nanorods. A non-coordinating solvent suppressed anisotropic growth and resulted in the formation of 0D nanospheres. Nanohexagons with the highest fraction of corner and edges active sites delivered the highest activity in dibenzothiophene hydrodesulfurization

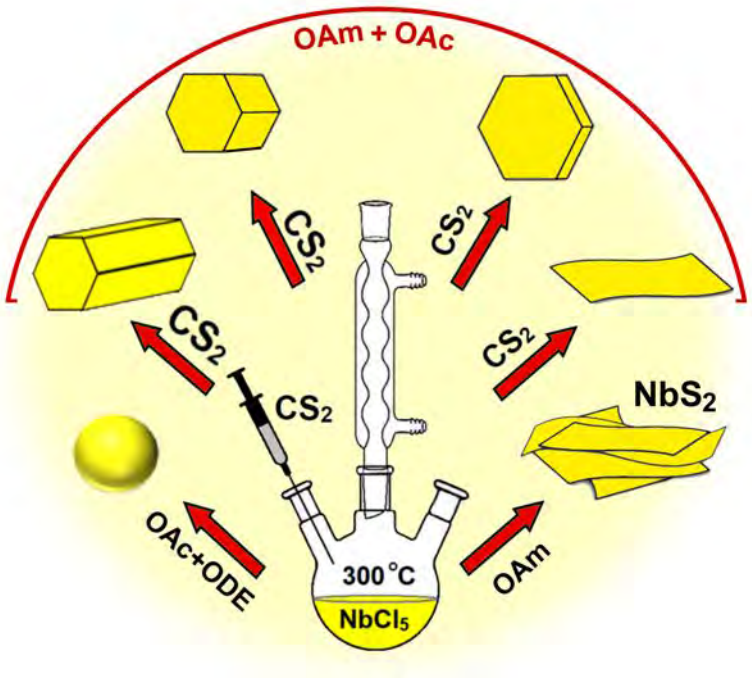

3.2 Introduction

Two-dimensional (2D) transition-metal dichalcogenides (TMDCs) are of particular interest due to their numerous exotic properties, especially when present as a single- or few atomic layers.[1–10] The lamellar van der Waals force allows the stabilization of single layers,[8,11,12] which, opposed to inert graphene, exhibit a tunable chemical versatility in catalysis, energy storage materials, and (opto)electronics.[7,11] The synthesis of such nanomaterials relies on the anisotropic growth of nanocrystals, which is attributed to the surface energy difference between the edge and planar facets.[13] Therefore, it is a challenging task, particularly when controlling the shape, size, and thickness is desired. Compared to the mechanical exfoliation and chemical vapor deposition methods,[14–18] colloidal synthesis provides promising advantageous, such as relative simplicity and a good control of the crystallinity and monodispersity of TMDCs.[1,2,4,7,13] Moreover, utilizing capping ligands with different electronic and geometric properties in the solution facilitates the size and structure control via tuning the thermodynamics and kinetics of crystallographic planes' growth.[2,19–22] Despite a great progress in this field, the size- and shape-controlled colloidal preparations of TMDCs are not well established and remain as a challenge of paramount importance.

This study demonstrates a reproducible ligand-directed synthesis protocol for a selective growth of shape-controlled 2D, 1D, and 0D TMDC colloids at mild conditions (Scheme 1). We chose niobium as a representative case because of its difficult gas-solid sulfidation that requires high-temperature (>750 °C) to produce NbS_2.[18,23,24] Herein, the 0D-2D classification is based on the number of dimensions which exceed 100 nm (i.e., are outside of the nano-size range). We discovered that, besides the amount of sulfur, a modulation between the capping ligands, possessing amine and carboxylic acid functional groups, directs the growth of nanocrystals and thus the dimension and shape evolution of NbS_2. An increased fraction of oleic acid (OAc) in oleylamine (OAm) promoted the formation of ultrathin nanosheets, whereas shape- and laterally confined 2D nanostructures were obtained at a reduced OAc content. The amount of CS_2 was found to be important to determine the lateral size, planar growth, and the final shape of nanostructures. To the best of our knowledge, this is the first report on the formation of a variety of 0D-2D TMDC nanostructures using a ligand-directed approach.

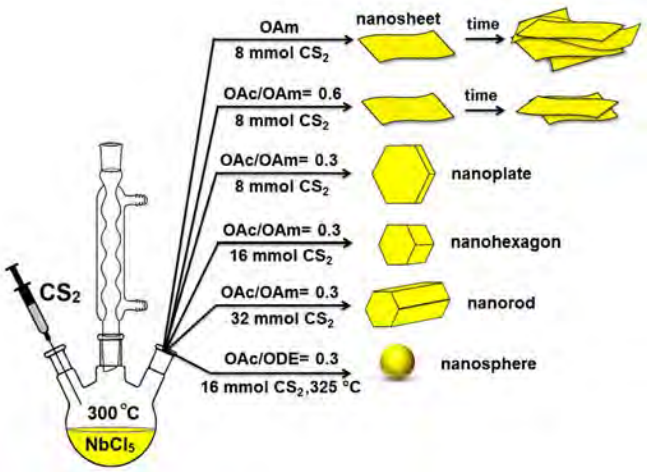

Scheme 1. Schematic illustration of colloidal synthesis protocol of NbS_2 nanostructures.

3.3 Experimental

The NbS_2 nanosheets were synthesized according to the procedure described previously with some modifications.[1,25] Briefly, 8 mmol of carbon disulfide (CS_2) was injected into a mixture of OAm and 0.23 mmol $NbCl_5$ stirring at 300 °C under an argon atmosphere. OAm may serve as a solvent, surfactant and a reducing agent depending on the conditions.[26] Its reaction with CS_2 results in *in situ* H_2S generation for sulfidation of a transition-metal chloride.[1]

3.3.1 Materials

Niobium (V) chloride ($NbCl_5$, 99%), oleylamine (OAm, ≥98 %), oleic acid (OAc, Technical grade, 90%), 1-octadecene (ODE, Technical grade, 90%), and carbon disulfide (CS_2, ≥99.9%) all from Sigma–Aldrich were used as received. 2-propanol (anhydrous 99.5%), ethanol (anhydrous, 90%), and *n*-hexane were purchased from Fischer Scientific. Gamma-alumina (γ-Al_2O_3 powder, Sasol CATALOX SBa-200, BET=200 m^2/g) was used as a support material. Dibenzothiophene (DBT, $C_{12}H_8S$, Sigma-Aldrich), *n*-dodecane (Sigma-Aldrich), and *n*-decane (Fischer Scientific) were used as a model fuel for HDS reaction. Ultra-high purity (99.999%) argon and hydrogen gases were purchased from Praxair, Canada.

3.3.2 Synthesis of NbS_2 nanosheets

In a three-neck flask, 0.23 mmol of $NbCl_5$ was dissolved in 20 ml of OAm. The solution was degassed using ultra-high purity argon gas at 100 °C for 15 min while mixing rigorously. Next, the mixture was heated up to 300 °C at 5 °C/min where 8 mmol of CS_2 was injected into the solution, generating hydrogen sulfide (H_2S) *in situ* to form NbS_2 nanosheets. This is indicated by an instant color change from yellow to dark brown. The sulfidation reaction was prolonged up to 15 min, 30 min, and 3 h. The obtained solution thickened during the synthesis procedure, which initiated after 30 min, correlating with the synthesis time. For OAc containing solution, OAc was added to OAm at an OAc/OAm molar ratio of either 0.3 or 0.6 and then the above-mentioned synthesis procedure was followed. The synthesized NbS_2 nanosheets were isolated by adding an excess mixture of ethanol and 2-propanol (1:3 volume ratio) to the synthesis solution followed by centrifugation at 8500 rpm for 5 min. The obtained nanosheets were then dispersed in *n*-hexane and then the vial was kept in an ultrasonic bath to obtain a macroscopically homogeneous solution. Next, the excess mixture of ethanol and 2-propanol was added again followed by centrifugation at the same conditions. This procedure was repeated twice after a quick removal of supernatant. Finally, the sample was washed with ethanol. For the OAm-containing solutions, the samples were washed six times following the same procedure.

3.3.3 Synthesis of the NbS_2 nanoplates

5 ml of OAc was mixed with 15 ml of OAm containing 0.23 mmol of $NbCl_5$. The solution was stirred under argon gas at 100 °C for 15 min and then heated up to 300 °C. After that, 8 mmol CS_2 was injected into the stirring solution while being purged with argon gas. The color of the

solution slowly changed to dark green. The difference in the color of the solutions between the nanosheets and the nanoplates indicates the different coordination of Nb ions. After 2 h, the mixture was cooled down to room temperature. The obtained colloids were macroscopically homogeneous. The nanoplates were collected using a mixture of ethanol and 2-propanol (1:3 volume ratio) and a centrifuge, as described in 3.3.2.

3.3.4 Synthesis of the NbS_2 nanohexagons

Similar to the synthesis procedure of the nanoplates, but 16 mmol of CS_2 was injected into the stirring solution at 300 °C while being purged with argon gas. The color of the solution slowly changed to brown. The mixture was clear and macroscopically homogeneous with no precipitation after 2 h. The obtained nanohexagons were collected using a mixture of ethanol and 2-propanol (1:3 volume ratio) and a centrifuge.

3.3.5 Synthesis of the NbS_2 nanorods

Similar to the synthesis protocol of the nanohexagons, 0.23 mmol of $NbCl_5$ was dissolved in a mixture of OAc and OAm (5:15 ml). Once the temperature of the stirring solution reached 300 °C, 32 mmol of CS_2 was injected into the stirring solution, changing the color to brown. The obtained colloids were clear and macroscopically homogeneous with no signs of precipitation after 2 h of sulfidation reaction at 300 °C. The synthesized nanorods were mixed with a mixture of ethanol and 2-propanol and then isolated by centrifuge, , as described in 3.3.2.

3.3.6 Synthesis of the NbS_2 nanospheres

A total of 0.23 mmol of $NbCl_5$ was dissolved in 5 ml of OAc and then mixed with 15 ml of ODE. After degassing at 100 °C for 15 min, the solution was heated up to 325 °C, at which point, 16 mmol of CS_2 was injected in the mixture, changing the color to dark red. After refluxing for 2 h, the obtained colloidal nanospheres, clear and macroscopically homogeneous, were collected using a centrifuge and a mixture of ethanol and 2-propanol, , as described in 3.3.2.

3.3.7 Al_2O_3-supported NbS_2 nanostructures

The colloidal solution of the synthesized nanostructures was mixed with 2 g of alumina support and an excess of ethanol and 2-propanol (1:3 volume ratio) at room temperature. The nanostructures were extracted from the synthesis solution and homogeneously deposited on the support. The obtained materials were dried at 80 °C overnight under a vacuum before the catalytic experiments.

3.3.8 Catalyst characterization

High-resolution transmission electron microscopy (HR-TEM) images were recorded using a JEOL JEM2100 device operating at 200 kV. The energy-filtered TEM image for niobium was acquired in a range of 195-215 eV with a slit width of 20 eV. The synthesis solution was washed three times with a mixture of ethanol and 2-propanol and then twice with pure ethanol to remove the ligands. Next, the centrifuged sample was dispersed in ethanol for TEM analysis. The

washed nanostructures were embedded in Spurr's resin at 70° C followed by being split into 100 nm sections using Ultramicrotome Leica EM UC6. Scanning transmission electron microscopy (STEM/EDX) analysis was performed on a JEOL JEM-ARM200cF S/TEM, which is equipped with a cold Field-Emission Gun (cFEG) and a probe Cs corrector. EDX maps were acquired with a Silicon Drift (SDD) EDX detector at an acceleration voltage of 200 kV. XRD patterns were recorded on a continuous scan at 2 degrees 2θ per minute with a step size of 0.01° using a Rigaku Ultima IV diffractometer equipped with a D/Tex detector, ad Fe Filter, and Co Kα radiation (λ = 1.78899 Å). Data interpretation was done using JADE 9.6 with the 2016 ICDD and 2016 ICSD databases. The AFM images were taken on a Bruker Dimension Edge system using the tapping mode. The cantilever is from Ted Pella TAP-300. The silicon wafer was covered with a 5 nm carbon film before deposition of NbS_2 nanosheets. XPS analyses were performed using the Kratos Axis 165 Xray photoelectron spectrometer and using the Mono Al Kα source, operating at 14 kV and 15 mA. The measured XPS doublets were calibrated with C 1 s at 284.8 eV and then analyzed using CasaXPS software. Raman spectra were recorded using a Thermo Scientific DXR2 Raman microscope with a 532 nm laser with a high-resolution grating (wavenumber resolution is about 2 cm^{-1}). The spectra were taken from different regions of the sample at 10-times exposures and 10 second exposure time. The UV-vis absorption spectra of colloidal nanostructures dispersed in ethanol were collected with a Varian Cary 50 Scan UV-visible spectrophotometer with 1 cm quartz cuvette. The elemental analyses of the supported catalysts were performed using an ICP-MS Perkin Elmer's Elan 6000 at ICP RF power of 1300 W.

3.3.9 Hydrodesulfurization (HDS) experiments

The synthesized catalysts were tested in HDS of DBT at 325 °C, 3.0 MPa H_2 in a packed-bed reactor. About 0.25 g of catalyst diluted with 4 g of silicon carbide (mesh 150) was used for each HDS test. Before each measurement, the catalysts were subjected to 3 h *in situ* sulfidation at 325 °C under 3.0 MPa of hydrogen using a 0.05 ml/min flow of 10 wt% of CS_2 in *n*-decane premixed with 100 ml/min of H_2. Neither a longer sulfidation pretreatment (20 h) nor higher sulfidation temperature (400 °C) improved the catalytic performance. The feed for the catalytic experiments contained 1000 ppmw S as DBT with 3.5 wt% of *n*-dodecane (internal standard) in *n*-decane as a solvent. The feed was introduced at 0.05 ml/min mixed with 100 ml/min of H_2 (H_2-to-liquid molar ratio of 16). The pH_2S/pH_2 ratio of approximately 10^{-4} was used (using DBT) to stabilize the sulfided state. Quantification of DBT and the reaction products were performed offline using a calibrated Agilent 7890A gas chromatograph. The carbon balance was within 95%. The catalytic activity was calculated according to the first-order reaction, as described below.

Rate constant for the first-order reaction

$$k_{DBT} = \frac{Ln\left(\frac{1}{1-X_{DBT}}\right) \times F_{DBT}}{C_{DBT} \times m_{cat.}}, \left(\frac{L}{kg_{cat.} \cdot s}\right) \quad (1)$$

F_{DBT} is the molar flow rate of DBT in the feed, mol/s; m_{cat} is the mass of the catalyst in the reactor, kg_{cat}; X_{DBT} is the conversion of DBT after 24 h of HDS, C_{DBT} is the concentration of DBT in the feed stream, mol/L; Reaction rate (at the initial DBT concentration in the feed):

$$-r_{DBT} = k_{DBT} \times C_{DBT}, \left(\frac{mol_{DBT}}{kg_{cat.} \cdot s}\right) \quad (2)$$

3.4 Results and discussion

The formation of nanosheets was confirmed by STEM-EDS analysis (Figures 1 and S1) and asymmetric XRD peaks[5,27] (Figure S2). XPS showed Nb *3d* binding energies centered at 203.0 eVand 205.8 eV[24,28,29] which are characteristic of NbS_2 (Figure 1b and Figure S3). Deconvolution of the Nb *3d* spectra collected *ex situ* after 180 min sulfidation showed that 67 at.% of surface Nb was sulfided as NbS_2, with the residual equally divided between Nb_2O_5 and partially oxidized NbO_x (Figure S3b). The oxides may form from the moisture-sensitive $NbCl_5$ precursor, as well as during the sulfided sample storage. The contribution of Nb_2O_5 diminishes with the sulfidation time (Figure 1b). Figure 1d illustrates the TEM image of the single-layer NbS_2 nanosheets and their structural transformation as the sulfidation reaction proceeds. Monolayer nanosheets with a thickness of 1.0 nm were formed within 15 min of sulfidation (Figure 1d, images on the left side). The XRD pattern of the corresponding sample showed no *c*-axis peaks (Figure S2), which is a characteristic pattern of monolayer nanosheets.[5,22] The *d*-spacing of the single-layer nanosheet was determined to be 58 Å (Figure S4). The atomic force microscopy (AFM) analysis in Figure 1c and Figure S5 show the lowest topographic height of ca. 1.0 nm, as a typical thickness of single-layer NbS_2.[30] According to the determined heights from AFM images (Figure S5), the synthesized nanosheets after 15 min sulfidation consist of one or two layers of NbS_2.

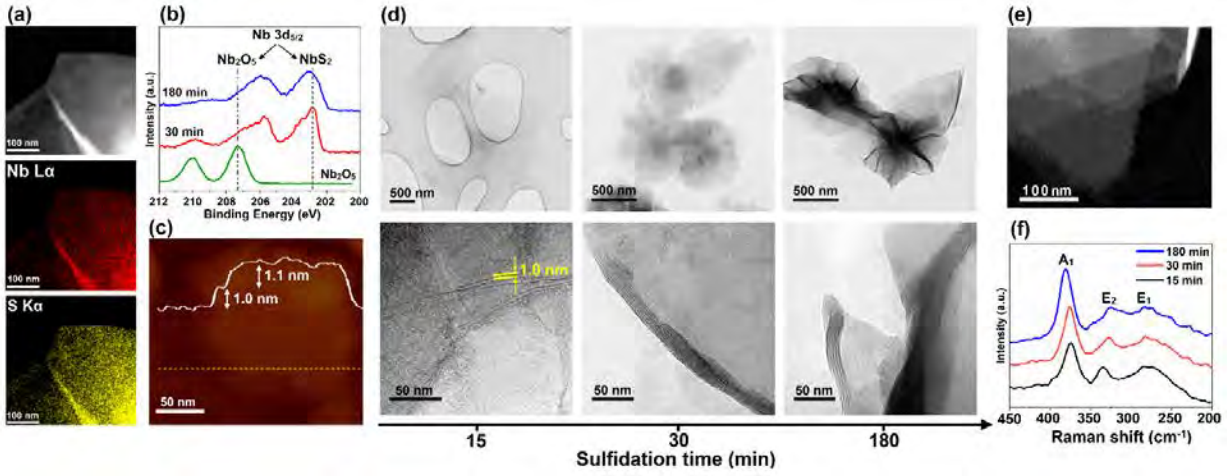

Figure 1. Characterization of the NbS_2 nanosheets synthesized in OAm at 300 °C using 8 mmol CS_2: (a) STEM-EDS mapping (oxygen mapping in shown in Figure S1 in the Supporting Information); (b) XPS Nb *3d* spectra of the NbS_2 nanosheets synthesized at 30 min and 180 min sulfidation times and bulk niobium oxide (Nb_2O_5) prepared by calcination of Nb precursor at 400 °C for 4 h in static air; the deconvolution can be found in Figure S3; (c) AFM image of single-layer nanosheets collected after 15 min sulfidation (additional images are in Figure S5 in the Supporting Information); (d) low- and high-magnification TEM images of the nanosheets collected at different sulfidation times; (e) energy-filtered TEM image of the overlayered monolayer nanosheets acquired for niobium after 180 min sulfidation; (f) Raman spectra of the nanosheets collected at different sulfidation times.

Stacking of the layers into multilayers nanosheets and a lateral size increase occurred when the sulfidation time was prolonged up to 180 min resulting in the formation of a flower-like structure (Figure 1d), as reported previously for WS_2 and the NbS_2 nanosheets;[2,25] however, monolayers were observed in the edge areas (Figure S6). The energy-filtered TEM image of the edge area acquired for niobium (in the range of 195-215 eV, slit width of 20 eV) visualizes the overlaying of single-layer nanosheets (Figure 1e). We also characterized the optical properties of the nanosheets using Raman and UV-vis absorption spectroscopies, showing thickness-dependent features. As the Raman spectra in Figure 1f show, A_1 phonons stiffened with a positive shift by the number of layers in the nanosheets, while E_2 phonons softened and negatively shifted, which is in line with former reports.[31,32] The UV-vis spectra exhibited a red shift from ca. 262 to 278 nm with the number of layers (Figure S7), which agrees with previous findings.[22,28,33]

The addition of OAc into OAm led to the significant structural changes, depending on the OAc/OAm molar ratio (Figure 2). We discovered that there is a threshold concentration of OAc in OAm under which shape-confined 2D nanostructures with a remarkably reduced lateral size (<100 nm) developed instead of nanosheets. OAc/OAm above 0.6 formed ultrathin (a single- and a few layers thick) nanosheets with a reduced lateral size after 180 min sulfidation (Figure 2, top left). Moreover, the formation of the flower-like structure was suppressed. The XRD intensities diminished remarkably with no *c*-axis peaks (Figure S8). This lateral and planar confinement can be attributed to the monomers' reactivity change during the nucleation and growth period[19–21] and a diffusion barrier that prevents the active monomers from reaching the crystal's surface.[34] Similarly, a former study showed that pure OAc stabilized laterally grown monolayer $MoSe_2$ and WSe_2 nanosheets compared to OAm and oleyl alcohol.[22] In contrast, the OAc/OAm of 0.3 developed single crystalline hexagonal nanoplates of 106 nm lateral size and 9.5 nm thickness (Figure 3a-d). As the side-view TEM image in Figure 3d shows, the ligand-removed nanoplates assembled along the *c*-axis into stacked nanostructures with a *d*-spacing of 3.2 Å, attributing to the (002) plane of NbS_2. Carboxylic acid and amine have different binding affinities toward the reactive edge facets.[22] Therefore, aside from providing the diffusion barrier for active monomers, the synergism between OAc and OAm explains the preferential growth of crystallographic facets and shape confinement.

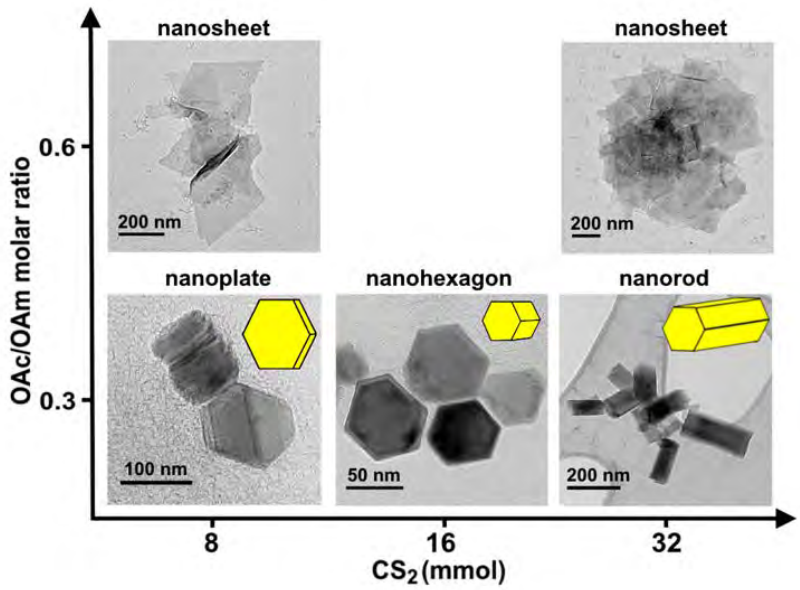

Figure 2. NbS_2 structure dependence on the OAc/OAm molar ratio and the amount of CS_2.

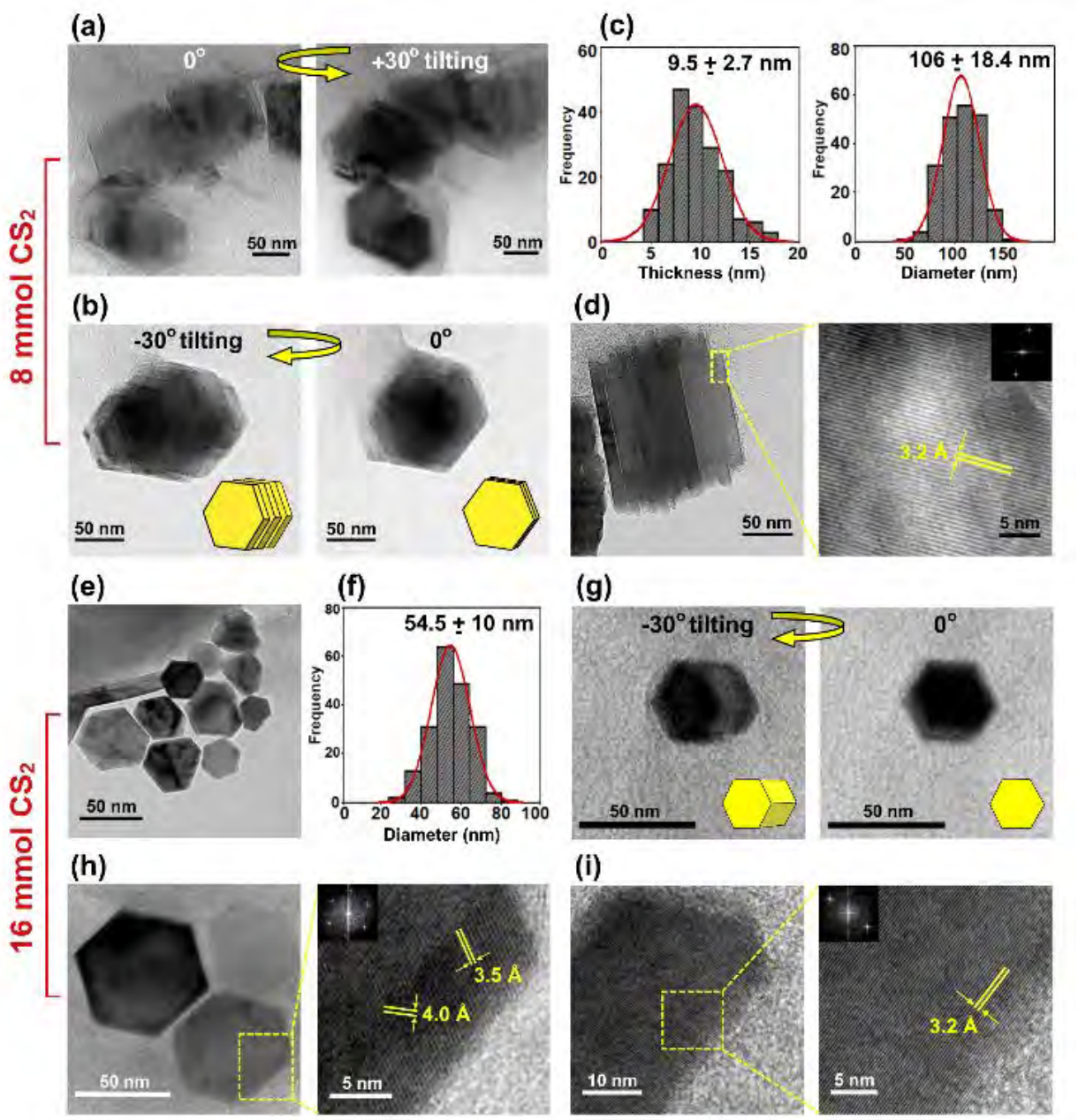

Figure 3. (a-d) TEM images of NbS_2 nanoplates and size distributions obtained by counting 200 nanoplates from different synthesis batches; (e-i) TEM images of nanohexagons; insets: fast Fourier transform (FFT) patterns

Apart from the capping ligands, the amount of CS_2 affected the selective evolution of nanocrystals, as observed before.[35,36] Increasing CS_2 from 8 to 32 mmol in the synthesis of the nanosheets in OAm resulted in multilayers nanosheets along with the flower-like structure within the early stage of sulfidation (30 min) (Figure S9). In contrast, OAc at the OAc/OAm of 0.6 confined the number of layers and the lateral size even after 3 h of sulfidation with 32 mmol of CS_2 (Figure 2 and Figure S10). Interestingly, completely different structures were formed at the reduced OAc/OAm of 0.3. 16 mmol CS_2 promoted the vertical growth of the nanocrystals and transformed the nanoplates into the corner- and edge-abundant single crystalline nanohexagons with eight facets, as evidenced by TEM tilting experiments (Figure 3e-i). Compared to the nanoplates, the lateral size decreased from 106 to 55 nm while the planar size multiplied (Figure 3c,f), however, the *d*-spacing remained constant (Figure 3d, i). The side facets of nanohexagons are larger than the diameter, but the precise measurement was not possible due to the low contrast of the side facets under the electron microscope. An increased sulfidation temperature of 325 °C had no influence on the size and morphology of the nanohexagons.

A further increase of CS_2 to 32 mmol converted nanohexagons into 1D nanorods with a hexagonal cross-section, according to the TEM images of oriented and cross-sectioned samples (Figure 4). The obtained nanorods are a single crystal with a fringe size of 3.5 Å, ascribing to the (004) plane of NbS_2. Similar to the nanohexagons, the nanorods possess an average diameter of 55 nm but with an increased length of 127 nm. The TEM image after 15 min of sulfidation (Figure S11) revealed that Nb species nucleated as near-spherical seeds and then evolved into a hexagonal nanostructure with a thickness correlating with the CS_2 amount. This suggests that an enhanced amount of sulfur accelerates the kinetics of anisotropic crystal growth vertically, which is attributed to the presence of various crystallographic facets in nanocrystals with different surface energies and levels of reactivities toward sulfur.[3,35,36]

When OAm was replaced with a non-coordinating and non-reducing solvent 1-octadecene (ODE) in nanohexagon synthesis procedure, single-crystalline 0D nanospheres with an average size of 24 nm and fringe spacing of 3.2 Å were formed after 2 h of sulfidation at 325 °C (Figure 5). OAm addition to the mixture of OAc and ODE at the OAc/OAm of 0.3 changed the morphology of the nanospheres into a non-defined shape structure with an increased size and fraction of corners and edges, but it was different from the nanohexagons (Figure S12). This shows that OAm suppresses the nucleation via reaction with CS_2[1,7] and acts as a coordinating solvent directing the anisotropic growth of nanostructures. Similarly, a previous work showed that OAm promoted the growth of FePt nanowires while its dilution with ODE facilitated the formation of spherical nanoparticles.[37] OAm, as a coordinating agent, preferentially binds to distinctive crystallographic facets, restricting the extent of precursor supersaturation and crystallographic planes growth.[21,38]

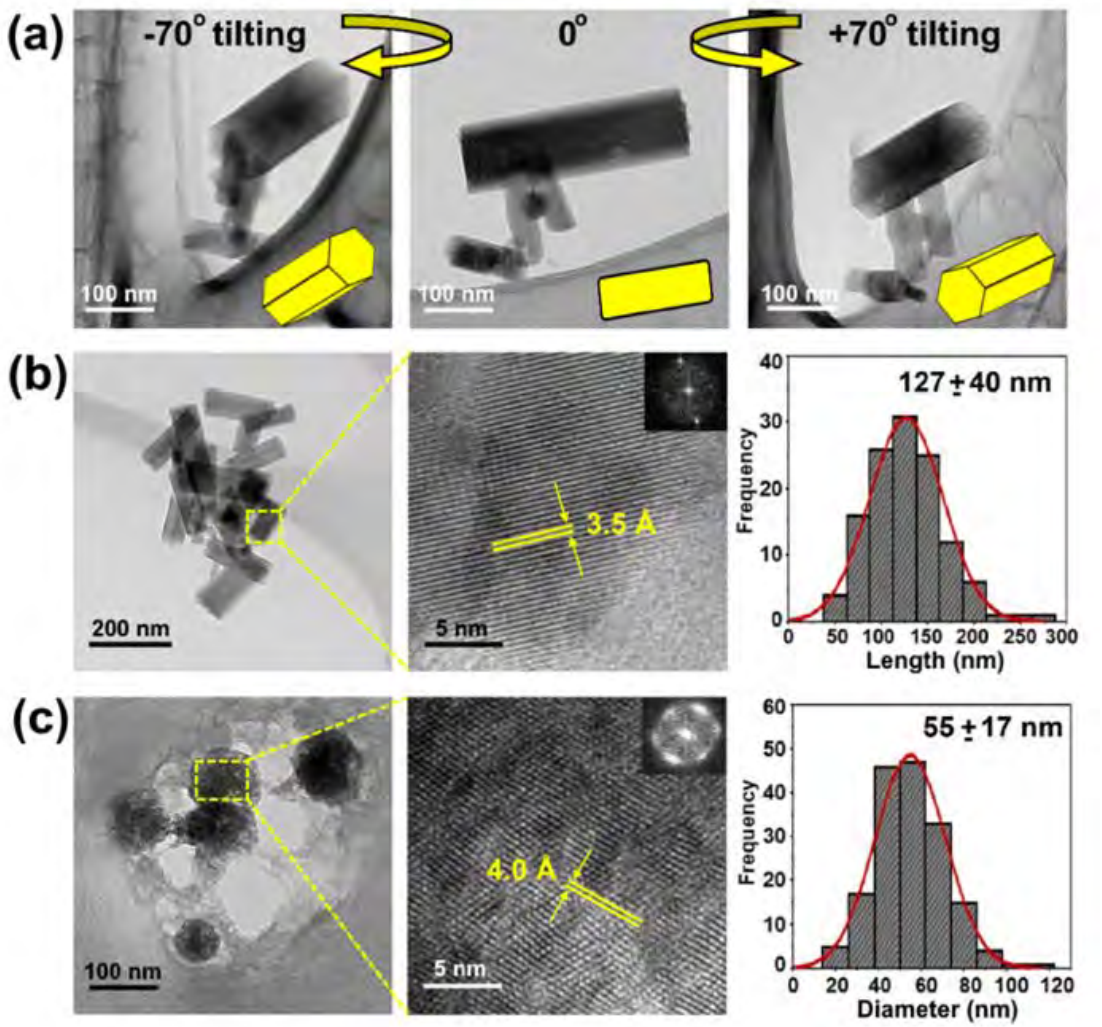

Figure 4. TEM images and size distributions of hexagonal NbS_2 nanorods (a, b) and (c) cross-sectional TEM images of the nanorods prepared by microtome sectioning; insets: FFT patterns.

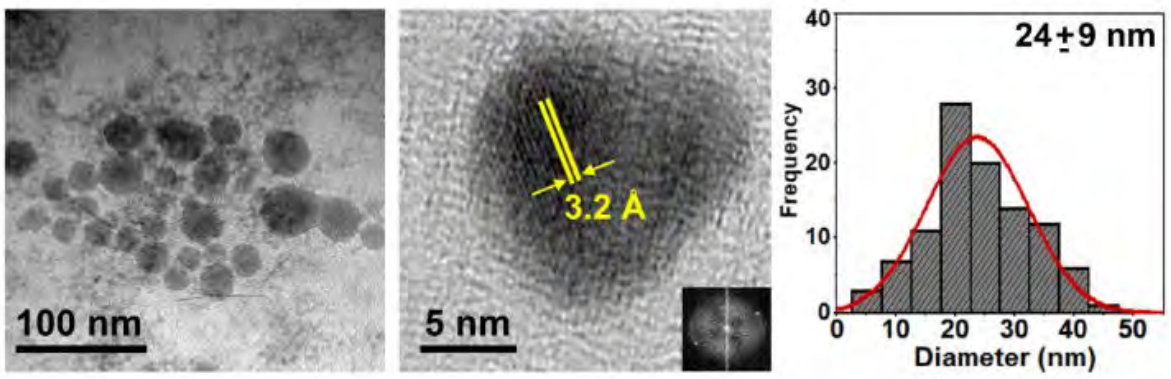

Figure 5. The TEM, HRTEM, and particle size distribution of NbS_2 nanospheres; inset: FFT pattern.

The synthesized colloidal nanostructures were precipitated on a γ-Al_2O_3 support, using a mixture of ethanol and 2-propanol, and then evaluated in hydrodesulfurization (HDS) of dibenzothiophene (DBT, Scheme S1[39]) at 325 °C and 3.0 MPa in a packed-bed reactor. The TEM images of the spent catalysts after 24 h of HDS revealed the structural stability of the nanostructures with no signs of aggregation and deformation (Figure S13). As shown in Table 1 and Table S1, the highest HDS activity was obtained by NbS_2 nanohexagons, followed by nanorods, nanospheres, and single-layer nanosheets. Although the nanospheres possessed a smaller size (25 nm), the nanohexagons delivered higher activity, which can be attributed to the enhanced fraction of corner and edge active sites. The HDS reaction rate and the sulfur-free yield delivered by the nanohexagon catalyst were about an order of magnitude higher than that of Nb-based bulk catalyst tested under the same conditions in our previous work.[24]

Table 1. Catalytic performance of Al_2O_3-supported NbS_2 catalysts in HDS of DBT at 325 °C and 3.0 MPa after 24 h on stream.

Catalyst	Reaction rate (10^{-5} mol_{DBT} mol_{Nb}^{-1} s^{-1})	Sulfur-free yield (10^{-5} mol $mol_{Nb}^{-1}s^{-1}$)
single-layer nanosheets[a]	7	6
multilayers nanosheets[b]	4	2
nanohexagon	98	49
nanorod	61	40
nanosphere	33	26

[a] after 15 min sulfidation in OAm
[b] after 180 min sulfidation in OAm

3.5 Conclusions

In summary, we reported a facile ligand-directed colloidal synthesis technique for the formation of a variety of shape-controlled NbS_2 nanostructures. A coordinating solvent is required for an anisotropic growth of nanostructures. Aside from the type and amount of capping ligands that control the growth, and, thus the dimensionality of nanocrystals, the sulfur content was found to be critical to directing the growth direction and thus the shape and size of nanostructures. The synthesized NbS_2 nanohexagons with the highest fraction of corners and edges active sites exhibited the highest activity in dibenzothiophene hydrodesulfurization. The study provides an insight into the selective growth and dimensionally-controlled formation of TMDC.

3.6 References

(1) Jeong, S.; Yoo, D.; Jang, J.; Kim, M.; Cheon, J. Well-Defined Colloidal 2-D Layered Transition-Metal Chalcogenide Nanocrystals via Generalized Synthetic Protocols. *J. Am. Chem. Soc.* **2012**, *134*, 18233–18236.
(2) Mahler, B.; Hoepfner, V.; Liao, K.; Ozin, G. A. Colloidal Synthesis of 1T-WS_2 and 2H-WS_2 Nanosheets: Applications for Photocatalytic Hydrogen Evolution. *J. Am. Chem. Soc.* **2014**, *136*, 14121–14127.
(3) Jang, J. T.; Jeong, S.; Seo, J. W.; Kim, M. C.; Sim, E.; Oh, Y.; Nam, S.; Park, B.; Cheon, J. Ultrathin Zirconium Disulfide Nanodiscs. *J. Am. Chem. Soc.* **2011**, *133*, 7636–7639.
(4) Yoo, D.; Kim, M.; Jeong, S.; Han, J.; Cheon, J. Chemical Synthetic Strategy for Single-Layer Transition-Metal Chalcogenides. *J. Am. Chem. Soc.* **2014**, *136*, 14670–14673.
(5) Seo, J. W.; Jun, Y. W.; Park, S. W.; Nah, H.; Moon, T.; Park, B.; Kim, J. G.; Kim, Y. J.; Cheon, J. Two-Dimensional Nanosheet Crystals. *Angew. Chemie - Int. Ed.* **2007**, *46*, 8828–8831.
(6) Jeong, S.; Han, J. H.; Jang, J. T.; Seo, J. W.; Kim, J. G.; Cheon, J. Transformative Two-Dimensional Layered Nanocrystals. *J. Am. Chem. Soc.* **2011**, *133*, 14500–14503.
(7) Han, J. H.; Kwak, M.; Kim, Y.; Cheon, J. Recent Advances in the Solution-Based Preparation of Two-Dimensional Layered Transition Metal Chalcogenide Nanostructures. *Chem. Rev.* **2018**, *118*, 6151–6188.
(8) Huang, W.; Gan, L.; Li, H.; Ma, Y.; Zhai, T. 2D Layered Group IIIA Metal Chalcogenides: Synthesis, Properties and Applications in Electronics and Optoelectronics. *CrystEngComm* **2016**, *18*, 3968–3984.
(9) Choi, W.; Choudhary, N.; Han, G. H.; Park, J.; Akinwande, D.; Lee, Y. H. Recent Development of Two-Dimensional Transition Metal Dichalcogenides and Their Applications. *Mater. Today* **2017**, *20*, 116–130.
(10) Lhuillier, E.; Pedetti, S.; Ithurria, S.; Nadal, B.; Heuclin, H.; Dubertret, B. Two-Dimensional Colloidal Metal Chalcogenides Semiconductors: Synthesis, Spectroscopy, and Applications. *Acc. Chem. Res.* **2015**, *48*, 22–30.
(11) Chhowalla, M.; Shin, H. S.; Eda, G.; Li, L. J.; Loh, K. P.; Zhang, H. The Chemistry of Two-Dimensional Layered Transition Metal Dichalcogenide Nanosheets. *Nat. Chem.* **2013**, *5*, 263–275.
(12) Jellinek, F.; Brauer, G.; Müller, H. Molybdenum and Niobium Sulphides. *Nature* **1960**, *185*, 376–377.
(13) Han, J. H.; Lee, S.; Cheon, J. Synthesis and Structural Transformations of Colloidal 2D Layered Metal Chalcogenide Nanocrystals. *Chem. Soc. Rev.* **2013**, *42*, 2581–2591.
(14) Yanase, T.; Watanabe, S.; Weng, M.; Wakeshima, M.; Hinatsu, Y.; Nagahama, T.; Shimada, T. Chemical Vapor Deposition of NbS_2 from a Chloride Source with H_2 Flow: Orientation Control of Ultrathin Crystals Directly Grown on SiO_2/Si Substrate and Charge Density Wave Transition. *Cryst. Growth Des.* **2016**, *16*, 4467–4472.
(15) Ge, W.; Kawahara, K.; Tsuji, M.; Ago, H. Large-Scale Synthesis of NbS_2 Nanosheets with Controlled Orientation on Graphene by Ambient Pressure CVD. *Nanoscale* **2013**, *5*, 5773–5578.
(16) Fu, Q.; Wang, X.; Zhou, J.; Xia, J.; Zeng, Q.; Lv, D.; Zhu, C.; Wang, X.; Shen, Y.; Li, X.; Hua, Y.; Liu, F; Shen, Z.; Jin, C; Liu, Z. One-Step Synthesis of Metal/Semiconductor Heterostructure NbS_2/MoS_2. *Chem. Mater.* **2018**, *30*, 4001–4007.

(17) Kozhakhmetov, A.; Choudhury, T. H.; Al Balushi, Z. Y.; Chubarov, M.; Redwing, J. M. Effect of Substrate on the Growth and Properties of Thin 3R NbS_2 Films Grown by Chemical Vapor Deposition. *J. Cryst. Growth* **2018**, *486*, 137–141.
(18) Simchi, H.; Walter, T. N.; Choudhury, T. H.; Kirkley, L. Y.; Redwing, J. M.; Mohney, S. E. Sulfidation of 2D Transition Metals (Mo, W, Re, Nb, Ta): Thermodynamics, Processing, and Characterization. *J. Mater. Sci.* **2017**, *52*, 10127–10139.
(19) Peng, X.; Thessing, J. Controlled Synthesis of High Quality Semiconductor Nanocrystals. *Struct. Bond.* **2005**, *118*, 79–119.
(20) Yu, W. W.; Peng, X. Formation of High-Quality CdS and Other II-VI Semiconductor Nanocrystals in Noncoordinating Solvents: Tunable Reactivity of Monomers. *Angew. Chemie - Int. Ed.* **2002**, *41*, 2368–2371.
(21) Kort, K. R.; Banerjee, S. Ligand-Mediated Control of Dislocation Dynamics and Resulting Particle Morphology of GdOCl Nanocrystals. *Small* **2015**, *11*, 329–334.
(22) Jung, W.; Lee, S.; Yoo, D.; Jeong, S.; Miro, P.; Kuc, A.; Heine, T.; Cheon, J. Colloidal Synthesis of Single-Layer MSe_2 (M = Mo, W) Nanosheets via Anisotropic Solution-Phase Growth Approach. *J. Am. Chem. Soc.* **2015**, *137*, 7266–7269.
(23) Obolonchik, V. A.; Radzikovskaya, S. V.; Bukhanevich, V. F. A Study of Niobium and Tantalum Sulfides. *Sov. Powder Metall. Met. Ceram.* **1965**, *4*, 877–881.
(24) Mansouri, A.; Semagina, N. Promotion of Niobium Oxide Sulfidation by Copper and Its Effects on Hydrodesulfurization Catalysis. *ACS Catal.* **2018**, *8*, 7621–7632.
(25) Zhang, J.; Du, C.; Dai, Z.; Chen, W.; Zheng, Y.; Li, B.; Zong, Y.; Wang, X.; Zhu, J.; Yan, Q. NbS_2 Nanosheets with M/Se (M = Fe, Co, Ni) Co-Dopants for Li^+ and Na^+ Storage. *ACS Nano* **2017**, *11*, 10599–10607.
(26) Mourdikoudis, S.; Liz-Marzán, L. M. Oleylamine in Nanoparticle Synthesis. *Chem. Mater.* **2013**, *25*, 1465–1476.
(27) Yang, D.; Jimenez Sandoval, S.; Divigalpitiya, W. M. R.; Irwin, J. C.; Frindt, R. F. Structure of Single-Molecular-Layer MoS_2. *Phys. Rev. B* **1991**, *43*, 12053–12056.
(28) Dash, J. K.; Chen, L.; Dinolfo, P. H.; Lu, T. M.; Wang, G. C. A Method Toward Fabricating Semiconducting 3R-NbS_2 Ultrathin Films. *J. Phys. Chem. C* **2015**, *119*, 19763–19771.
(29) Wu, X.; Tao, Y.; Ke, X.; Zhu, J.; Hong, J. Catalytic Synthesis of Long NbS_2 Nanowire Strands. *Mater. Res. Bull.* **2004**, *39*, 901–908.
(30) Zheng, J.; Zhang, H.; Dong, S.; Liu, Y.; Nai, C. T.; Shin, H. S.; Jeong, H. Y.; Liu, B.; Loh, K. P. High Yield Exfoliation of Two-Dimensional Chalcogenides Using Sodium Naphthalenide. *Nat. Commun.* **2014**, *5*, 2995-3002.
(31) Lee, C.; Yan, H.; Brus, L. E.; Heinz, T. F.; Hone, J.; Ryu, S. Anomalous Lattice Vibrations of Single- and Few-Layer MoS_2. *ACS Nano* **2010**, *4*, 2695–2700.
(32) Zhao, S. H.; Hotta, T.; Koretsune, T.; Watanabe, K.; Taniguchi, T.; Sugawara, K.; Takahashi, T.; Shinohara, H.; Kitaura, R. Two-Dimensional Metallic NbS_2: Growth, Optical Identification and Transport Properties. *2D Mater.* **2016**, *3*, 9.
(33) Zhao, W.; Ghorannevis, Z.; Chu, L.; Toh, M.; Kloc, C.; Tan, P. H.; Eda, G. Evolution of Electronic Structure in Atomically Thin Sheets of WS_2 and WSe_2. *ACS Nano* **2013**, *7*, 791–797.
(34) Zhou, J.; Pu, C.; Jiao, T.; Hou, X.; Peng, X. A Two-Step Synthetic Strategy toward Monodisperse Colloidal CdSe and CdSe/CdS Core/Shell Nanocrystals. *J. Am. Chem. Soc.* **2016**, *138*, 6475–6483.

(35) Hayashi, T.; Keiji Ueno; Saiki, K.; Koma, A. Investigation of the Growth Mechanism of an InSe Epitaxial Layer on a MoS_2 Substrate. *J. Cryst. Growth* **2000**, *219*, 115–122.
(36) Park, K. H.; Jang, K.; Kim, S.; Kim, H. J.; Son, S. U. Phase-Controlled One-Dimensional Shape Evolution of InSe Nanocrystals. *J. Am. Chem. Soc.* **2006**, *128*, 14780–14781.
(37) Wang, C.; Hou, Y.; Kim, J.; Sun, S. A General Strategy for Synthesizing FePt Nanowires and Nanorods. *Angew. Chemie - Int. Ed.* **2007**, *46*, 6333–6335.
(38) Meng, F.; Morin, S. A.; Jin, S. Growth of Nanomaterials by Screw Dislocation. *Acc. Chem. Res.* **2013**, *46*, 1616–1626.
(39) Infantes-Molina, A.; Romero-Perez, A.; Finocchio, E.; Busca, G.; Jimenez-Lopez, A.; Rodriguez-Castellon, E. HDS and HDN on SBA-Supported RuS_2 Catalysts Promoted by Pt and Ir. *J. Catal*. **2013**, *305* 101-117.

3.7 Supporting information

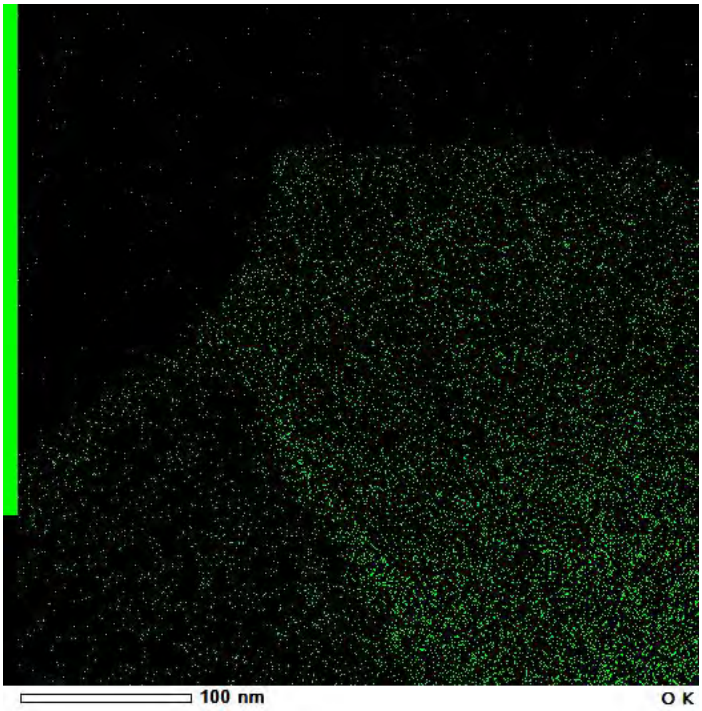

Figure S1. STEM-EDS oxygen mapping of the corresponding NbS_2 nanosheet in Figure 1a. The composition was determined as 46 at.% Nb, 37 at.% S and 17% O.

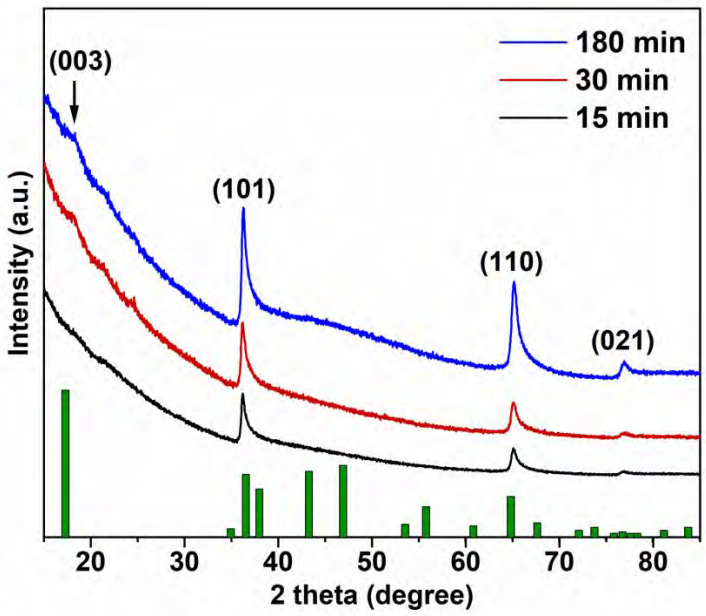

Figure S2. The XRD patterns of the NbS_2 nanosheets synthesized in OAm at 300 °C collected at different sulfidation times. The peaks could be indexed in the Rhombohedral R3m group 160 (PDF # 00-038-1367), shown by a bar chart. The asymmetric peaks are typical for nanosheets, whose intensities increase by the sulfidation time. The XRD pattern of single-layer nanosheets obtained after 15 min of sulfidation shows no *c*-axis peak, but multilayer nanosheets obtained after 30 min and 180 min of sulfidation reaction exhibit this (003) peak, however, the high-level background masks this peak.

a)

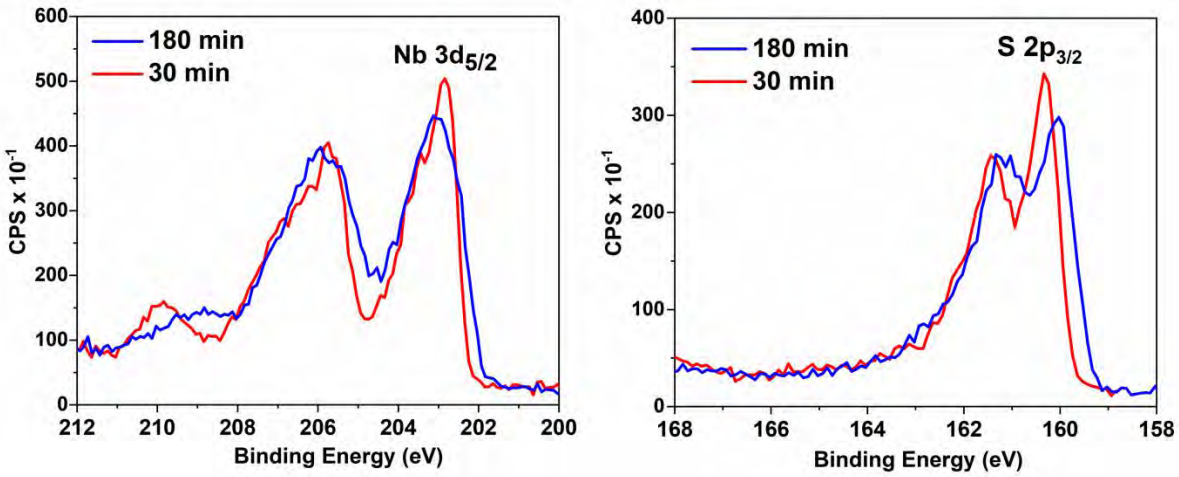

b)

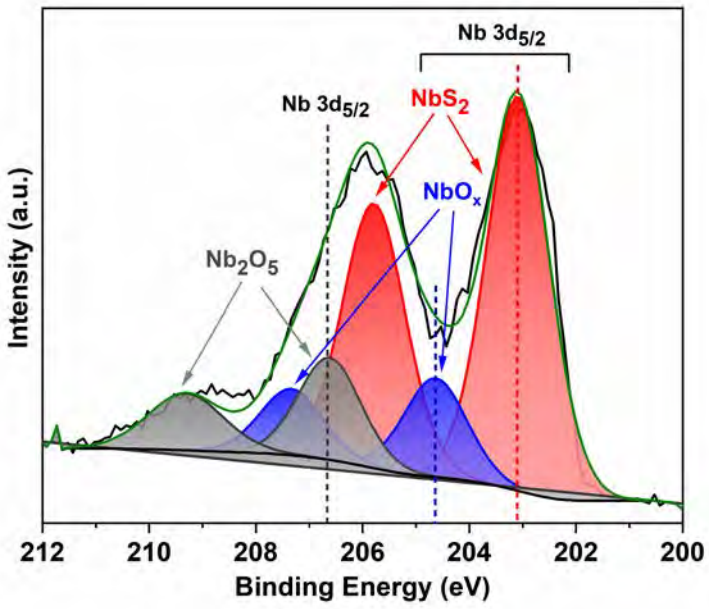

Figure S3. a) Nb 3d and S 2p XPS spectra of the NbS_2 nanosheets synthesized in OAm collected after 30 min and 180 min of sulfidation reaction at 300 °C; b) deconvolution of Nb 3d spectra after 180 min sulfidaiton

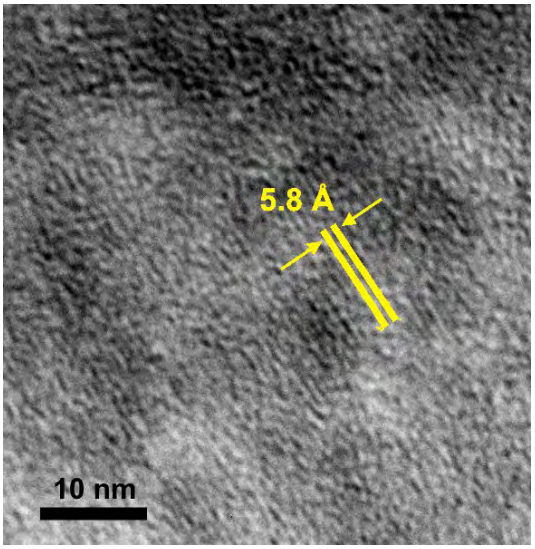

Figure S4. HRTEM analysis of a single layer nanosheet, synthesized in OAm for 15 min sulfidation at 300 °C.

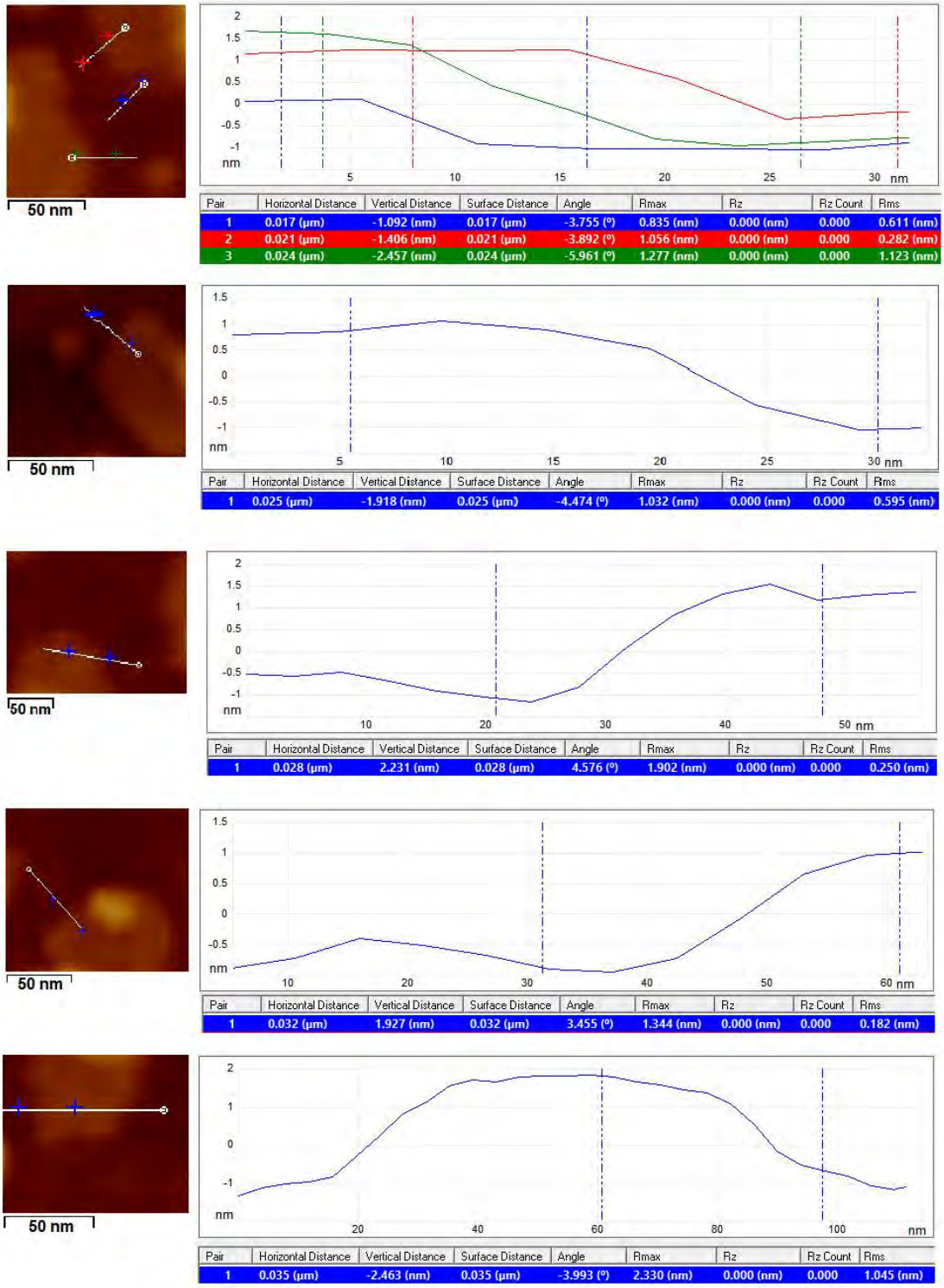

Figure S5. AFM images of the NbS_2 nanosheets collected after 15 min sulfidation in OAm. The lowest height of 1.0 nm suggests the formation of single-layer nanosheets which agrees with the TEM analysis (Figure 1d in the main text). The layer thickness deviation (± 0.4 nm) in some images could be due to the presence of residual oleylamine.

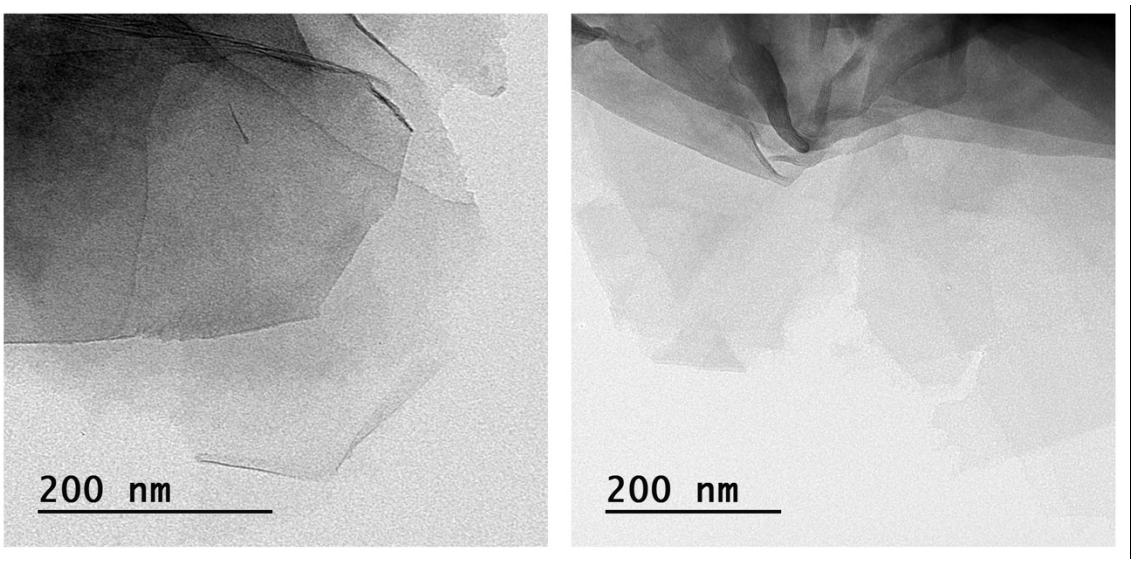

Figure S6. The TEM images of different edge areas showing single-layer nanosheets (synthesized in OAm at 300 °C for 3 h using 8 mmol CS_2).

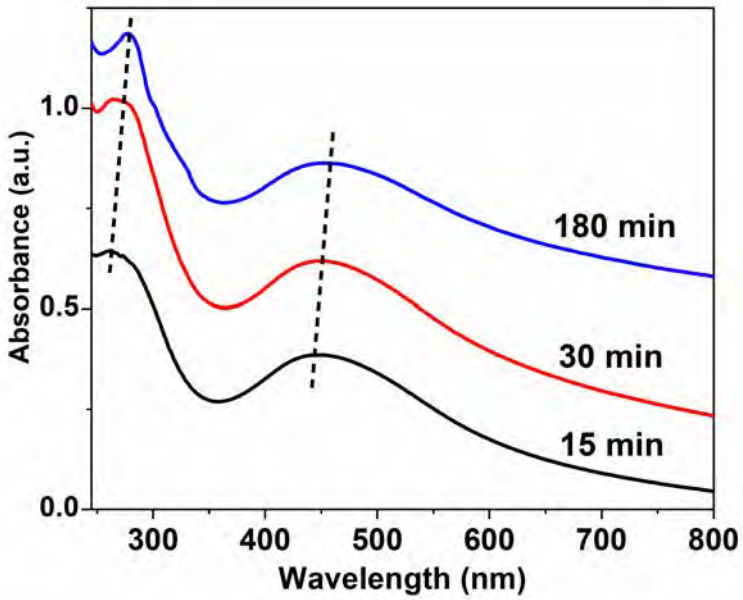

Figure S7. The UV-vis absorption spectra of the NbS2 nanosheets synthesized in OAm at 300 °C using 8 mmol of CS2 at different sulfidation times. The nanosheets were dispersed in ethanol as solvent. Ethanol spectrum was subtracted. A shift toward a higher wavelength is observed by increasing the number of layers in the nanosheets.

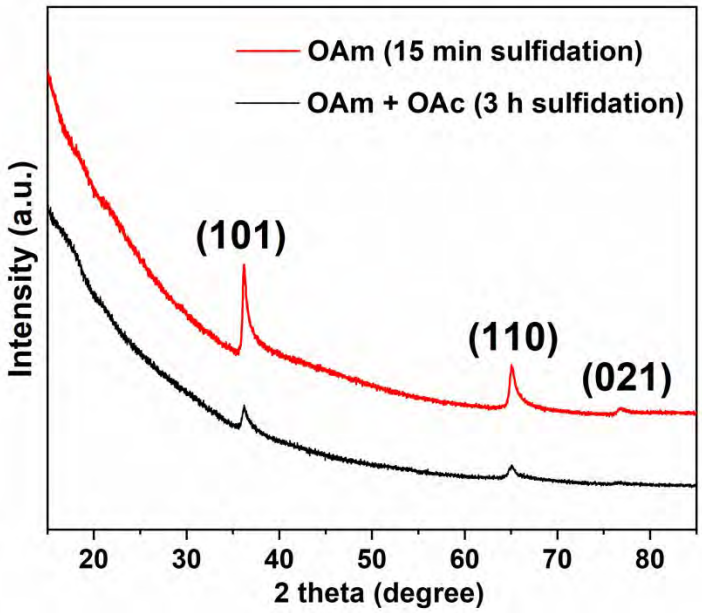

Figure S8. The XRD patterns of the colloidal NbS_2 nanosheets synthesized in OAm after 15 min sulfidation reaction and in a mixture of OAm and OAc at the OAc/OAm molar ratio of 0.6 after 3 h sulfidation reaction, both at 300 °C using 8 mmol CS_2. The XRD pattern shows no *c*-axis-related (003) peak and the peaks' intensities significantly reduced in the presence of OAc.

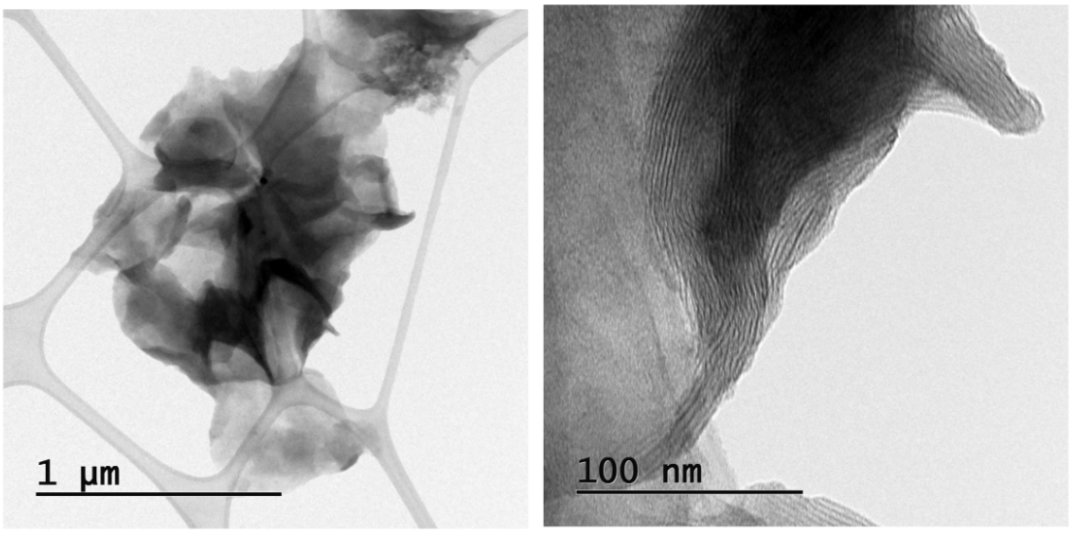

Figure S9. The TEM images of the NbS_2 nanosheets synthesized in OAm at 300 °C for 30 min using 32 mmol of CS_2. The number of layers increased compared to the single-layer nanosheets prepared by 8 mmol of CS_2.

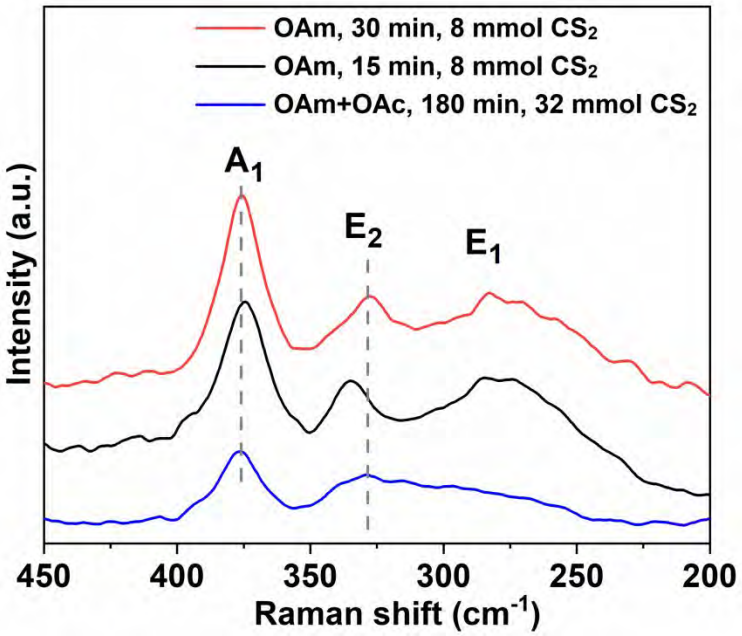

Figure S10. Raman spectra of the NbS_2 nanosheets synthesized in the mixture of OAm and OAc (OAc/OAm molar ratio of 0.6) after 3 h of sulfidation at 300 °C using 32 mmol of CS_2. The number of layers is less than in the sample prepared in OAm, which used less CS_2 (8 mmol), for 30 min of sulfidation.

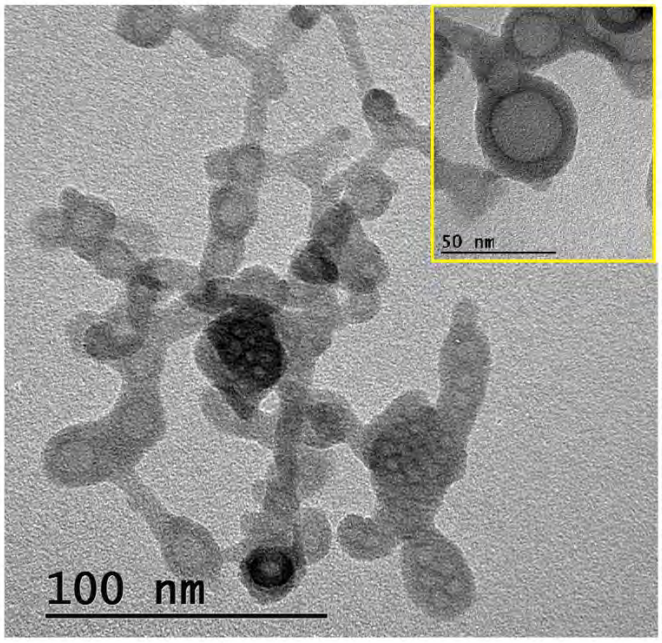

Figure S11. The TEM image taken after 15 min of sulfidation at OAc/OAm of 0.3.

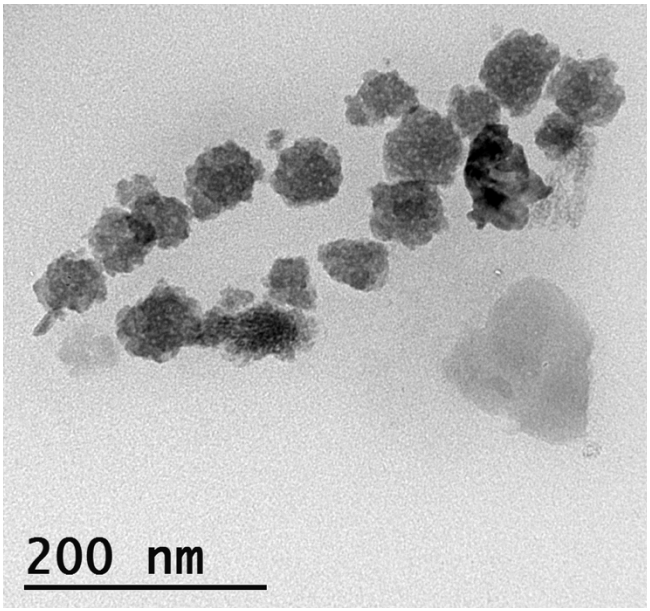

Figure S12. The TEM image of the NbS_2 nanospheres prepared in the mixture of OAm and OAC (OAc/OAm of 0.3) in ODE as a solvent.

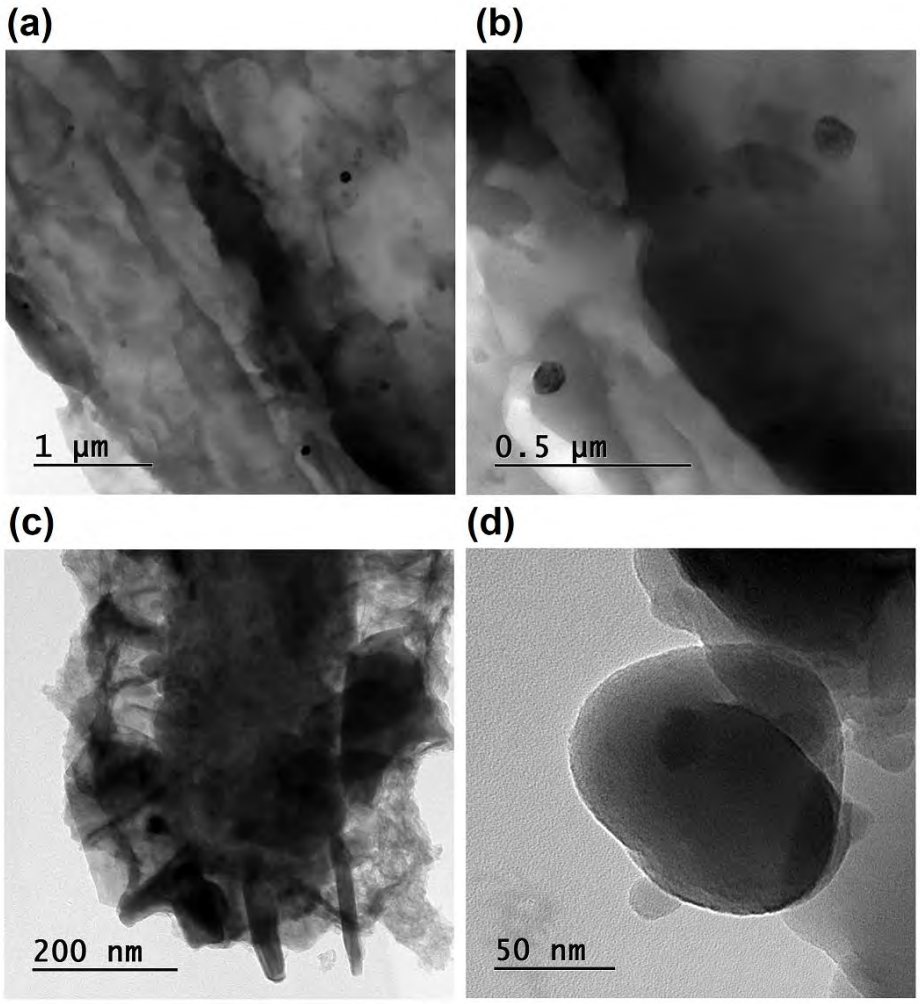

Figure S13. TEM images of the spent Al_2O_3-supported NbS_2 catalysts: (a, b) nanohexagons, (c) nanorods, and (d) nanospheres; all after the HDS reactions at 325 °C and 3.0 MPa for 24 h on stream.

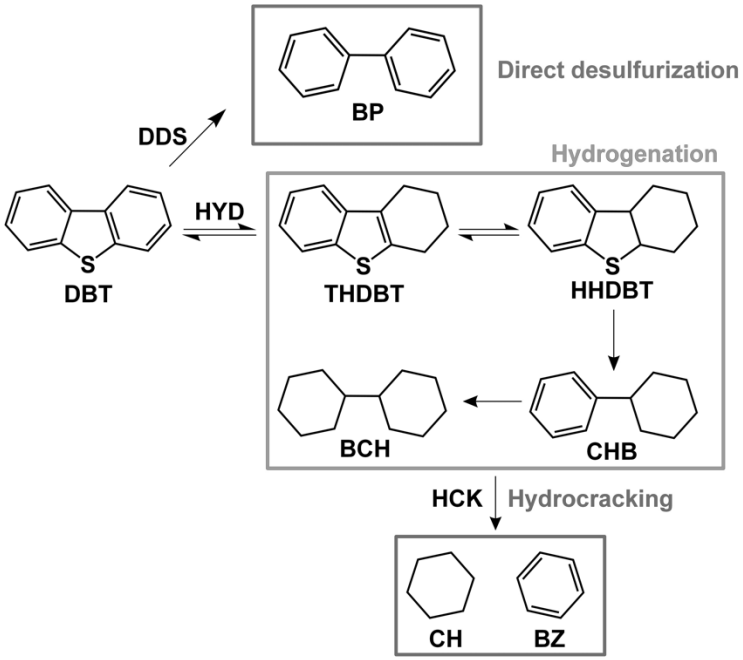

Scheme S1. DBT Hydrodesulfurization Pathways. Modified from Infantes-Molina, A.; Romero-Perez, A.; Finocchio, E.; Busca, G.; Jimenez-Lopez, A.; Rodriguez-Castellon, E. HDS and HDN on SBA-supported RuS_2 catalysts promoted by Pt and Ir. J. Catal. **2013**, 305 101-117. Copyright 2013, Elsevier, Amsterdam.

Table S31. Catalytic performance of Al_2O_3-supported NbS_2 catalysts in HDS of DBT at 325 °C and 3.0 MPa after 24 h on stream.

catalyst	Nb loading[c] (wt%)	DBT conversion (%)	Reaction rate[d] (10^{-5} mol_{DBT} mol_{Nb}^{-1} s^{-1})	Selectivity (mol %)								
				DDS	HYD					HCK		
				BP	BCH	CHB	HHDBT	THDBT	Total	BZ	CH	Total
Monolayer nanosheet[a]	0.97	9.6	7.4	62	2	8	2	21	33	4	1	5
Multilayer nanosheet[b]	0.94	4.6	3.5	66	7	5	0	11	23	2	9	11
nanohexagon	0.96	74.0	98.2	80	3	13	0	1	17	3	0	3
nanorod	1.00	55.3	60.7	96	<1	2	0	1	3	<1	0	0
nanosphere	1.00	36.5	33.1	76	4	16	0	3	23	1	0	1

[a] after 15 min sulfidation in OAm

[b] after 180 min sulfidation in OAm

[c] measured by inductively coupled plasma mass spectrometry (ICP-MS)

[d] rates were calculated based on the first order reaction as described in Experimental Section

4 SUPPORTED COPPER-NIOBIUM SULFIDE LAYERED STRUCTURE AS HYDRODESULFURIZATION CATALYSTS

This section was published as a chapter of Ph.D. Thesis of Ali Mansouri.

4.1 Introduction

Two-dimensional transition metal sulfides (TMS) with a general formula of MS_2 have attracted significant attentions for their versatile striking properties in catalysis, energy storage, and electronic devices.[1–9] In contrast to graphene that is chemically inert, TMS exhibited activities in a wide range of applications while providing the benefits of dimensionality and tunable electronic structure simultaneously.[8] TMS are dominant as layered structures in which packed layer of earth-abundant metal atoms such as Mo, W, and Nb covalently sandwiched between two layers of sulfur atoms.[8,10] The weak van der Waals forces between the layers allow the stabilization of single layers as in graphene.[8] TMS can catalyze a wide range of reactions such as oil hydroprocessing[11–14], hydrogenation of olefins, ketones, and aromatics, dealkylation, ring opening of aromatics, isomerization of paraffins, Fischer–Tropsch, alcohol synthesis, and direct coal liquefaction.[15] In addition, the tunable structural and electronic properties of layered TMS make them attractive in optoelectronic,[16] energy storage materials,[3–5] solar cells,[17,18] and recently as photo- and electrocatalyst for hydrogen evolution[9,19,20] and CO_2 reduction[6,7]. Molybdenum sulfide (MoS_2) as the most commonly used TMS also exhibited a promising performance in bio-oil upgrading.[21] However, to maintain the catalysts active during the reaction, an appropriate amount of sulfur (i.e., H_2S) should be added to the feed, which deprives the advantage of bio-oil low-sulfur content.[21] Therefore, the research for alternative TMS delivering a higher activity while requires lower sulfur in the feed is always underway.

Niobium sulfide (NbS_2) with similar layered feature as MoS_2 but different *d*-band filling could be a promising candidate. The required pH_2S/pH_2 to stabilized NbS_2 is around 10^{-11}, three orders of magnitude lower than the required value for MoS_2 (10^{-8}).[22] NbS_2 has also exhibited exotic properties not shown by other TMS.[10,23–25] For instance, previous studies revealed that NbS_2 is intrinsically more active than MoS_2 and WS_2 in HDS of dibenzothiophene (DBT)[26–29] and hydrogenation of biphenyl (BP)[27]. It should be noted that MoS_2 it is not able to meet the current stringent environmental regulations, minimizing the sulfur content of fuels to 10 ppmw, even after being promoted with either cobalt or nickel species.[11,12,26,30–36] Moreover, in contrast to the conventional NiMo HDS catalysts, the activity and durability of Nb-based catalyst were not diminished by H_2S as a side product of HDS reaction.[32,37,38] Nonetheless, NbS_2 catalysts have not found many catalytic applications because of stability of niobium oxides, Nb_2O_5 and NbO_2, against reduction/sulfidation with the heats of formation of –380 and –395 kJ/mol, respectively.[39] The Gibbs free energies of sulfidation of NbO_2 and Nb_2O_5 using H_2S at 600 K are +82 and +108 kJ/mol, respectively.[22] This causes the reduction/sulfidation of niobium oxides occurring above 800 °C, which is not feasible industrially.[39–41]

We showed above that copper facilitates the reduction and sulfidation of niobium oxides. However, for the supported niobium oxides, the sulfidation and reduction behavior (kinetic and thermodynamic) are strongly influenced by the nature of the support material.[26,22,42,43] In particular, in the case of basic materials in which Nb^{5+} strongly incorporates into the support.[43] For instance, Nb_2O_5 supported on Al_2O_3 and ZrO_2 showed no redox properties whereas trace and significant redox products were observed in the case of TiO_2 and SiO_2, respectively.[43,44] A higher degrees of niobium oxides sulfidation and thus HDS activity was achieved when carbon employed as a support instead of alumina.[26,42] These behaviors are due to the weak metal-support interactions between niobium species and supports such as silica and carbon. Furthermore, niobium trisulfide (NbS_3) that is more active but less stable than NbS_2 under hydrotreatment conditions only detected on a carbon support using , not alumina.[26,27,37] Carbon-supported NbS_2 catalyst exhibited higher thiophene HDS activity than MoS_2 on the same support revealing higher intrinsic activity of supported NbS_2 than MoS_2.[26]
Cracking is an intrinsic property of oxidized and sulfided Nb-based catalysts.[27,45] Lacroix et. al.[27] observed that among the first- and second-row transition metal sulfides, only NbS_2 promoted the hydrocracking reaction in the low-temperature hydrogenation of biphenyl. Bulk and supported niobia (Nb_2O_5) were found exclusively acidic. Bulk Nb_2O_5 is well known for its Brønsted acid sites but when supported on oxides exhibited Lewis acid properties as coordinatively unsaturated sites.[2] Besides the effects of support material, the surface coverage of Nb species on the support strongly affects the formation of different types of niobium oxides with various acidic and catalytic characters.[41,43,46–48] Jehng and Wachs[2] reported that niobium oxides at low loading behaved as coordinatively unsaturated Lewis acid sites (CUS). The number of these Lewis acid sites decreased by surface coverage of the niobium oxide overlayers achieved at increased Nb loadings.[49,50] At a very high loading above monolayer coverage, bulk niobia with Brønsted acid sites forms on the surface. This also affects the reduction and sulfidation properties of layered transition metal oxides. For example, an increased metal loading (number of layers) promoted sulfidation and reduction of tungsten and nickel oxides.[51] The structure of niobia on oxide supports has been studied extensively. Nonetheless, the literature on niobium supported on carbon-based materials is rare.

In this contribution, we present the sulfidation and HDS performances of niobium supported on mesoporous carbon via impregnation at different Nb loading of 2.0, 6.0, and 12.0 wt%. The catalysts were also promoted with copper at various Cu/Nb ratios. We observed that addition of copper facilitated the reduction and sulfidation of niobium oxides over the entire range of metal loadings and Nb sulfidation increased by Cu/Nb ratio. Nb sulfidation varied by Nb loading and a high sulfidation degree was only obtained at the highest Nb loading of 12.0 wt%. Raman spectroscopy showed that various niobium oxide species formed at different Nb loadings; distorted NbO_6 at low loading (2.0 wt% as Nb_2/C) and bulk-like niobia (amorphous with some degrees of crystallinity) at the highest Nb loading (12.0 wt% as Nb_{12}/C). These structures showed different catalytic performance. The former compound with the lowest degree of sulfidation functioned as coordinatively unsaturated Lewis acid sites in the HDS of DBT and delivered the highest activity per mole of Nb as compared to Nb species in Nb_6/C and Nb_{12}/C catalysts. The high acidity of Nb_2/C catalyst resulted in an unprecedented hydrocracking (HCK) selectivity of around 70 % while Nb_6/C and Nb_{12}/C showed 40 % and 25 % at similar

conversions, respectively (Scheme 1). Copper enhanced the DDS selectivity and reduced the HCK selectivity in all synthesized catalysts at different loadings. However, it was more pronounced in the case of Nb_2/C in which HCK selectivity was reduced from 70 % to around 15 % and DDS improved from about 18 % to more than 60 %. Kinetic studies at different weight times showed that bimetallic NbCu catalyst performed better, in terms of DDS selectivity and sulfur removal, under severe conditions (high feed flow rates).

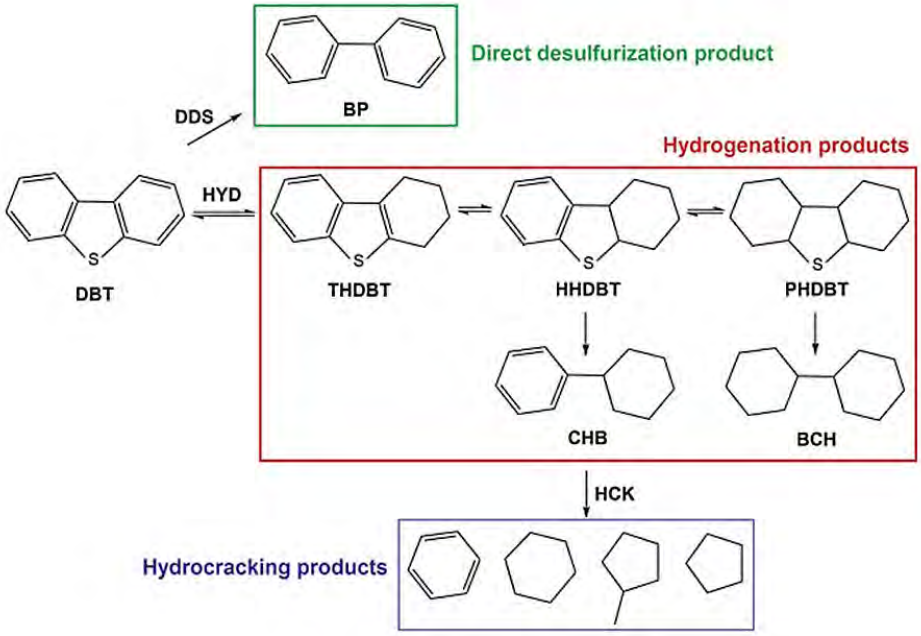

Scheme 1. Reaction pathway and product distribution of DBT hydrodesulfurization.

4.2 Experimental

4.2.1 Materials

Copper (II) nitrate trihydrate ($Cu(NO_3)_2.3H_2O$), ammonium niobate (V) oxalate hydrate ($C_4H_4NNbO_9{\cdot}xH_2O$), nickel (II) nitrate hexahydrate ($Ni(NO_3)_2.6H_2O$), and ammonium heptamolybdate tetrahydrate ($(NH_4)_6Mo_7O_{24}.4H_2O$) all from Sigma–Aldrich were used as precursors. Oxalic acid ($(COOH)_2.2H_2O$, from Caledon) and distilled water were used as received. Mesoporous carbon (Nano powder, <500 nm particle size, from Sigma-Aldrich) and alumina were used as the catalyst support. Different types of alumina such as gamma-alumina (γ-Al_2O_3, CATALOX SBa-200, BET=200 m^2/), theta-alumina (θ-Al_2O_3, PURALOX TH 100/90, BET=103 m^2/g), and alpha-alumina (α-Al_2O_3, PURALOX SCCa-25/5, BET=7 m^2/g) were provided by Sasol. delta-alumina (δ-Al_2O_3) was prepared by calcination of γ-Al_2O_3 in static air at 950 °C for 5 h. 1000 ppmw sulfur as dibenzothiophene (DBT, $C_{12}H_8S$, Sigma-Aldrich) was dissolved in *n*-decane (Fisher Scientific) as a solvent containing 3.5 wt% *n*-dodecane (Fisher Scientific) as the internal standard and was used as a model fuel for HDS reactions. Carbon disulfide (CS_2, Sigma-

Aldrich) was dissolved in *n*-decane at 10 wt% and used for sulfidation of the catalysts. Ultra-high purity (99.999%) argon and hydrogen gases were purchased from Praxair.

4.2.2 Catalyst preparation

Mono- and bimetallic NbCu catalyst supported on either mesoporous carbon (C) or different phases of alumina (Al_2O_3) were synthesized using incipient wetness impregnation (IWI) method. For a typical synthesis of bimetallic catalyst, niobium and copper solution were prepared separately in two vials to prevent precipitation of copper with oxalate species of niobium precursor. The total volume of both solutions together equals to the support pore volume except for the mesoporous carbon support. Next, niobium and copper solutions were added dropwise to the support simultaneously. For monometallic catalysts supported on carbon at the metal loading of below 2 wt%, the pH of impregnation solution was adjusted at 1.0 using oxalic acid, similar to the concentrated solution used for higher loadings. The synthesized catalysts were dried at room temperature for 2 h and then in static air at 70 °C overnight followed by calcination in a continuous flow system using pure helium at 400 °C for 4 h.

4.2.3 Catalyst characterization

High-resolution (scanning) transmission electron microscopy (HRSTEM) images coupled with energy dispersive X-ray spectroscopy (EDS) were recorded using a JEOL JEM-ARM200CF (probe aberration-corrected S/TEM with a cold field emission gun (cFEG)) operating at 200 kV. Nickel TEM grid was used for EDS analysis. Powder X-ray diffraction (XRD) patterns of calcined and sulfided catalysts were recorded using ex-situ Rigaku Ultima IV diffractometer equipped with a D/Tex detector, an Fe Filter, and Co Kα radiation (λ = 1.78899 Å). The diffraction patterns were collected over 5° to 90° on a continuous scan at 2 degrees 2θ per minute with a step size of 0.02°. Data interpretation was done using JADE 9.6 with the 2016 ICDD and 2016 ICSD databases. X-ray photoelectron spectroscopy (XPS) of the calcined and sulfided catalysts (after the sulfidation at 400 °C) was performed using Kratos Axis 165 X-ray photoelectron spectrometer using Mono Al Kα source operating at 14 kV and15 mA. Background subtraction and peaks analysis were performed using CasaXPS software package. All the XPS core–level spectra were corrected with C 1s at 284.8 eV. Specific surface area (BET) and pore size distribution (BJH) analyses were conducted using an Autosorb-iQ Quantachrome. About 0.3 g of sample was degassed with Ar at 120 °C for 2 h before each analysis. Temperature-programmed reduction (TPR) was performed using Micromeritics Autochem II 2920 apparatus equipped with a TCD detector. About 100 mg of the calcined catalysts were degassed by helium at 350 °C for 1 h. TPR analysis was performed after cooling down the sample to room temperature using a 10 ml/min of 10 mol% H_2/Ar at the heating rate of 10 °C/min from room temperature up to 900 °C where remained for 10 min. Raman spectra were recorded using a Thermo Scientific DXR2 Raman microscope at 532 nm laser with a high-resolution grating (wavenumber resolution is about 2 cm^{-1}). The spectra were taken using 10-times exposures and 10 second exposure time.

4.2.4 Catalytic experiments

Hydrodesulfurization of dibenzothiophene (DBT) was conducted at 325 °C and 3 MPa hydrogen pressure using a fixed-bed plug flow reactor (stainless steel, L=22", i.d.=0.5"). The catalysts were diluted with silicon carbide (mesh 120, 15:1 weight ratio) to achieve isothermal plug-flow conditions in the reactor. The effects of reactor wall and axial dispersion were negligible.[52] Heat transfer limitations, external and internal mass transfer limitations were not present as verified by Mears and Weisz-Prater criterion. The calculated values of $6.9x10^{-4}$ for heat transfer and $6.9x10^{-9}$ for external mass transfer limitations are much lower than Mears criterion of 0.15. The catalysts were sulfided *in situ* before each HDS reaction. Briefly, the pressurized reactor under pure hydrogen gas at 3 MPa was heated up to 175 °C at a heating rate of 8 °C/min where the sulfidation feed (10 wt% CS_2 in *n*-decane) at 0.05 ml/min pre-mixed with 100 ml/min hydrogen was introduced into the reactor using a Series II high-pressure pump. Then, the temperature ramped at 5 °C/min up to 400 °C for 20 h. Next, the system cooled down to 325 °C while flowing sulfidation feed and hydrogen. A model liquid fuel containing 1000 ppmw sulfur as DBT with 3.5 wt% *n*-dodecane as the internal standard in *n*-decane (as solvent) was then introduced into the reactor at 0.05 ml/min. The liquid feed was mixed with 100 ml/min hydrogen gas to reach the hydrogen-to-liquid molar ratio of 16. All the HDS experiments were performed for 24 h on-stream including overnight stabilization to reach the steady-state conditions. During the HDS reactions, the pH_2S/pH_2 was adjusted at $2.55x10^{-4}$ using the concentration of DBT in the feed stream to stabilize the structure in its sulfide state. This ratio is seven orders of magnitude higher than the required thermodynamic value.[22]

A series of HDS experiments were performed over sulfided catalysts at different weight-times but at a constant ratio of liquid to hydrogen flow rates similar to what reported previously with some modifications.[53] Weight time in this study is the ratio of the catalyst weight to the liquid molar flow. Right after sulfidation, the catalyst was subjected to 24 h stabilization at the highest weight time (5.7 g h/mol) which was the lowest flow rate. Then, experimental data were collected at different points while decreasing the weight times (increasing liquid and hydrogen flow rates at a constant ratio). Each sample point was taken after reaching steady state conditions within several hours. Although the system stabilized in 4-5 h after changing the weight time, we let the system to treat 45 ml of sulfur-containing feed for each point and then started collecting the samples. This is to ensure that the off-line sample represents the new weight time. Several samples were collected for each measuring point at different times. During the sampling, a parallel condenser was used in order to prevent pressure fluctuations and disruption of the steady state conditions.

The reaction products were identified out off-line by gas chromatography-mass spectrometry (GC-MS) using a Thermo Scientific Trace GC Ultra, equipped with a Thermo Scientific TR-5 column (30m, 0.25mm, 0.25um, µm film thickness) as described previously. DBT and reaction products were quantified using a calibrated flame ionization detector (Agilent 7890A gas chromatograph) equipped with a H-PONA Agilent capillary column (50 m, 0.25 mm, 0.25 µm film thickness) using the internal standard present in the feed. As shown in Scheme 1, the molar selectivity to the direct desulfurization (DDS) path was calculated based on the amount of

biphenyl (BP) formation divided by the amount of converted DBT. Selectivity to hydrogenation (HYD) path is the summation of selectivities to cyclohexylbenzene (CHB), bicyclohexyl (BCH), perhydro-dibenzothiophene (PHDBT), hexahydro-dibenzothiophene (HHDBT), and tetrahydrodibenzothiophene (THDBT). Hydrocracking selectivity (HCK) includes single-ring products such as benzene, cyclohexane, cyclopentane, and methylcyclopentane. The reported conversions are subject to 15% experimental error. Two standard deviations in selectivities are 3%. The carbon mass balance was above 95%. Integral activity refers to the activity based on conversion and flow rate, which is different from the reaction rate. More details can be found in the Supporting Information.

4.3 Results and Discussion

4.3.1 Catalyst characterization

Table 1 shows the physicochemical properties of the synthesized catalysts. The BET surface areas were measured after calcination and sulfidation at 400 °C. As can be seen, the surface areas of sulfided catalysts dramatically decreased compared to the area of the carbon support, correlating with the total metal loading (Nb and Cu). However, the pore diameter did not change (adsorption-desorption data in Figure S1, Supporting Inofrmation).

Table 1. Textural properties of the synthesized catalysts.

Catalyst	Metal loading (wt%)		BET (m^2/g)	average pore diameter (nm)
	Nb	Cu		
Nb_{12}/C	12.0	0.0	–	–
$Nb_{12}Cu_1/C$	12.0	1.0	–	–
$Nb_{12}Cu_2/C$	12.0	2.0	98	7.0
$Nb_{12}Cu_4/C$	12.0	4.0	–	–
$Nb_{12}Cu_8/C$	12.0	8.0	–	–
Nb_6Cu_1/C	6.0	1.0	119	7.0
$Nb_2Cu_{0.3}/C$	2.0	0.3	135	7.0

BET surface area of mesoporous carbon = 205 nm^2/g

Figure 1 shows the electron microscopy analyses of sulfided $Nb_{12}Cu_2/C$ and $Nb_2Cu_{0.3}/C$ catalysts (sulfidation at 400 °C for 20 h). The bright-field TEM image in Figure 1.a shows the homogeneous distribution of carbon particles supporting non-spherical nanostructures as shown in the dark-field image of Figure 1a. The EDS mapping analysis acquired on the sulfided $Nb_{12}Cu_2/C$ catalyst confirmed the spatial association of niobium, copper, and sulfur elements on the carbon support (Figure 1b). However, EELS or Auger electron spectroscopy analysis should be used for a detailed surface quantification. A typical layered structure including disordered stacked planes was observed in the HRTEM images of both low- and high-loading samples

(Figure 1a,c). Similar stacking slabs structure of NbS_2 supported on alumina was observed in a previous study[26] analogous to WS_2 and MoS_2. The number of overlayers in $Nb_{12}Cu_2$/C was higher than that of $Nb_2Cu_{0.3}$/C catalyst. The maximum stacking number in $Nb_{12}Cu_2$/C catalyst was 13 and the longest slab was around 15 nm (Figure S2a, Supporting Information). On the other hand, the number of slabs decreased remarkably in $Nb_2Cu_{0.3}$/C to a maximum of seven (Figure S2b, Supporting Information).

The interplanar spacing of 0.65 nm seen in the HRTEM images of both samples can be assigned to the (002) basal plane of $Cu_{0.65}NbS_2$ (according to the PDF no. 00-015-0409). This value is higher than that of (002) plane in monometallic NbS_2 (0.59 nm, PDF no. 00-041-0980) suggesting the incorporation of copper atoms in niobium structure (Cu intercalated NbS_2 as $Cu_{0.65}NbS_2$).[54] Accordingly, the fringe size of 0.28 nm can be attributed to the (101) plane of $Cu_{0.65}NbS_2$. For $Nb_2Cu_{0.3}$/C, the fringe size of 0.33 nm can be assigned to the (004) plane of $Cu_{0.65}NbS_2$ (PDF no. 00-015-0409). The formation of such crystalline bimetallic phases was further confirmed by XRD analyses (Figure 1d). However, Nb_{12}/C was mostly amorphous even after sulfidation. We also identified the d-spacing of 0.25 nm and 0.32 nm in a close proximity of the layered Nb structure of both catalysts. Unambiguous assignment of these fringes is difficult since they can be attributed to the bimetallic $Cu_{0.65}NbS_2$ structure or residual copper species unreacted with niobium and present as copper sulfide (CuS).

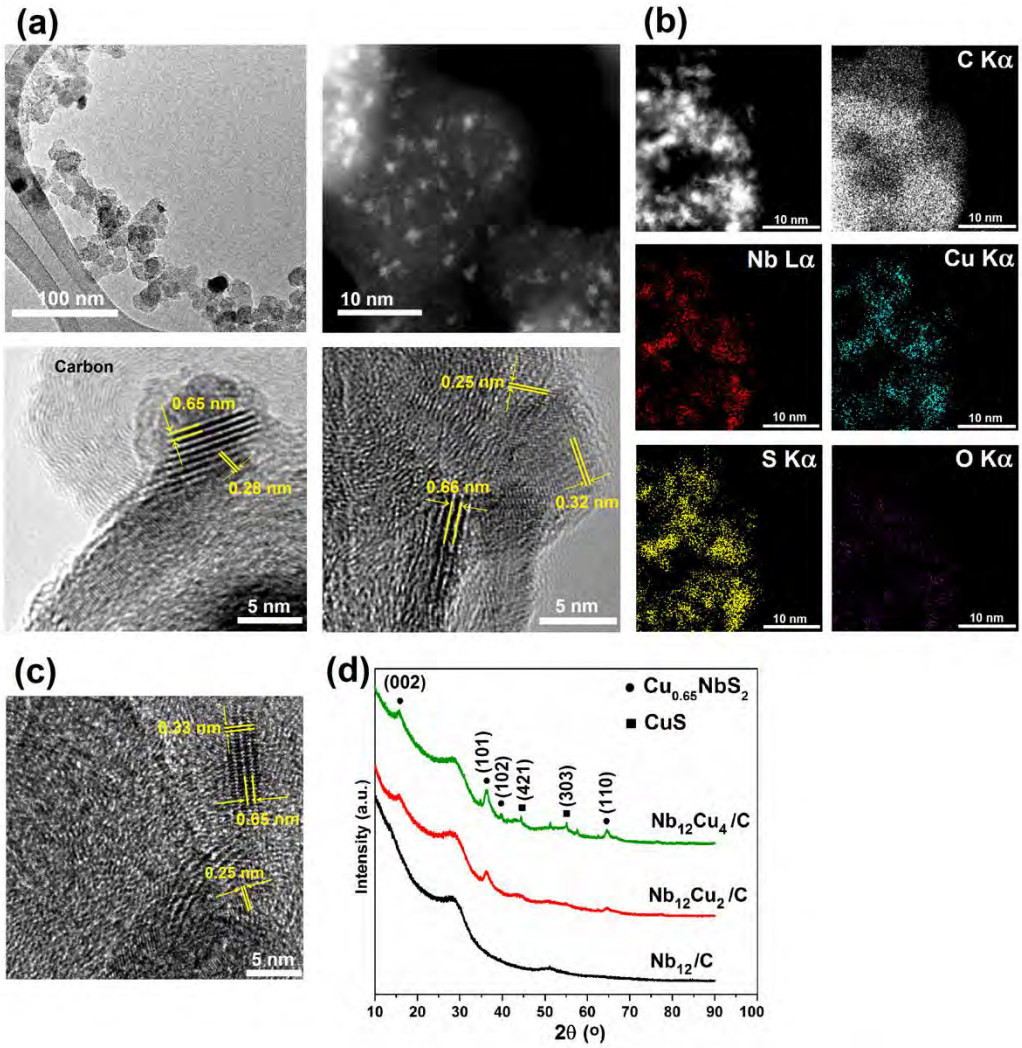

Figure 1. Textural analyses; (a) TEM and HRTEM images (bright- and dark-field TEM images on top left and righ, respectively); (b) STEM-EDS mapping of sulfided $Nb_{12}Cu_2$/C; (c) HRTEM image of $Nb_2Cu_{0.3}$/C, and (d) XRD patterns of monometallic Nb_{12}/C and bimetallic NbCu sulfide catalysts at different Cu/Nb ratios; all samples were sulfided at 400 °C for 20 h before analysis.

Figure 2 shows the TPR profiles of calcined mono- and bimetallic catalysts supported on carbon and different phases of alumina. The ratios of Nb loading to BET surface area were constant for all the samples. The reduction temperature of alumina-supported Nb was higher than that of bulk niobia (730 °C)[40], which is due to the strong metal-support interactions. Except for the alpha phase of alumina (α-Al_2O_3), no reduction peak was observed below 800 °C on oxide supports. Note that spinel $AlNbO_4$ structure did not form as its formation occurs beyond 850 °C.[55] The reduction profiles of carbon-supported catalysts are shown in Figure 2b. The reduction of monometallic catalyst (Nb_{12}/C) occurred at around 650 °C, which is lower than the reduction temperature of bulk niobia. Nevertheless, the temperature is still very high for many applications.[41] Addition of copper to Nb catalysts shifted the reduction peak of Nb_2O_5 to lower temperaturesto around 350-450 °C suggesting the formation of bimetallic NbCu structures.

Increasing the Cu/Nb ratio reduced more niobia species as its reduction peak merged with the reduction peak of CuO at a high Cu content.

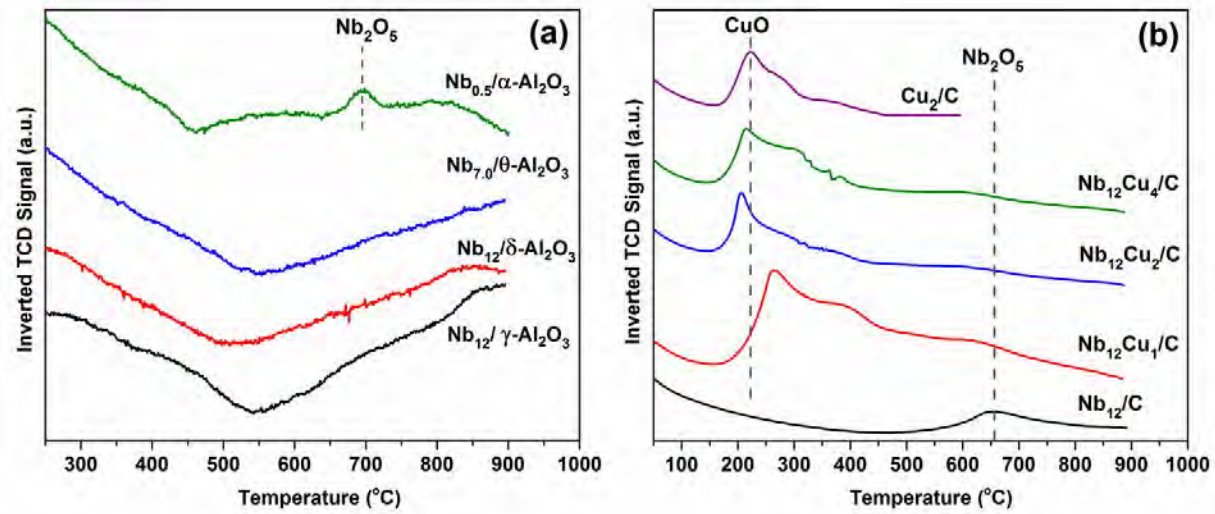

Figure 2. TPR profiles: (a) calcined Nb catalyst supported on different alumina phases, and (b) carbon-supported mono- and bimetallic catalysts.

XPS spectra were acquired on the fresh calcined and sulfided catalysts in which the effects of Cu/Nb ratios and total metal loading on the sulfidation behavior of Nb were investigated (Figure 3). The Nb 3d binding energies (BEs) of the monometallic Nb_{12}/C catalyst at 208.2 and 211.0 eV, corresponding to niobia[56], negatively shifted by around 0.7 eV in bimetallic CuNb samples (Figure 3a). The same amount of shift was observed when the Nb loading in the bimetallic catalysts decreased to 6.0 and 2.0 wt% (Figure 3b). This indicates the charge transfer between copper and niobium species and formation of bimetallic structures irrespective of the metal loading. Compared to the calcined fresh samples, the Nb 3d peaks in the XPS spectra of the sulfided catalysts (at 12.0 wt% Nb loading) shifted to the lower BEs (Figure 3c) and a new peak at around 204.1 eV appeared. This new peak corresponds to the formation of niobium disulfide (NbS_2).[39,57] The area and intensity of this peak increased by an addition of copper to the catalyst correlating with the Cu content (Figure 3c, 4a, Table 3). Surprisingly, the same behavior was not observed when the total metal loading decreased to 7.0 wt% (Nb_6Cu_1/C) and 2.3 wt% ($Nb_2Cu_{0.3}$/C) at the same Cu/Nb ratio of $Nb_{12}Cu_2$/C sample. Only a negligible shift in niobia BEs was detected besides the formation of a very low amount of NbS_2 (less than 5 % as shown in Table 3). S 2p core levels in Figure 3e showed the different type of sulfur-niobium interaction at high and low metal loadings. The BE of 162.2 eV, corresponding to NbS_2,[57] only observed in the XPS of $Nb_{12}Cu_2$/C. Nevertheless, copper species were found in their reduced state in all samples at different loadings (Figure 3f). The XPS data clearly reveal that Nb sulfidation directly depends on the Nb loading in the catalyst. A higher Nb sulfidation was only obtained at a high Nb loading. The same behavior was reported in the literature in the case of supported tungsten (W) and nickel (Ni) layered structures in which higher W and Ni sulfidation was achieved at increased metal loading.[51]

Table 2. Binding energy values of Nb 3d in the sulfided catalysts.

Sample	Binding Energy (eV)					
	NbS_2		NbO_x		Nb_2O_5	
	Nb $3d_{5/2}$	Nb $3d_{3/2}$	Nb $3d_{5/2}$	Nb $3d_{3/2}$	Nb $3d_{5/2}$	Nb $3d_{3/2}$
Nb_{12}/C	204.2	206.9	206.0	208.8	207.9	210.7
$Nb_{12}Cu_2/C$	204.1	206.8	205.6	208.3	207.9	210.7
$Nb_{12}Cu_4/C$	204.0	206.8	205.1	205.8	208.0	210.7

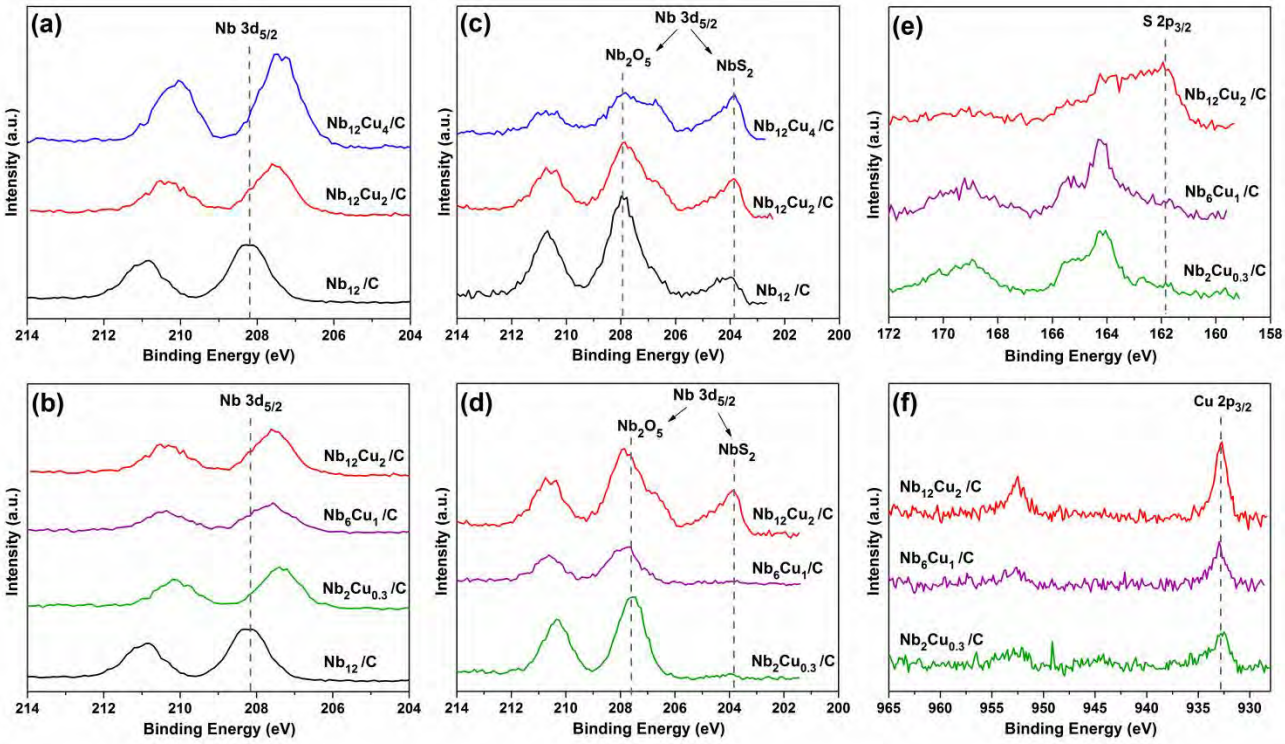

Figure 3. XPS spectra: Nb 3d core levels of (a) fresh calcined samples at different Cu/Nb ratios, and (b) at different total metal loading at constant Nb/Cu ratio; (c, d) Nb 3d core levels after sulfidation at 400 °C for 20 h; (e) S 2p core levels of sulfided samples; (f) Cu 2p core levels of the sulfided materials.

Deconvoluted XPS spectra of bimetallic catalysts (12.0 wt% Nb) at different Cu/Nb molar ratios revealed that Nb sulfidation (fraction of NbS_2 in the sample) linearly increased with the copper content of the catalyst (Figure 4a,b, Table 3). The surface concentration of copper also enhanced by the Cu/Nb ratio. In addition, copper enhanced the fraction of partially reduced niobium oxide (NbO_x), which is a mixture of NbO_2 and NbO (Table 3). However, in contrast to the bulk materials, niobium oxides are dominated in the sulfided samples, especially in the case of low loading materials, which are highly resistant to sulfidation (Figure 4c and Table 3). These findings suggest the presence of different niobium oxide species at low and high Nb loadings

that exhibited various sulfidation behaviors. In fact, there is a threshold Nb loading (number of overlayers) that essentially requires achieving a considerable level of Nb sulfidation.

Table 3. Amount of sulfided, partially reduced and unreacted Nb_2O_5 in the sulfided catalysts calculated by the areas of corresponding deconvoluted peaks; elemental surface composition of the sulfided samples.

sample	fraction in the sample (%)			surface composition (atomic %)		
	NbS_2	NbO_x	Nb_2O_5	Nb	Cu	S
Nb_{12}/C	20	7	73	41	–	59
$Nb_{12}Cu_2/C$	32	5	63	33	6	61
$Nb_{12}Cu_4/C$	47	11	42	26	9	65
Nb_6Cu_1/C	4	0	96	23	8	69
$Nb_2Cu_{0.3}/C$	2	0	98	44	6	50

The ambient Raman spectroscopy was performed on calcined and sulfided catalysts at different metal loadings to obtain fundamental information on the molecular structures of surface species (Figure 5). Raman spectra of calcined monometallic catalysts are presented in Figure 5a. The spectrum of bulk amorphous niobia was also shown for comparison in which three strong bands exhibited at 257, 630, and 980 cm^{-1} consistent with a previous work.[58] Such multiple Raman bands indictes the presence of various niobia species with different reactivities in the reaction.[2] The Raman spectra of supported catalysts were clearly distinguished from bulk niobia revealing the formation of surface two-dimensional niobium oxide species.[59] As-received carbon support did not show any Raman bands within the measured range but the carbon impregnated with oxalic acid followed by annealing in inert at 400 °C exhibited two strong bands at 558 and 1095 cm^{-1}. No significant difference was identified in the Raman spectra of the monometallic Nb_2/C and Nb_6/C (Figure 5a). A major Raman band at around 803 cm^{-1} besides two weak peaks at ~950 and ~990 cm^{-1} occurred in the spectra of both Nb_2/C and Nb_6/C samples. In contrast, increasing the Nb loading to 12.0 wt% (Nb_{12}/C) resulted in additional Raman bands at ~235 and ~675 cm^{-1} besides a shoulder at ~315 cm^{-1}. However, the peak at 558 cm^{-1} overlapped with the one at 675 cm^{-1} difficult to discriminate any peaks within this region. Almost the same peak positions were observed in the case of niobia supported on alumina and silica.[59] In addition, increasing Nb loading on alumina and silica resulted in a new peak at ~680 cm^{-1} and ~647 cm^{-1}, respectively.[59]

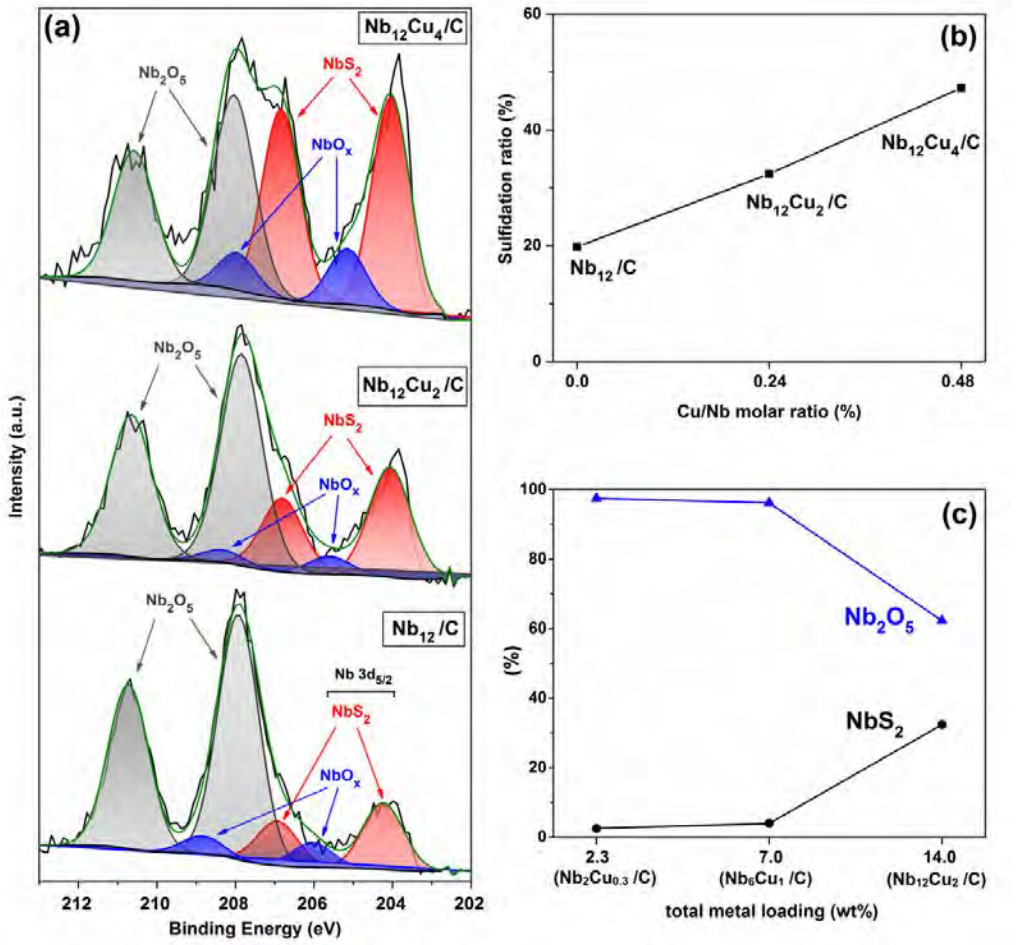

Figure 4. (a) Deconvoluted XPS spectra of the sulfided catalysts; (b) effect of Cu/Nb molar ratio on Nb sulfidation ratio; (c) fraction of NbS_2 and Nb_2O_5 in the sulfided samples as a function of total metal (Nb+Cu) loading at constant Nb/Cu ratio; sulfidation of all samples at 400 °C for 20 h.

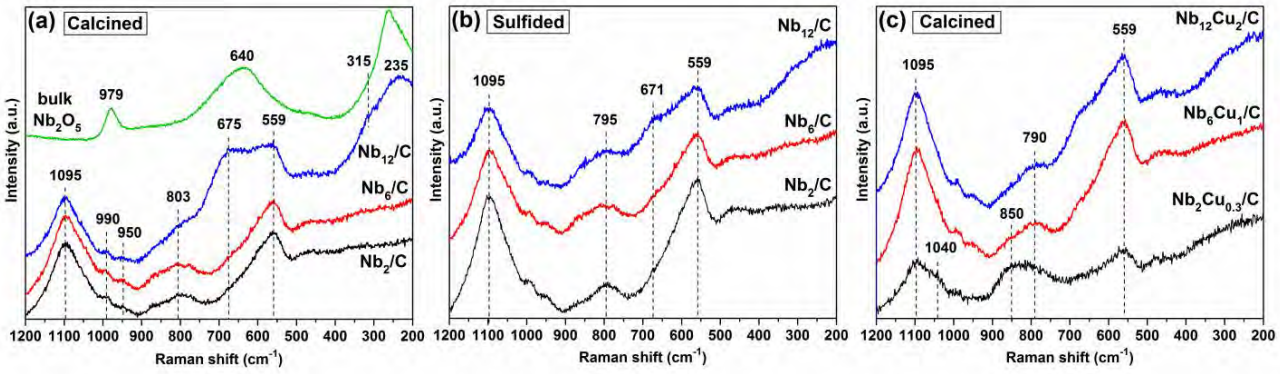

Figure 5. Raman spectra of (a) calcined and (b) sulfided monometallic catalysts at different Nb loadings; (c) calcined bimetallic catalysts at different metal loadings (at constant Cu/Nb ratio).

In literature, the Raman bands above 800 cm^{-1} were assigned to the surface niobium oxide and the ones between 600-700 cm^{-1} corresponed to either bulk or hydroxyl-coordinated niobium oxide surface species.[2] Terminal Nb=O bond occurs at around 850-1000 cm^{-1} and Nb–O bonds between 500-700 cm^{-1}.[43] The Raman spectra of the synthesized catalysts are different from fully hydrated niobia ($Nb_2O_5 . nH_2O$).[60,61] Accordingly, the weak bands at ~950 and ~990 cm^{-1} can be attributed to mono-oxo Nb=O stretching mode of highly distorted octahedra NbO_6 species with different niobium–oxygen bond lengths.[2,43,59] NbO_6 occurs at low Nb loading in which each Nb atom is coordinated with six ogygen atoms and one oxygen atom in the corner connects two adjacent NbO_6.[61] A weak metal-support interaction between Nb and carbon especially at high Nb loading might have promoted the level of distortions through tilting two adjacent NbO_6.[2,59] The Raman band of Nb_{12}/C was not perfectly matched with amorphous niobia with some changes toward crystalline niobia consistent with the formation of T or TT-Nb_2O_5. Therefore, the bands at ~235 and ~675 cm^{-1} in the spectrum of Nb_{12}/C can be assigned to the amourphos niobia with bending mode of Nb–O–Nb linkages that partially transformed to T or TT-Nb_2O_5 (low-temperature crystal phase of Nb_2O_5).[2,58,61–64] These bands occured at high loading on oxide supports when Nb exceeds monolayer surface coverage.[58,59]

After sulfidation (Figure 5b), the peaks at ~803 cm^{-1} in the spectra of calcined Nb_2/C and Nb_6/C slightly shifted to the lower wavenumber at 795 cm^{-1} with no significant changes in the position of other bands. A weak peak at this position also appeared in the spectrum of Nb_{12}/C. This negative shift could be due to the partial reduction or sulfidation of niobium oxides leading to a lower metal–oxygen bond order (i.e. from Nb=O to Nb–O).[61] Furthermore, the intensities of the peaks assigned to bulk niobia at 675 and 235 cm^{-1} greatly decreased upon sulfidation suggesting that niobia sulfidation was more significant at enhanced Nb loading, which is consistent with the XPS data. The addition of copper to calcined Nb_2/C changed the Raman feature in the region above 750 cm^{-1} (Figure 5c). The peak at ~803 cm^{-1} shifted to a higher wavenumber (~850 cm^{-1}) in $Nb_2Cu_{0.3}$/C and the weak peak at 950 cm^{-1} disappeared while a new shoulder at 1040 cm^{-1} appeared. Nb_6Cu_1/C only exhibited a negative shift from 803 to 790 cm^{-1}. The peaks at 675 and 235 cm^{-1} were not observed in the spectrum of $Nb_{12}Cu_2$/C. The peaks corresponding to copper (oxides)[65] were not identified in the Raman spectra of bimetallic samples. These changes in the presence of copper can be attributed to the incorporation of acidic Nb^{+5} into basic copper oxide species and formation of bimetallic CuNb structures.[59]

Accordingly, there are different types of niobium oxides on the carbon surface at different Nb loadings. Jehng and Wachs[2] reported that niobium oxides at low loading (distorted NbO_6 possessing Nb=O bonds) exhibited Lewis acid properties serving as coordinatively unsaturated acid sites (CUS). These Lewis acid sites on the oxide supports only formed below ~1/3 monolayer coverage.[64] The HDS performance of catalyst towards alkyl DBTs was improved through increasing the concentration and intensity of Lewis acid sites.[66] CUS of CoMo sulfide also exhibited Lewis acidity, changed by metal loading, and promoted hydrocracking and HDS activity.[67] Therefore, an increased HDS activity and hydrocracking selectivity at low Nb loadings is expected. It was also found that the most active acid sites on the oxide supports were the ones highly resistant to reduction.[64] A decreased in the number of Lewis acid sites by increasing the Nb loading on oxide supports (above 5.0 wt%) was observed in previous works attributed to

the surface coverage of the metal oxide overlayer, not strucutral changes.[49,50] However, on the other hand, increasing niobia overlayers to the bulk niobia increases the number Brønsted acid sites (–OH).

4.3.2 Catalytic Performance

The synthesized catalysts were evaluated in HDS of DBT at 325 °C and 3 MPa. The catalysts were sulfided *in situ* before the HDS reaction at 400 °C for 20 h. The amount of sulfur in the feed as DBT was adjusted to achieve a partial pressure $p(H_2S)/p(H_2)$ of $2.55x10^{-4}$ stabilizing Nb and Cu in their sulfide phases (required $p(H_2S)/p(H_2)$ for Nb and Cu are 10^{-11} and 10^{-5}, respectively).[22] Figure 6a shows the DBT conversions and activities of the carbon-supported Nb-based catalysts. We also measured the activity of monometallic molybdenum (Mo) catalyst supported on carbon at 12.0 wt% Mo loading (Mo_{12}/C). DBT conversion on reduced Nb-based catalyst without prior sulfidation (400 °C, 20 h) was only 6.3 % revealing the importance of sulfidation pretreatment for Nb. Sulfided Nb_{12}/C exhibited a higher DBT conversion than Mo_{12}/C catalyst consistent with previous studies[27,29] and bulk catalysts discussed above. In contrast, copper did not improve the activity of Nb as opposed to the bulk materials. The DBT conversion decreased from 78 % for Nb_{12}/C to 69 % for $Nb_{12}Cu_2$/C (with 3% experimental deviation in conversion). However, the conversion at the highest Cu content (8.0 wt%) suppressed dramatically to around 35 % likely due to the surface segregation of inactive copper sulfide that cover Nb active sites.

We also investigated the HDS performance of Nb supported on different phases of alumina, carbon nanotube (CNT), and graphene (Table S1, Supporting Information). Nb supported on mesoporous carbon delivered the highest HDS activity (per mole of Nb and mass of catalyst) due to the weak metal-support interactions between Nb and carbon. In addition, Nb supported on alpha-alumina (α-Al_2O_3) showed more activity (per mole of Nb) than other phases of alumina. However, the activity per mass of catalyst was lower than γ-Al_2O_3 and carbon-supported catalysts. The activities of Nb-based catalysts supported on carbon and γ-Al_2O_3 showed different trends over time-on-stream (Figure 6b). Carbon-supported Nb catalysts (mono- and bimetallic catalysts) exhibited an increasing conversion over time, while γ-Al_2O_3-supported catalysts gradually deactivated especially in the presence of copper. The activity of Nb-based samples per mass of catalyst, per mole of Nb, and per BET surface area were higher than Mo-based (Mo_{12}/C) except for the bimetallic NbCu with 8.0 wt% Cu (Figure 6c).

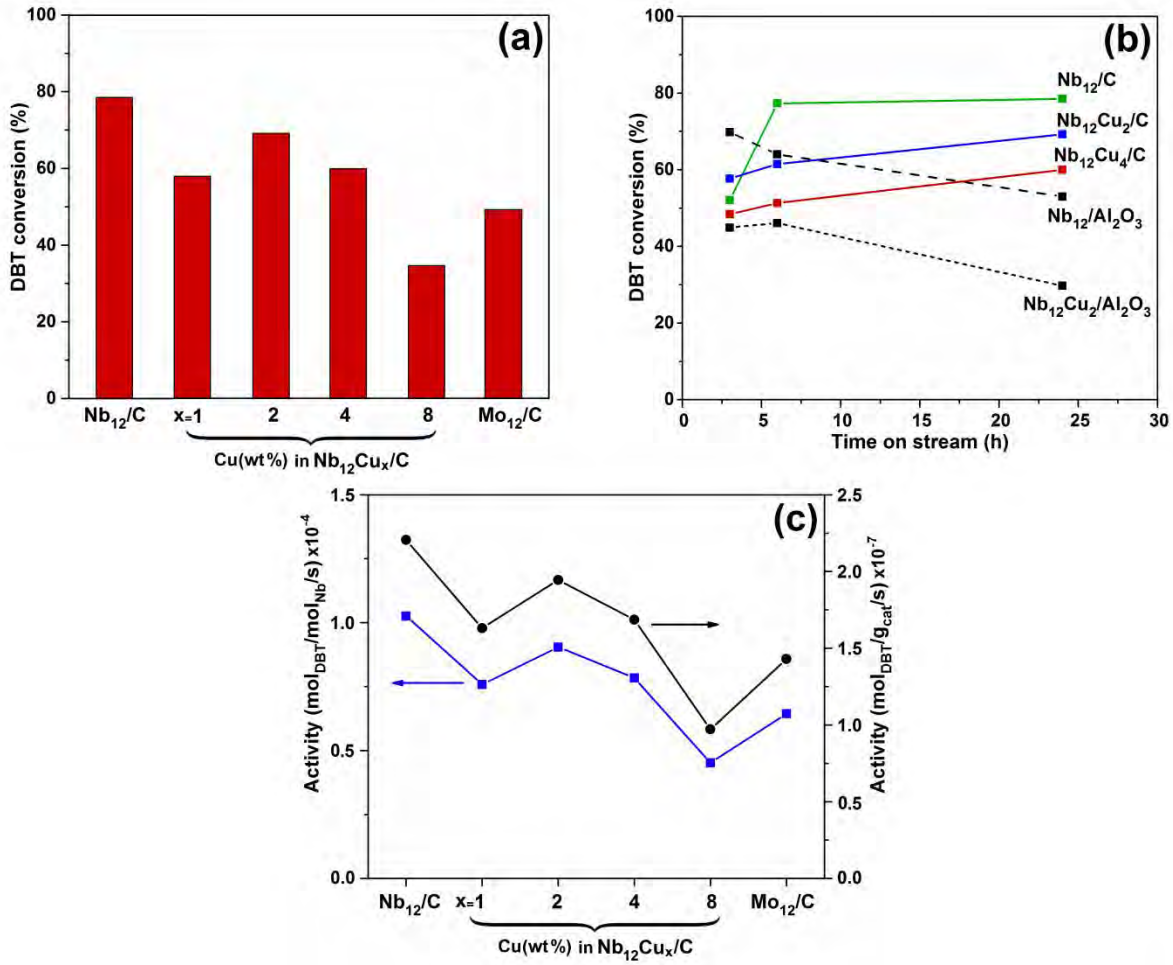

Figure 6. (a) DBT conversion after 24 h on stream for carbon-supported catalysts, and (b) at different time-on-stream and support materials; (c) integral activities after 24 h on-stream per mole of Nb (Mo) and total mass of catalyst; (d) activities per BET surface area of the sulfided catalysts The catalysts were pre-sulfided *in situ* at 400 °C for 20 h.

According to the HDS reaction mechanism (Scheme 1), there are three major reaction products including biphenyl as direct desulfurization (DDS) route, hydrogenation products, and sulfur-free hydrocracking compounds with 5- and 6-membered rings. Figure 7 shows the selectivities and products yields obtained at 325 °C and 3MPa. In contrast to Mo_{12}/C with a high HYD selectivity of 53 %, monometallic Nb_{12}/C was more selective to HCK and DDS (Figure 7a). The higher intrinsic activity and DDS selectivity of the Nb catalyst than Mo one were already reported in HDS of thiophene.[42] In addition, Nb catalysts in both oxide and sulfide phases are acidic.[27,45] According to the fraction of Nb_2O_5 determined by XPS (Table 3), one can find a correlation between the HCK selectivity and unreduced niobium oxides in the sample. Adding copper to Nb_{12}/C changed the selectivity significantly. Similar to the bulk catalysts, DDS selectivity increased by the Cu content, from ~39 % in Nb_{12}/C to 66 % in $Nb_{12}Cu_8$/C for the DBT conversions of ~78% and ~35 %, respectively. On the other hand, HCK selectivity decreased from 25.1 to 8.5 % for the same materials. In addition, copper decreased HYD selectivity from

36.2 to 25.3 %. Accordingly, the selectivity towards CHB, as one of the main HYD products, decreased for bimetallic NbCu catalysts as compared to monometallic Nb_{12}/C and Mo_{12}/C (Figure 7b). This behavior is different from what observed for the bulk catalysts in which there was a volcano trend versus Cu/Nb ratio for the HYD selectivities and CHB formation. However, a decreasing trend of BCH selectivity is similar to the bulk catalysts. The selectivities to sulfur-containing molecules such as HHDBT and THDBT (from HYD route) were almost unchanged in the presence of copper. On the contrary, the selectivities toward these compounds over Mo_{12}/C were one order of magnitude higher than Nb-based samples. The S-free selectivity was 87 % on Mo_{12}/C as compared to around 98 % for the Nb-based sample. This reveals a higher H_2S resistance of the Nb catalysts that delivered a higher level of sulfur removal.[32,37,38] Among different Cu/Nb ratios, the catalysts with 2.0 and 4.0 wt% copper loading delivered a better performance; however, $Nb_{12}Cu_2$/C showed the highest activity. Therefore, we chose this sample for additional experiments.

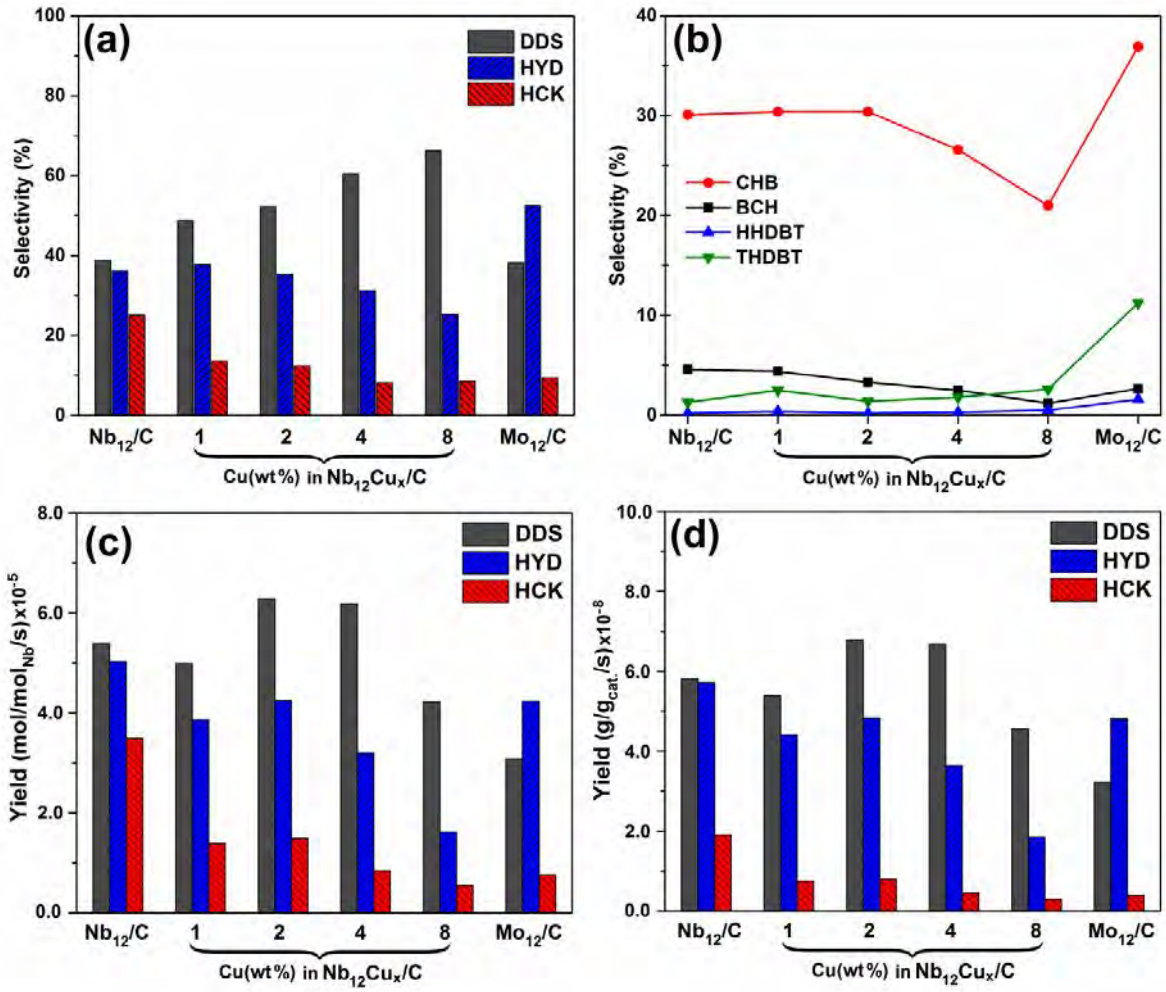

Figure 7. Selectivity and yields: (a, b) selectivity as a function of Cu/Nb molar ratio at the conversions reported in **Error! Reference source not found.**a (in range between 61 and 79% except 35 % for $Nb_{12}Cu_8$/C and 49 % for Mo_{12}/C); (c) yield (mole of products per mole of active

metal), and (d) mass of products per mass of catalyst; all after 24 h on stream at 325 °C and 3 MPa; the catalysts were sulfided *in situ* at 400 °C for 20 h.

A series of HDS reactions were performed at different weight times (catalyst weight to the total liquid molar flow rate) over Nb_{12}/C, $Nb_{12}Cu_2$/C, Mo_{12}/C, and nickel-promoted Mo_{12}/C catalysts ($Mo_{12}Ni_2$/C). Each sample point was taken after reaching steady state conditions within several hours which correspond to treating 45 ml of sulfur-containing feed. Figure 8 displays the DBT conversion at different weight times. As can be seen, the activities of Nb-based catalysts outperformed monometallic Mo-based catalyst (Mo_{12}/C) over the entire range of weight times, however, lower than that of NiMo catalyst supported on carbon ($Mo_{12}Ni_2$/C). Considering 3 % error in the conversion, Nb_{12}/C and $Nb_{12}Cu_2$/C both delivered the same level of catalytic activities.

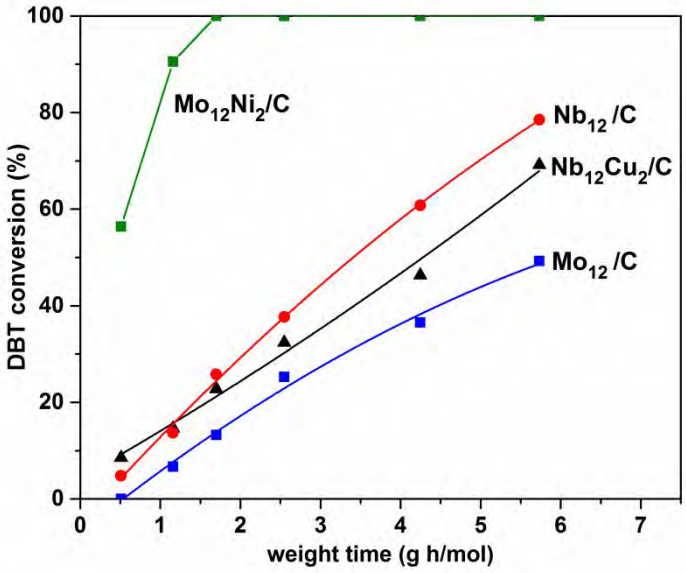

Figure 8. DBT conversion at different weight times at 325 °C and 3MPa.

Figure 9 exhibits the selectivities at different weight times. Nb_{12}/C and Mo_{12}/C catalysts showed the same level of DDS selectivities. The copper addition as $Nb_{12}Cu_2$/C improved the DDS selectivity over the whole weight time range with an increasing trend by lowering the weight time. On the contrary, Mo_{12}/C showed higher HYD selectivities than Nb-based catalysts at the weight times higher than 1.16 g h/mol. HYD selectivity is defined as the summation of selectivities to BCH, CHB, and sulfur containing intermediates such as THDBT and HHDBT, termed as S-HYD in Figure 9. The fully hydrogenated intermediate perhydro-dibenzothiophene (PH-DBT) was not detected most likely because of its slow formation and high reactivity. As can be seen, in contrast to Nb-based catalysts, Mo_{12}/C is highly selective to S-HYD products especially at low weight times. This implies the weaker capability of Mo for sulfur removal

compared to Nb. Furthermore, Mo_{12}/C showed the lowest BCH selectivity among the measured catalysts revealing the poisoning of hydrogenation active sites by H_2S. On the other hand, Nb_{12}/C showed the highest BCH selectivity that decreased by feed flow rates. This reveals the presence of hydrogenation active sites that poisoned at low weight times. However, a high intrinsic acidity of Nb promoted the transformation of HYD products to HCK species over the whole range of measurement with a similar trend to BCH vs. decreasing the weight time. Besides improving the DDS selectivity of Nb, copper remarkably changed the hydrogenation and hydrocracking activity of Nb. It suppressed the HCK selectivity of Nb_{12}/C, i.e. from 25.1 to 12.4 % at the highest weight time. With no significant changes at high weight times, copper reduced the HYD selectivity of Nb_{12}/C from 35.7 to 24.6 % when we increased the feed flow rate to the maximum value. Various behaviors were observed for HYD products at different weight times. Similar HCK, copper reduced BCH selectivities. More importantly, the selectivity of Nb_{12}/C to sulfur-containing hydrogenation intermediates (S-HYD) sharply increased by decreasing the weight time whereas $Nb_{12}Cu_2$/C showed a significant improvement, i.e. from 22.2 to 10.0 % at the highest feed flow rate.

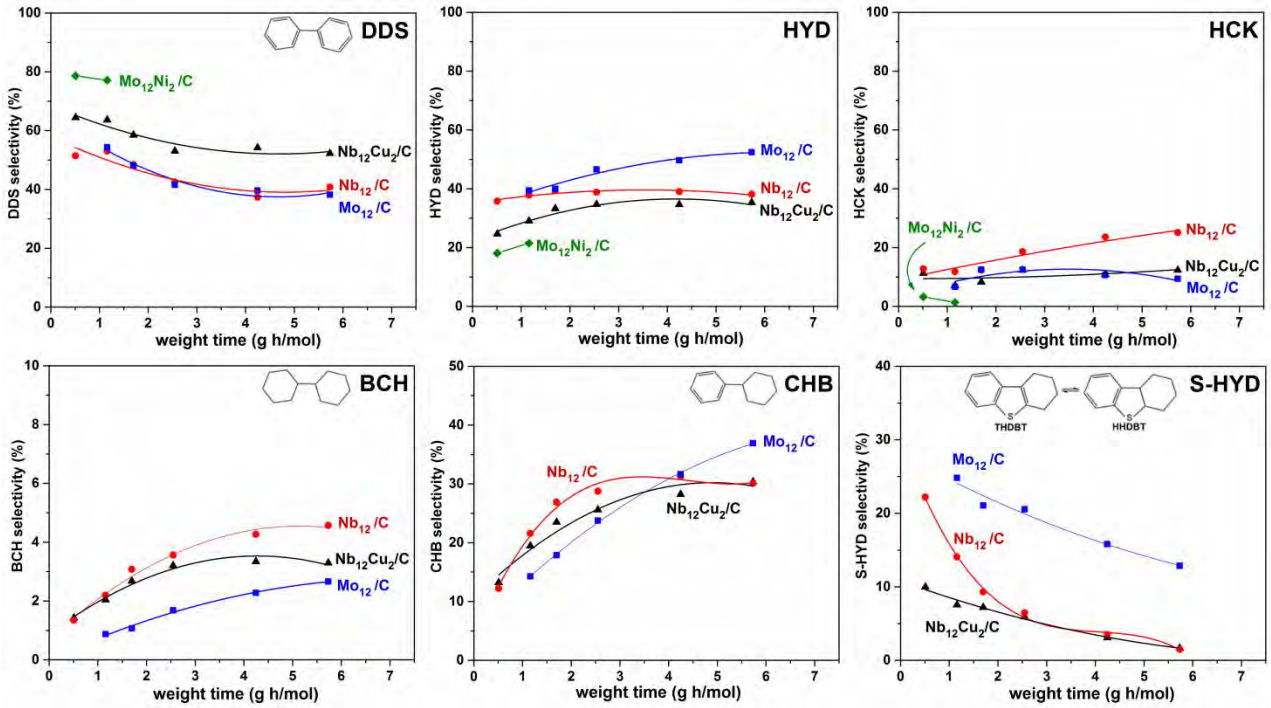

Figure 9. Selectivities at different weight times; all at 325 °C and 3 MPa.

The yields of reaction products at different weight times are shown in Figure 10. In general, bimetallic NbCu performed better than Nb_{12}/C at low weight times. Biphenyl (BP) as the DDS product was the major product over all the catalysts. The formation of BP occurred easily as the yield increased at the low weight times. The DDS yields of Nb-based catalysts were higher than Mo_{12}/C. Moreover, the addition of copper to Nb_{12}/C enhanced the formation of BP, especially when the feed flow rate increased. However, in contrast to the bulk catalysts, copper did not improve the hydrogenation performance of Nb supported on carbon. The second major

product was cyclohexylbenzene (CHB) followed by bicyclohexyl (BCH). The superior formation of DDS and CHB than BCH suggests that the synthesized catalysts are highly active and selective to DDS instead of HYD, which facilitates the low-pressure operation of HDS reaction. $Nb_{12}Cu_2$/C diminished the formation of hydrogenated intermediate (CHB and BCH) as compared to Nb_{12}/C, except for the lowest weight time. HYD and DDS occur via two different chemisorption modes of σ and π in which DBT adsorbs on the active site through the sulfur atom and flat-lying benzene ring, respectively.[68] Accordingly, this difference suggests that copper changed the adsorption mode of DBT on Nb active sites probably by changing the *d*-band filling of Nb.

As discussed before, Mo_{12}/C showed the highest S-HYD selectivity. Accordingly, Mo highly yielded S-HYD compounds over the measured weight times increased exponentially by feed flow rate. Nb-based catalysts showed an increasing trend as well. However, excluding the highest weight time, $Nb_{12}Cu_2$/C decreased the S-HYD yields. The yield of sulfur free products (S-free) was enhanced on Nb-based catalysts compared to Mo_{12}/C revealing the better performance of Nb catalysts in desulfurization than Mo.

We also studied the effect of metal loadings on the HDS performance of the synthesized catalysts. As explained in the Experimental part, we prepared monometallic Nb/C at Nb loading of 2.0 wt% (Nb_2/C) and 6.0 wt% (Nb_6/C). In addition, we synthesized bimetallic Nb_6Cu_1/C and $Nb_2Cu_{0.3}$/C counterparts at constant Cu/Nb ratio analogous to $Nb_{12}Cu_2$/C. Figure 11 shows the performance of the catalysts. Different amount of catalyst was loaded into the reactor to achieve comparable DBT conversions for a reliable comparison of the selectivities. As can be seen, the catalytic activity per mole of Nb increased by when the Nb loading decreased from 12.0 to 2.0 wt%. Copper slightly reduced the activities and conversions but remarkably improved the selectivities. In general, the effects of copper on selectivities were greater at the lower Nb loadings. For example, the DDS selectivity in the case of Nb_2/C catalyst increased from ~15 % to ~60 % by adding 0.3 wt% of copper ($Nb_2Cu_{0.3}$/C catalyst), while increased from 34.8 in Nb_6/C to ~52 % in Nb_6Cu_1/C, and from 39 in Nb_{12}/C to 52 % in $Nb_{12}Cu_2$/C. With no improvement in the HYD selectivity at 12.0 wt% Nb loading ($Nb_{12}Cu_2$/C vs. Nb_{12}/C), copper enhanced the HYD selectivities of low loading catalysts. For instance, the HYD selectivity of Nb_2/C increased from ~14 % to ~27 % in $Nb_2Cu_{0.3}$/C. More importantly, the HCK selectivity of Nb_2/C reduced from ~72 % to 13 % in the presence of copper. Interestingly, the HCK selectivity did not exceed 15 % in the bimetallic CuNb even at different weight times. This indicates that copper deactivated the HCK active sites. The HCK product distribution exhibited a significant difference at different Nb loadings. As shown in Table 4, high Nb loading (both 6 and 12 wt% Nb) promoted the formation of six-member-ring products such as benzene. On the other hand, low-loaing Nb (2 wt%) remarkably enhaned the formation of (alkyl-substituted) five-member-rings such as cyclopentane and methylcyclopentane. Interestingly, the selectivity to benzene decreased from ~19 % in the case of Nb_6/C to less than 1 % in Nb_2/C. This suggests the higher acidity of the active sites in Nb_2/C rather than other samples promoted the isomerization of benzene to CP and MCP.

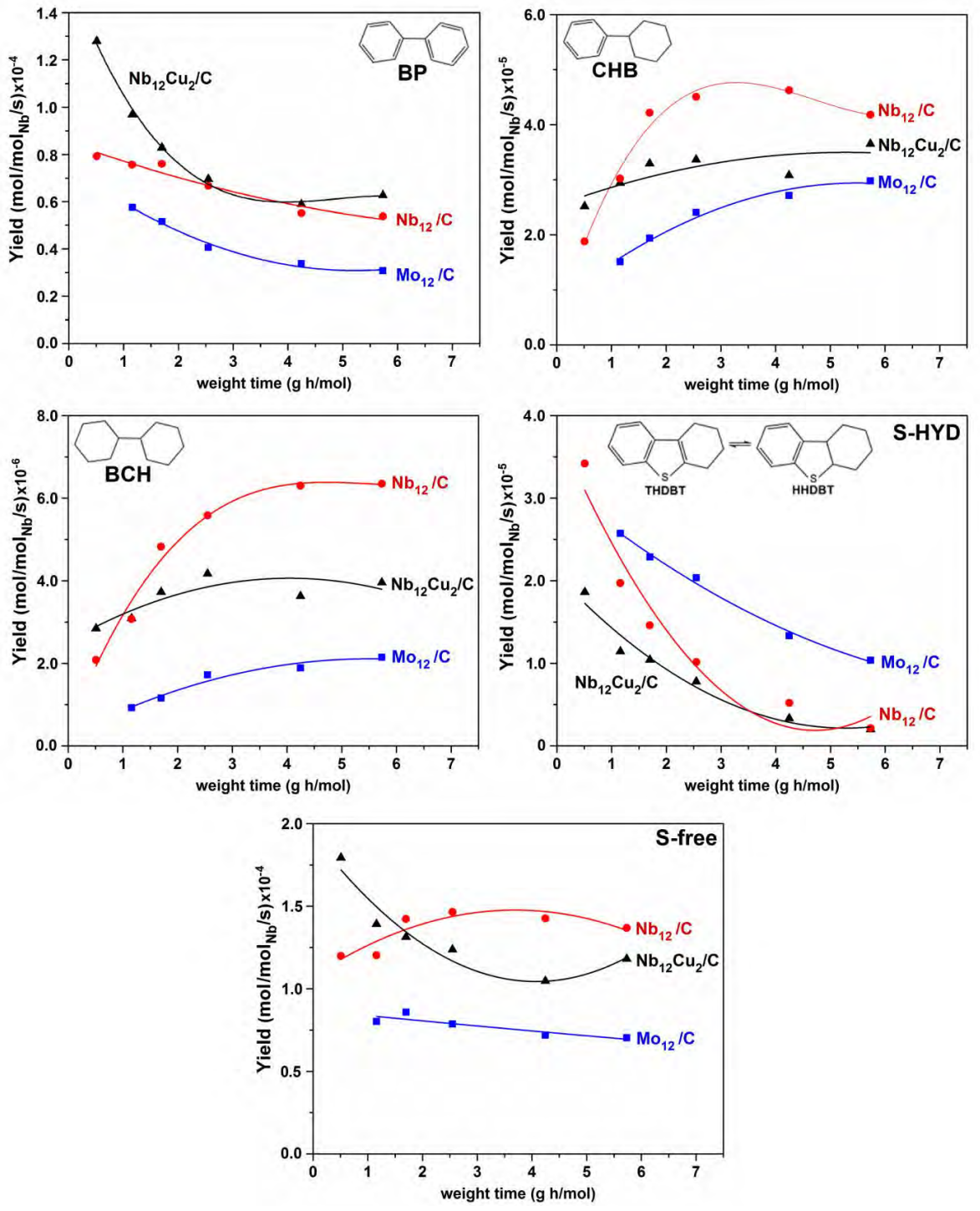

Figure 10. Product yields at different weight times at 325 °C and 3 MPa.

According to the Raman data, niobium oxides at low Nb loading (highly distorted NbO_6) functioned as coordinatively unsaturated Lewis acid sites (CUS)[2] that promoted hydrocracking and HDS activity.[66,67] They were highly resistant to sulfidation as the sulfidation ratios of less than 5 % were obtained in the case of $Nb_2Cu_{0.3}$/C and Nb_6Cu_1/C as compared to 32 % in $Nb_{12}Cu_2$/C. Note that the DBT conversions on reduced $Nb_2Cu_{0.3}$/C and $Nb_{12}Cu_2$/C samples (only reduction at 400 °C for 20 h) were below 10 %, implying the importance of sulfidation pretreatment before HDS reaction irrespective of Nb loading. The higher HDS activity of $Nb_2Cu_{0.3}$/C than Nb_6Cu_1/C can be attributed to the higher dispersion of Nb species (increased fraction of corners and edges). Copper reduced the HCK selectivity probably through an acid-base interaction with highly acidic Nb species which also changed the electronic properties of Nb active sites (*d*-band filling) that led to a DDS selectivity improvement. Sulfidation of high loading catalyst resulted in a high stacking of NbS_2 slabs as showed by HRTEM which could reduce the accessibility of the active sites.

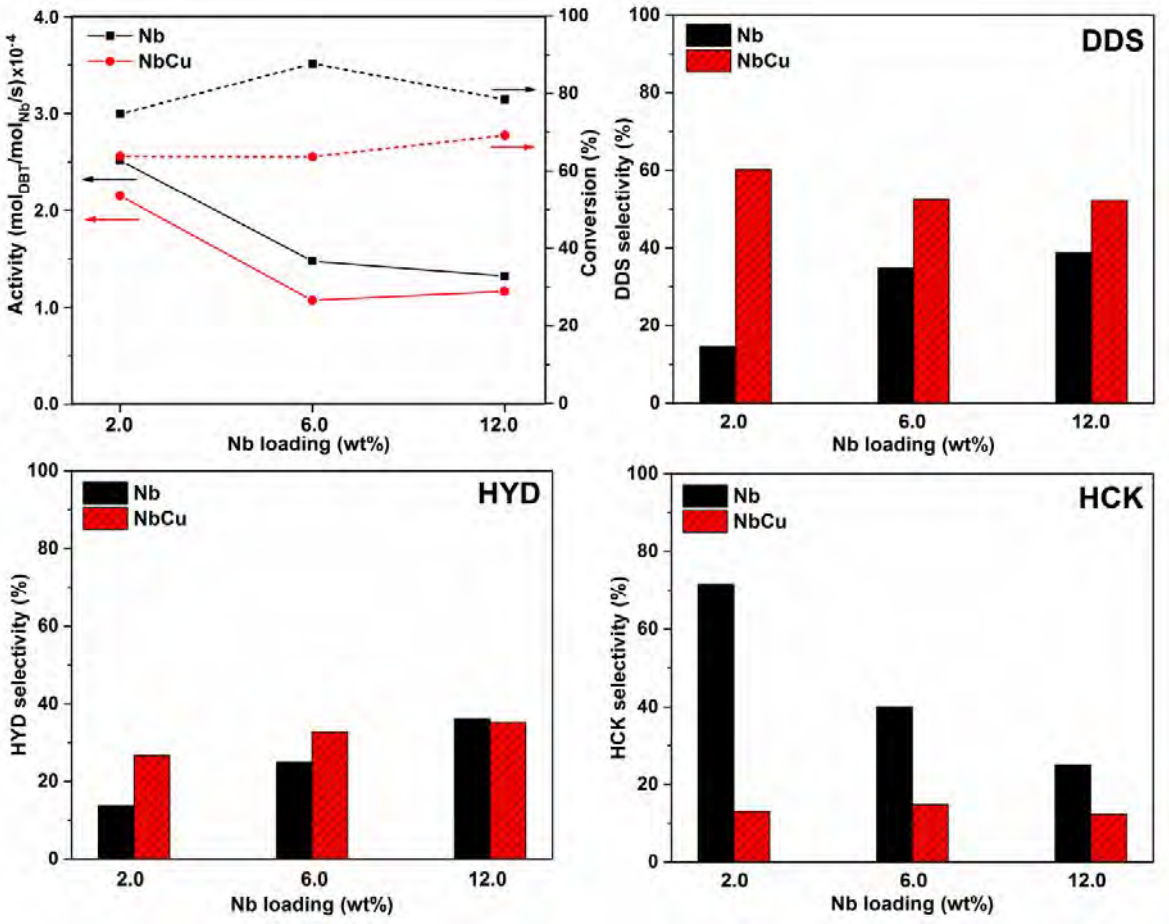

Figure 11. Activity and selectivities at different metal loadings (constant Cu/Nb ratio) of $Nb_2Cu_{0.3}$/C, Nb_6Cu_1/C, and $Nb_{12}Cu_2$/C; all after 24 h on stream at 325 °C and MPa; the catalyst were sulfided at 400 °C for 20 h; the amount of the catalysts in the reactor was adjusted to

achieve comparable conversions in a range between 64 % to 87 %. We loaded 0.09 g, 0.18 g, and 0.27 g for respectively Nb_{12}/C, Nb_6/C, and Nb_2/C and their bimetallic counterparts.
Table 4. Product distribution (mol. %) of the catalysts at different Nb loadings; X represents DBT conversion; the amount of the catalysts in the reactor was adjusted to achieve comparable conversions.

catalyst	X (%)	CP	MCP	Benzene	CH	BCH	CHB	BP	HHDBT	THDBT
Nb_{12}/C	78.5	5	4	14	2	5	30	39	<0.1	1
$Nb_{12}Cu_2$/C	69.2	4	2	5	1	3	31	53	<0.1	1
Nb_6/C	87.6	8	6	19	7	5	19	35	<0.1	1
Nb_6Cu_1/C	63.7	4	1	7	3	3	27	53	<0.1	2
Nb_2/C	74.7	41	28	1	2	<1	12	15	<0.1	1
$Nb_2Cu_{0.3}$/C	63.8	5	4	4	1	2	23	60	<0.1	1

4.4 Conclusions

A series of bimetallic NbCu catalysts at different Cu/Nb ratios were supported on mesoporous carbon and different phases of alumina via incipient wetness impregnation method. The synthesized catalysts were assessed in HDS of DBT at 325 °C and 3 MPa. Electron microscopy data showed that copper and niobium sulfide species formed layered structures as $Cu_{0.65}NbS_2$, as revealed by XRD. Copper decreased the reduction and sulfidation temperature of niobium oxide species correlating with the copper content. However, copper segregated on the surface at a high Cu/Nb ratio reduced the catalytic activity. Raman spectroscopy showed that various niobium oxide species formed on the carbon support at different Nb loadings with different sulfidation and catalytic behaviors. Niobium species at low loading of 2.0 wt% showed the least sulfidation degree (less than 5 %) which increased to 20 % at the Nb loading of 12.0 wt%. The former compound with the lowest degree of sulfidation functioned as coordinatively unsaturated Lewis acid sites in the HDS of DBT and delivered a higher HDS activity as compared to Nb_6/C and Nb_{12}/C catalysts. The high acidity of Nb_2/C catalyst resulted in an unprecedented hydrocracking (HCK) selectivity of around 70 % while Nb_6/C and Nb_{12}/C showed 40 % and 25 %, respectively. Low-loading Nb (Nb_2/C) promoted five-member-ring products such as (methyl) cyclopentane through isomerization of six-member ring as benzene. Copper significantly improved the direct desulfurization selectivity and reduced the hydrocracking selectivity in all synthesized catalysts at different loadings.

4.5 References

(1) Seh, Z. W.; Yu, J. H.; Li, W.; Hsu, P.-C.; Wang, H.; Sun, Y.; Yao, H.; Zhang, Q.; Cui, Y. Nat. Commun. 2014, 5, 5017.
(2) Jehng, J. M.; Wachs, I. E. Catal. Today 1990, 8, 37–55.
(3) Pang, Q.; Liang, X.; Kwok, C. Y.; Nazar, L. F. Nat. Energy 2016, 1, 16132.
(4) Lai, C.-H.; Lu, M.-Y.; Chen, L.-J. J. Mater. Chem. 2012, 22, 19–30.
(5) Ou, X.; Xiong, X.; Zheng, F.; Yang, C.; Lin, Z.; Hu, R.; Jin, C.; Chen, Y.; Liu, M. J. Power Sources 2016, 325, 410–416.
(6) Asadi, M.; Kumar, B.; Behranginia, A.; Rosen, B. a; Baskin, A.; Repnin, N.; Pisasale, D.; Phillips, P.; Zhu, W.; Haasch, R.; Klie, R. F.; Král, P.; Abiade, J.; Salehi-Khojin, A. Nat. Com. 2014, 5, 4470.
(7) Asadi, M.; Kim, K.; Liu, C.; Addepalli, A. V.; Abbasi, P.; Yasaei, P.; Phillips, P.; Behranginia, A.; Cerrato, J. M.; Haasch, R.; Zapol, P.; Kumar, B.; Klie, R. F.; Abiade, J.; Curtiss, L. A.; Salehi-Khojin, A. Science 2016, 353, 467–470.
(8) Chhowalla, M.; Shin, H. S.; Eda, G.; Li, L.-J.; Loh, K. P.; Zhang, H. Nat. Chem. 2013, 5, 263–275.
(9) Kibsgaard, J.; Chen, Z.; Reinecke, B. N.; Jaramillo, T. F. Nat. Mater. 2012, 11, 963–969.
(10) Jellinek, F.; Brauer, G.; Müller, H. Nature 1960, 185, 376–377.
(11) Aray, Y.; Zambrano, D.; Cornejo, M.; Ludeña, E. V.; Iza, P.; Vidal, A. B.; Coll, D. S.; Jímenez, D. M.; Henriquez, F.; Paredes, C. J. Phys. Chem. C 2014, 118, 27823–27832.
(12) Gutiérrez, O. Y.; Singh, S.; Schachtl, E.; Kim, J.; Kondratieva, E.; Hein, J.; Lercher, J. A. ACS Catal. 2014, 4, 1487–1499.
(13) Bara, C.; Plais, L.; Larmier, K.; Devers, E.; Digne, M.; Lamic-Humblot, A. F.; Pirngruber, G. D.; Carrier, X. J. Am. Chem. Soc. 2015, 137, 15915–15928.
(14) Eijsbouts, S.; Anderson, G. H.; Bergwerff, J. A.; Jacobi, S. Appl. Catal. A, Gen. 2013, 458, 169–182.
(15) Chianelli, R. R.; Berhault, G.; Torres, B. Catal. Today 2009, 147, 275–286.
(16) Wang, Q. H.; Kalantar-Zadeh, K.; Kis, A.; Coleman, J. N.; Strano, M. S. Nat. Nanotechnol. 2012, 7, 699–712.
(17) Montoya, J. H.; Seitz, L. C.; Chakthranont, P.; Vojvodic, A.; Jaramillo, T. F.; Nørskov, J. K. Nat. Mater. 2016, 16, 70–81.
(18) Tsai, M.-L.; Su, S.-H.; Chang, J.-K.; Tsai, D.-S.; Chen, C.-H.; Wu, C.-I.; Li, L.-J.; Chen, L.-J.; He, J.-H. ACS Nano 2014, 8, 8317–8322.
(19) Ha, E.; Liu, W.; Wang, L.; Man, H.-W.; Hu, L.; Tsang, S. C. E.; Chan, C. T.-L.; Kwok, W.-M.; Lee, L. Y. S.; Wong, K.-Y. Sci. Rep. 2017, 7, 39411-39419.
(20) Staszak-Jirkovský, J.; Malliakas, C. D.; Lopes, P. P.; Danilovic, N.; Kota, S. S.; Chang, K.-C.; Genorio, B.; Strmcnik, D.; Stamenkovic, V. R.; Kanatzidis, M. G.; Markovic, N. M. Nat. Mater. 2015, 15, 197–203.
(21) Wang, H.; Male, J.; Wang, Y. ACS Catal. 2013, 3, 1047–1070.
(22) Zdražil, M. Catal. Today 1988, 3, 269–365.
(23) Kadijk, F.; Jellinek, F. J. Less Common Met. 1969, 19, 421–430.
(24) Liu, Z. L.; Cai, L. C.; Zhang, X. L. J. Alloys Compd. 2014, 610, 472–477.
(25) Afanasiev, P.; Bezverkhyy, I. Appl. Catal. A, Gen. 2007, 322, 129–141.
(26) Allali, N.; Marie, A. M.; Danot, M.; Geantet, C.; Breysse, M. J. Catal. 1995, 156, 279–289.

(27) Lacroix, M.; Boutarfa, N.; Guillard, C.; Vrinat, M.; Breysse, M. J. Catal. 1989, 120, 473–477.
(28) Allali, N.; Leblanc, A.; Danot, M.; Geantet, C.; Vrinat, M.; Breysse, M. Catal. Today 1996, 27, 137–144.
(29) Hermann, N.; Brorson, M.; Topsøe, H. Catal. Letters 2000, 65, 169–174.
(30) Shafi, R.; Hutchings, G. J. Catal. Today 2000, 59, 423–442.
(31) Babich, I. V.; Moulijn, J. A. Fuel 2003, 82, 607–631.
(32) Stanislaus, A.; Marafi, A.; Rana, M. S. Catal. Today 2010, 153, 1–68.
(33) Song, C. Catal. Today 2003, 86, 211–263.
(34) Allali, N.; Marie, A. M.; Danot, M.; Geantet, C.; Breysee, M. J. Catal. 1995, 156, 279–289.
(35) Gaborit, V.; Allali, N.; Danot, M.; Geantet, C.; Cattenot, M.; Breysse, M.; Diehl, F. Catal. Today 2003, 78, 499–505.
(36) Mansouri, A.; Khodadadi, A. A.; Mortazavi, Y. J. Hazard. Mater. 2014, 271, 120–130.
(37) Danot, M.; Afonso, J.; Des, C. T.; Portefaix, J. L.; Breysse, M. Catal. Today 1991, 10, 629–643.
(38) Egorova, M.; Prins, R. , J. Catal. 2004, 225, 417–427.
(39) Dash, J. K.; Chen, L.; Dinolfo, P. H.; Lu, T. M.; Wang, G. C. J. Phys. Chem. C 2015, 119, 19763–19771.
(40) Wachs, I. E.; Briand, L. E.; Jehng, J.-M.; Burcham, L.; Gao, X. Catal. Today 2000, 57, 323–330.
(41) Wachs, I. E.; Chen, Y.; Jehng, J.M.; Briand, L. E.; Tanaka, T.; Catal. Today 2003, 78, 13–24.
(42) Geantet, C.; Afonso, J.; Breysse, M.; Allali, N.; Danot, M. Catal. Today 1996, 28, 23–30.
(43) Wachs, I. E.; Jehng, J. M.; Deo, G.; Hu, H.; Arora, H. Catal. Today 1996, 28, 199–205.
(44) Jehng, J.-M.; Wachs, I. E. J. Mol. Catal. A Chem. 1991, 67, 369–387.
(45) Ziolek, M. Catal. Today 2003, 78, 47–64.
(46) Tanaka, T.; Yoshida, T.; Yoshida, H.; Aritani, H.; Funabiki, T.; Yoshida, S.; Jehng, J.-M.; Wachs, I. E. Catal. Today 1996, 28, 71–78.
(47) Yoshida, S.; Tanaka, T.; Hanada, T.; Hiraiwa, T.; Kanai, H.; Funabiki, T. Catal. Letters 1992, 12, 277–285.
(48) Gao, X.; Wachs, I. E.; Wong, M. S.; Ying, J. Y. Catal. 2001, 203, 18–24.
(49) Datka, J.; Turek, A. M.; Jehng, J. M.; Wachs, I. E. J. Catal. 1992, 135, 186–199.
(50) Turek, A. M.; Wachs, I. E.; DeCanio, E. J. Phys. Chem. 1992, 96, 5000–5007.
(51) Cui, G.; Wang, J.; Fan, H.; Sun, X.; Jiang, Y.; Wang, S.; Liu, D.; Gui, J. Fuel Process. Technol. 2011, 92, 2320–2327.
(52) Pérez-Ramírez, J.; Berger, R. J.; Mul, G.; Kapteijn, F.; Moulijn, J. A. Catal. Today 2000, 60, 93–109.
(53) Niquille-Röthlisberger, A.; Prins, R. J. Catal. 2006, 242, 207–216.
(54) De Rridder, R.; Van Tendeloo, G.; Van Landuty, J.; Van Dyck, D.; Amelinckx S. phys. stat. sol. 1976, 37, 591–606.
(55) Papulovskiy, E.; Khabibulin, D. F.; Terskikh, V. V.; Paukshtis, E. A.; Bondareva, V. M.; Shubin, A. A.; Andreev, A. S.; Lapina, O. J. Phys. Chem. C 2015, 119, 10400–10411.
(56) Sarma, D. D.; Rao, C. N. R. J. Electron Spectros. Relat. Phenomena 1980, 20, 25–45.
(57) Wu, X.; Tao, Y.; Ke, X.; Zhu, J.; Hong, J. Mater. Res. Bull. 2004, 39, 901–908.
(58) Pittman, R. M.; Bell, A. T. J. Phys. Chem. 1993, 97, 12178–12185.

(59) Jehng, J.-M.; Wacbs, I. E. J. Phys. Chem. 1991, 95, 7373–7379.
(60) Gao, X.; Wachs, I. E.; Wong, M. S.; Ying, J. Y. J. Catal. 2001, 203, 18–24.
(61) Jehng, J.-M.; Wachs, I. E. Chem. Mater. 1991, 3, 100–107.
(62) Burcham, L. J.; Datka, J.; Wachs, I. E. J. Phys. Chem. B 1999, 103, 6015–6024.
(63) Jehng, J.-M.; Turek, A. M.; Wachs, I. E. Appl. Catal. A Gen. 1992, 83, 179–200.
(64) Jehng, J.-M.; Wachs, I. E. Catal. Today 1993, 16, 417–426.
(65) Deng, Y.; Handoko, A. D.; Du, Y.; Xi, S.; Yeo, B. S. ACS Catal. 2016, 6, 2473–2481.
(66) Zhang, Z.; Zhou, Y.; Zhang, S.; Xu, C. Energy and Fuels 2006, 20, 2293–2298.
(67) Huo, Q.; Dou, T.; Zhao, Z.; Pan, H. Appl. Catal. A Gen. 2010, 381, 101–108.
(68) Mansouri, A.; Semagina, N. Appl. Catal. A Gen. 2017, 543, 43–50.

4.6 Supporting Information

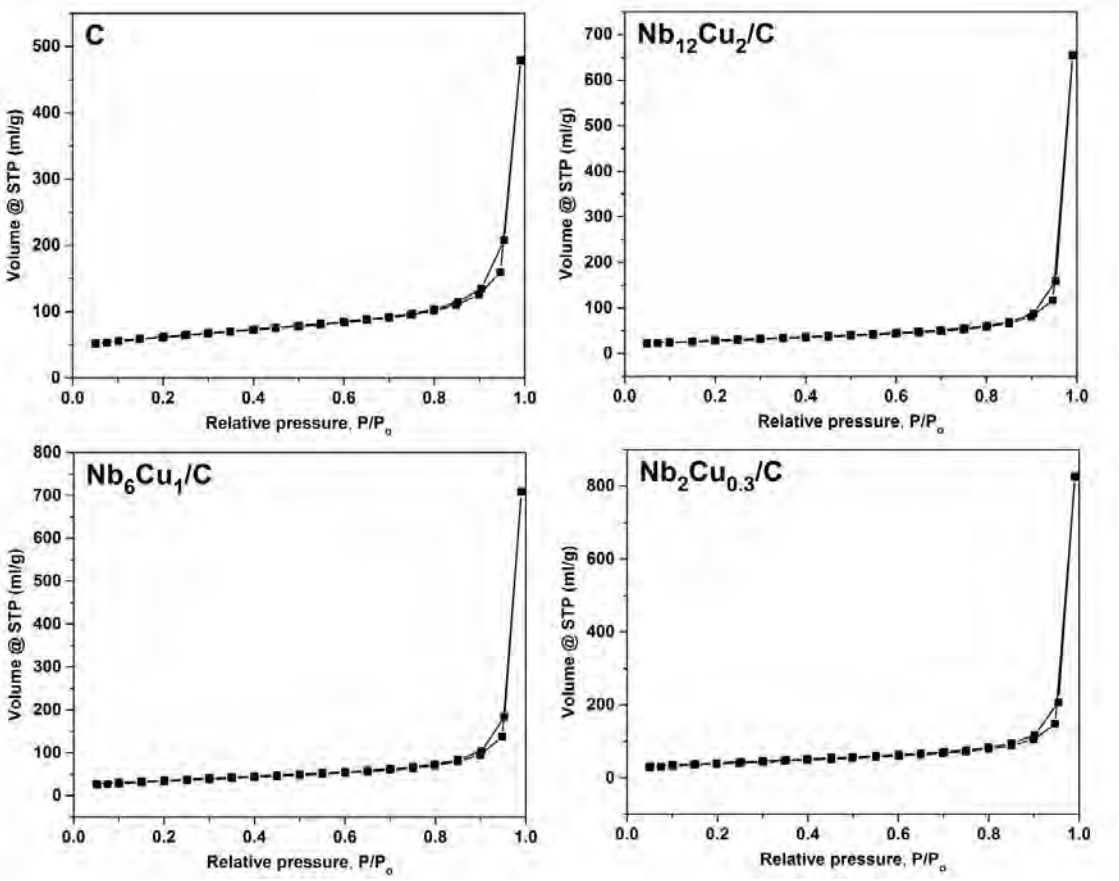

Figure S1. Adsorption-desorption data on sulfided catalyst.

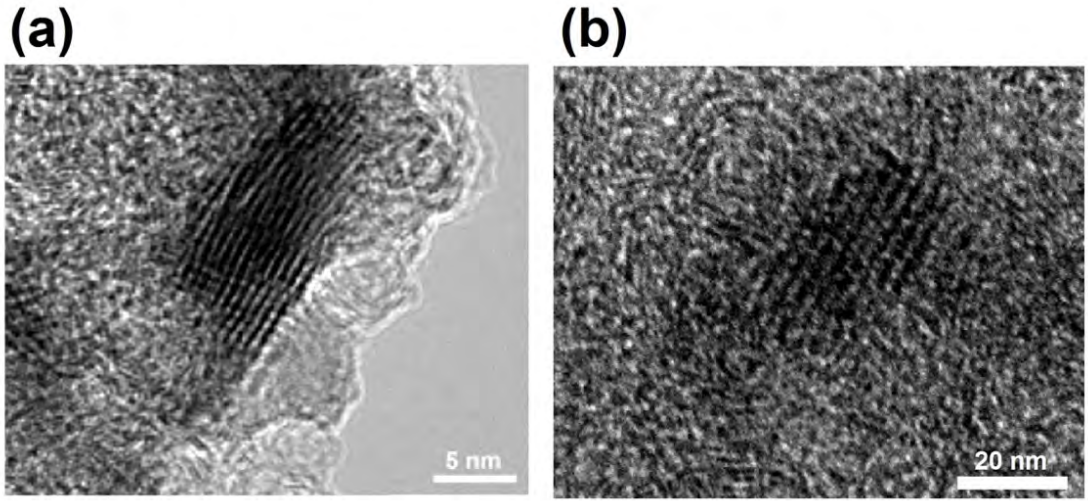

Figure S2. HRTEM image of sulfided (a) $Nb_{12}Cu_2$/C and (b) $Nb_2Cu_{0.3}$/C with the highest length and stacking number.

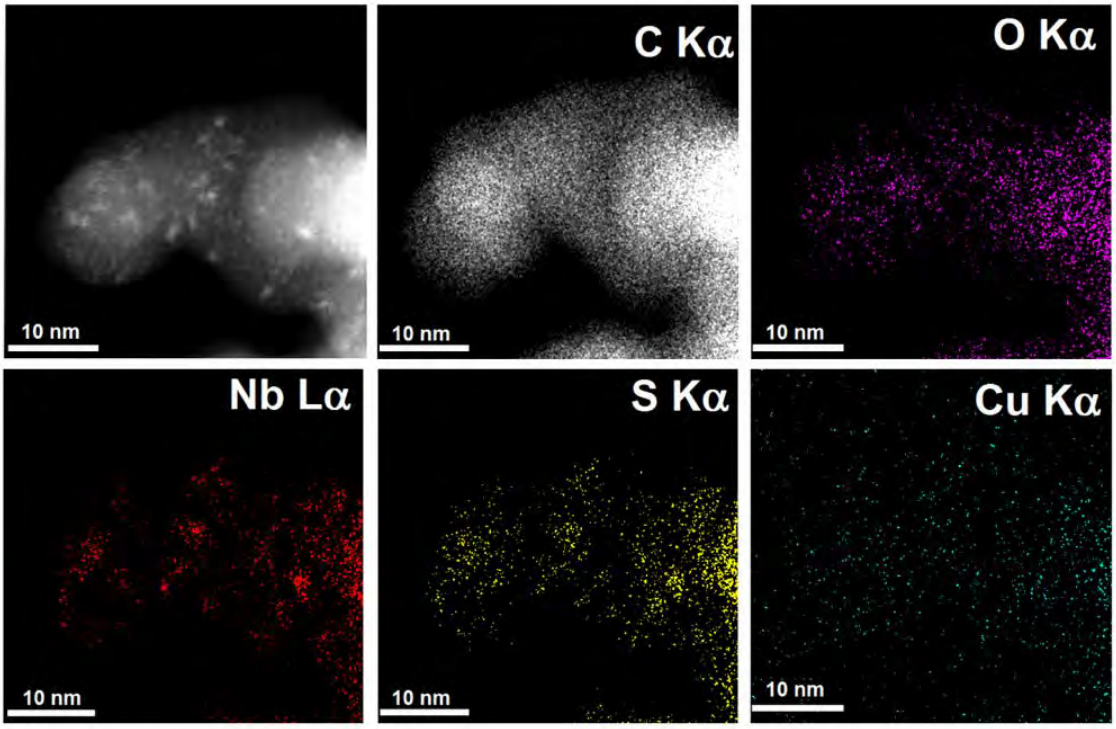

Figure S3. STEM-EDS of sulfided $Nb_{12}Cu_2$/C; second region.

Table S1. Catalytic activity of Nb catalysts supported on γ-Al_2O_3, θ-Al_2O_3, and α-Al_2O_3 (at constant Nb loading/BET ratio) in HDS of DBT at 300 °C and 30 bar H_2 after 24 h on stream. Sulfidation at 300 °C for 4 h. Dried samples were used without calcination.

Catalyst	cat. (g)	Nb (mg)	Conversion (%)	Activity ($\mu mol_{DBT}/mol_{Nb}/s$)	Selectivity (mol %)		
					DDS	HYD	HCK
Nb_{12}/γ-Al_2O_3 - dried	0.34	40.8	17.4	7.7	69.2	21.4	9.4
Nb_{12}/γ-Al_2O_3 - calcined	0.29	34.8	11.4	6.0	65.1	22.6	12.3
$Nb_{6.8}$/θ-Al_2O_3- dried	0.6	40.8	30.2	13.5	59.6	26.2	14.2
$Nb_{0.4}$/α-Al_2O_3- dried	2.0	8.0	18.2	41.5	60.7	26.3	13.0
$Nb_{1.5}$/α-Al_2O_3- dried	2.0	30	45.2	27.4	50.8	35.2	14.0
$Nb_{1.5}$/α-Al_2O_3- dried	2.0	30	28.2	17.2	43.7	41.4	13.9
Nb_{12}/MesC-dried	0.15	18.0	37.6	38.0	45.6	36.2	18.2
Nb_{12}/CNT-dried	0.15	18.0	23.6	23.8	47.5	28.7	23.8
Nb_{12}/Graphene-dried	0.15	18.0	19.3	19.5	52.5	19.7	27.7

HDS experimental setup and reaction procedure

A continuous fixed-bed flow reactor was used in this work to evaluate the catalytic activity and kinetic study of the synthesized catalysts in hydrodesulfurization process under industrially relevant operating conditions. Scheme S1 shows schematic of the experimental setup for the HDS reaction. A LabVIEW program was designed to control the reaction from start to finish. Two liquid containers were considered for sulfidation and main liquid feed streams. Identification and quantification of the reaction products was performed off-line by gas chromatograph (GC) equipped with a mass spectrometry and a calibrated FID detector. All the HDS tests were studied for at least 18 h including overnight stabilization at reaction conditions. Two parallel stainless steel condensers were used to collect liquid samples for quantification analyses. In this way, pressure fluctuations inducing system instability were prevented during sampling. For each point, we let the system to treat at least 40 ml of the liquid feed to make sure that the sample is taken at new condition.

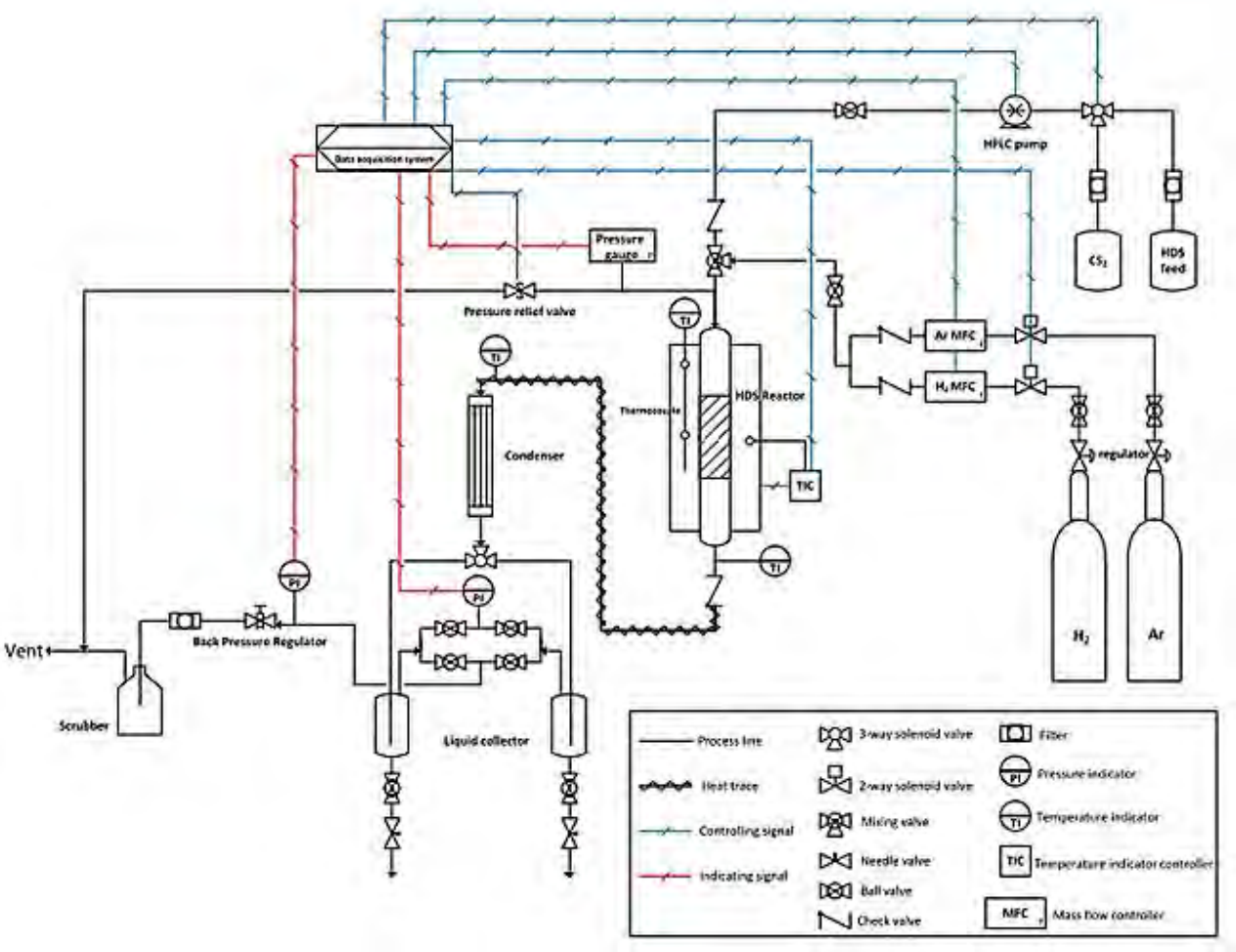

Scheme 1. Hydrodesulfurization (HDS) experimental setup.

Sulfidation procedure

A solution of 10 wt% CS_2 in *n*-decane at 0.05 ml/min was used as sulfidation feed under the desired reaction conditions with 100 sccm ultra-high purity hydrogen gas. The sulfidation procedure was optimized to achieve the highest activity in HDS of 1000 ppmw S as DBT at 325 °C and 3 MPa hydrogen pressure. For a typical sulfidation method, the loaded catalyst inside the pressurized reactor is heated up to 170 °C at 8 °C/min under hydrogen flow rate of 100 sccm. Then, CS_2 solution was injected into the reactor at 0.05 ml/min, and then the temperature increased to 400 °C at 5 °C/min and kept at this temperature for 20 h.

Calculations of initial rates and turn over frequency (TOF)

Following equations have beed used to calculate initial rates and TOF.

Rate constant for the first order reaction:

$$k_i = \frac{\mathrm{Ln}\left(\frac{1}{1-X_i}\right) \times F_i \times 1000}{C_i \times m_{cat.}} \ , \left(\frac{L}{kg_{cat.} \cdot s}\right) \quad (2.1)$$

F: molar flow rate , m: mass of catalyst , X: conversion (mol) , C: initial concentration , i: DMDBT or BP

Initial rate:

$$r_i = k_i \times C_i \ , \left(\frac{mol_i}{kg_{cat.} \cdot s}\right) \quad (2.2)$$

TOF$_i$:

$$r'_i = \frac{r_i \times MW_{Pd}}{wt\%_{Pd}} \ , \left(\frac{mol_i}{mol_{Pd} \cdot s}\right) \quad (2.3)$$

$$TOF_{DMDBT} = \frac{r'_{DMDBT} \times mol_{Pd}}{mol_{CO}} \ , \left(\frac{mol_{DMDBT}}{mol_{surf.\ Pd} \cdot s}\right) , \text{mol CO} = \text{mol surf. Pd} \quad (2.4)$$

$$TOF_{BP} = \frac{r'_{BP} \times mol_{Pd}}{mol_{CO}} \ , \left(\frac{mol_{BP}}{mol_{surf.\ Pd} \cdot s}\right) , \text{mol CO=mol surf. Pd} \quad (2.5)$$

TOF$_{DDS}$, TOF$_{HYD}$:

$$Y_{DDS} = \frac{X_{DMDBT} \times F_{DMDBT} \times S_{DMBP}}{mol_{surf.\ Pd}} \ , \left(\frac{mol_{DMBP}}{mol_{surf.\ Pd} \cdot s}\right) \quad (2.6)$$

$*$ S: selectivity (mol %)

$$Y_{HYD} = \frac{X_{DMDBT} \times F_{DMDBT} \times S_{HYD}}{mol_{surf.\ Pd}} \ , \left(\frac{mol_{HYD}}{mol_{surf.\ Pd} \cdot s}\right) \quad (2.7)$$

$$Y_{HCK} = \frac{Y_{HYD}}{2} \ , \left(\frac{mol_{HCK}}{mol_{surf.\ Pd} \cdot s}\right) \quad (2.8)$$

$$TOF_{DDS} = \frac{Y_{DDS} \times TOF_{DMDBT}}{Y_{HYD} + Y_{DDS} + Y_{HCK}} \ , \left(\frac{mol_{DMBP}}{mol_{surf.\ Pd} \cdot s}\right) \quad (2.9)$$

$$TOF_{HYD} = \frac{(Y_{HYD} + Y_{HCK}) \times TOF_{DMDBT}}{Y_{HYD} + Y_{DDS} + Y_{HCK}} \ , \left(\frac{mol_{HYD}}{mol_{surf.\ Pd} \cdot s}\right) \quad (2.10)$$

Verification of kinetic regime and plug-flow behavior in HDS reaction

Mass and heat transfer limitations play an important role in heterogeneous catalysis. The reaction rate is influenced by diffusion or mass transfer of species (reactants or products) involved in the reactions. The reaction competes with internal diffusion and external mass transfer inside the pore and outer layer of solid catalysts, respectively. To be in the kinetic regime, mass transfer from the bulk to the particle surface and diffusion from the surface to the

pore should be very fast as compared to the reaction rate. Table S2 shows the equations to verify the absence of diffusion, heat, and mass transfer limitations as well as axial dispersion and wall effects. The calculations were provided for an exemplary catalyst (see PhD thesis of Ali Mansouri, Chapter 4).

Table S2. Calculations on the absence of internal and external mass and heat transfer limitations

Phenomenon	**criterion**	**calculated value for the criterion**
external heat transfer limitations[1]	$\Delta T_{film} = \frac{-r_{A(obs)} \times \rho_b \times R \times E_a \times (-\Delta H_{rxn})}{R_g \times h \times T^2} < 0.15$	$2.6 \times 10^{-6} < 0.15$
external mass transfer limitations (Mears criterion)[1]	$\frac{-r_{A(obs)} \times R \times n \times \rho_b}{k_c \times C_{Ab}} < 0.15$	$7.8 \times 10^{-4} < 0.15$
internal mass transfer limitations (Weisz-Prater criterion for the 1st order reaction)[1]	$\frac{-r_{A(obs)} \times R^2 \times \rho_c}{D_e \times C_{As}} < 0.3$	$0.03 < 0.3$
plug-flow behavior (no axial dispersion and wall effects)[2, 3]	$\frac{d_t}{d_p} > 8.0$ $\frac{L_{bed}}{d_p} > 50.0$	$127.0 > 8.0$ $800.0 > 50.0$

Table S3. Parameters used to estimate heat and mass transfer limitations for an exemplary catalyst.

Parameter	**Definition and Unit**	**Equation and Value**
$k_{i(obs)}$	Observed rate constant @ 623 K and X_{DMDBT} = 35.9 % [L/kg.s]	$k_i = \frac{Ln\left(\frac{1}{1-X_i}\right) \times F_i}{C_i \times m_{cat.}} = 2.06 \times 10^{-3}$
$-r_{A(obs)}$	Observed reaction rate @ 623 K and X_{DMDBT} = 35.9 % [mol/kg.s]	$-r_{A(obs)} = k_i \times C_i = 3.5 \times 10^{-5}$
$m_{cat.}$	Weight of catalyst [g]	0.18
F_i	DMDBT molar flow rate [mol/s]	1.41×10^{-8}
C_i	Initial concentration of DMDBT [mol/L]	0.017

ρ_c	Catalyst density [kg/m^3]	4000
ϕ	Bed porosity	0.4
ρ_b	Catalyst bed density [kg/m^3]	$\rho_b = (1-\varepsilon) \times \rho_c = 2400$
R	Catalyst particle radius [m]	0.00005
E_a	Activation energy for the 1st order gas phase reaction [kJ/mol]	200 [1]
ΔH_{rxn}	Heat of reaction calculated from the enthalpies of formation of each compounds in Scheme 1 provided in ref. [4], [kJ/mol]	-148.5
Rg	Universal gas constant [J/mol.K]	8.314
T	Reaction temperature [K]	623
d_p	Catalyst particle diameter [m]	0.0001
ρ_g	Density at 623 K and 30 bar [kg/m^3]	1.17
μ	Viscosity at 623 K [kg/m.s]	1.42×10^{-5}
Re	Reynolds number at 623 K for the fluid velocity of 0.022 m/s (in the reactor i.d. 0.5") assuming the bed porosity of 0.4	$\mathrm{Re} = \frac{U \times \rho_g \times d_p}{(1-\phi) \times \mu} = 0.18$
Sh, Nu	Sherwood and Nusselt numbers	2.0
k_{H2}	Thermal conductivity of hydrogen at 623 K, [W/m.K]	0.25
h	Heat transfer coefficient [kW/m^2.K]	$h = \frac{Nu \times k_{H2}}{d_p} = 1.5$
n	Reaction order, HDS of 4,6-DMDBT on Pd-based catalyst is known to follow a pseudo-first-order kinetics[5]	1.0
$C_{Ab} \approx C_{As}$	Bulk DMDBT gas phase concentration considering hydrogen gas [mol/m^3]	0.107
M	DMDBT molecular weight [g/mol]	212.3
D_{AB}	Estimated gas phase DMDBT diffusivity in H_2 at 623 K and 30 bar [m^2/s]; the molar volumes of H_2 and 4,6-DMDBT are 7.07 and 271.76 cm^3/mol, respectively.	$D_{AB} = \frac{10^{-3}\ T^{1.75}\left[\frac{1}{M_A}+\frac{1}{M_B}\right]^{0.5}}{P\left[\left(\sum v_i\right)_A^{1/3}+\left(\sum v_i\right)_B^{1/3}\right]^2} = 2.61 \times 10^{-6}$

k_c	Mass transfer coefficient [m/s]	$k_c = \frac{D_{AB} \times Sh}{d_p} = 0.05$
d_{pore}	Catalyst pore diameter [nm]	5.8
D_k	Knudsen diffusivity [m^2/s]	$D_K = 48.5 \times d_{pore} \times \sqrt{\frac{T}{M}} = 4.8 \times 10^{-7}$
D_{pore}	Diffusivity in a pore [m^2/s]	$D_{pore} = \left(\frac{1}{D_{AB}} + \frac{1}{D_K}\right)^{-1} = 4.1 \times 10^{-7}$
S	BET surface area [m^2/g]	155
ε_p	Particle porosity	$\varepsilon_p = \frac{S \times \rho_c \times d_{Pore}}{4} = 0.9$
τ	Tortuosity	3.9
D_e	Effective diffusivity [m^2/s]	$D_{eff} = \frac{\varepsilon_P \times D_{pore}}{\tau} = 9.5 \times 10^{-8}$
d_t	Reactor diameter [m]	0.0127
L_{bed}	Catalyst bed length [m]	0.08

Mass spectrometry (GC-MS)

Hydrocracking products identified by GC-MS are shown in Figure S4.

(1) Fogler, H.S. Elements of chemical reaction engineering, 4th Ed., Prentice Hall, 2005.R.E.
(2) Perez-Ramirez, J.; Berger, R.J.; Mul, G.; Kapteijn, F.; Moulijn, J. A. Catal. Today 2000, 60, 93-109.
(3) Le Page, J.F. Applied heterogeneous catalysis, TechniP, 1987.
(4) Q. Yu, Q.; Zhang, L.; Guo, R.; Sun, J.; Fu, W.; Tang, T.; Tang, T. Fuel Process. Technol. 2017, 159, 76-87.
(5) Niquille-Röthlisberger, A.; Prins, R. J. Catal. 2006, 242, 207–216.

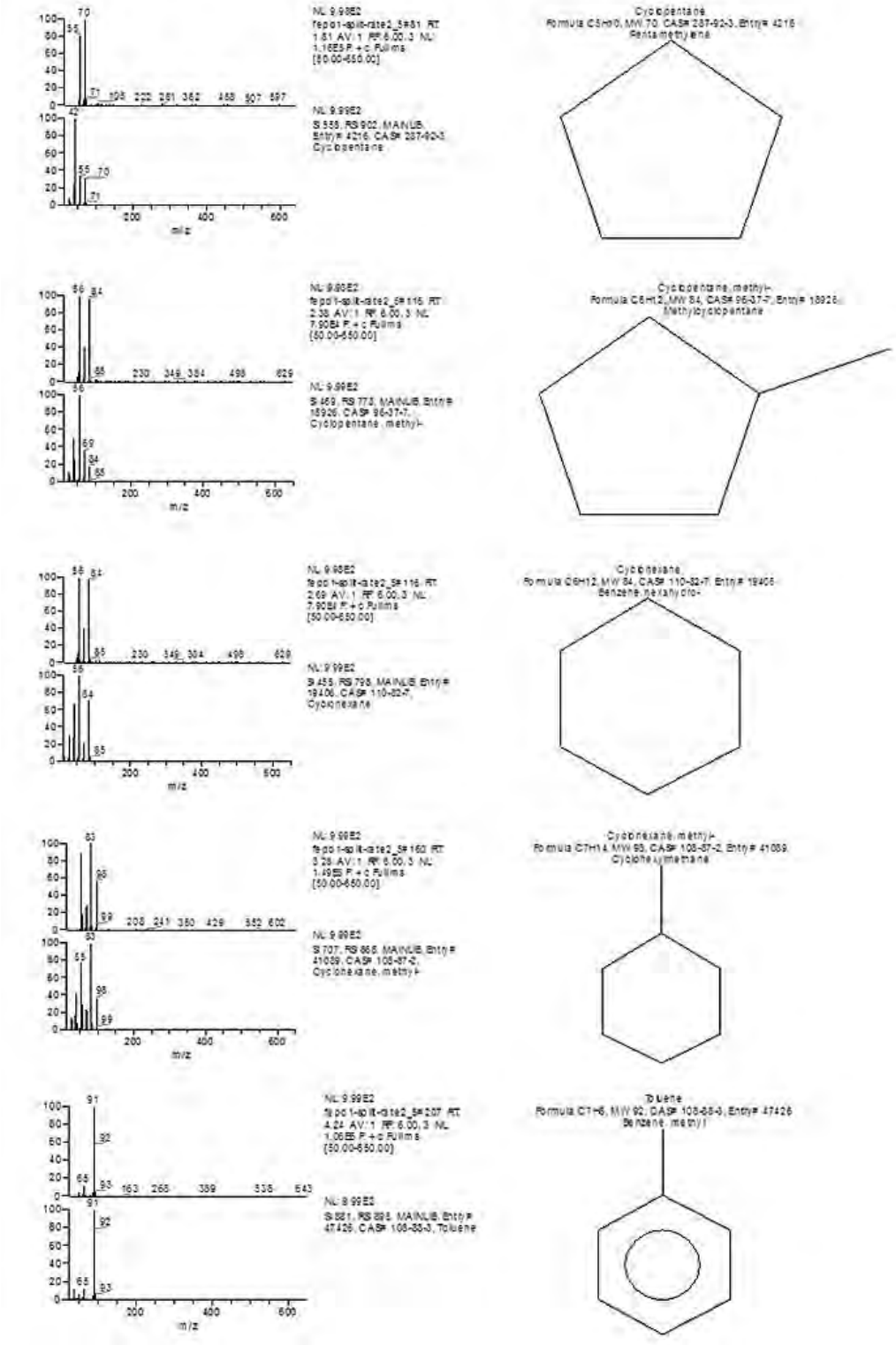

Figure S4. Hydrocracked products identified in HDS of 4,6-DMDBT on Pd/Al_2O_3 catalyst.

5 NITROGEN INHIBITION OF LOW-TEMPERATURE DIOLEFIN HYDROGENATION

J. Shen, N. Semagina. This section is intended for submission to *Chemical Engineering Science* (2020) subject to the approval for the release of information.

5.1 Introduction

Bitumen from Canadian oil sands is too viscose and dense for pipeline transportation. Its partial upgrading is an alternative approach to the dilution; one of the practiced technologies involves thermal cracking, which, in addition to desirable fractions, yields olefins and conjugated diolefins (24 wt.%) [1-4]. They must be removed before a hydrotreater to prevent fouling and catalyst deactivation. From the transportation viewpoint, pipeline specifications mandate a maximum of 1 wt.% of the olefins the feed. Thus, before the transportation or further upgrading, naphtha needs to be hydrogenated at rather low temperatures (below 250 ^{o}C). Conjugated diolefins with internal double bonds are more difficult to be saturated than those with terminal double bonds; the addition of branches at double bonds in olefins could lead to a significant drop in their hydrogenation reactivity. Conventional hydrotreating catalysts (sulfided NiMo and CoMo) are typically used [1].

Olefin and diolefin hydrogenations have been addressed in literature over metal sulfides catalysts [2-8], as well as metal phosphides [9-11]. The reactivity of olefin/diolefin depends strongly on the structure of the olefinic hydrocarbons [2,4,7,8]. In the study of reactivity of C4 – C6 olefins, Magyar et al. concluded that olefin hydrogenation rate decreases with increasing carbon number in linear olefins; while terminal olefins are readily converted to olefin isomers to an equilibrium composition [8]. Olefins with internal double bonds are more difficult to be saturated than those with terminal double bonds. Xin et al. compared the reactivities of different olefinic compounds; 1,3-hexadiene, with one C=C bond at the terminal position, is more reactive than 2-methl-2-pentene [2]. The addition of branches at double bonds in the olefin/diolefin molecules leads to significant drop in its hydrogenation reactivity. It has been found that hydrogenation rate of 2,5-dimethyl-2,4-hexadiene is several times lower than that of the 1-heptene, due to the steric hindering effect [12]. Hydrogenation product distribution depends strongly on reaction temperature and catalyst [8]. Karakhanov et al. observed high selectivity toward alkene and isomerized alkene yields (total 98 – 99%) during 2,5-dimethyl-2,4-hexadiene conversion over Pd catalysts at 70 °C [13]. For the same branched alkadiene structure, however, Alzaid et al. observed a 93% selectivity to full hydrogenation product at 180 °C, over a sulfided NiMo catalyst [4]. In an early work, Bond and Wells found that Ni, Pd and Fe have higher tendency to isomerize olefinic hydrocarbons than Pt and Ir [14].

Transition metal sulfides, particularly NiMo and CoMo, are effective catalysts for hydrogenation, hydrodesulfurization, hydrodenitrogenation and hydrodemetallation [1]. In a US patent, sulfided NiW catalyst could hydrogenate C3 and C4 diolefins at 100 – 200 °C and 150 – 200 psig, with the presence of sulfur contamination in feed stream [5]. Other than the expensive Pd [12,13,15,16], Ni-containing catalyst is accepted as the most active olefin hydrogenation catalyst [15]. In a kinetic study of olefin hydrogenation over sulfide NiMo and

CoMo catalysts, Badawi et al. observed stronger olefin adsorption/less steric hindrance on NiMo than that over CoMo, with nearly no influence by the olefinic structure, which supported the observed faster olefin conversion rates over sulfide NiMo catalyst [6]. Other transition metal sulfides, such as Co, Fe, Co and Nb have all shown relatively good activities toward olefin/diolefin hydrogenations [15,17-20]. Among them, Nb-containing metal sulfides are considered as a potential alternative to Mo, because hexagonal NbS_2 exhibits similar overall features as MoS_2 [21].

Non-Pt-group transition metals allow for a relatively high sulfur tolerance [22]. The naphtha product derived from thermal cracking contains high concentrations of S and N contaminates, for instant, 1.68 wt% S and 237 ppmw N, reported by Syncrude's R&D [23]. Toba et al. investigated the activity of various olefins in the HDS of FCC gasoline [7]. An interesting finding is that the C6 olefin conversion increased with the increment of sulfur content from 61.8 ppm to 1982.6 ppm in the feedstock [7]. The author discussed that H_2S (from HDS) reacts with olefins to form thiols that is further desulfurized and produced saturated hydrocarbons, same as olefin hydrogenation products [7]. This is in agreement with Kirsch and Shull's observation during the selective hydrogenation of butadiene over a sulfide CoMo catalyst; it is suggested that adding sulfur is essential to preserve the activity and selectivity of metal sulfide catalysts [24]. According to literature, the effect of S compound on olefin hydrogenation is minor over metal sulfide catalysts; instead, Hatanaka observed that thiophene HDS is strongly retarded by only 1 mol% olefinic hydrocarbon due to competitive adsorption of olefins on active HDS sites [25]. Comparing to sulfur, nitrogen compounds are a much stronger inhibitor in hydrotreating processes, by competitive adsorption on active sites of catalysts. Few studies have focused on the inhibiting effect by quinoline on hydrogenation [26-28]. Jacobsen et al. performed simultaneous catalytic HDS, HDN and HYD reactions over various transition metal sulfide catalysts at high T (300 – 375 °C) and high P (50 bar). The hydroprocessing reaction rate follows the order of naphthalene HYD < DBT HDS < indole HDN, for all studied sulfided catalysts [19]. However, a majority of N inhibiting effect was performed at temperatures above those used for olefin hydrogenation.

The present work is focused on the development of cost-efficient catalysts for partial upgrading process to reduce diolefin content from naphtha feedstock, as well as on the kinetic study of the nitrogen inhibiting effect. A conjugated diolefin with steric hindrance at its internal double bonds, 2,5-dimethyl-2,4-hexadiene, was hydrogenated in the presence of dibenzothiophene (DBT) and quinoline (Q) inhibitors. We investigated hydrogenation activities of the synthesized transition metal nanocatalysts, at 150 – 180 °C and 10 – 20 bar, in presence of up to 1000 ppmw S and 250 ppmw N to mimic the S and N levels in naphtha feedstock. Sulfur and nitrogen inhibiting effects on a promising sulfide Ni catalyst were examined. Diolefin and quinoline hydrogenation rate constants were determined over a NiS catalyst. Issue with catalyst deactivation due to catalyst structure change and N-poisoning were also addressed.

5.2 Experimental

5.2.1 Materials

Nickel(II) acetylacetonate ($Ni(acac)_2$, 95%, Sigma Aldrich), Cobalt(II) acetylacetonate ($Co(acac)_2$, 97%, Sigma Aldrich), iron(III) acetylacetonate ($Fe(acac)_3$, 97%, Sigma Aldrich), niobium pentachloride ($NbCl_5$, 99%, Sigma Aldrich), copper(II) acetate hydrate ($Cu(AcO)_2 \cdot xH_2O$, 98%, Sigma Aldrich), nickel(II) acetate tetrahydrate ($Ni(AcO)_2 \cdot 4H_2O$, 98%, Sigma Aldrich), cobalt(II) acetate tetrahydrate ($Co(AcO)_2 \cdot 4H_2O$, ≥98%, Sigma Aldrich), iron(II) acetate ($Fe(AcO)_2$, 99.99%, Sigma Aldrich), polyvinylpyrrolidone (PVP, MW 29 000, Sigma Aldrich), thiourea (99%, Sigma Aldrich), oleylamine (OAm, technical grade, 70%, Sigma Aldrich), oleic acid (OAc, technical grade, 90%, Sigma Aldrich), trioctylphosphine (TOP, 97%, Sigma Aldrich), 1,2-tetradecandiol (technical grade, 90%, Sigma Aldrich), sulfur (99.5 – 100.5%, Sigma Aldrich), benzyl ether (BE, 98%, Sigma Aldrich), 2-propanol (IPA, ≥99.5%, Fisher Chemical), hexanes (Fisher Scientific), acetone (Fisher Scientific), gamma-aluminum oxide (□-Al_2O_3, particle size 150 mesh, average pore size 58 Å, surface area 155 m^2/g, Sigma Aldrich), 2,5-dimethyl-2,4-hexadiene (diolefin, 96%, Sigma Aldrich), dibenzothiophene (DBT, 98%, Sigma Aldrich), quinoline (98%, Sigma Aldrich), dodecane (≥99%, Sigma Aldrich), and decahydronaphthalene (decalin, ≥99%, Sigma Aldrich). Milli-Q water was used throughout the work. Ultra-high purity (99.999%) nitrogen and hydrogen gases were purchased from Praxair Canada.

5.2.2 Catalyst preparation

NiS, CoS, FeS, and NbS nanoparticles were synthesized in oleylamine, which acts as a surfactant and reducing agent [29]. Additional capping agent and reducing agent were introduced in the synthesis, depending on the specific metal nanoparticles being synthesized. The final metal sulfide nanoparticles were achieved by "hot-injection" of OAm-sulfur solution, which provides the sulfur source for sulfidation. Upon heating to certain temperatures, the sulfide ions react with excess amine to generate H_2S that combines with the metal nanoparticles to form metal sulfide [30].

NiS. In a 250 mL three-neck flask, 0.6 mg of $Ni(acac)_2$ and 8 mL of OAm were dissolved in 60 mL BE. The mixture was stirred and purged by Ar for 5 min, and then followed by the addition of 5 mL TOP under Ar environment. The mixture was heated to 230 °C with a heating rate of 5 °C/min, and stayed at 230 °C for 15 min to form Ni nanoparticles [31]. Then 10 mL of OAm solution containing 0.107 g (3.337 mmol) elemental sulfur (S/Ni molar ratio = 1.5) was rapidly injected into the hot Ni nanoparticle solution. After 1 h reaction at 230 °C, homogenous solution of NiS nanoparticles were obtained without any precipitation. After cooling down to room temperature, NiS nanoparticles were collected by adding 60 mL ethanol, followed by centrifugation (8500 rpm, 10 min). The black precipitates of NiS nanoparticles were further washed 3 times by redispersing in minimum volume of hexane (< 5 mL), and then precipitated by adding 30 mL ethanol, followed by centrifugation. The cleaned NiS nanoparticles were deposit on γ-Al_2O_3 support (target loading 0.5 wt% Ni) through sonication of the nanoparticle

and γ-Al_2O_3 support in hexane/acetone mixture (volumetric ratio of 1/1). The final NiS/γ-Al_2O_3 sample was further purified 2 times by redispersing and precipitation in hexane/acetone mixture to get rid of oleylamine completely. Finally, NiS/γ-Al_2O_3 catalyst was dried in an oven at 60 °C for overnight under static air environment.

CoS. CoS/γ-Al_2O_3 catalyst was prepared by the same experimental procedures as described for NiS/γ-Al_2O_3 sample above, except 0.6 g of $Co(acac)_2$ was used as metal precursor.

FeS. In a 250 mL three-neck flask, 0.706 g of $Fe(acac)_3$, 2 mL OAm, 1.92 mL OAc, and 2.3 g 1,2-tetradecandiol were dissolved in 25 mL BE at room temperature. After purging Ar for 10 min, the solution was heated up to 215 °C, and stayed for 30 min; the mixture was further heated to 265 °C and stayed for another 30 min [32,33]. Then 10 mL of OAm solution containing 0.096 g elemental sulfur (3 mmol, S/Fe molar ratio = 1.5) was rapidly injected to the hot FeO_x solution; the reaction continued at 265 °C for 30 min tom complete sulfidatin. FeS nanoparticles were collected, washed, and deposit on γ-Al_2O_3 support according to the same procedures as described for NiS/γ-Al_2O_3 sample.

NbS. NbS/γ-Al_2O_3 catalyst was prepared by the same method as FeS/γ-Al_2O_3, except 0.540 g of $NbCl_5$ was used as metal precursor.

M (M = Ni, Co, Cu, Fe)-doped NbS nanocatalysts were prepared using hydrothermal method, according to method published by Liu et al. [34]. For example, for the synthesis of Cu-NbS catalyst, 0.040 g (0.2 mmol) of $Cu(OAc)_2 \cdot H_2O$, 0.050 g of PVP (MW = 29 000, PVP/Cu molar ratio = 2.25), 0.036 g thiourea (thiourea/Cu molar ratio = 2.36), and 0.050 g NbS (pre-synthesized according to NbS method described above) were mixed in 50 mL of 30 vol% IPA/water solution. A homogeneous solution was obtained by sonication for 10 min. The solution was then transferred to an autoclave, followed by hydrothermal treatment at 160 °C for 24 h. After reaction, the precipitate was collected by centrifugation (8500 rpm, 10 min), and washed three times by water. The washed Cu-NbS sample was then deposit on γ-Al_2O_3 by dry impregnation, with desired Nb and Cu loadings of 0.7 wt% and 0.254 wt%, respectively. Ni, Co, and Fe-doped NbS catalysts were prepared using the same synthesis method as described for Cu-NbS sample.

A Ni/$MgAl_2O_4$ catalyst contains metallic Ni nanoparticles (10 nm diameter, 6.5 wt% Ni loading by NAA) was prepared by deposition precipitation technique using urea as precipitation agent. Detailed experimental procedures can be found in our previously published work [35].

A **MoS_2/γ-Al_2O_3** reference catalyst was prepared by dry impregnating commercial MoS_2 on g-Al2O3 support. A **Ni-MoS_2/γ-Al_2O_3** reference catalyst was prepared by the same hydrothermal treatment method for M-doped NbS samples as described above, except 0.05 g commercial MoS_2 and 0.051 g (0.2 mmol) of $Ni(OAc)_2 \cdot 4H_2O$ were introduced to the synthesis.

5.2.3 Diolefin hydrogenation

Catalyst screening. Hydrogenation reactions were carried out in a semibatch stainless steel reactor (300 mL autoclave, Parr Instrument 4560 mini Bench Top Reactor) equipped with a high-temperature fabric heating mantle, a gas burette for the continuous isobaric hydrogen supply, and a thermocouple. The hydrogenation of 2,5-dimethyl-2,4-hexadiene (diolefin) was investigated at 150 °C and 10 bar absolute pressure over the prepared metal sulfide nanocatalysts. For a typical reaction, the reactor was filled with 100 g reaction solution containing 0.5 wt% diolefin, 0.5 wt% dodecane (C12, internal standard for GC quantitative analysis) in decalin and 1 g of as-prepared catalyst. The reaction mixture was flashed by nitrogen and stirred to ramp to the reaction temperature. Once the desired reaction temperature was achieved, the reactor was then pressurized with hydrogen to the desired operating pressure. The stirring speed was 1200 rpm, which has previously confirmed the absence of mass transfer limitations [36]. Diolefin hydrogenation was also investigated with the presence of 300 ppmw S (0.170 wt% DBT) and 100 ppmw nitrogen (0.095 wt% Quinoline). Due to the catalyst poisoning effects by S and N, in each run 3 g of catalyst was tested at 150 – 180 °C and 10 – 20 bar. Liquid samples of 1 mL were withdrawn from the system after 2 h of diolefin hydrogenation without S or N molecules, and after 5 h with the presence of 300 ppm S and 100 ppm N.

Product analysis and quantification. The hydrogenation products were identified by gas chromatography coupled with mass spectrometry (GC-MS) (Chemistry department, University of Alberta) and found to be in agreement with the reaction mechanisms in Scheme 1. The quantitative analyses of hydrogenation products were performed offline using a calibrated Agilent 7890A gas chromatogram (GC) equipped with a flame ionization detector (FID). The GC capillary column was H-PONA Agilent capillary column, 50 m length × 0.25 mm inner diameter × 0.25 μm film thickness. Initially, the oven temperature was stabilized at 40 °C for 1 min and then increased to 300 °C with a ramping rate of 10 °C/min. The mass balance was closed within 96 – 99%. Therefore, diolefin conversion was calculated as the amount of 2,5-dimethyl-2,4-hexadiene converted in hydrogenation over the original amount in the feed solution. According to GC-MS analysis, 2,5-dimethyl-2-hexene and trans-2,5-dimethyl-3-hexene are the only two diolefin hydrogenation products. The selectivity (on mass basis) was determined as the amount of each alkene product divided by the amount of total alkene products (alkene + isomerized alkene). The quinoline conversion was calculated as the amount of quinoline converted in hydrogenation over the amount of quinoline in feed solution.

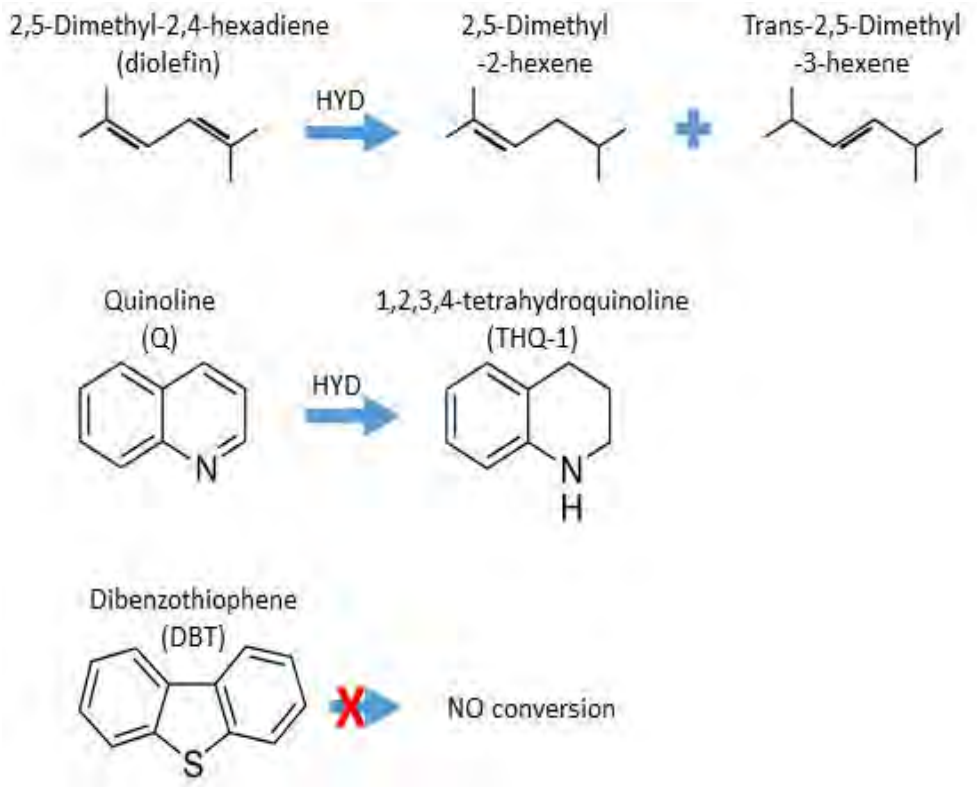

Scheme 1. Product distribution in the 2,5-dimethyl-2,4-hexadiene hydrogenation with the presence of 1000 ppms S and 50 – 250 ppm N at 150 – 180 °C and 10 – 20 bar H_2 pressure. Quinoline is hydrogenated to 1,2,3,4-tetrahydroquinoline; dibenzothiophene is inactive at the studied conditions. Reaction products were confirmed by GC-MS analysis.

Kinetic study. The kinetics of 2,5-dimethyl-2,4-hexadiene hydrogenation in the presence of S and N inhibitors were studied over 3 g of NiS/γ-Al_2O_3 catalyst at a fixed 10 bar H_2 pressure. The feed solution contains 0.5 wt% diolefin (fixed), 1000 ppmw S (fixed), varying N concentration (50 – 250 ppmw) and 0.5 wt% C12 (internal standard), balanced in decalin. Temperature effect on diolefin hydrogenation rate was also studied in the range of 90 – 170 °C at a fixed 100 ppm N level (experiments were performed, but not analyzed by GC). Liquid samples of 1 mL were collected at operating temperate and pressure every 30 min and for 5 h.

5.2.4 Catalyst characterization

The developed metal sulfide nanocatalysts were characterized by neutron activation analysis (NAA), scanning transmission electron microscopy (STEM), energy-dispersive X-ray spectroscopy (EDX) mapping, and X-ray photoelectron spectroscopy (XPS).

5.3 Results and discussion

5.3.1 Catalyst synthesis

Transition metal sulfide nanoparticles, NiS, CoS, FeS and NbS, were prepared by wet chemistry techniques in benzyl ether. Oleylamine is used as surfactant and mild reducing agent for the controlled preparation of metal nanocrystals. Other surfactants were also used in combination with oleylamine. For example, Fe and Nb nanoparticles were stabilized by the mixture of oleylamine and oleic acid; while Ni was prepared by oleylamine and trioctylphosphine. The reduction of Fe and Nb precursors requires a stronger reducing agent, 1,2-tetradecandiol, where the role of OAm is limited to act as a surfactant only. After synthesis of metallic nanoparticles, a solution of elemental sulfur dissolved in oleylamine was injected into the hot synthesis flask, and then allowed to continue heating for 1 h to form the desired metal sulfide nanocrystals. The polysulfide ions react with excess amine to generate H_2S, which combines with the metal nanoparticles to form metal sulfide [29]. Table 1 shows detailed synthesis parameters.

Table 1. Summary of the synthesized nanoparticles and supported catalysts.

catalyst	Precursors	Synthesis method	Solvent	Capping agent	Reducing ageng	S source	Metal loadings, wt%
NiS	$Ni(acac)_2$	Wet chemistry in organic solvent	BE	OAm, TOP	OAm	Elemental S	Ni: 0.345
CoS	$Co(acac)_2$	Wet chemistry in organic solvent	BE	OAm, TOP	OAm	Elemental S	Co: 0.5
FeS	$Fe(acac)_3$	Wet chemistry in organic solvent	BE	OAm, OAc	1,2-tetradecandiol	Elemental S	Fe: 0.5
NbS	$NbCl_5$	Wet chemistry in organic solvent	BE	OAm, OAc	1,2-tetradecandiol	Elemental S	Nb: 0.7
CuS	$Cu(AcO)_2$	Hydrothermal treatment	IPA/H_2O	n.a.	n.a.	thiourea	Cu: 0.254
Cu-NbS	$Cu(AcO)_2$	Hydrothermal treatment	IPA/H_2O	n.a.	n.a.	thiourea	Nb: 0.7 Cu: 0.254
Ni-NbS	$Ni(AcO)_2$	Hydrothermal treatment	IPA/H_2O	n.a.	n.a.	thiourea	Nb: 0.7 Ni: 0.235
Co-NbS	$Ni(AcO)_2$	Hydrothermal treatment	IPA/H_2O	n.a.	n.a.	thiourea	Nb: 0.7 Co: 0.235
Fe-NbS	$Fe(AcO)_2$	Hydrothermal treatment	IPA/H_2O	n.a.	n.a.	thiourea	Nb: 0.7 Fe: 0.223
Ref Ni-MoS_2	$Ni(AcO)_2$ Commercial MoS_2	Hydrothermal treatment	IPA/H_2O	n.a.	n.a.	thiourea	Ni: 0.319 Mo: 1.420
Ref Ni^0	$Ni(NO_3)_2$	Deposition precipitation with urea	H_2O	n.a.	H_2	n.a.	Ni: 6.5

A representative scanning TEM image (Fig. 1) of as-synthesized NiS nanoparticles shows monodispersed and spherical particles with an average diameter of 7.6 ± 1.0 nm. The STEM-EDX mapping displays both sulfur and phosphine elements on Ni surface. During Ni nanoparticle synthesis, oleylamine and trioctylphosphine bind to the surface of Ni atoms while leaving Ni in metallic state [31]. After synthesis, oleylamine is removed completely by repetitive hexane washing, leaving only phosphine on Ni surface atoms. EDX mapping also validates the employed sulfidation process by hot injecting S-OAm solution. Due to the pre-formation of metallic nanocrystals, the sulfidation occurred only on the surface of transition metal nanoparticles. This is further confirmed by the low S/Ni molar ratio (0.11) by EDX elemental analysis. Since only the surface metal atoms are sulfide, the catalysts were named as MS, without number notations corresponding to the metal/sulfur molar ratio. During Ni nanoparticle synthesis, TOP stabilized Ni nanoparticles to prevent aggregation. The formation of Ni-TOP complexes is further decomposed to form phosphide Ni upon heating [37]. The P/Ni molar ratio detected by EDX mapping is 0.22. Similar to sulfidation, the phosphidation is believed to be on Ni surface.

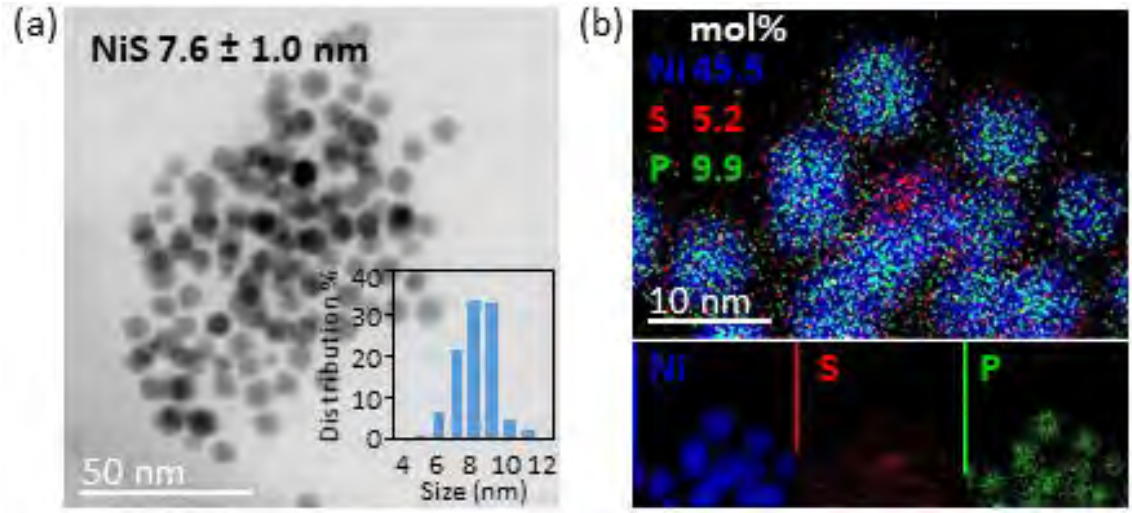

Figure 1. (a) bright field STEM image of as-synthesized NiS nanoparticles and their size distribution; (b) STEM-EDX mapping as-synthesized NiS nanoparticles.

A series of transition metal-promoted NbS catalysts consisting of Ni, Co, Fe, or Cu dispersed on NbS nanoparticles were prepared using hydrothermal method published by Liu et al. with modifications [34]. First, NbS nanoparticles were synthesized according to the experimental procedures described in above session. These NbS nanoparticles were mixed with thiourea-M complex, followed by hydrothermal treatment at 160 °C for 24 h. During the hydrothermal process, the thiourea-M complex refilled some of the surface sulfur vacancy sites of NbS[34]. Due to the relatively high activity of Cu-NbS catalyst (will be discussed in following session), a reference CuS catalyst was prepared using the same hydrothermal method as for Cu-NbS, but without NbS nanoparticles.

5.3.2 Diolefin hydrogenation: catalyst screening

The developed monometallic and bimetallic metal sulfide catalysts were examined in diolefin hydrogenation with and without S and N poisons in the feed solution. A conjugated diolefin with methyl branches attached on its internal double bonds, 2,5-dimethyl-2,4-hexadiene, was selected as the model compound, as it requires a sterically demanding flat-lying adsorption on a catalyst as compared to perpendicular adsorption of terminal C=C bonds. Hydrogenations are highly exothermic and fast reactions; they do not require high temperature as other hydrotreating processes, such as hydrodesulfurization and hydrodenitrogenation. From the viewpoint of cost-effective partial upgrading to hydrogenate diolefins, a rather mild operating condition, 150 – 180 °C and 10 – 20 bar H_2 pressure, was selected in the present work.

According to the GC-MS analysis, diolefin is hydrogenated to alkenes without detectable complete hydrogenation to alkane. Two types of alkene composition confirmed by GC-MS analysis: 2,5-dimethyl-2-hexene and trans-2,5-dimethyl-3-hexene. The main reaction product was 2,5-dimethyl-2-hexene, with the selectivity of 50 – 80%. Although the isomerized alkene (trans-2,5-dimethyl-3-hexene) is less pronounced, it is considered as a more thermodynamically stable product [13]. Unlike single atom catalysis, the relatively large NiS nanoparticle size allows the flat-lying π-adsorption mode during hydrogenation; this is especially important for branched diene structures. Both double bonds of 2,5-dimethyl-2,4-hexadiene could simultaneous coordinate on NiS particles. An isomerization mechanism proposed by Karakhanov et al. suggested that the terminal alkenes can be isomerized to the more stable cis- or trans-2,5-dimethyl-3-hexene isomers, with the trans-isomer being the most thermodynamically stable structure [13]. This is in line with our observed hydrogenation product distribution, i.e., no cis-isomer was detected by GC-MS.

Diolefin HYD without S and N. Figure 2 compares catalytic activities in diolefin hydrogenation for the developed metal sulfide nanocatalysts without S or N. At 150 °C and 10 bar H_2, NiS is the most active hydrogenation catalyst that converted nearly 100% diolefin to alkene after 2 h reaction. While all other metal sulfide catalysts reveal similarly low diolefin conversions in the range of 10 – 20%. It is known that the first row transition metals could selectively catalyze partial hydrogenation; among them, Ni is the most active [20]. For example, the hydrogenation of penta-1,3-diene over Ni catalyst required the lowest reaction temperature comparing to those over Co, Fe and Cu catalysts [15]. The surface phosphorus resulted from TOP stabilization may also contribute the superior activity of Ni. Nozaki and coworkers explored diolefin hydrogenation over transition metal phosphide catalysts [9-11]. It has been found that butadiene hydrogenation activities of Co_2P and FeP are extremely lower than that of Ni_2P; a 200 °C of reaction temperate is needed for Co and Fe phosphide catalysts to reach similar activity level as Ni_2P [10]. Similarly, in low temperature diolefin hydrogenation, CoS (also stabilized by TOP) displays poor hydrogenation activity as comparing to NiS. Moreover, Bonita and Hicks

reviewed that metal phosphides, particularly Ni_2P, outperform metal sulfides and carbides in hydroprocessing; this is related to the charge transfer in Ni-P bond favors the activation of H_2 and reactant molecules being hydrotreated [37].

A reference metallic Ni nanoparticle catalyst (without TOP, OAm, or elemental S) deposit on $MgAl_2O_4$ support was prepared. The use of a different catalyst support, $MgAl_2O4$, was to ensure the formation of small metallic Ni nanoparticles without introducing TOP and OAm stabilizers during synthesis. Metallic Ni catalyst was tested in the hydrogenation of diolefin (without S or N poinsons), and its performance was compared with the NiS catalyst. Partial hydrogenation of 2,5-dimethyl-2,4-hexadiene favors sulfided Ni catalyst. NiS catalyst (3.5 mg active Ni in reaction) allows 100% diolefin conversion after 3 h reaction at 150 °C and 10 bar (Fig 2); while metallic Ni catalyst shows only 70 % diolefin conversion at the same conditions, but with more catalyst loaded in the reactor (5.3 mg Ni). The formation of isomerized alkene on metallic Ni catalyst is less favorable than that over NiS catalyst.

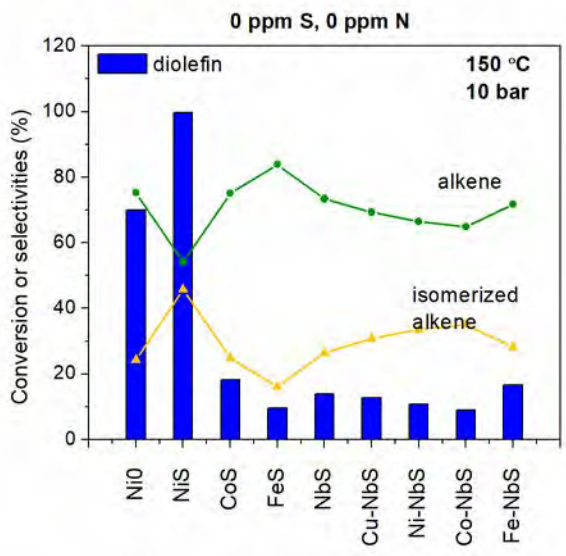

Figure 2. Diolefin hydrogenation without S and N molecules over 1 g of γ-Al_2O_3 supported metal sulfide catalyst (as-synthesized) at 150 °C and 10 bar H_2 pressure. Feed solution: 0.5 wt% 2,5-dimethyl-2,4-hexadiene, 0.5 wt% C12 (internal standard), balanced in decalin; liquid samples were collected after 2 h.

Figure 2 shows that niobium-containing sulfide catalysts did not show promising results in low temperature diolefin hydrogenation. Niobium in either oxide or sulfide form is usually used as a catalyst, a promoter or catalyst support in HDS and HDN. Similar to our observation, low HYD rate was also observed for NbS catalyst in a study of simultaneous HDS, HDN and HYD reactions [19]. In the present study, one of the reasons for the poor activity of Nb-containing catalysts could be low degree of surface sulfidation during synthesis. Previously, our group has discussed

that the high affinity of Nb to O could result in extremely stable NbO_x material with the heats of formation of -380 – -395 kJ/mol [38]. Most likely, NbO_x nanoparticles were formed first; the following sulfidation step by injecting OAm-S solution at 300 °C might not be efficient to sulfide surface niobium. The hypothesis is further confirmed by performing EDX mapping on as-synthesized $NbS/\gamma\text{-}Al_2O_3$ catalyst (Fig. S1). It is difficult to distinguish Nb and S from EDX analysis, due to the overlapping of the second peak from NbLa and SKa. Thus, the EDX count signal from SKb was used to qualitatively analyze the presence of surface sulfur for Nb-containing samples. EDX mapping reveals no signal at SKb, proving no surface Nb sulfidation or extremely low degree of sulfidation.

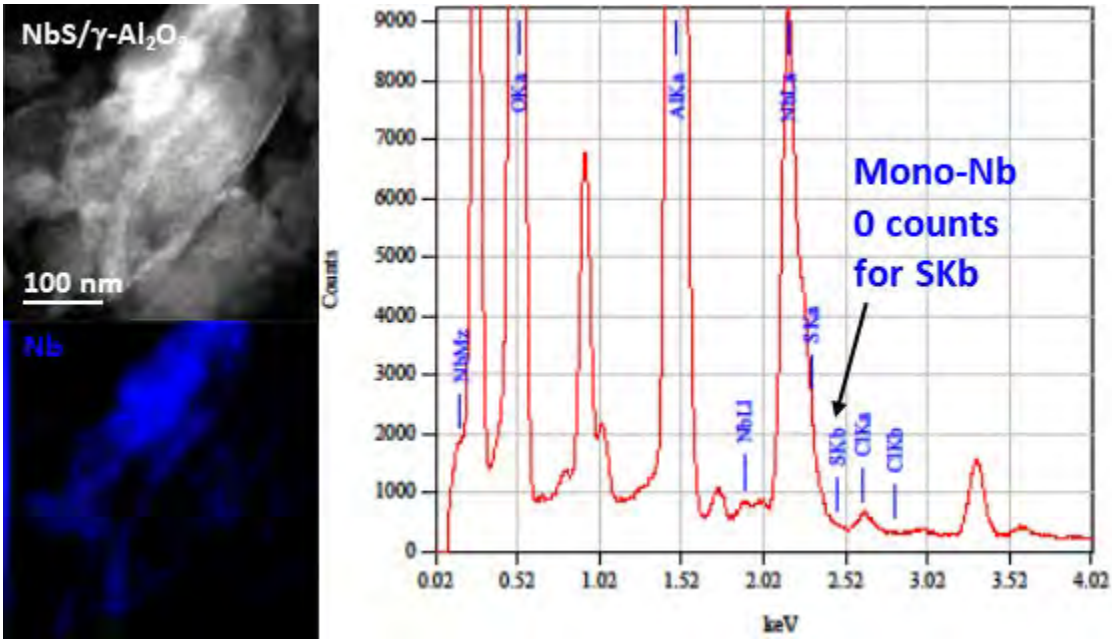

Figure S1. STEM-EDX mapping of as-synthesized $NbS/\gamma\text{-}Al_2O_3$ catalyst.

S and N effects on diolefin HYD. The hydrogenation of diolefin over the developed metal sulfide catalysts were investigated with the presence of DBT and quinoline. The inhibiting effect by S-molecule was also studied separately without the presence of quinoline. Under such conditions, the 2,5-dimethyl-2,4-hexadiene was hydrogenated to alkene and its trans-isomer; quinoline was hydrogenated to 1,2,3,4-tetrahydroquinoline (THQ-1); whereas dibenzothiophene conversion was negligible regardless of its concentration in the feed, as shown in Scheme 1.

In Figure 3, diolefin hydrogenation was investigated in the presence of up to1000 ppmw S in the feed over a $NiS/\gamma\text{-}Al_2O_3$ catalysts at 150 °C and 10 bar. At this condition, no DBT conversion was detected, so DBT only acted as hydrogenation inhibitor by competitive adsorption on NiS surface, or vice versa. Figure 3 shows that, at low DBT concentration (50 ppmw S), diolefin hydrogenation conversion maintained nearly 100%. Only 35% diolefin conversion drop was

observed when S level was increased to 1000 ppmw. It can be concluded that the S poisoning effect on hydrogenation is mild over sulfide Ni catalyst. Transition metal sulfides are known to have high hydrogenation activity and relatively high resistance to sulfur poisoning [39]. For example, Kirsch and Shull observed that sulfide cobalt-molybdena was superior to copper chromite on the basis of resistance to sulfur poisoning [24]. A slight increase in trans-isomerized alkene was produced along with increasing DBT in feed (Fig. 3). In the study of 1,3-butadiene hydrogenation over rhenium catalyst, Grant et al. indicated that the hydrogen addition mode could change from 1,2-addition to a 1,4-addition when Re was contaminated by S, leading to an increased selectivity to trans- or cis-2-betene and reduced butane yield [40].

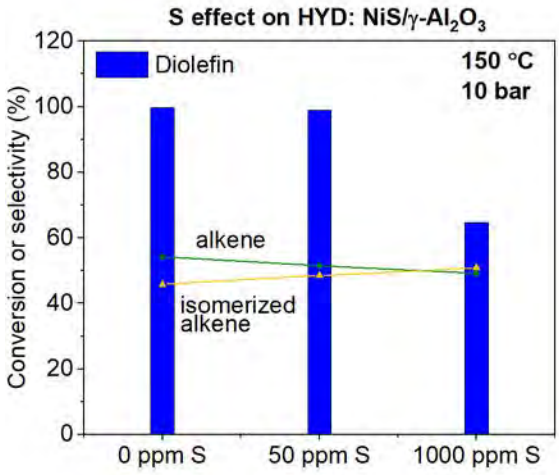

Figure 3. Sulfur inhibiting effect on diolefin hydrogenation over 1 g of NiS/γ-Al_2O_3 catalyst at 150 °C and 10 bar H_2 pressure. Feed solution: 0.5 wt% 2,5-dimethyl-2,4-hexadiene, 0.5 wt% C12 (internal standard) and 0 – 1000 ppmw S (0 – 5.8 wt% DBT), balanced in decalin; liquid samples were collected after 3 h.

The developed metal sulfide catalysts were further investigated in diolefin hydrogenation in the presence of 300 ppmw S and 100 ppmw N molecules, as shown in Figure 4. Sulfide Ni, Co and Fe catalysts display similar activity trend as the case without S and N. It can be seen that the hydrogenation activity of NiS is suppressed dramatically by 100 ppmw N. Only 30 % of diolefin was converted to alkene over 3 g NiS/γ-Al_2O_3 catalyst after 5 h of reaction vs 100 % conversion over 1 g NiS//γ-Al_2O_3 without N (Fig 3), at the same reaction conditions (150 °C and 10 bar). Nitrogen molecules are strong catalyst poisoners; they slow down other hydrotreating reactions rapidly with less than 50 ppm in the feed [41]. In the study of inhibiting HYD and HDS reactions with quinoline, Minaev et al. concluded that the conversions of both naphthalene hydrogenation and hydrodesulfurization were substantially suppressed by quinoline in the feed (100 – 1000 ppm N) [26]. The inhibiting effect by quinoline is because of the competitive

adsorption of quinoline and its product (THQ-1 in the present study). Due to the preferential adsorption of quinoline on NiS sites, the quinoline hydrogenation to THQ-1 is a much faster reaction than diolefin partial hydrogenation.

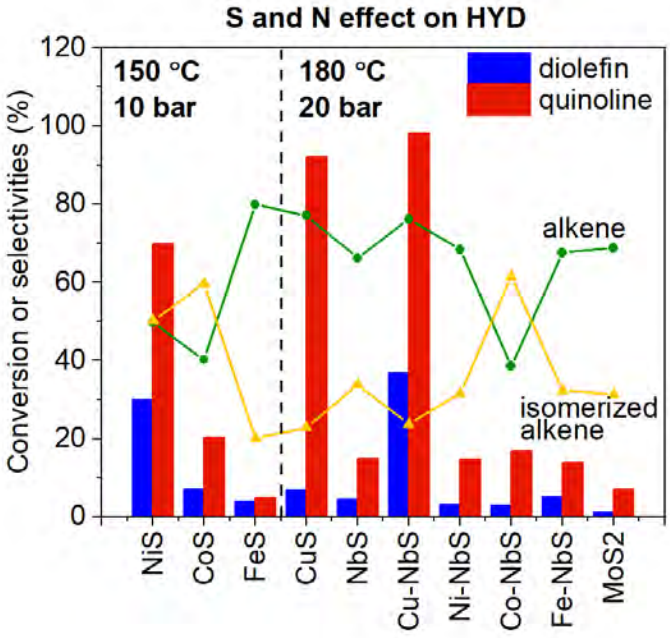

Figure 4. S and N inhibiting effects on diolefin hydrogenation over 3 g of γ-Al_2O_3 supported metal sulfide catalyst (as-synthesized) at 150 – 180 °C and 10 – 20 bar H_2 pressure. Feed solution: 0.5 wt% 2,5-dimethyl-2,4-hexadiene, 0.5 wt% C12 (internal standard), 300 ppmw S (0.17 wt% DBT) and 100 ppmw N (0.09 wt% Q), balanced in decalin; liquid samples were collected after 5 h.

Figure 4 also shows that diolefin and quinoline hydrogenation performances of **niobium-based catalysts**, which were tested at elevated conditions, 180 °C and 20 bar, due to their relatively low hydrogenation property. Niobium alone might not be a suitable catalyst for partial upgrading. Although it exhibits the same overall features as MoS_2 [21], they always requires promoting effect by other metals (commonly Ni and Co). In this study, a commercial mono-MoS_2 was tested and displays poor HYD activity. Among the Nb-containing catalysts, **Cu-doped NbS** catalyst showed 40% and 90% for the hydrogenation of diolefin and quinoline, respectively. Mono-CuS is only active toward quinoline hydrogenation; while NbS displays poor activity for both diolefin and quinoline conversions. It has been discussed that hot injecting OAm-S solution could not sulfide Nb; however, when hydrothermally treating niobium along with copper and thiourea, the S from thiourea could sulfide niobium. This is evidenced by EDX mapping of as-synthesized Cu-NbS/γ-Al_2O_3 sample; a low intensity peak for SKb can be observed in EDX spectrum (Fig. S2). Figure S2 also shows the formation of small Cu nanoparticles sitting on Nb upon hydrothermal treatment. According to EDX analysis and the synthesize strategy, the Cu-NbS catalyst may consist Cu nanoparticles chemically sitting on NbS

substrates. For the as-synthesized catalyst, these Cu nanoparticles are most likely in the oxidized form instead of sulfide form, as EDX did not show intense S signals in Cu particles. The reduction of copper oxide to metallic Cu could occur at low temperature in the range 75 – 225 °C in a flow of 5% H_2/Ar gas mixture at atmospheric pressure [42]. Thus, at our hydrogenation conditions (180 °C and 10 Bar H_2), CuO_x nanoparticles could be easily reduced to form metallic Cu that facilitated hydrogen activation. An earlier work has discussed that, during H_2 activation, copper atoms could form a dihydride structure, which is favorable for concerted hydrogenation at elevated pressure and temperature though [43]. According to EDX analysis, the degree of Nb sulfidation has been improved by the following hydrothermal treatment with thiourea. The united properties of Cu and NbS therefore improved the hydrogenation activities vs its monometallic forms. Moreover, the synthesis strategy was adopted from Co-MoS_2 preparation method published by Liu et al. [34]. By conducting experimental work and DFT analysis, the author observed a large number of sites at the interface between Co and Mo atoms on the MoS_2 basal plans [34]. According to their theory, the synergistic effect observed in Cu-NbS catalyst can be ascribed to the presence of sulfur vacancies in Cu-S-Nb interfacial sites [34]. Nonetheless, such synergistic effect was not observed in Ni-, Co- or Fe- doped NbS catalyst.

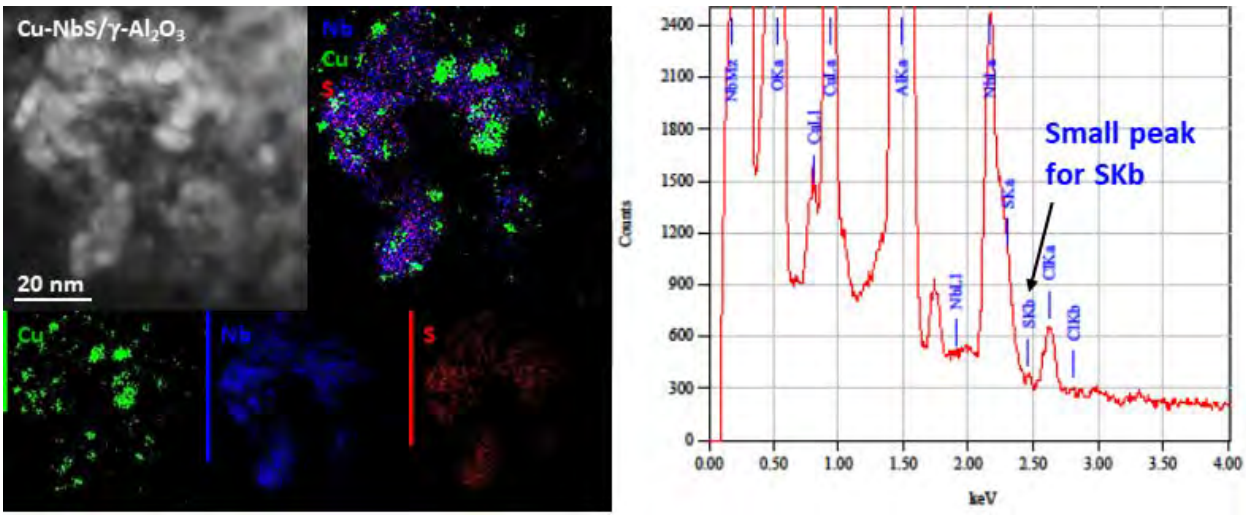

Figure S2. STEM-EDX mapping of as-synthesized Cu-NbS/γ-Al_2O_3 catalyst.

5.3.3 Kinetic study

Diolefin (2,5-dimethyl-2,4-hexadiene) was partially hydrogenated to alkene (2,5-dimethyl-2-hexene) and isomerized alkene (trans-2,5-dimethyl-3-hexene) with no detectable alkane. Quinoline was hydrogenated to 1,2,3,4-tetrahydroquinoline; no DBT conversion was detected at the studied conditions. Among mentioned transition metal sulfide catalysts, NiS/γ-Al_2O_3 allows for the highest hydrogenation activity at the lowest T and P with and without S and N

compounds. The reaction kinetics was studied over NiS/γ-Al_2O_3 catalyst at fixed S concentration (1000 ppmw) and varying N composition (0 – 250 ppmw) and temperatures.

Diolefin hydrogenation without quinoline is first order with respect to diolefin (Fig. 5). Quinoline not only inhibits the hydrogenation but also changes the diolefin hydrogenation reaction order to zero with respect to the diolefin. The reaction order of diolefin hydrogenation with respect to the total N concentration is negative first. The quinoline hydrogenation itself also follows 0^{th} order kinetics to Q (Fig. 6). A similar zero order to Q was found in an earlier work at temperatures below 40 °C [44].

The reaction kinetics suggests that there are several types of active sites for the activation and hydrogenations of the diolefin and quinoline, including those poisoned by quinoline and its hydrogenation product, and those where quinoline and diolefin competitive hydrogenations occur.

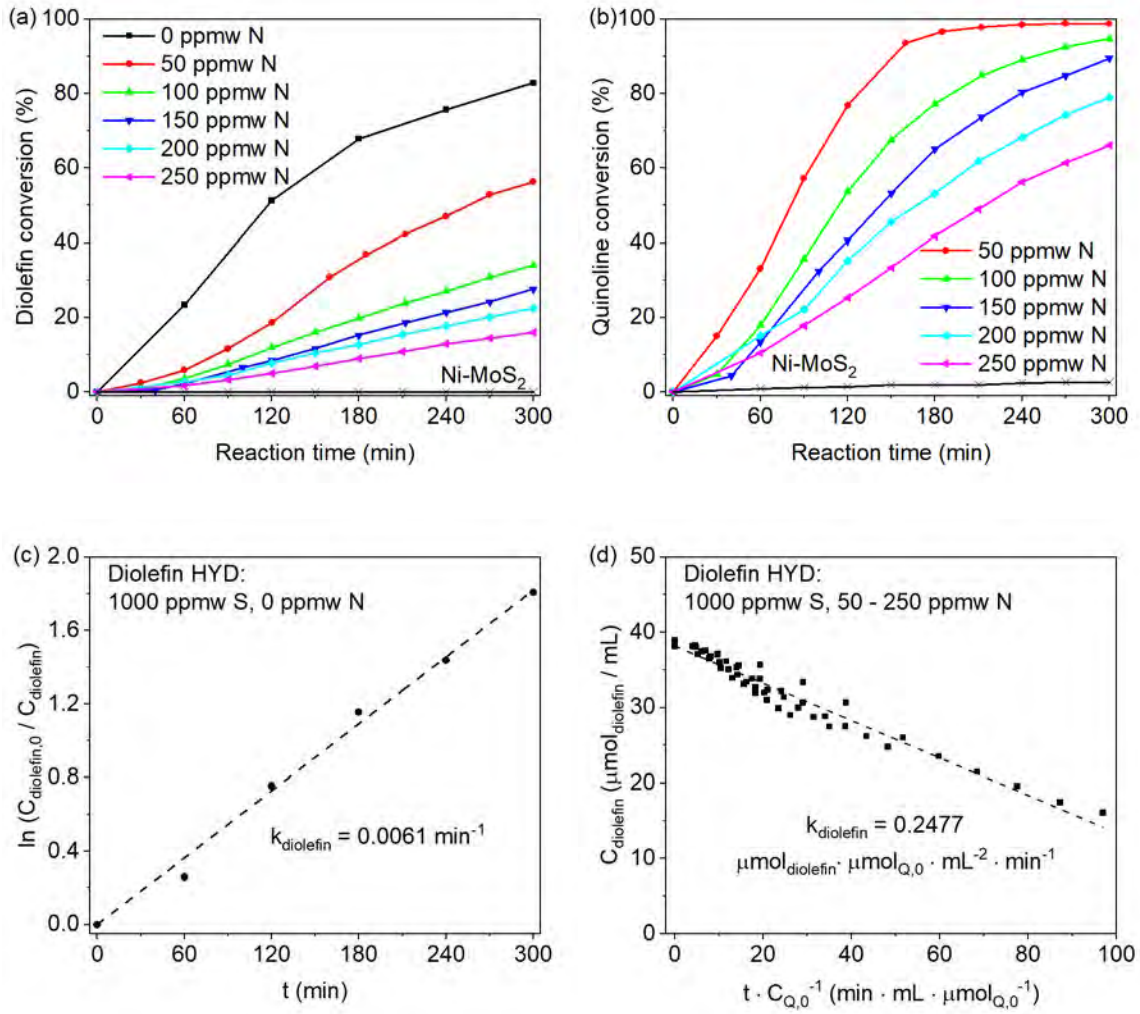

Figure 5. Kinetic study of 2,5-dimethyl-2,4-hexadiene to alkene over 3 g of NiS/γ-Al_2O_3 catalyst at 150 °C, 10 bar H_2, in the presence of 1000 ppmw S (5.8 wt% DBT) and 0 – 250 ppmw N (0.23 wt% Q). (a) diolefin conversions vs time; (b) quinoline conversions vs time; (c) diolefin hydrogenation rate constant ($k_{diolefin}$) determined at 1000 ppmw S and 0 ppmw N; (d) diolefin hydrogenation rate constant ($k_{diolefin}$) determined 1000 ppmw S and 50 – 250 ppmw N.

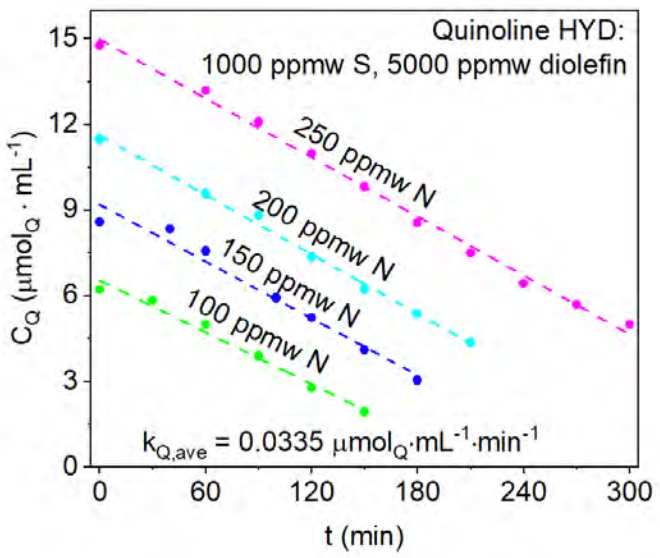

Figure 6. Kinetic study of quinoline (Q) to 1,2,3,4-tetrahydroquinoline (THQ-1) over 3 g of NiS/γ-Al_2O_3 catalyst at 150 °C, 10 bar H_2. Experimental details were the same as described in Fig. 5.

For NiS/γ-Al_2O_3 catalyst, the Arrhenius plots for 2,5-dimethyl-2,4-hexadiene and quinoline hydrogenation were obtained over the temperature range of 125 – 150 °C and 10 bar, with the presence of 1000 ppmw S and 100 ppm N compounds, as shown in Figure 7. Activation energies calculated from Arrhenius plots are 113 kJ/mol and 71 kJ/mol for the hydrogenation of diolefin and quinoline, respectively. Generally, diolefin hydrogenation alone without inhibitors requires relatively low activation energies. For example, Wells et al reported that the activation energies for alkadienes (1,3-butadiene and 1,3-pentadiene) hydrogenation is in the range of 29 – 63 kJ/mol, depending on the reaction temperature studied, as well as the type of metal that catalyzed hydrogenation reactions [15,20,40]. The olefinic molecule studied in the present work is a conjugated diene with methyl groups attached on internal double bonds; thus its hydrogenation requires higher activation energy (113 kJ/mol) than diolefins studied in literatures with one double bonds and without steric hindrance. In addition to the type of diolefin being studied, the presence of S and N compounds could also introduce extra difficulty for diolefin hydrogenation. The hindering effect by N compound is more severely than sulfur. As discussed in the above session, quinoline slows down diolefin hydrogenation by competitive adsorption on catalyst active sites. The E_a for quinoline obtained in our study is in good

agreement with literature data; an activation energy of 44 kJ/mol was reported previously over Pt catalyst in the temperature range of 15 – 230 °C [44].

The number of active sites performing diolefin hydrogenation is higher than those catalyzing the quinoline hydrogenation in the presence of poisoning quinoline, as seen from the preexponential factors of the Arrhenius laws (Figure 7).

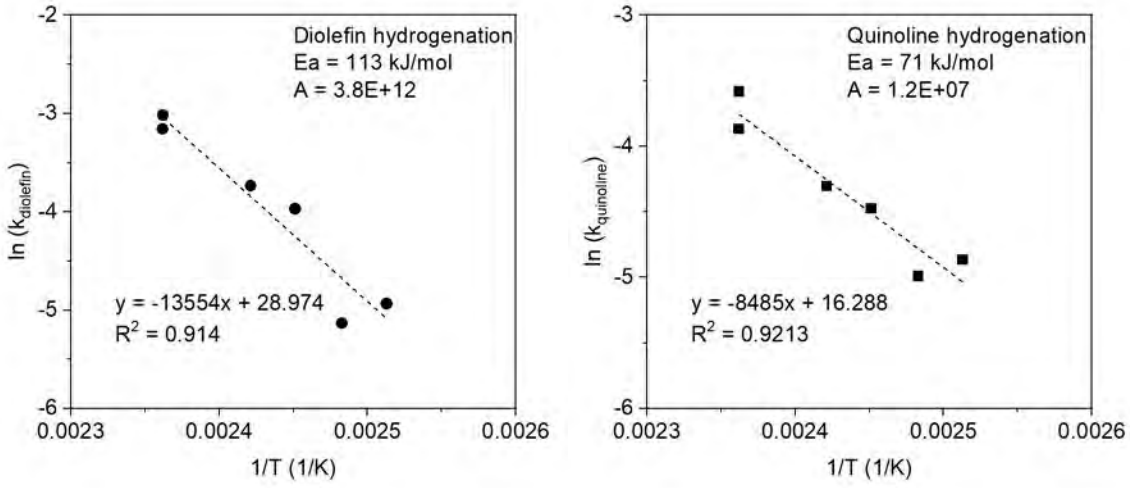

Figure 7. Arrhenius plots and activation energies for diolefin hydrogenation and quinoline hydrogenation over 3 g of NiS/γ-Al_2O_3 catalyst at 125 – 150 °C, 10 bar H_2, in the presence of 1000 ppmw S (5.8 wt% DBT) and 100 ppmw N (0.09 wt% Q).

5.3.4 Catalyst deactivation

Table 2 shows the stability test of NiS catalyst at 150 °C, 10 bar H_2 and 5 h for each cycle, with addition of fresh reaction solution mixture after each batch of test. It is important to note that active Ni nanoparticle leaching into solution occurred during hydrogenation reactions. Ni loading is 0.268 wt% in a spent NiS/γ-Al_2O_3 catalyst vs 0.345 wt% in a fresh NiS/γ-Al_2O_3 sample before reaction. Thus for the catalyst deactivation study, nanoparticle leaching must be taken into consideration as well. The amount of Ni leached into solution must be compensated by adding more used catalysts in the spent cycle 1 and cycle 2 tests to maintain 10 mg of active Ni available in reactions. The spent catalyst was rinsed with acetone for several times; thus, it is assumed that there is no significant Ni leaching between cycle 1 and cycle 2 tests. Obvious catalyst deactivation of NiS catalyst was observed, with rate constants dropped by order of magnitude. The main reason for catalyst deactivation should be nitrogen poisoning.

According to EDX analysis (Fig. 8), the amount of S remaining on Ni surface is beyond the EDX detecting limit, indicating the decomposition of surface Ni-S at the employed hydrogenation conditions. In a selective HYD of butadiene, the author indicated that adding H_2S is essential to preserve the activity of sulfide metal catalysts [24]. However, at the studied HYD condition, there was no continuous H_2S being supplied or produced via DBT HDS. EDX mapping in Figure 7 also shows that P separated from Ni surface and then segregated onto alumina support, which is another evidence of catalyst deactivation.

In conclusion, the three main causes for catalyst deactivation for the most promising NiS catalyst is N-poisoning, S loss and P loss from Ni surface. Deactivation by Ni nanoparticle sintering is negligible due to the low reaction temperature and low Ni loading on alumina.

Table 2. Effect of catalyst deactivation on diolefin and quinoline hydrogenation rate constants. Reaction conditions: 150 °C and 10 bar H_2 pressure; feed solution: 0.5 wt% 2,5-dimethyl-2,4-hexadiene, 0.5 wt% of C12 (internal standard), 1000 ppmw S, and 250 ppmw N, balanced in decalin; liquid samples were collected every 30 min for 5 h.

$NiS/\gamma\text{-}Al_2O_3$ sample[a]	Diolefin conversion, %	Quinoline conversion, %	$k_{diolefin}$, $\mu mol_{diolefin} \cdot \mu mol_{Q,0} \cdot mL^{-2} \cdot min^{-1}$	k_Q min^{-1}
fresh cycle	16	66	0.0240	0.0345
spent cycle 1	7	39	0.0108	0.0194
spent cycle 2	7	15	0.0038	0.0092

[a] 3 g $NiS/\gamma\text{-}Al_2O_3$ catalyst (10 mg Ni) was used in fresh run; 4 g of spent catalyst was used in cycle 1 to compensate NiS particle leaching in solution; and 4 g of spent catalyst collected from cycle 1 condition was used in cycle 2.

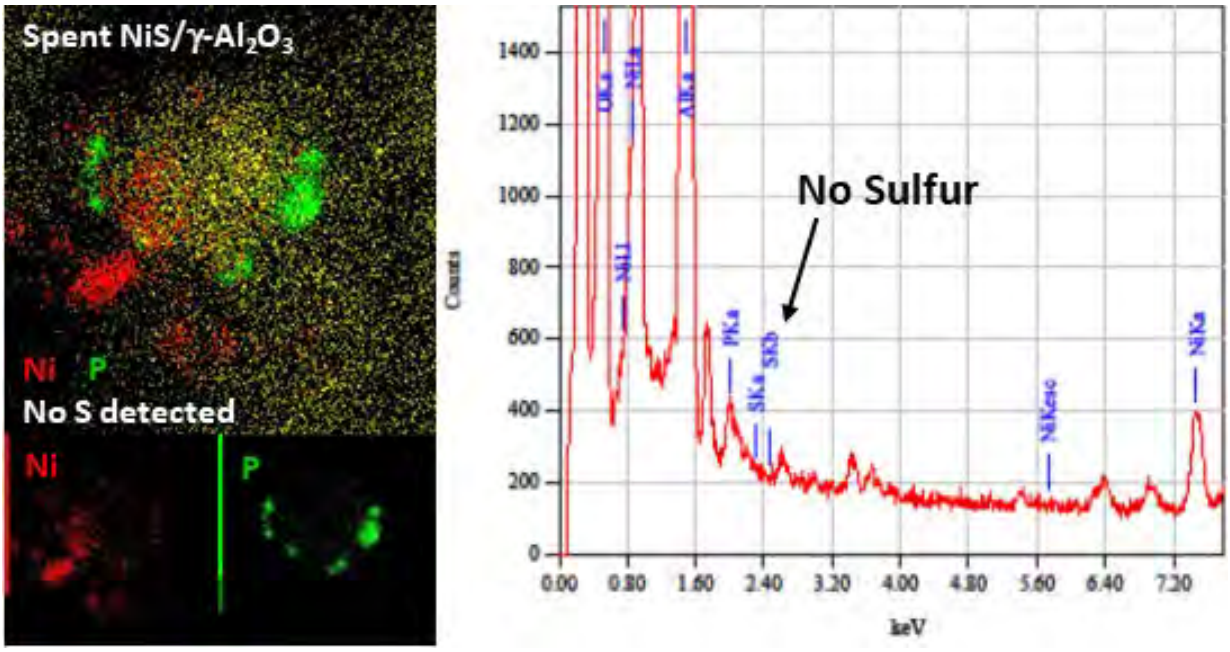

Figure 8. STEM-EDX mapping of spent NiS/γ-Al_2O_3 catalyst.

The XPS analysis of fresh NiS/γ-Al_2O_3 catalyst shows Ni $2p_{3/2}$ peak from NiS and/or Ni, centered at 853.1 eV (and its satellite at 859.2 eV). After hydrogenation reaction, the NiS/NiP peak shifted to a lower binding energy at 852.5 eV (and its satellite at 858.6 eV) observed in NiS spent sample, indicating the decomposition of NiS and NiP, and therefore, formation of metallic Ni in catalyst surface. As the spent catalyst was reused in hydrogenation reactions, the metallic Ni $2p_{3/2}$ peak centered at 858.8 eV (and its satellite at 863.0 – 963.2 eV) becomes more defined. The XPS analysis of NiS/γ-Al_2O_3 catalysts at different stages of hydrogenation reaction is in agreement with the observed catalyst deactivation due to loss of S and P from Ni surface.

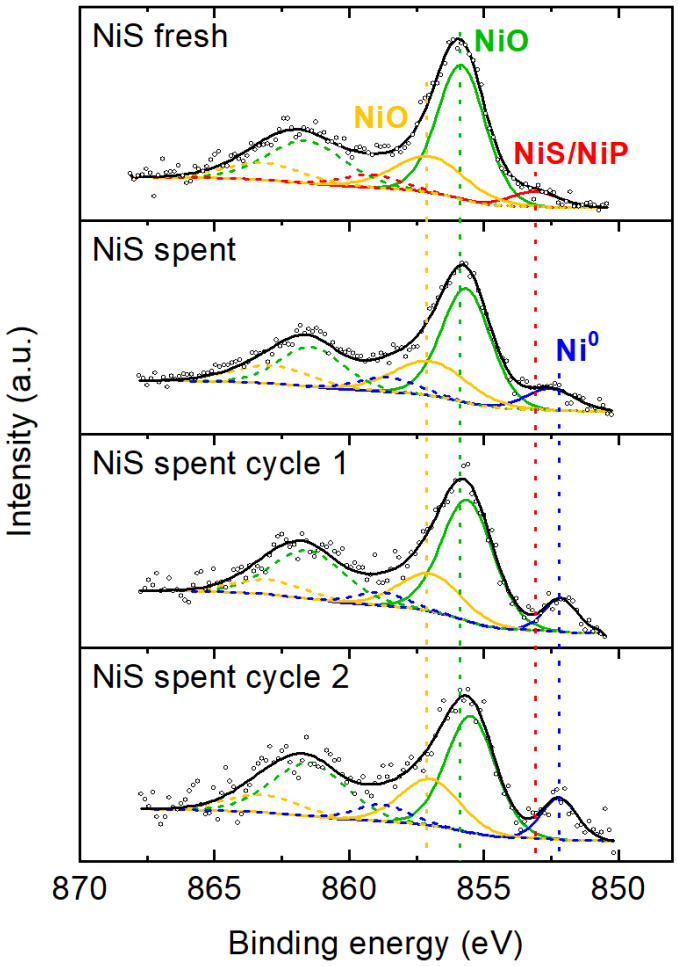

Figure 9. XPS spectra of Ni $2p_{3/2}$ for NiS/γ-Al_2O_3 catalysts: fresh, spent, spent cycle 1 and spent cycle 2. Reaction conditions: 150 °C, 10 bar H_2, 1000 ppmw S (5.8 wt% DBT) and 250 ppmw N (0.23 wt% Q). Spent catalysts were collected after 5 h hydrogenation reaction. Solid lines are Ni $2p_{3/2}$; dash lines are corresponding Ni $2p_{3/2}$ satellite.

5.4 Conclusions

Monometallic transition metal sulfide catalysts, NiS, CoS, FeS and NbS supported on γ-Al_2O_3 were prepared by wet chemistry method with the presence of oleylamine as a stabilizer to prevent nanoparticle agglomeration. Ni-, Co-, Fe- and Cu-doped NbS catalysts, as well as a mono-Cu reference catalyst were prepared by hydrothermally treating as-prepared NbS and doping metal precursor with the presence of thiourea as sulfur source. EDX analysis of as-synthesized NiS catalyst suggest the surface sulfidation and phosphidation of Ni. While hot-injecting elemental S – OAm solution at 300 °C was not sufficient to sulfide Nb. For the Nb-containing bimetallic samples, the hydrothermal treatment improved the degree of Nb sulfidation.

Diolefin hydrogenation was investigated over the synthesized metal sulfide catalysts at mild conditions (150 – 180 °C and 10 – 20 bar H_2 pressure) in the presence of benzothiophene and quinoline. NiS/γ-Al_2O_3 is the most active catalyst for both diolefin and quinoline hydrogenation. The sulfur inhibiting effect by DBT is considered as minor. A strong inhibiting effect by N-compouns is observed, leading to rapid drops in hydrogenation conversions as N concentration increased from 50 – 250 ppm. Cu-NbS outperforms its monometllic forms due to synergistic effect and improved Nb sulfidation; it shows comparable hydrogenation activities with NiS at elevated T and P though (180 °C and 20 bar H_2 pressure).

A kinetic study of diolefin hydrogenation was performed over NiS catalyst at 150 °C and 10 bar H_2 in the presence of 1000 ppmw S and 50 – 250 ppmw N. It has been found that quinoline hydrogenation is zero order respect to quinoline concentration; while diolefin hydrogenation rate constant follows zero order with respect to concentration of diolefin and negative first order to quinoline feed concentration.

Three main causes for catalyst deactivation for the most promising NiS/γ-Al_2O_3 catalyst was N-poisoning, S loss from Ni surface as H_2S, and P migration from Ni surface to alumina support.

5.5 References

[1] Gray, M. R. Fundamentals of partial upgrading of bitumen. *Energy & Fuels* **2019***, 33*, 6843-6856.
[2] Xin, Q.; Alvarez-Majmutov, A.; Dettman, H. D.; Chen, J. Hydrogenation of olefins in bitumen-derived naphtha over a commercial hydrotreating catalyst. *Energy & Fuels* **2018***, 32*, 6167-6175.
[3] Alzaid, A.; Wiens, J.; Adjaye, J.; Smith, K. J. Catalyst deactivation and reactor fouling during hydrogenation of conjugated cyclic olefin over a commercial Ni-Mo-S/γ-Al2O3 Catalyst. *Energy & Fuels* **2018***, 32*, 6213-6223.
[4] Alzaid, A.; Wiens, J.; Adjaye, J.; Smith, K. J. Impact of molecular structure on the hydrogenation and oligomerization of diolefins over a Ni-Mo-S/γ-Al2O3 catalyst. *Fuel* **2018***, 221*, 206-215.

[5] Chomyn, K. D.; Dover, N. J. US3696160, 1972.
[6] Badawi, M.; Vivier, L.; Duprez, D. Kinetic study of olefin hydrogenation on hydrotreating catalysts. *J. Mol. Catal. A* **2010***, 320*, 34-39.
[7] Toba, M.; Miki, Y.; Matsui, T.; Harada, M.; Yoshimura, Y. Reactivity of olefins in the hydrodesulfurization of FCC gasoline over CoMo sulfide catalyst. *Appl. Catal. B* **2007***, 70*, 542-547.
[8] Magyar, S.; Hancsok, J.; Kallo, D. Reactivity of several olefins in the HDS of full boiling range FCC gasoline over PtPd/USY. *Fuel Process. Technol.* **2008***, 89*, 736-739.
[9] Nozaki, F.; Adachi, R. Chemical composition of the catalyst prepared by reducrion of nickel orthophosphate in hydrogen and catalytic activity for partial hydrogenation of 1,3-butadiene. *J. Catal.* **1975***, 40*, 166-172.
[10] Nozaki, F.; Tokumi, M. Hydrogenation activity of metal phosphides and promoting effect of oxygen. *J. Catal.* **1983***, 79*, 207-210.
[11] Nozaki, F.; Kitoh, T.; Sodesawa, T. Promoting effect of oxygen for hydrogenation of butadiene over Ni2P catalyst. *J. Catal.* **1980***, 62*, 286-293.
[12] Cerveny, L.; Paseka, I.; Tobola, S.; Ruzicka, V. Hydrogenation of 2,5-dimethyl-2,4-hexadiene and cis-2-heptene on palladium black modifued by lead, thallium and cadmium. *J. Chem. Tech. Biotechnol.* **1986***, 36*, 144-151.
[13] Karakhanov, E.; Maximov, A.; Kardasheva, Y.; Semernina, V.; Zolotukhina, A.; Ivanov, A.; Abbott, G.; Rosenberg, E.; Vinokurov, V. Pd nanoparticles in dendrimers immobilized on silica-polyamine composites as catalysts for selective hydrogenation. *Appl. Mater. Interfaces* **2014***, 6*, 8807-8816.
[14] Bond, G. C.; Wells, P. B. The Mechanism of the Hydrogenation of Unsaturated Hydrocarbons on Transition Metal Catalysts. *Adv. Catal.* 1965*, 15*, 91-226.
[15] Wells, P. B.; Wilson, G. R. The hydrogenation of alkadiene. Part V. The hydrogenation of trans- and of cis-penta-1,3-diene catalysed by cobalt, nickel, copper, palladium, and platinum. *J. Chem. Soc. A* 1970, 2442-2447.
[16] Karakhanov, E. A.; Maximov, A. L.; Zakharyan, E. M.; Zolotukhina, A. V.; Ivanov, A. O. Palladium nanoparticles on dendrimer-containing supports as catalysts for hydrogenation of unsaturated hydrocarbons. *Mol. Catal.* **2017***, 440*, 107-119.
[17] Wang, Z.; Wang, G.; Louis, C.; Delannoy, L. Novel non-noble bimetallic Cu-Zn/TiO2 catalysts for selective hydrogenation of butadiene. *J. Catal.* **2017***, 347*, 185-196.
[18] Yi, H.; Xia, Y.; Yan, H.; Lu, J. Coating Pd/Al2O3 catalysts with FeOx enhances both activity and selectivity in 1,3-butadiene hydrogenation. *Chinese J. Catal.* **2017***, 38*, 1581-1587.
[19] Jacobsen, C. J. H.; Tornqvist, E.; Topsoe, H. HDS, HDN and HYD activities and temperature-programmed reduction of unsupported transition metal sulfides. *Catal. Lett.* **1999***, 63*, 179-183.
[20] Phillipson, J. J.; Wells, P. B. The hydrogenation of alkadienes. Part III. The hydrogenation of buta-1,3-diene catalysed by iron, cobalt, nickel, and copper. *J. Chem. Soc. A* **1969**, 1351-1363.
[21] Geantet, C.; Afonso, J.; Breysse, M.; Allali, N.; Danot, M. Niobium sulfides as catalysts for hydrotreating reactions. *Catal. Today* **1996***, 28*, 23-30.
[22] Liu, S.; van Muyden, A. P.; Bai, L.; Cui, X.; Fei, Z.; Li, X.; Hu, X.; Dyson, P. J. Metal-sulfide catalysts derived from lignosulfonate and their efficient use in hydrogenolysis. *ChemPubSoc* **2019***, 12*, 3271-3277.
[23] Yui, S.; Chung, K. H. Processing oilsands bitumen. *Oil & Gas J.* **2001***, 99, 17*, 46-53.

[24] Kirsch, F. W.; Shull, S. Selective hydrogenation of butadiene. Catalyst poisoning and stabilization. *I&EC Prodct Research and Development* **1963**, 48-52.
[25] Hatanaka, S.; Yamada, M. Hydrodesulfurization of catalytic cracked gasoline. 2. The difference between HDS active site and olefin hydrogenation active site. *Ind. Eng. Chem. Res.* **1997***, 36*, 5110-5117.
[26] Minaev, P. P.; Koklyukhin, A. S.; Maslakov, K. I.; Nikulshin, P. A. Inhibiting HDS and HYD reactions with qinoline on Co(Ni)–PMo(W)/Al2O3 catalysts: Effect of active phase composition on stability in the hydrotreatment of a model petroleum raw material. *Catal. Ind.* **2017***, 9*, 149-155.
[27] Sanchez-Delgado, R. A.; Machalaba, N.; Ng-a-qui, N. Hydrogenation of quinoline by ruthenium nanoparticles immobilized on poly(4-vinylpyridine). *Catal. Commun.* **2007***, 8*, 2115-2118.
[28] Ulan, J. G.; Maier, W. F. Mechanism of 2-hexyne hydrogenation on heterogeneous palladium. *J. Mol. Catal.* **1989***, 54*, 243-261.
[29] Mourdikoudis, S.; Liz-Marzan, L. M. Oleylamine in nanoparticle synthesis. *Chem. Mater.* **2013***, 25*, 1465-1476.
[30] Thomson, J. W.; Nagashima, K.; Macdonald, P. M.; Ozin, G. A. From sulfur-amine solutions to metal sulfide nanocrystals: Peering into the oleylamine-sulfur black box. *J. Am. Chem. Soc.* **2011***, 133*, 5036-5041.
[31] Zhang, S.; Hao, Y.; Su, D.; Doan-Nguyen, V. V. T.; Wu, Y.; Li, J.; Sun, S.; Murray, C. B. Monodisperse core/shell Ni/FePt nanoparticles and their conversion to Ni/Pt to catalyze oxygen reduction. *J. Am. Chem. Soc.* **2014***, 136*, 15921-15924.
[32] Zhu, H.; Zhang, S.; Huang, Y. X.; Wu, L.; Sun, S. Monodisperse MxFe3−xO4 (M = Fe, Cu, Co, Mn) Nanoparticles and Their Electrocatalysis for Oxygen Reduction Reaction. *Nano Lett.* **2013***, 13*, 2947-2951.
[33] Hou, Y.; Xu, Z.; Sun, S. Controlled Synthesis and Chemical Conversions of FeO Nanoparticles. *Angew. Chem. Int. Ed.* **2007***, 46*, 6329-6332.
[34] Liu, G.; Robertson, A. W.; Li, M. M. J.; Kuo, W. C. H.; Darby, M. T.; Muhieddine, M. H.; Lin, Y. C.; Suenaga, K.; Stamatakis, M.; Warner, J. H.; Tsang, S. C. E. MoS2 monolayer catalyst doped with isolated Co atoms for the hydrodeoxygenation reaction. *Nat. Chem.* **2017***, 9*, 810-816.
[35] Shen, J.; Reule, A. A. C.; Semagina, N. **Ni/MgAl2O4 catalyst for low-temperature oxidative dry methane reforming with CO2**. *Int. J. Hydrog. Energy* **2019***, 44*, 4616-4629.
[36] Ma, R.; Semagina, N. Nanoparticle shape effect study as an efficient tool to reveal the structure sensitivity of olefinic alcohol hydrogenation. *J. Phys. Chem. C* **2010***, 114*, 15417-15423.
[37] Bonita, Y.; Hicks, J. C. In *Chapter 3 Metal phosphides and their applications in catalysis;* Hargreaves, J. S. J., McFarlane, A. R. and Laassiri, S., Eds.; Alternative catalytic materials: carbides, nitrides, phosphides and amorphous boron alloys; Royal Society of Chemistry: 2018; pp 46-70.
[38] Mansouri, A.; Semagina, N. Promotion of niobium oxide sulfidation by copper and its effects on hydrodesulfurization catalysis. *ACS Catal.* **2018***, 8*, 7621-7632.
[39] de Leon, J. M. D.; Kumar, C. R.; Antunez-Garcia, J.; Fuentes-Moyado, S. Recent Insights in Transition Metal Sulfide Hydrodesulfurization Catalysts for the Production of Ultra Low Sulfur Diesel: A Short Review. *Catal.* **2019***, 9*, 87.

[40] Grant, J.; Moyes, R. B.; Wells, P. B. Hydrogenation of alkadienes IX. 1,3-Butadiene hydrogenation catalyzed by rhenium and by sulfur-contaminated rhenium. *J. Catal.* **1978***, 51*, 355-363.
[41] Furimsky, E. Hydrodenitrogenation of petroleum. *Catal. Rev.* **2005***, 47*, 297-489.
[42] Hoang, D. L.; Dang, T. T. H.; Engeldinger, J.; Schneider, M.; Radnik, J.; Richter, M.; Martin, A. TPR investigations on the reducibility of Cu supported on Al2O3, zeolite Y and SAPO-5. *J. Sol. State Chem.* **2011***, 184*, 1915-1923.
[43] Yefremenko, I. G.; Zilberberg, I. L.; Zhidomirov, G. M.; Pak, A. M. Hydrogen activation on copper catalytic sites in stereoselective alkyne hydrogenation. *React. Kinet. Catal. Lett.* **1995***, 56*, 77-86.
[44] Trimbel, A. T. The catalytic hydrogenation of quinoline, Georgia Institute of Technology, Atlanta, USA, 1949.

6 CONCLUSIONS AND RECOMMENDATIONS

6.1 Conclusions

The primary scientific significance is that we suggested and demonstrated a concept that a promoter may catalyze synthesis of active sites. During the catalytic action, the promoter behaves only as a spectator, unless it is used at high surface concentrations. We proved the concept for the sulfided catalysts, but it can be applied for other catalysts that could not be synthesized otherwise because of thermodynamic limitations.

In terms of applied knowledge, we identified Nb-based catalysts as materials with similar HDS and HDN functions as conventional CoMo or NiMo catalysts, but in addition, they possess high hydrocracking activity towards monocyclic hydrocarbons, with no lights formation. Potentially, the Nb catalysts could be beneficial for hydrotreatment of high molecular-weight feeds due to their enhanced cracking and hydrogenating ability, as opposed to CoMo and Mo.

The Nb catalysts could also be used for low-severity hydrotreatment, but they were surpassed by more active and less expensive NiS. The latter demonstrated the higher activity to diolefin hydrogenation than the conventional NiMo catalyst (prepared in-house). None of the open studies, to our knowledge, had addressed the effect of basic nitrogen compounds on olefin/diolefin hydrogenation and catalyst deactivation during low-severity hydrogenations. The nitrogen presence not only suppresses the hydrogenation rate but also changes the reaction order. These findings must be beneficial to practitioners working on olefin hydrogenation of the thermally cracked feed. We recommend comparing the industrial NiMo catalyst with NiS only, as the in-house catalysts showed the superior ability of the Ni-only catalyst for conjugated diolefin and quinoline hydrogenation.

6.2 Recommendations for Future Work

The work relies on the use of hydrogen for upgrading operations, although potentially may be extended to other hydrogen donors. We used a mixture of model sulfur, nitrogen and olefin compounds in this work and identified that certain Nb catalysts can achieve hydrodesulfurization and hydrodenitrogenation, similarly to the conventional promoted Mo catalysts, but the former also possess a remarkable mild cracking activity with no lights formation. As opposed to highly acidic zeolites, the Lewis acidity of Nb sulfide and oxide may provide reduction in the molecular weight of heavy feeds without overcracking and ultrafast coking. It is recommended to assess the Nb catalysts in the real feed hydrotreatment.

We also established a significant reason of catalyst deactivation in olefin hydrotreatment, which is active site poisoning by nitrogen compounds. Our best identified catalyst was a monometallic nickel sulfide and it performed better than MoS_2 or promoted MoS_2. This finding may improve the olefin hydrogenation operations, as currently practiced. It is recommended to assess the NiS catalyst performance in the real feed.

7 APPENDIX A: LIST OF PUBLICATIONS

Refereed journal articles (in preparation, to be submitted)

J. Shen, N. Semagina, Effect of nitrogen inhibition on olefin hydrogenation in sulfur- and nitrogen-containing feed. ***Chemical Engineering Science*** (2020).

Refereed journal articles (published)

A. Mansouri, N. Semagina, Promotion of niobium oxide sulfidation by copper and its effects on hydrodesulfurization catalysis, ***ACS Catalysis***, 8, 7621-7632 (2018).

A. Mansouri, N. Semagina, Colloidal synthesis protocol of shape- and dimensionally-controlled transition-metal chalcogenides and their hydrodesulfurization activities, ***ACS Applied Nano Materials***, 1, 4408-4412 (2018).

Conference presentations

A. Mansouri, N. Semagina,* Promoters catalyze synthesis of active sites. *25th Canadian Symposium on Catalysis*, May 8-11, 2018, Saskatoon, Canada. Oral.

J. Shen,* N. Semagina. Kinetics of olefin hydrogenation inhibited by quinoline. To be submitted and presented at the *17th International Congress on Catalysis*, June 2019, San Diego, USA.

Other

Mansouri A. Toward Earth-abundant metals in hydrodesulfurization catalysts. Ph.D. Thesis, University of Alberta, 2017.

Detailed annual technical reports submitted to IOSI.

Final report to NSERC.

Five progress report presentations given at the biannual meetings/teleconferences with the industrial partner.

8 APPENDIX B: PERMISSIONS TO REPRINT

Title: Promotion of Niobium Oxide Sulfidation by Copper and Its Effects on Hydrodesulfurization Catalysis
Author: Ali Mansouri, Natalia Semagina
Publication: ACS Catalysis
Publisher: American Chemical Society
Date: Aug 1, 2018
Copyright © 2018, American Chemical Society

Logged in as:
Natalia Semagina
Account #: 3000364152
LOGOUT

Quick Price Estimate

Permission for this particular request is granted for print and electronic formats, and translations, at no charge. Figures and tables may be modified. Appropriate credit should be given. Please print this page for your records and provide a copy to your publisher. Requests for up to 4 figures require only this record. Five or more figures will generate a printout of additional terms and conditions. Appropriate credit should read: "Reprinted with permission from {COMPLETE REFERENCE CITATION}. Copyright {YEAR} American Chemical Society." Insert appropriate information in place of the capitalized words.

I would like to...	reuse in an Application/Technical Report
Requestor Type	Author (original work)
Portion	Full article
Format	Print
Will you be translating?	No
Select your currency	USD - $
Quick Price	Click Quick Price

QUICK PRICE CONTINUE

This service provides permission for reuse only. If you do not have a copy of the article you are using, you may copy and paste the content and reuse according to the terms of your agreement. Please be advised that obtaining the content you license is a separate transaction not involving Rightslink.

To request permission for a type of use not listed, please contact the publisher directly.

Copyright © 2019 Copyright Clearance Center, Inc. All Rights Reserved. Privacy statement. Terms and Conditions.
Comments? We would like to hear from you. E-mail us at customercare@copyright.com

Copyright Clearance Center RightsLink®

Home Account Info Help

ACS Publications Most Trusted. Most Cited. Most Read.

Title: Promotion of Niobium Oxide Sulfidation by Copper and Its Effects on Hydrodesulfurization Catalysis
Author: Ali Mansouri, Natalia Semagina
Publication: ACS Catalysis
Publisher: American Chemical Society
Date: Aug 1, 2018
Copyright © 2018, American Chemical Society

Logged in as:
Natalia Semagina
Account #: 3000364152
LOGOUT

PERMISSION/LICENSE IS GRANTED FOR YOUR ORDER AT NO CHARGE

This type of permission/license, instead of the standard Terms & Conditions, is sent to you because no fee is being charged for your order. Please note the following:

- Permission is granted for your request in both print and electronic formats, and translations.
- If figures and/or tables were requested, they may be adapted or used in part.
- Please print this page for your records and send a copy of it to your publisher/graduate school.
- Appropriate credit for the requested material should be given as follows: "Reprinted (adapted) with permission from (COMPLETE REFERENCE CITATION). Copyright (YEAR) American Chemical Society." Insert appropriate information in place of the capitalized words.
- One-time permission is granted only for the use specified in your request. No additional uses are granted (such as derivative works or other editions). For any other uses, please submit a new request.

BACK CLOSE WINDOW

Copyright © 2019 Copyright Clearance Center, Inc. All Rights Reserved. Privacy statement. Terms and Conditions.
Comments? We would like to hear from you. E-mail us at customercare@copyright.com

Copyright Clearance Center RightsLink®

Home Account Info Help

ACS Publications Most Trusted. Most Cited. Most Read.

Title: Colloidal Synthesis Protocol of Shape- and Dimensionally-Controlled Transition-Metal Chalcogenides and Their Hydrodesulfurization Activities

Author: Ali Mansouri, Natalia Semagina

Publication: ACS Applied Nano Materials

Publisher: American Chemical Society

Date: Sep 1, 2018

Copyright © 2018, American Chemical Society

Logged in as:
Natalia Semagina
Account #:
3000364152
LOGOUT

PERMISSION/LICENSE IS GRANTED FOR YOUR ORDER AT NO CHARGE

This type of permission/license, instead of the standard Terms & Conditions, is sent to you because no fee is being charged for your order. Please note the following:

- Permission is granted for your request in both print and electronic formats, and translations.
- If figures and/or tables were requested, they may be adapted or used in part.
- Please print this page for your records and send a copy of it to your publisher/graduate school.
- Appropriate credit for the requested material should be given as follows: "Reprinted (adapted) with permission from (COMPLETE REFERENCE CITATION). Copyright (YEAR) American Chemical Society." Insert appropriate information in place of the capitalized words.
- One-time permission is granted only for the use specified in your request. No additional uses are granted (such as derivative works or other editions). For any other uses, please submit a new request.

BACK CLOSE WINDOW

Copyright © 2019 Copyright Clearance Center, Inc. All Rights Reserved. Privacy statement. Terms and Conditions.
Comments? We would like to hear from you. E-mail us at customercare@copyright.com